

High-resolution study of the Gamow-Teller
strength distribution in the light nuclei ${}^9\text{B}$
and ${}^{13}\text{N}$ using the $({}^3\text{He},t)$ charge-exchange
reaction at 420 MeV beam energy

Inaugural-Dissertation
zur Erlangung des Doktorgrades
der Mathematisch-Naturwissenschaftlichen Fakultät
der Universität zu Köln

vorgelegt von
Clemens Scholl
aus Salzburg

Köln 2010

Berichterstatter:

Prof. Dr. P. von Brentano
Prof. Dr. J. Jolie

Tag der mündlichen Prüfung: 7. Juli 2010

硼

窒

Chinese characters (Kanji) for Boron (硼^{ホウ}) and Nitrogen (窒^{チツ}).

Zusammenfassung

In dieser Arbeit wurden angeregte Zustände in den leichten Kernen ^9B und ^{13}N mit Hilfe der $(^3\text{He},t)$ Ladungsaustauschreaktion untersucht. Dazu wurden am *research center for nuclear physics* (RCNP) in Osaka, Japan Targets aus ^9Be und ^{13}C mit ^3He -Kernen beschossen, die durch das RCNP Ring-Zyklotron auf 420 MeV beschleunigt wurden. Die Tritonen wurden mit dem Magnetspektrometer GRAND RAIDEN analysiert. Mit Hilfe des GRAND RAIDEN Spektrometers und der dispersiven Strahlführung im "WS course" des RCNP ist es möglich die $(^3\text{He},t)$ Reaktion mit rund 30 keV Energieauflösung zu untersuchen, was rund eine Größenordnung besser ist als die Auflösung die mit der (p,n) Ladungsaustauschreaktion erzielbar ist. Die hohe Auflösung erlaubt es Zustände besser zu trennen und schwache Anregungen aufzuspüren. Insgesamt wurden 19 Zustände in ^{13}N und 20 Zustände in ^9B untersucht. In ^{13}N wurden 9 dieser Zustände und in ^9B 10 dieser Zustände als Gamow-Teller Anregungen identifiziert. Ladungsaustauschreaktionen sind mit dem Betazerfall verwandt, und bei verschwindendem Impulsübertrag existiert eine einfache Proportionalität zwischen dem Wirkungsquerschnitt der Ladungsaustauschreaktion und der Fermi (F) oder Gamow-Teller (GT) Stärke im Betazerfall. Während die Fermi Stärke $B(F)$ im Übergang in den isobaren Analogzustand konzentriert ist, verteilt sich die Gamow-Teller Stärke $B(GT)$ auf die angeregten Zustände. Das Hauptziel dieser Arbeit ist die Bestimmung von $B(GT)$ Stärken in den Kernen ^9B und ^{13}N . Die einzige Studie des Kerns ^9B mit Hilfe einer Ladungsaustauschreaktion wurde vor 30 Jahren mit der (p,n) Reaktion durchgeführt. Viele Zustände, vor allem bei hoher Anregungsenergie, konnten in dieser Studie nicht aufgelöst werden. In dieser Arbeit konnten viele schwach angeregte Zustände mit kleinen Zerfallsbreiten bei hohen Anregungsenergien (12-19 MeV) getrennt beobachtet werden. Die Verteilung der $B(GT)$ Stärken wurde ebenfalls bestimmt mit Hilfe neuer Daten aus dem Betazerfall von ^9C und ^9Li . Die Ergebnisse deuten darauf hin, dass es starke Unterschiede in der Kernstruktur der niedrigliegenden Zustände von ^9B und den hochangeregten Zuständen gibt. Dieses Ergebnis wird auch durch theoretische Rechnungen und Daten aus dem Betazerfall bestätigt. Darüber hinaus konnte die Information über Anregungsenergien und Zerfallsbreiten in beiden Kernen signifikant verbessert werden. Der Kern ^{13}N wurde zuletzt 2001 mit Hilfe der (p,n) Reaktion untersucht. Ein $(^3\text{He},t)$ Experiment wurde ebenfalls vor einigen Jahren (2004) am RCNP Osaka durchgeführt, allerdings mit niedrigerer Auflösung von rund 300 keV. In dieser Arbeit wurde die $(^3\text{He},t)$ Reaktion mit hoher Auflösung (30 keV) benutzt um die Verteilung der $B(GT)$ Stärken in ^{13}N zu bestimmen. Die Targetanreicherung und die hohe Auflösung der Spektren erlaubte es den $T=3/2$ Zustand bei 15.1 MeV vom ^{12}N Grundzustand zu trennen und ermöglichte somit eine präzise Untersuchung der Verteilung der GT Stärke in ^{13}N .

Abstract

Excited states in the light nuclei ${}^9\text{B}$ and ${}^{13}\text{C}$ were studied using the $({}^3\text{He},\text{t})$ charge-exchange reaction on ${}^9\text{Be}$ and ${}^{13}\text{C}$ targets. The measurements were performed at the research center for nuclear physics (RCNP) in Osaka, Japan, using the magnetic spectrometer GRAND RAIDEN and the dispersive WS course. The ${}^3\text{He}$ beam with an energy of 420 MeV was accelerated by the RCNP Ring Cyclotron. The GRAND RAIDEN spectrometer and the WS course allow to study the $({}^3\text{He},\text{t})$ charge-exchange reaction with an energy resolution of around 30 keV, which is one order of magnitude better than measurements with the (p,n) charge-exchange reaction. The high resolution allows to better separate individual states and to determine weak excitation strengths because of low background in the spectra. A total of 19 states in ${}^{13}\text{N}$ were studied, and a total of 20 states were observed in ${}^9\text{B}$. Of these, 9 states in ${}^{13}\text{C}$ and 10 states in ${}^9\text{B}$ were identified as being excited by a Gamow-Teller transition. Charge-exchange reactions are related to beta-decay, and at zero momentum transfer a simple proportionality exists between the cross-section of the charge-exchange experiment and the Fermi (F) or Gamow-Teller (GT) beta-decay strength. While the Fermi strength $B(\text{F})$ is concentrated in the transition to the isobaric analog state, the Gamow-Teller strength $B(\text{GT})$ is scattered among the excited states. The main aim of the present study is to determine the $B(\text{GT})$ strengths in the nuclei ${}^9\text{B}$ and ${}^{13}\text{N}$. The only charge-exchange study of ${}^9\text{B}$ was made 30 years ago with the (p,n) reaction and a resolution of around 300-400 keV. Many states, especially at high excitation energy, could not be resolved by this study. The present work was able to separate many weakly excited states with small decay width at high excitation energies (12-19 MeV) in ${}^9\text{B}$ and determine the $B(\text{GT})$ strength distribution by using recent high-precision beta-decay data. The results point to a strong difference in spatial structure between the low-lying levels of ${}^9\text{B}$ and the levels with high excitation energy. This result is also corroborated by beta-decay measurements and theoretical calculations. Furthermore, the information on excitation energies and decay widths in both nuclei could significantly be improved. The nucleus ${}^{13}\text{N}$ has last been studied in 2001 using the (p,n) reaction. A $({}^3\text{He},\text{t})$ experiment was also performed at the RCNP Osaka a few years ago (2004), however with a lower resolution of around 300 keV. In the present work, the $({}^3\text{He},\text{t})$ reaction with high resolution (30 keV) was used to determine the $B(\text{GT})$ strength distribution in ${}^{13}\text{N}$. The target enrichment and high resolution of the spectrum allowed to isolate the $T=3/2$ state at 15.1 MeV from the ${}^{12}\text{N}$ ground state and thus provide a high-precision analysis of the GT strength distribution in ${}^{13}\text{N}$.

Contents

1	Introduction	1
1.1	Gamow-Teller transitions and charge-exchange reactions	1
1.2	The determination of B(GT) strengths using charge-exchange reactions .	4
1.3	The proportionality and experimental requirements	7
1.4	Nuclei studied in this work	9
2	Experiments	11
2.1	Overview of the performed experiments	11
2.2	The Grand Raiden Spectrometer	12
2.3	The focal plane detector and trigger system	15
2.4	Beam matching techniques and beam tuning	18
2.4.1	Lateral and angular dispersion matching	18
2.4.2	Faint beam tuning	21
2.4.3	Off-focus mode	24
3	Spectrum reconstruction	27
3.1	Particle identification	27
3.2	Track reconstruction in the multiwire drift chambers	31
3.3	Reconstruction of the scattering angle	35
3.4	Correction of ϕ and θ -aberrations	38
4	Data Analysis	41
4.1	Projections of 2D Spectra and calibration	41
4.2	Peak fitting	41
4.3	Determination of errors	43
4.4	Identification of contaminant peaks	43

4.5	The $^{13}\text{C}(^3\text{He},t)^{13}\text{N}$ spectrum	44
4.5.1	Excitation energies from 0 to 6.5 MeV	44
4.5.2	Excitation energies from 6 to 16 MeV	47
4.5.3	Excitation energies from 17 to 30 MeV	51
4.6	The $^9\text{Be}(^3\text{He},t)^9\text{B}$ spectrum	54
4.6.1	Excitation energies from 0 to 10 MeV	54
4.6.2	Excitation energies from 10 to 16 MeV	59
4.6.3	Excitation energies from 16 to 25 MeV	60
4.7	Identification of $\Delta L=0$ states in the $(^3\text{He},t)$ reaction	63
4.8	Determination of Cross-sections	66
5	Extraction of Gamow-Teller strengths	75
5.1	DWBA calculations	75
5.1.1	Q-values	75
5.1.2	DWBA calculation parameters	76
5.2	Angular distribution of cross-sections	77
5.3	Cross-sections of the $^{13}\text{C}(^3\text{He},t)^{13}\text{N}$ reaction	79
5.4	Cross-sections of the $^9\text{Be}(^3\text{He},t)^9\text{B}$ reaction	87
5.5	Gamow-Teller strengths for the ^{13}C target	94
5.6	Gamow-Teller strengths for the ^9Be target	100
6	Interpretation of the obtained results and comparison with previous studies	103
6.1	GT strength in ^{13}N	103
6.2	B(GT) strengths in ^9B	107
6.3	Clusters, the NCSM and beta-decay	111
7	Summary	117
	Appendix	I
A	Beam optics	I
A.1	Beam coordinates	I
A.2	Beam transformation	II

B	Angular calibration procedure	VII
B.1	Reconstruction of the scattering angle	VII
B.1.1	Reconstruction of ϕ_{tgt}	IX
B.1.2	Reconstruction of θ_{tgt}	XXIX
B.1.3	Results of the multi-hole slit calibration	LV
B.2	Correction of aberrations	LVIII
B.2.1	The aberration as a mapping	LVIII
B.2.2	Cubic spline interpolation	LVIII
B.2.3	Implementation in computer code	LXIV
C	Energy calibration procedure	LXIX
D	RAY-ID data from the MWDCs for both experiments	LXXVII
E	Calculation of the factor $F(\omega, 0^\circ)$ using DWBA	LXXIX
F	Publication List	LXXXIII
F.1	Journal publications	LXXXIII
F.2	Conference proceedings	LXXXVI

Chapter 1

Introduction

1.1 Gamow-Teller transitions and charge-exchange reactions

"I decided to get a Ph.D. in experimental physics because experimental physicists have their own room in the Institute where they can hang their coat, whereas theoretical physicists have to hang their coat at the entrance."

George Gamow (1904-1968)

Charge-exchange reactions in nuclear collisions result from the exchange of a proton and a neutron between the projectile and the target nucleus. In this work, the focus is on the ($^3\text{He}, t$) charge-exchange reaction at intermediate beam energy ($E/A=140$ MeV/nucleon).

Charge-exchange reactions share many similarities with beta-decay, where the neutron is converted into a proton (β^- decay) or *vice versa* (β^+ decay) as a result of the weak interaction. In beta-decay, allowed transitions (that is, those transitions that can be described in an approximation where the transition operator is independent of the positions and velocities of the nucleons [Boh69]) can be divided in two types. One is the *Fermi* transition (F), where the operator is independent of the nucleon spin, and only mediated by the isospin operator τ^\pm , which transforms a neutron into a proton and *vice versa*. The other is the *Gamow-Teller* (GT) transition, where the operator is proportional to the spin operator (σ) of the decaying nucleon. The operator of the GT transition is the spin-isospin operator $\sigma\tau^\pm$, and the corresponding reduced transition strength $B(\text{GT})$ for a system with a number A of nucleons is defined as

$$\begin{aligned} B(\text{GT}_\pm; J_i, T_i, T_{zi} \rightarrow J_f, T_f, T_{zf}) &= \frac{1}{2(2J_i + 1)} \left| \left\langle J_f T_f T_{zf} \left| \sum_{j=1}^A \sigma_j \tau_j^\pm \right| J_i T_i T_{zi} \right\rangle \right|^2 \\ &= \frac{\langle T_i T_{zi} \Delta T \Delta T_z | T_f T_{zf} \rangle^2}{2(2J_i + 1)(2T_f + 1)} M_{\text{GT}}(\sigma\tau^\pm)^2. \end{aligned} \quad (1.1)$$

As with electromagnetic reduced transition strengths, it is important to be careful about the direction of the transition (initial and final state).

Experimentally, the $B(GT)$ value can be obtained from the beta-decay partial half-life t_i of a state via the ft value if there is no Fermi part in the decay:

$$B(GT) = \frac{K}{g_V^2} \cdot \frac{1}{\lambda^2 ft_i} \quad (1.2)$$

where K is a constant defined by [Har09]

$$\frac{K}{g_V^2} = \frac{2\pi^3 \hbar^7 \ln 2}{m_e^5 c^4 g_V^2} = 6147(7)s \quad (1.3)$$

and $\lambda = g_A/g_V$ is the ratio of weak interaction coupling constants which has a value of $-1.2695(29)$ [Har06]. As K/g_V^2 and ft are measured in seconds, $B(GT)$ is a dimensionless quantity. It should however be noted that some authors include the factor λ^2 into the $B(GT)$ value so special attention is required to make sure which definition of $B(GT)$ (including or not including the factor λ^2) was used for the determination of a quoted $B(GT)$ value. The present work does not include λ^2 in the $B(GT)$ value, which is the common standard used in studies involving charge-exchange reactions.

For the transition between isobaric analog states (IAS), which can be mediated by the τ operator alone, the resulting Fermi strength has to be taken into account. The reduced transition strengths $B(GT)$ and $B(F)$ (for the Fermi transition) then connect to the ft value as follows:

$$B(F) + \lambda^2 B(GT) = \frac{K}{g_V^2} \cdot \frac{1}{ft_i} \quad (1.4)$$

The Fermi strength is concentrated in the transition to the isobaric analog state of the ground state of the initial nucleus and has the value $|N - Z|$ (Fermi sum rule) [Ost92, Orm95].

Both the Fermi and the Gamow-Teller transitions have spin, isospin and parity selection rules which are summarized in table 1.1.

While $B(GT)$ values can accurately be determined in beta-decay studies, their main limitation is the decay Q -value so that only low-lying states can be studied, and only the transition in one direction. In order to overcome this limitation and obtain $B(GT)$ values at higher excitation energies, charge-exchange (CE) reactions of the (p,n) or (n,p) type can be used.

When using the nuclear reaction, the projectile-target interaction becomes important. This interaction is usually very complicated, depending on the energy of the incident particle and the properties of the target nucleus. Solving the scattering problem involves the strong interaction NN-potentials, which result in a final weak *effective* interaction. Love and Franey [Lov81, Fra85] wrote the effective interaction V_{12} between the nucleons 1 and 2 involved in the reaction as a sum of central (C), spin-orbit (LS) and tensor (T) terms with spin-isospin decomposition:

$$\begin{aligned} V_{12}(r) = & V_0^C(r) + V_\sigma^C(r)\sigma_1\sigma_2 + V_\tau^C(r)\tau_1\tau_2 + V_{\sigma\tau}^C(r)\sigma_1\sigma_2\tau_1\tau_2 \\ & + (V_0^{LS}(r) + V_\tau^{LS}(r)\tau_1\tau_2) L_{12} \cdot S \\ & + (V_0^T(r) + V_\tau^T(r)\tau_1\tau_2) S_{12}(\hat{r}) \end{aligned} \quad (1.5)$$

Table 1.1: Selection rules for Fermi (F) and Gamow-Teller (GT) transitions. The transitions connect an initial state with angular momentum and parity J_i^π and isospin quantum numbers T_i, T_{zi} to a final state with quantum numbers J_f^π, T_f, T_{zf} .

FERMI	
$J_i = J_f$	$\Delta J = 0$
$T_f = T_i \neq 0$	$\Delta T = 0$, but $0 \rightarrow 0$ forbidden
$T_{zf} = T_{zi} \pm 1$	$\Delta T_z = \pm 1$
$\Delta \pi = 0$	no parity change
GAMOW-TELLER	
$\Delta J = 0, \pm 1$	but $J_i = 0 \rightarrow J_f = 0$ forbidden
$\Delta T = 0, \pm 1$	but $T_i = 0 \rightarrow T_f = 0$ forbidden
$T_{zf} = T_{zi} \pm 1$	$\Delta T_z = \pm 1$
$\Delta \pi = 0$	no parity change

where $S = s_1 + s_2$ is the total two-nucleon spin, L_{12} the relative angular momentum operator between the two nucleons and $S_{12}(\hat{r}) = 3\sigma_1 \hat{r} \sigma_2 \hat{r} - \sigma_1 \sigma_2$ is the tensor operator. All interaction coefficients depend on the relative coordinate $r = r_1 - r_2$ of the two nucleons.

The spin-isospin mode which is of interest for the study of GT transitions is excited via the $V_{\sigma\tau}^C(r)\sigma_1\sigma_2\tau_1\tau_2$ component of the interaction. This component should thus be maximized against other components to study GT strengths. The energy and momentum transfer dependence of the components of the effective interaction were studied by Love and Franey[Lov81, Fra85], and the energy and momentum transfer dependence of the components is reproduced in the figures 1.1 and 1.2. They show clearly that at intermediate bombarding energies ($E \approx 100$ -140 MeV) and at zero momentum transfer, the $\sigma\tau$ component becomes dominant, while the τ component becomes suppressed.

The low momentum transfer is achieved at forward angles. Since at small momentum transfer a multipole expansion of the transition operator is possible, a simple relation between the cross-section at zero degrees scattering angle and the beta-decay strength can be expected. Indeed, a simple proportionality [Goo80] was discovered. This proportionality has been studied in detail both theoretically and experimentally by Taddeucci *et al.* [Tad87], resulting in the formula

$$\frac{d\sigma}{d\Omega}(q, \omega) = K(E_i, \omega) \cdot N^D(q, \omega) \cdot |J_{GT}|^2 \cdot B(GT) \quad (1.6)$$

where K is a kinematic factor, N^D a distortion factor and J_{GT} represents the volume integral of the nucleon-nucleus effective interaction central component $V_{\sigma\tau}^C$. The momentum transfer is denoted by q , the energy of the incident particle by E_i and $\omega = E_x - Q_{gs}$ is the energy loss (excitation energy of excited state expressed in terms of excitation energy relative to the ground state of the target nucleus). The kinematic and distortion factors

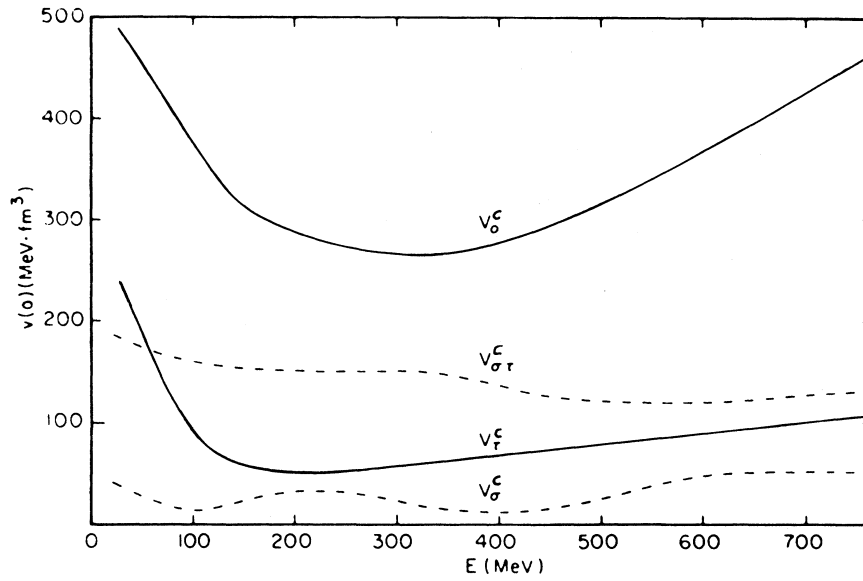


Figure 1.1: Energy dependence of the central components of the effective interaction V_{12} at zero momentum transfer, including direct and exchange terms. Figure taken from [Ost92]. The horizontal axis is the bombarding energy expressed in MeV/nucleon.

are given by

$$K(E_i, \omega) = \frac{E_i E_f k_f}{(\hbar^2 c^2 \pi)^2 k_i} \quad (1.7)$$

$$N^D(q, \omega) = \frac{\frac{d\sigma}{d\Omega}(DW; q, \omega)}{\frac{d\sigma}{d\Omega}(PW; q = 0, \omega = 0)}. \quad (1.8)$$

The distortion factor N^D is defined by the ratio of plane-waves and distorted-waves cross-sections.

The proportionality relation (1.6) allows to determine B(GT) strengths for higher excitation energy regions when a reference B(GT) value is known.

1.2 The determination of B(GT) strengths using charge-exchange reactions

The proportionality of eq. (1.6) was established and tested using the (p,n) reaction. Owing to the time of flight (TOF) measurement used in the neutron analysis, the energy resolution is of the order ≈ 300 keV, which greatly restricts the study of individual levels in mirror nuclei.

Despite the complexity of the projectile and ejectile, the ($^3\text{He}, t$) reaction offers an interesting alternative to the (p,n) reaction. At intermediate energies of 100-200 MeV per nucleon, the ($^3\text{He}, t$) reaction mechanism is expected to become simpler and can be approximated as a one-step reaction mechanism. The triton ejectile can be analyzed by a

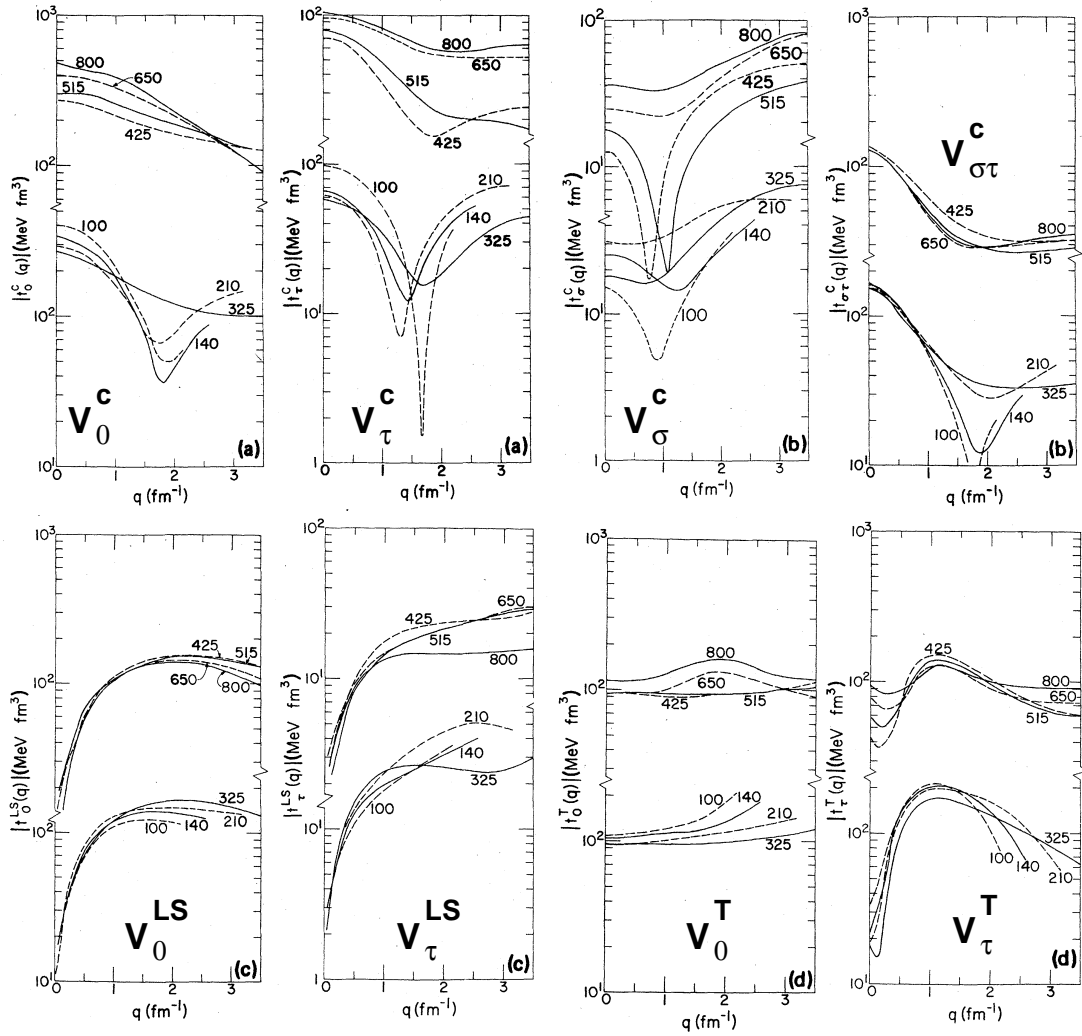


Figure 1.2: The strength of the components of the effective interaction V_{12} as a function of bombarding energy (number on curve) and momentum transfer, including direct and exchange terms. It can be seen that at zero momentum transfer, the non-central terms of the interaction can be neglected at intermediate energy (100-140 MeV), while the strength of $V_{\sigma\tau}^C$ is maximal. Figure taken from [Lov81], slightly edited.

magnetic spectrometer, thus enabling studies with much higher resolution (e.g. [Fuj99a, Fuj02b]). The proportionality relation (1.6) has also been shown to hold for the ($^3\text{He},t$) probe at intermediate energies. At the research center for nuclear physics (RCNP) in Osaka, an energy resolution of ≈ 30 keV can nowadays be achieved for the ($^3\text{He},t$) reaction at beam energy 140 MeV/nucleon.

For experimental purposes, the proportionality relation between the $B(GT)$ strength and the differential cross-section can be rewritten in a simpler form, as

$$\left. \frac{d\sigma}{d\Omega} \right|_{q=0} = \hat{\sigma}_{GT} B(GT) \quad (1.9)$$

with the *unit cross section* $\hat{\sigma}_{GT}$ acting as the proportionality factor. This unit cross-section can be determined when a $B(GT)$ value is known from beta-decay by relating it to the cross-section at $q=0$.

Experimentally, the $q=0$ cross-section has to be extrapolated from measurements at finite scattering angle around zero degrees. Depending on the excitation energy, the unit cross section also has to be adjusted for the kinematic and distortion factor, which is done by a DWBA calculation.

For the transition to the IAS, a similar proportionality relation holds, involving the Fermi unit cross-section $\hat{\sigma}_F$ and the Fermi strength $B(F)$:

$$\left. \frac{d\sigma}{d\Omega} \right|_{q=0} = \hat{\sigma}_F B(F) + \hat{\sigma}_{GT} B(GT) \quad (1.10)$$

When analyzing the transition to the IAS, the Fermi part of the total differential cross-section thus has to be isolated in order to obtain the $B(GT)$ strength. In cases where both a pure $B(GT)$ transition is known (to determine $\hat{\sigma}_{GT}$) and the IAS $B(GT)$ is known, $\hat{\sigma}_F$ can be determined.

The unit cross sections $\hat{\sigma}_F$ and $\hat{\sigma}_{GT}$ and their nuclear mass and energy dependence have been studied in detail for the (p,n) reaction (see figure 1.3). The mass dependence takes the form of a rather smooth curve. Being able to roughly calibrate the unit cross section via such a systematic mass dependence is very useful when not all $B(GT)$ values required for a calibration of the cross-section are available. A unit cross-section determined from systematics can then be used as a placeholder in order to determine $B(GT)$ strengths via the CE reaction.

A systematic study [Zeg07] was recently carried out using the available ($^3\text{He},t$) data to determine the mass A dependence of the unit cross-sections at beam energy 140 MeV/nucleon.

The empirical relations

$$\hat{\sigma}_F = 72 \cdot A^{-1.06} \text{ mb/sr} \quad (1.11)$$

$$\hat{\sigma}_{GT} = 109 \cdot A^{-0.65} \text{ mb/sr} \quad (1.12)$$

were found as best fits to the experimental data (see fig. 1.4). It has been shown [Col06] that contributions from the tensor- τ part of the effective central interaction (V_τ^T) produce interferences between the $\Delta L=0$ GT amplitude and $\Delta L=2$ amplitudes, which experimentally lead to higher than expected unit cross-sections in some cases. The correction

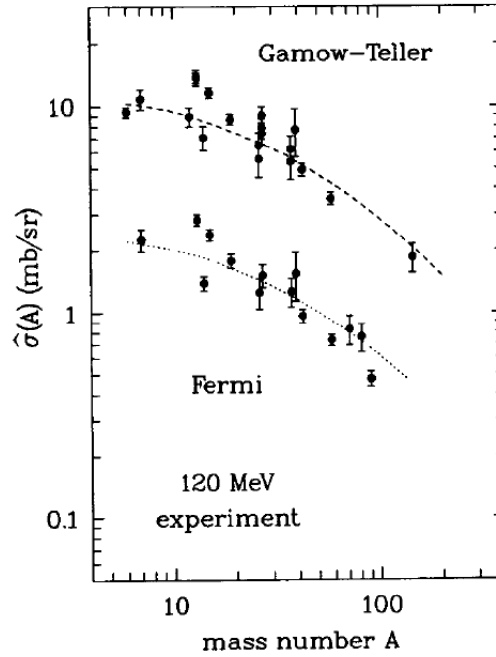


Figure 1.3: $\hat{\sigma}_{F,GT}$ as a function of mass number A for (p,n) reactions at 120 MeV. Figure taken from [Tad87].

deduced from the treatment of V_τ^T has the right sign and magnitude to account for the deviations.

The unit cross-sections for a given nucleus and beam energy are also often presented in the literature via the ratio R^2

$$R^2 = \frac{\hat{\sigma}_{GT}}{\hat{\sigma}_F}. \quad (1.13)$$

1.3 The proportionality and experimental requirements

In order to study GT strengths with CE reactions and to use the proportionality relation between cross-section and $B(GT)$ strength, several requirements have to be fulfilled in the measurement. They are, in summary, the following:

- The proportionality is only valid for states that are excited via angular momentum transfer $\Delta L=0$. Other states, which are not of Fermi and/or Gamow-Teller nature may also be excited by the reaction. It must be possible to isolate these states in the measurements obtained with the probe. In the $(^3\text{He},t)$ reaction, this is done via the angular distribution of cross-sections, which is strongly forward-peaked for $\Delta L=0$ transitions (see 4.7). Zero angular momentum transfer is a requirement for obtaining states excited with the $\sigma\tau$ operator. In case L is not a good quantum number, $\Delta L=0$ means that the wavefunctions of the initial and the final states have components with the same values of L .

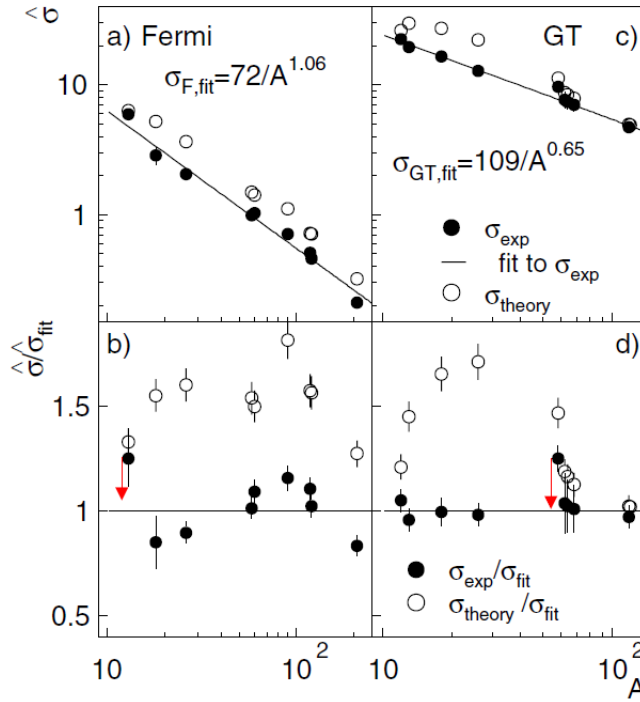


Figure 1.4: $\hat{\sigma}_{F,GT}$ as a function of mass number A for $(^3\text{He}, t)$ reactions at 140 MeV/nucleon. Figure taken from [Zeg07]. The arrows show the correction if the effect from the tensor- τ interaction is removed (see text).

- The reaction must take place under conditions such that the reaction is well-described as a single-step transition. The $(^3\text{He}, t)$ probe at intermediate energies fulfils this requirement.
- The proportionality is given for momentum transfer $q=0$ and energy loss $\omega=0$. Experimentally, this requires the extrapolation to the scattering angle at zero degrees and the extrapolation to zero Q -value by using DWBA. The zero-degree measurements with the GRAND RAIDEN spectrometer at the RCNP Osaka allow for the extrapolation to zero degrees scattering angle due to the high angle resolution (see 4.8).
- It was shown by Love and Franey [Lov81, Fra85] and used by Taddeucci *et al.* [Tad87] that the effect of the $\sigma\tau$ operator is best isolated at intermediate beam energies (100-150 MeV/nucleon). This result does not depend on the probe structure, so it is generally fulfilled for any charge-exchange reaction. The main physical reason is that the mass of the pion is around 140 MeV/ c^2 so that, at a beam energy of around 140 MeV/nucleon, the probability of one-pion exchange is maximal, and so the action of the $\sigma\tau$ operator.

1.4 Nuclei studied in this work

Based on the main principles outlined in this introduction, this work was aimed at determining $B(\text{GT})$ strengths in the nuclei ${}^9\text{B}$ and ${}^{13}\text{N}$ by using the $({}^3\text{He}, t)$ reaction on ${}^9\text{Be}$ and ${}^{13}\text{C}$ targets at 140 MeV/nucleon beam energy.

In the $A=13$ system, beta-decay information is available for calibrations purposes for the ${}^{13}\text{N}(\beta^+)$, the ${}^{13}\text{O}(\beta^+)$ and the ${}^{13}\text{B}(\beta^-)$ decays. The isobar diagram of the $A=13$ system is shown as a reference in figure 1.5. The nucleus ${}^{13}\text{N}$ has already been studied in (p, n) , most recently by Wang *et al.* [Wan01], and in $({}^3\text{He}, t)$ (with much lower resolution) by Fujimura *et al.* [Fuj04a] and Zegers *et al.* [Zeg08]. While Zegers *et al.* mainly focused on the determination of the $B(\text{GT})$ value of the 3.5 MeV state in ${}^{13}\text{N}$, this work will give a detailed analysis of the $B(\text{GT})$ distribution up to 20 MeV excitation energy. Our results compare well to the (p, n) results by Wang *et al.*, as will be shown in 5.5.

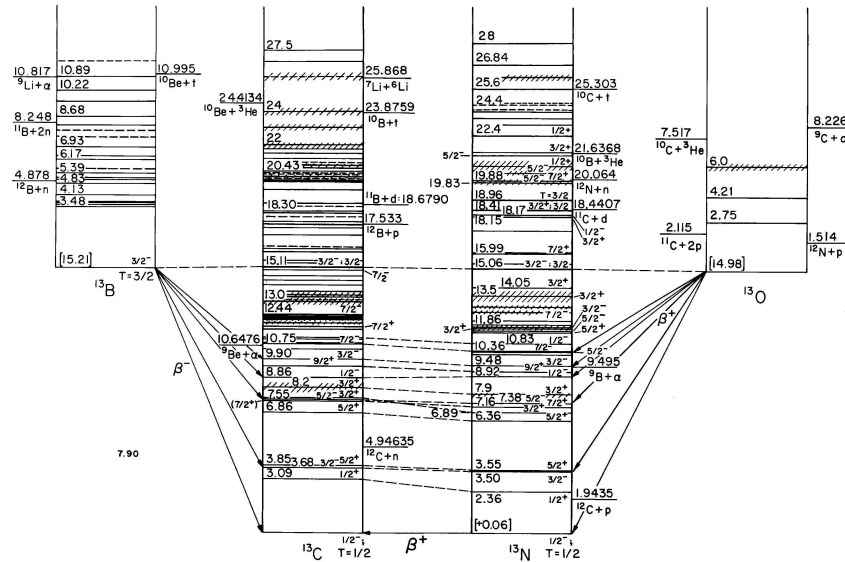


Figure 1.5: Isobar diagram of the $A=13$ system, reproduced from [AS91].

The $A=9$ system (whose isobar diagram is shown in fig. 1.6) has not been extensively studied with charge-exchange reactions. In 1980, a ${}^9\text{Be}(p, n)$ experiment was carried out at 135 MeV proton energy at the Indiana University Cyclotron Facility (IUCF) [Pug85, Faz82] with an energy resolution of about 300-400 keV. At that time, beta-decay data was not available to determine $B(\text{GT})$ values, so only cross-sections were determined. Recent high-precision data is available for the beta decays of ${}^9\text{Li}$ and ${}^9\text{C}$ so that a calibration using the ground-state decays of those nuclei was possible, although their $B(\text{GT})$ strengths are very weak. $B(\text{GT})$ strengths in ${}^9\text{B}$ are more difficult to calibrate since there is no ground-state beta decay between ${}^9\text{B}$ and ${}^9\text{Be}$. The present study made use of the mass-number systematics of the R^2 value in order to estimate the Fermi part of the ground state transition. The higher resolution and sensitivity of the $({}^3\text{He}, t)$ reaction also made the characterization of highly-excited states easier, so that the cross-sections of individual states could be established.

The experimental work was carried out at the cyclotron facility of the research center

for nuclear physics (RCNP) in Osaka, Japan. The next chapter will deal in detail with the experimental setup and the techniques used to obtain a high-resolution spectrum.

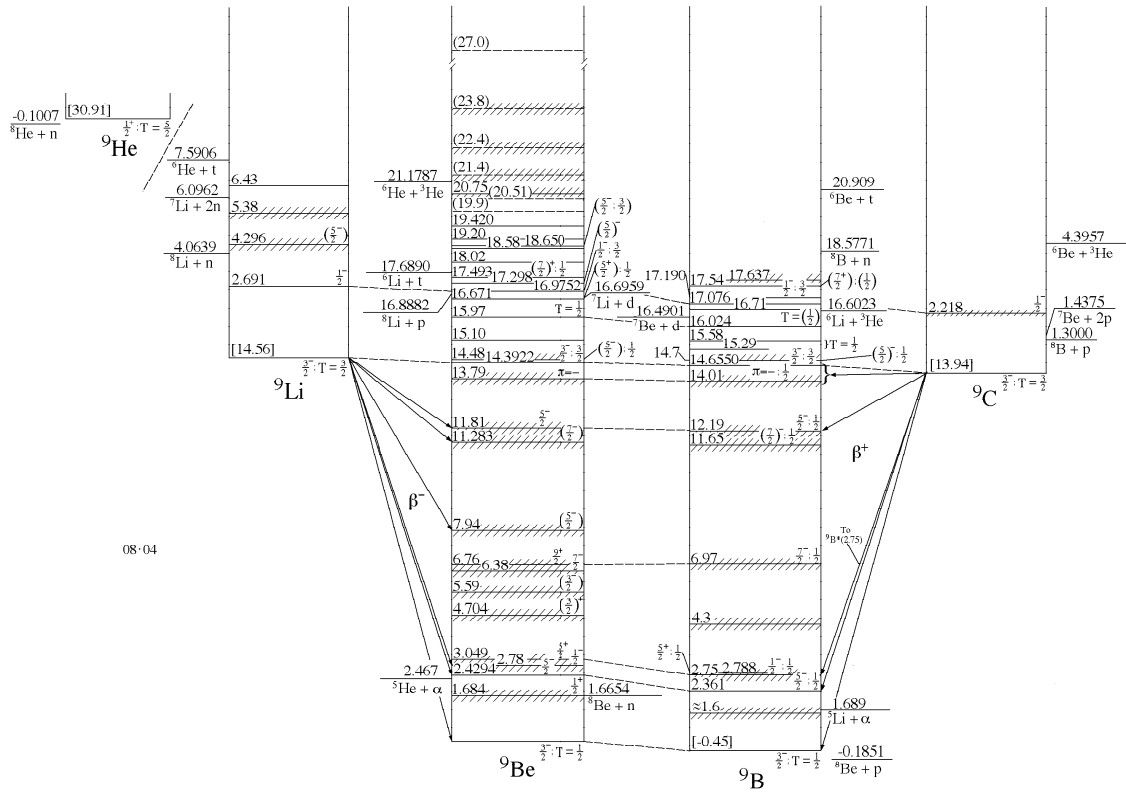


Figure 1.6: Isobar diagram of the A=9 system, reproduced from [Til04].

Chapter 2

Experiments

This chapter describes the experiments carried out within the scope of the thesis. It will describe in detail the experimental setup at the accelerator facility of the RCNP Osaka, and various techniques used for the achievement of beam and detector conditions suitable for the experiments.

2.1 Overview of the performed experiments

The experiments were performed at the *Research Center for Nuclear Physics*¹ (RCNP), Osaka University. The ^3He beam was accelerated by the K=120² AVF³ Cyclotron, boosted up to 420 MeV (140 MeV/A) by the K=400 Ring Cyclotron and guided to the target through the WS beam line. Details on the beam tuning, focussing and matching will be given in subsequent sections. Targets of metallic ^9Be under vacuum (thickness of 1.73 mg/cm²) and ^{13}C in the form of 99% enriched polyethylene⁴ (thickness 0.5 mg/cm²) were used to study excited states in ^9B and ^{13}N via the ($^3\text{He}, t$) reaction. The specification of other targets used for calibration can be found in the Appendix C, Table C.1. The outgoing tritons ($A/Z=3$) were momentum-analyzed by the GRAND RAIDEN spectrometer which will be explained in more detail in the next section. Scattered $^3\text{He}^{++}$ ($A/Z=3/2$) particles were dumped into the Faraday cup installed in the first dipole magnet (D1), which was also used to monitor the beam current. At the focal plane, the particles were traced using multiwire drift chambers (MWDC) for track reconstruction and plastic scintillators for particle identification and triggering of the MWDCs. The data was taken at a spectrometer angle of zero degrees.

¹Japanese name: おおさかだいがくかくぶつりけんきゅう 大阪大学 核物理研究センター (*Ōsaka Daigaku Kakubutsuri Kenkyū Sentā*)

²The K number of a cyclotron gives the energy up to which ions can be accelerated. If ions have a charge Q (given in units of the elementary charge e) and a mass A (given in units of the atomic mass unit u), then for a given K number these ions can be accelerated up to the energy $E_{\text{acc}} = K \frac{(Q/e)^2}{A}$, where E_{acc} is given in MeV [Kat89, Cla90].

³Azimuthally varying field

⁴ $[-\text{H}_2\text{C} - \text{CH}_2-]_n$

Table 2.1: Specifications of the RCNP cyclotrons [Kat89].

	Ring Cyclotron	AVF Cyclotron
Number of sector magnets	6	3
Injection radius [m]	2	
Extraction radius [m]	4.04	1
Magnet gap [cm]	6	20.7 (min)
Proton max. energy [MeV]	400	84
α particle energy [MeV]	400	130
^3He energy [MeV]	510	160
Weight of magnet [t]	2000	400
Main coil power [kW]	450	450
Trim coil power [kW]	250	265
Number of cavities	3	1
Radio frequency (RF) power [kW]	250x3	120

2.2 The Grand Raiden Spectrometer

The spectrometer GRAND RAIDEN⁵ consists of three dipole magnets (D1,D2, and DSR), two quadrupole magnets (Q1 and Q2), a sextupole magnet (SX) and a multipole magnet (MP). The schematic arrangement of the magnets that make up the GRAND RAIDEN is shown in fig.2.2, and its specifications and ion-optical properties are summarized in table 2.2. Its stand-out features are the high momentum resolution $p/\Delta p$ and its large magnetic rigidity⁶. In order to gain a large acceptance for vertical scattering angles⁷, a strong quadrupole magnet (Q1) is placed near the scattering chamber. Second-order ion-optical properties like the tilting angle of the focal plane are adjusted by the sextupole magnet (SX). The multipole magnet (MP) which is placed between the two dipole magnets (D1 and D2) can generate quadrupole, sextupole, octupole and decapole fields to correct higher order aberrations. The third dipole magnet (DSR) was installed for measurements of the in-plane polarization transfer, and was not used in the experiments. A comprehensive review of the GRAND RAIDEN spectrometer can be found in the paper by M. Fujiwara *et al.* [Fuj99b].

⁵named after らいでん ためえもん 雷電 爲右衛門 (*Raiden Tameemon*) (1767-1825), considered one of the greatest sumo wrestlers in history.

⁶The magnitude of the magnetic field B times the gyroradius of a charged particle equals to its momentum per unit charge, also called magnetic rigidity ($B \cdot r = \frac{mv\perp}{|q|}$)

⁷The vertical angle is crucial for the identification of $\Delta L=0$ transitions, see details regarding the *overfocus mode* in section 2.4.3.

Table 2.2: Specifications of the Grand Raiden magnetic spectrometer [Kat89, Ada07, Shi05].

Mean orbit radius	3m
Total deflection angle	162°
Measurable angle	-4° to 90°
Momentum range	5%
Momentum dispersion	15.45 m
Momentum resolution ($p/\Delta p$)	37000
Tilting angle of focal line	45°
Focal plane length	120 cm
Maximum magnetic rigidity	5.4 T·m
Maximum field strength (D1, D2)	1.8 T
Maximum magnetic gradient (Q1)	0.13 T/cm
Maximum magnetic gradient (Q2)	0.033 T/cm
Horizontal magnification ($x x$)	-0.417
Vertical magnification ($y y$)	5.98
Horizontal acceptance angle	± 20 mrad
Vertical acceptance angle	± 70 mrad
Maximum solid angle	~ 5.6 msr
Flight path for the central ray	20 m

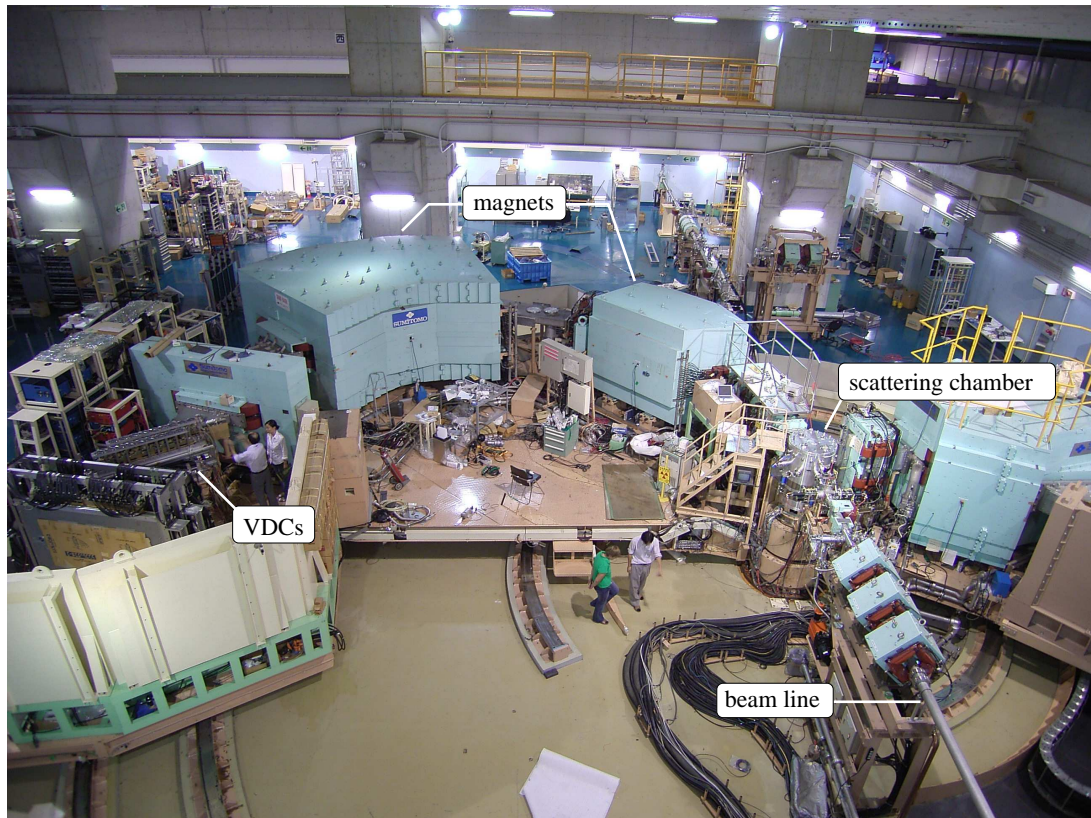


Figure 2.1: The Grand Raiden Spectrometer.

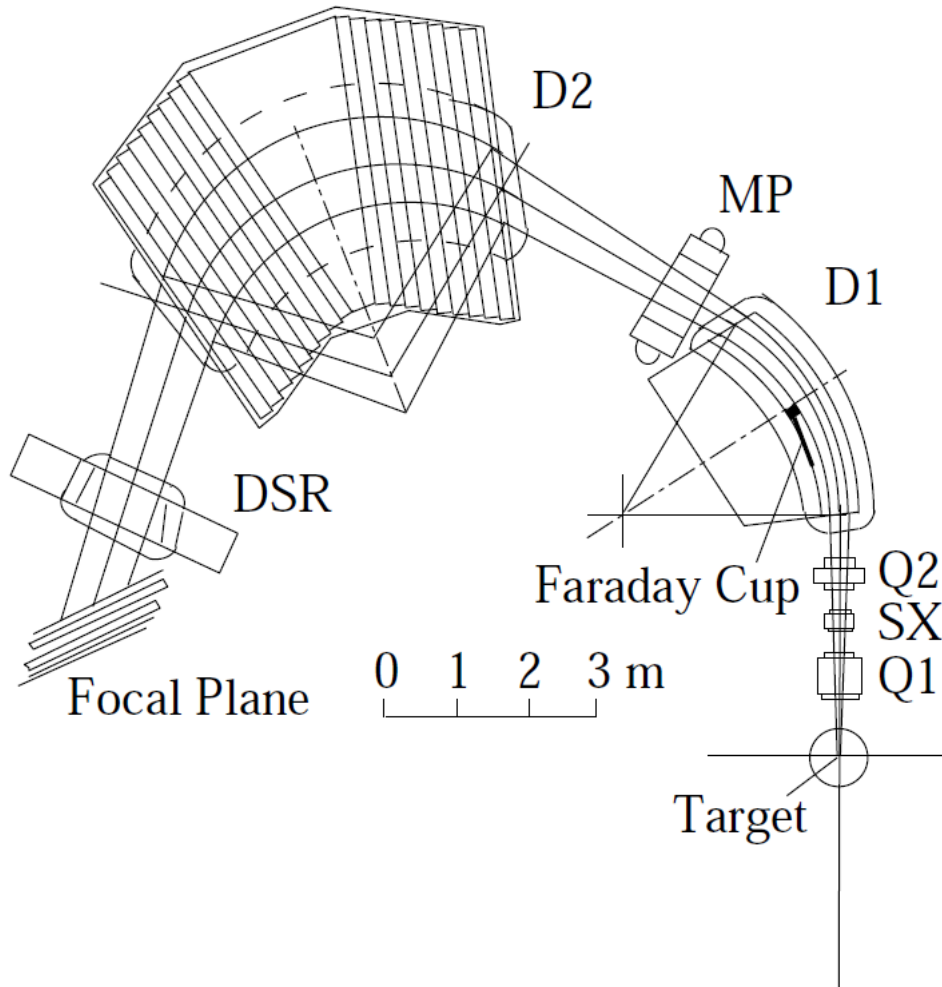


Figure 2.2: *Layout of the GRAND RAIDEN Spectrometer with scale. D1, D2 and DSR are dipole magnets, Q1 and Q2 are quadrupole magnets, SX is a sextupole magnet and MP a multipole magnet. The scattering chamber is on the lower right side of the picture.*

2.3 The focal plane detector and trigger system

The detector system placed at the focal plane of the GRAND RAIDEN spectrometer is used to determine the positions as well as the incident angles of particles. The layout is shown in fig. 2.3. Multiwire drift chambers (MWDCs), which are also called vertical drift chambers (VDCs), are used for the determination of positions and angles. The plastic scintillators PS1 and PS2 produce a signal that is proportional to the energy loss of the incident particles and were used for particle identification (here: to separate the tritons from scattered $^3\text{He}^+$ ions⁸) and to provide trigger signals. A detailed description of the VDC setup can be found in the 1991 annual report of the RCNP Osaka [Nor91]. Each VDC consists of two anode-wire planes (called X and U) that are sandwiched by three cathode planes. The anode-wire planes contain sense wires and potential wires. The structure of such a plane is schematically illustrated in fig. 2.4. The sense wires are placed 6mm apart in the X-planes and 4mm apart in the U-planes. The potential wires create a uniform electric field between the cathode planes and the anode plane. When a charged particle crosses the VDC, an avalanche process in the gas which is contained in the chamber occurs near to the sense wires. For example, in the illustration of fig. 2.4, the particle trajectory can be reconstructed using the drift-time information from four different wires. The potential resolution is around $300\text{ }\mu\text{m}$ (FWHM⁹).

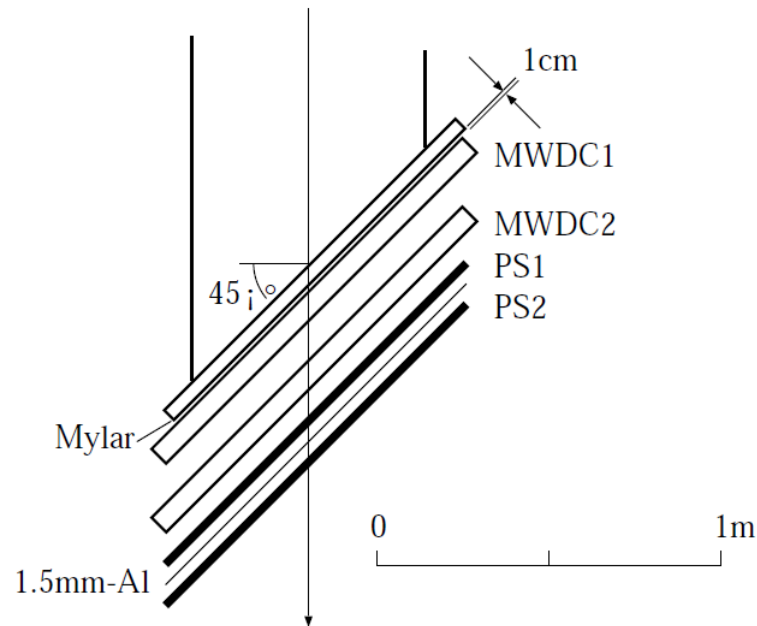


Figure 2.3: Layout of the focal plane detector system. The system consists of two sets of vertical drift chambers (VDCs), MWDC1 and MWDC2, and a trigger system consisting of two plastic scintillators, PS1 and PS2. The MWDCs have two anode planes, X and U, where X1 (of MWDC1) coincides with the focal plane of the spectrometer, and the U planes are tilted at an angle of 48.2° relative to the X planes.

The gas used in the MWDCs is a mixture of argon (71.4%), isobutane (28.6%) and

⁸See 3.1 for a detailed discussion of the particle identification

⁹Full width at half maximum

a small amount of isopropyl alcohol (2-propanol), added to the argon gas at 2°C with vapor pressure to reduce deterioration (like polymerization of gas on the wire surfaces). The two plastic scintillators PS1 and PS2 have a thickness of 10mm, and they are positioned behind the MWDCs. The area of the scintillators ($W \times H$) is 1200mm \times 120mm. The scintillation was detected by photomultiplier tubes (PMTs), model HAMAMATSU H1161, placed on both sides of the plastic scintillators. The signals from these scintillators were used to generate GRAND RAIDEN event signals (trigger) and as energy loss counters for particle identification.

Table 2.3: Specifications of the MWDCs [Nor91, Ada07, Shi05].

Wire configuration	X (0°=vertical), U (48.2°)
Active area ($W \times H$)	1150 mm \times 120 mm
Number of sense wires	192 (X), 208 (U)
Cathode-anode gap	10 mm
Anode wire spacing	6 mm (X), 4 mm (U)
Sense wires	\varnothing 20 μ m gold-plated tungsten wire
Potential wires	\varnothing 50 μ m gold-plated beryllium-copper wire
Cathode	10 μ m carbon-aramid film
Cathode voltage	-5.6 kV
Potential wire voltage	-350 V (X), -500 V (U)
Gas mixture	Argon + Isobutane + Isopropyl alcohol (71.4%) (28.6%) (2°C vapor pressure)
Entrance and exit window	12.5 μ m aramid film
Distance between two MWDCs	25 mm
Preamplifier	LeCroy 2735DC

The trigger system of the focal plane scintillators is set up in the following way: the output signals from the PMTs first go through constant fraction discriminators (CFDs), which eliminate smaller signals produced by γ -rays. The CFD outputs are subsequently separated. One part goes into a time-to-digital (TDC) system, consisting of a time-to-FERA converter (TFD) followed by FERAs¹⁰. Another part goes into Mean Timers. The signals are averaged by the Mean Timers for the left and right PMTs of the scintillators and then enter the LeCroy 2366 Universal Logic Modules (ULM) consisting of FPGA¹¹ chips[Yos96].

¹⁰Fast Encoding and Readout ADCs (Analog-to-digital converter)

¹¹Field Programmable Gate-Array

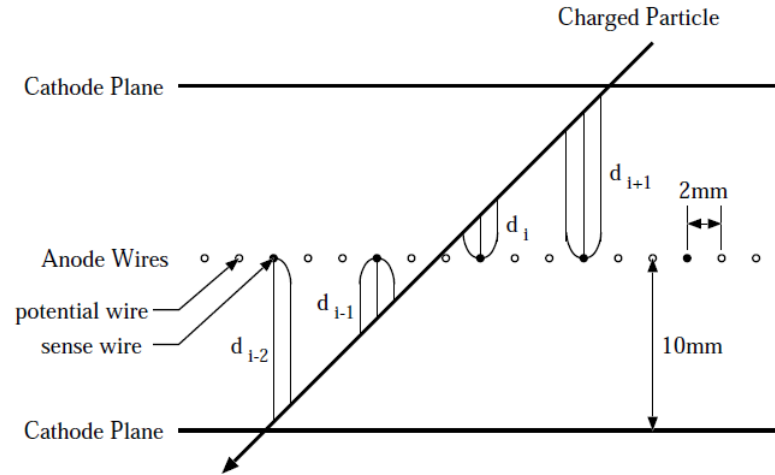


Figure 2.4: Schematic illustration of the structure of an X-plane of a VDC. The anode wires are sandwiched between two cathode planes with alternating sense and potential wires. The arrow indicates a typical track of a charged particle.

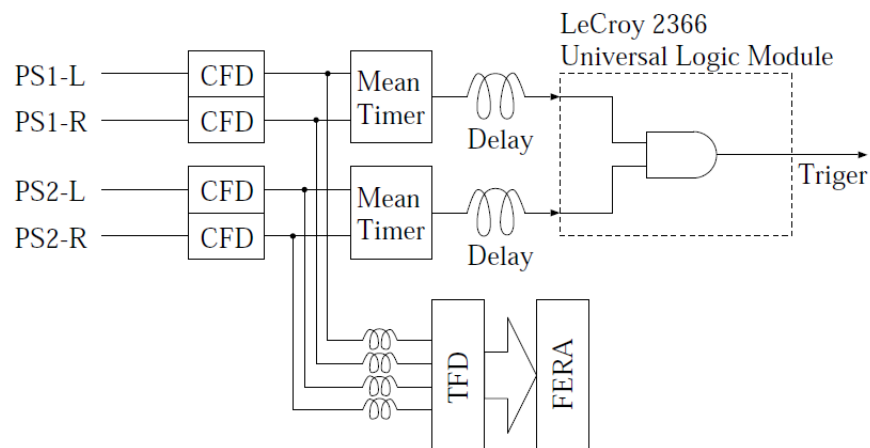


Figure 2.5: Circuit diagram of the trigger system of the focal plane scintillators.

2.4 Beam matching techniques and beam tuning

This section will focus on the details of the beam matching techniques used and applied at the RCNP facility in order to obtain high-resolution particle spectra. An early review on the resolution of accelerator magnetic analyzing systems from 1959 by B.L. Cohen [Coh59] gives the basic concepts of this problem. Papers published by Y. Fujita *et al.* [Fuj97], H. Fujita *et al.* [Fuj02a, Fuj01] and T. Wakasa *et al.* [Wak02] cover the RCNP-specific details of beam matching techniques via the WS course beamline and the ion-optical resolution of the GRAND RAIDEN spectrometer. Further details regarding the optics of high resolution magnetic spectrometers can also be found in [Liy99, Mar83].

The central result of the beam transformation (explained in detail in appendix A) are the relations

$$\begin{aligned}
 x_{fp} &= x_0 (s_{11}b_{11}T + s_{12}b_{21}) \\
 &+ \theta_0 (s_{11}b_{12}T + s_{12}b_{22}) \\
 &+ \delta_0 (s_{11}b_{13}T + s_{12}b_{23} + s_{13}C) \\
 &+ \Theta (s_{12} + s_{13}K)
 \end{aligned} \tag{2.1}$$

$$\begin{aligned}
 \theta_{fp} &= x_0 (s_{21}b_{11}T + s_{22}b_{21}) \\
 &+ \theta_0 (s_{21}b_{12}T + s_{22}b_{22}) \\
 &+ \delta_0 (s_{21}b_{13}T + s_{22}b_{23} + s_{23}C) \\
 &+ \Theta (s_{22} + s_{23}K)
 \end{aligned} \tag{2.2}$$

$$\delta_{fp} = \delta_2 = K\Theta + C\delta_0 \tag{2.3}$$

which give the focal plane coordinates of position (x_{fp}), horizontal scattering angle (θ_{fp}) and fractional momentum deviation (δ_{fp}) as functions of the incoming beam coordinates (x_0, θ_0, δ_0) and the spectrometer and beam line transformation matrices (s_{ij}) and (b_{ij}). This result is derived and explained in detail in appendix A and is the basis of the resolution improvement achieved at RCNP through lateral and angular dispersion matching.

2.4.1 Lateral and angular dispersion matching

The intrinsic resolution of the GRAND RAIDEN spectrometer is about 20 keV for a 420 MeV ^3He beam with a 1mm horizontal spread. However, the energy spread of the beam produced by the cyclotron reduces the energy resolution to typically 100 keV in achromatic beam transportation. A high-resolution measurement using this beam can only be achieved by matching the spectrometer and the beam line [Fuj97, Wak02, Fuj02a].

These matching techniques and their applications will be briefly described in this section.

The first three terms in eq. (2.1) in the previous section depend on the source point

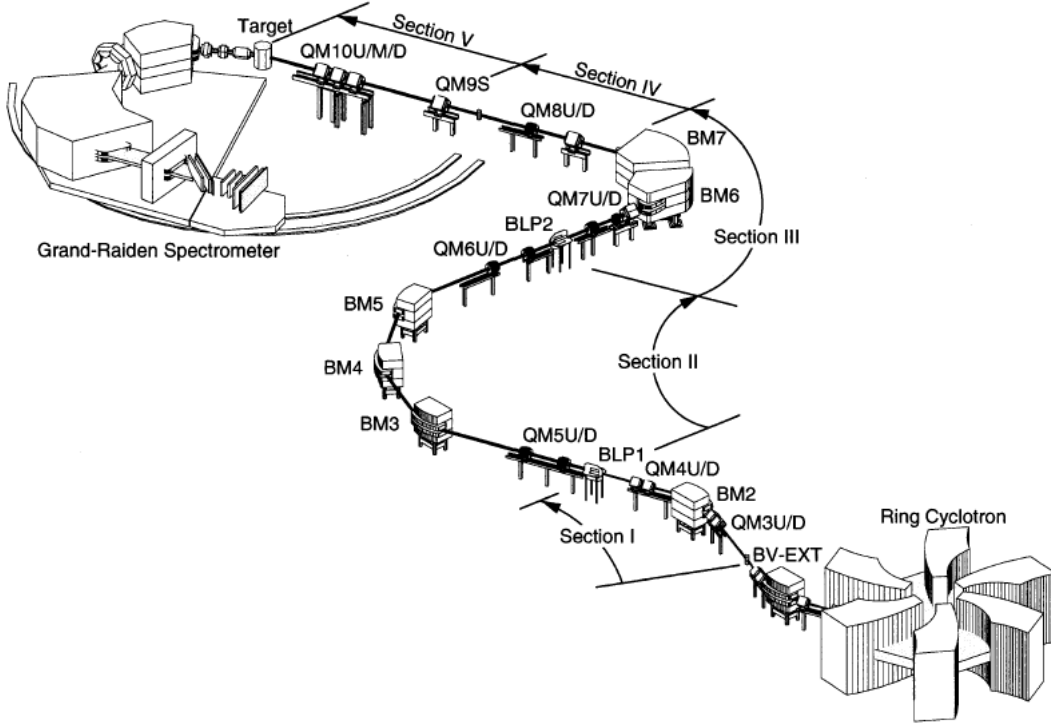


Figure 2.6: Layout of the WS course beam line setup at the RCNP Ring Cyclotron Facility.

parameters x_0, θ_0 and δ_0 and on the beam line and spectrometer matrix elements b_{ij} and s_{ij} . In order to reduce uncertainties in the position x_{fp} at the focal plane, the horizontal spread x_0 of the incoming beam should be minimized first. Subsequently, the minimum horizontal spread at the target (and thus the best resolution) can be achieved if the coefficients of the θ_0, δ_0 and Θ in eq. (2.1) are zero.

These matching conditions are called *focus matching* (θ_0 -coefficient is zero), *dispersion matching* (δ_0 -coefficient is zero) and *kinematics correction* (Θ -coefficient is zero). To obtain a good angle resolution (of the horizontal scattering angle θ), the δ_0 -term in eq. (2.2) should also be minimized (preferably zero), as it has the biggest influence on θ_{fp} once *dispersion matching* is realized.

All matching conditions can, in principle, be achieved simultaneously. However, the order of the steps taken to achieve the matching conditions is important as the corrections influence each other. The general way is to first compensate the kinematic broadening of the beam in the spectrometer (*kinematics correction*), then to adjust the kinematic defocusing and finally to implement the dispersion matching conditions.

The *kinematics correction* is relatively easy and can be achieved by adjusting the settings of the spectrometer magnets (the strength of the horizontal quadrupole) only, as the Θ -coefficient in eq. (2.1) and (2.2) depends only on spectrometer matrix elements. If $s_{12} = -s_{13}K$, then *dispersion matching* (δ_0 -coefficient is zero in eq. (2.1) and (2.2)) is achieved if (using $s_{11}s_{22} - s_{12}s_{21} = 1$)

$$b_{13} = \frac{s_{13}}{s_{11}} (1 + s_{11}s_{23}K - s_{21}s_{13}K) \frac{C}{T} \quad (\text{lateral dispersion matching}) \quad (2.4)$$

and

$$b_{23} = (s_{21}s_{13} - s_{11}s_{23})C \quad (\text{angular dispersion matching}) \quad (2.5)$$

These relations show that the beam line parameters b_{13} (lateral dispersion matching) and b_{23} (angular dispersion matching) have to be changed while staying adjusted to the *kinematics correction*, i.e. the spectrometer parameters required for the correct matching relating to the reaction of interest at the target.

The resolving power of the matched system is given by [Fuj97, Mar83]

$$R = \frac{1}{2x_0} \frac{s_{13}}{s_{11}b_{11}T - s_{13}b_{21}K} = \frac{1}{2x_0} \frac{s_{13}}{M} \quad (2.6)$$

where M is the x_0 -coefficient in eq. (2.1) with *kinematics correction* applied ($s_{12} = -s_{13}K$), and represents the overall horizontal magnification of the beam spread.

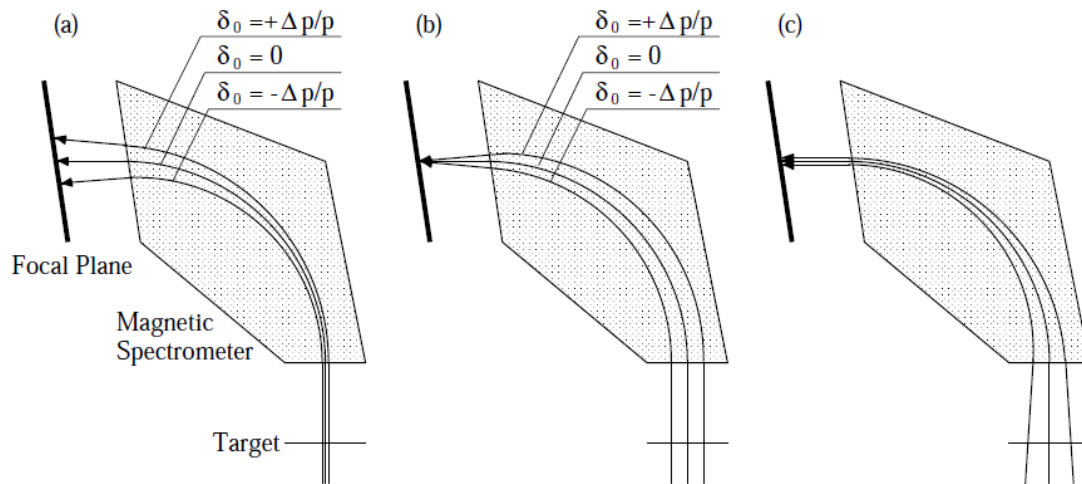


Figure 2.7: Schematic trajectories for zero-degree scattering under different matching conditions. The rays shown correspond to the trajectories of particles with zero degrees scattering angle, having different momenta. (a) achromatic focus - the momentum spread of the focused beam results in a broadened image at the focal plane due to the momentum-analyzing character of the spectrometer. (b) lateral dispersion matching - lateral matching conditions ensure that momentum deviations in the incident beam are cancelled at the focal plane. The broadening in the horizontal scattering angle however remains. (c) lateral and angular dispersion matching - the horizontal scattering angle broadening is cancelled by matching the angles of incident rays accordingly, while still maintaining the lateral dispersion matching as in (b).

The result of different matchings of beamline and spectrometer at the focal plane are shown in fig. 2.7. The figure shows only central rays scattered at zero degrees, with three different momenta, $\delta_0 = 0, \delta_0 = +\Delta p/p$ and $\delta_0 = -\Delta p/p$. In part (a) of the figure, the trajectories are shown with *achromatic* focus at the target position (this means $b_{13}=b_{23}=0$, i.e. there is no momentum influence from the beam line transformation on x and θ). Particles with different momenta are thus “momentum-analyzed” by the spectrometer and the beam spread at the focal plane is proportional to the beam momentum spread.

Part (b) of the figure shows trajectories with only lateral dispersion matching realized (b_{13} matched according to eq. (2.4), while $b_{23}=0$). In this case, rays with different momenta are focused at different positions on the target (*dispersive monochromatic focus*), and this dispersion at the target is compensated by the dispersion of the spectrometer (thus *dispersion matching*).

However, in this case, rays with different momenta cross the focal plane with different angles, thus showing that lateral dispersion matching alone gives rise to uncertainty in the scattering angle. The angles can be made accurate by obtaining the right incident angles for rays with different momenta at the target, as shown in part (c) of the figure. This adjustment of the angle dispersion is the *angular dispersion matching*.

Table 2.4: Overview of matching conditions.

NAME	LATERAL	ANGULAR
kinematics correction	$s_{12} + s_{13}K = 0$	$s_{22} + s_{23}K = 0$
focus matching	$s_{11}b_{12}T + s_{12}b_{22} = 0$	$s_{21}b_{12}T + s_{22}b_{22} = 0$
dispersion matching	$b_{13} = \frac{s_{13}}{s_{11}} (1 + s_{11}s_{23}K - s_{21}s_{13}K) \frac{C}{T}$	$b_{23} = (s_{21}s_{13} - s_{11}s_{23}) C$

2.4.2 Faint beam tuning

Achieving the desired matching conditions discussed in the previous section requires a monitoring of the beam (beam diagnostics). Beam viewers coated with phosphorescent zinc sulfide (ZnS) are placed inside the beam line at the target position and at focusing points; however, the achieving of matching conditions cannot be judged by the beam spot profile on these viewers as both a defocused beam and a dispersed beam have a broad profile.

A beam diagnostic method using the spectrometer was proposed by Fujita *et al.* [Fuj02a] and is used at the RCNP to tune the beam in order to achieve the matching conditions, called *faint beam tuning*. It uses the fact that the matching between beamline and spectrometer can be verified at the focal plane by using the beam going directly into the spectrometer, without any target, as the beam envelope is kept intact by the spectrometer. Therefore, the image at the focal plane directly shows the condition of the beam. The schematic images of four different cases are shown in fig. 2.8. The desired beam condition is (a).

There are two issues when using this method. The first one is that the beam intensity has to be substantially reduced, as even a few nanoamperes of beam intensity would be damaging the detector system. Therefore, wire grid attenuators were placed downstream

of the ion source, reducing the beam current to a few thousand particles per second. Despite the much lower intensity, the faint beam still has the same emittance¹² and momentum spread as the beam used for the charge-exchange experiment.

Table 2.5: Magnet settings of the WS course used for the experiments E237 and E273. Deviations can be as high as $\pm 0.3\%$. See fig. 2.6 for the position of the magnets in the WS course.

MAGNET	CURRENT	MAGNET	CURRENT
QM3U	-17.18 A	QM7U	0.02 A
QM3D	14.62 A	QM7D	-11.06 A
QM4U	13.79 A	QM8U	21.45 A
QM4D	-14.23 A	QM8D	-33.00 A
QM5U	40.91 A	QM9S	21.10 A
QM5D	20.73 A	QM10U	24.67 A
QM6U	20.71 A	QM10M	-40.64 A
QM6D	40.88 A	QM10D	24.60 A

The second tuning problem is related to the charge-exchange experiment. The faint beam tuning method requires that the particles are correctly focused on the focal plane, therefore the GRAND RAIDEN magnets have to be set to focus ^3He particles (^3He mode). But the matching conditions for the dispersive mode depend on the spectrometer matrix elements as well, which means that for the ($^3\text{He}, t$) reaction, the beamline has to be adjusted together with the spectrometer in triton mode. The magnet settings of GRAND RAIDEN for the triton mode and the ^3He mode are very different at 420 MeV beam energy, which means that if the beamline is tuned by using the ^3He beam at the focal plane, the matching will break down as the spectrometer is set to analyze tritons from the charge-exchange reaction.

This problem is solved by trying to obtain (in the ^3He faint beam tuning at 420 MeV) similar matrix elements to the ion optics of the triton mode at 420 MeV. The focus tuning for the faint beam was performed by using the ($^3\text{He}, ^3\text{He}'$) elastic scattering at 10° spectrometer angle on a 1.93 mg/cm^2 ^{197}Au target, and setting the over-focus (Q1 magnet) somewhat lower. Then, the beamline is adjusted to reach the required matching conditions. This was done mainly by adjusting the Q8U (lateral dispersion), Q9U (angular dispersion) and Q10U/M/D (focus) magnets (see fig. 2.6 for the position of the magnets in the WS course).

After installing a target, the relative momentum ratio C (see eq. (A.13)) changes. In order to adjust for this change and fine-tune the dispersion matching, additional adjustments were made using the triton mode with the ($^3\text{He}, t$) reaction on an ^{27}Al target at zero degrees spectrometer angle. The final settings of the dispersive mode of the beamline used for the experiments E237 and E273 are shown in table 2.5.

¹²The beam emittance of a particle accelerator is the extent occupied by the particles of the beam in space and momentum phase space as it travels. A low-emittance particle beam is a beam where the particles are confined to a small distance and have nearly the same momentum.

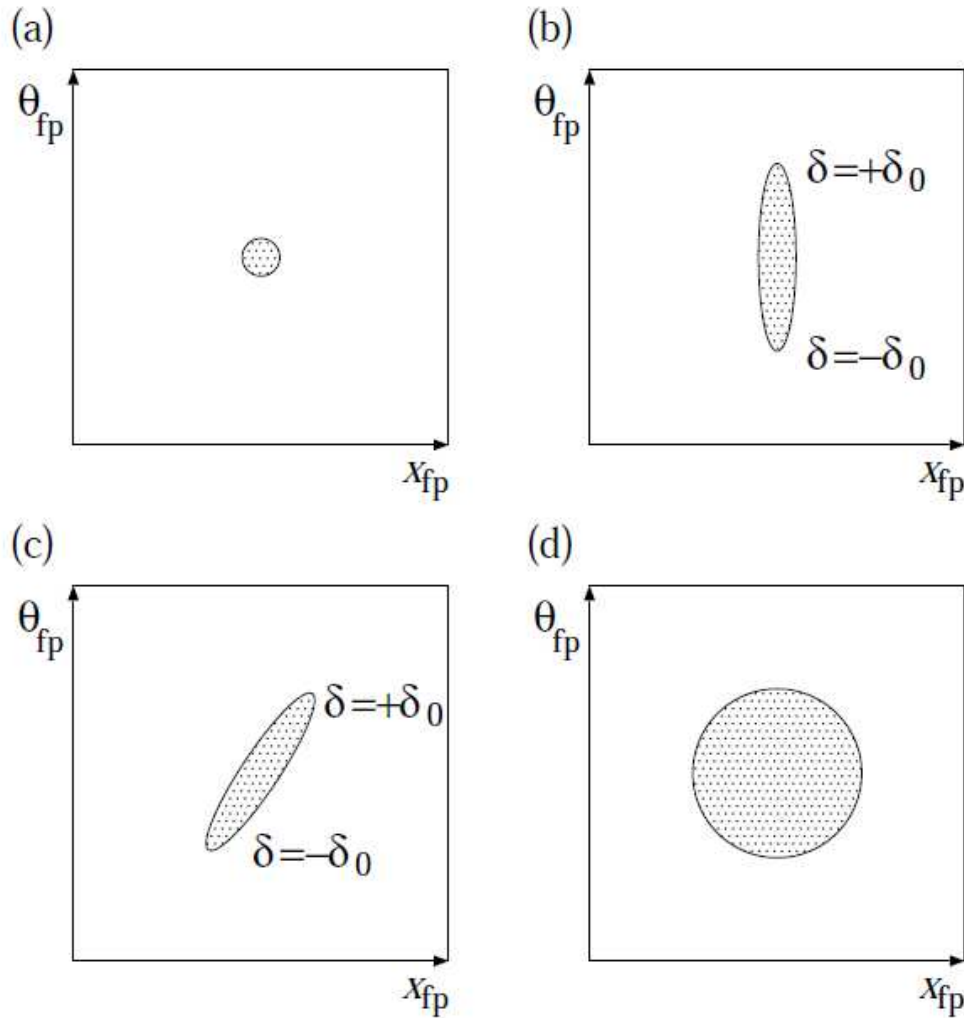


Figure 2.8: Schematic illustration of the beam image at the focal plane in x_{fp} - θ_{fp} coordinates for different matching conditions. When no matching conditions are realized, the beam image is broad in the x - and θ -dimension at the focal plane, as in (d). If only focus matching but no dispersion matching condition is met, particles with different momenta have different impact points at the focal plane and the beam image has the shape of a tilted ellipse, as in (c). If focus and lateral dispersion matching is achieved, the beam image is observed as an elongated ellipse, but without slope, as in (b). Finally, if all matching conditions are met, the spatial and angular spread of the beam image at the focal plane becomes small, as shown in (a). The matching procedure using the faint beam method consists in minimizing the image size of the faint beam at the focal plane.

2.4.3 Off-focus mode

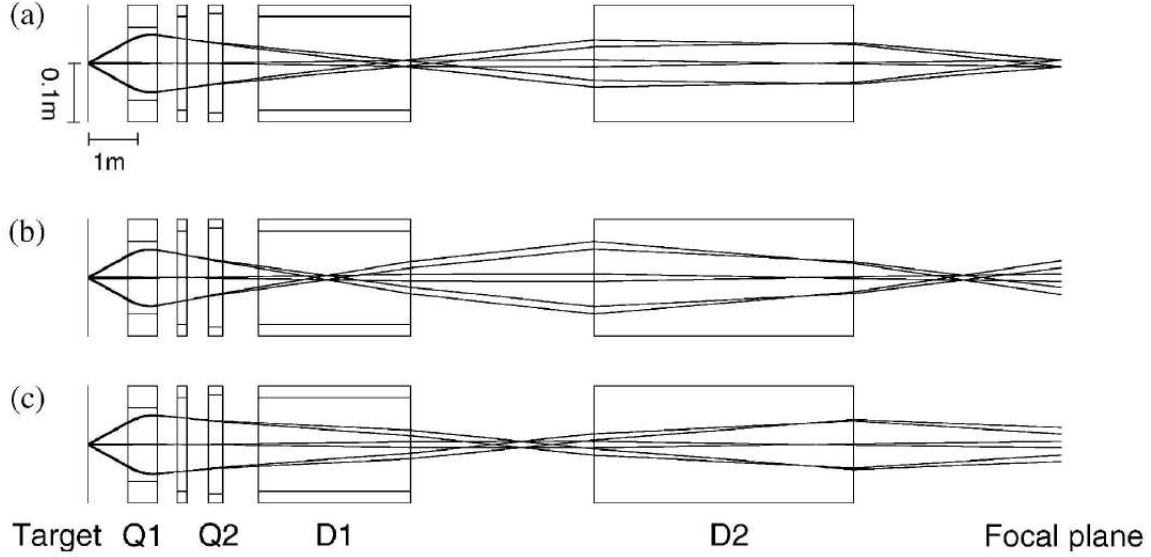


Figure 2.9: Vertical beam envelope inside the GRAND RAIDEN spectrometer for different focus conditions. (a) Normal focus (b) Over-focus (c) Under-focus.

To distinguish states excited by $\Delta L=0$ transitions, which have a strongly forward-peaked angular distribution (see 4.7), a good resolution of the scattering angle is important. The scattering angle depends on the vertical (ϕ) as well as the horizontal (θ) angles (eq. (A.1) and fig. A.1). Good resolution for the horizontal angle is achieved via the angular dispersion matching, but a good resolution is also required for the vertical angle.

Since the GRAND RAIDEN is a horizontal bending spectrometer, a vertical focusing quadrupole magnet (Q1, see fig. 2.2) is placed near the target chamber in order to obtain a large vertical acceptance. As a result, the vertical angle magnification becomes small. Trajectories inside the GRAND RAIDEN for normal vertical focus are shown in fig. 2.9(a) from the target position on to the horizontal focus plane. The vertical angle is scaled by a factor ≈ 0.17 , meaning that reaction products with rather large vertical scattering angle are observed at small angle at the focal plane. The MWDCs (2.3) have an angle resolution of around 2 mrad, so this means that with normal focus, the best possible vertical angle resolution is 12 mrad.

It is thus necessary to defocus the beam in vertical direction using the Q1 magnet in order to improve the vertical angle resolution. The defocusing of the beam in vertical direction does not pose a problem for the analysis as the vertical scattering angle can be reconstructed from the vertical position (y_{fp}) in the detector plane. The defocusing can either be achieved by increasing the strength of the Q1 quadrupole magnet (over-focus mode) or decreasing it (under-focus mode). The y_{fp} position depends only on ϕ_{tgt} in first order (at a given x_{fp} position), but also depends in second order on the horizontal angle θ_{tgt} , the horizontal position x_{tgt} , and the relative momentum δ of the incoming beam. The calibration of the vertical angle (as well as the adjustment of the horizontal

angle) was performed offline by software (see Appendix B for the detailed procedure) to obtain the high-resolution spectra from calibration runs using a sieve slit.

A good vertical angle resolution can be achieved in the over-focus mode by increasing the strength of the Q1 magnet current by about 17% compared to the normal (point-to-point) focus. In total, the vertical defocusing and the lateral and angular dispersion matching provide an angle resolution of around 8 mrad.

It should be noted that since the matching conditions depend to some extent on the Q1 magnet strength, the beamline has to be matched to the spectrometer to realize angular and lateral dispersion matching conditions *after* the over-focus mode has been set.

Chapter 3

Spectrum reconstruction

石の上に三年
Three years on a stone
*(japanese proverb)*¹

In order to obtain a clean high-resolution spectrum of the nucleus under consideration, the raw data must be processed in a variety of sophisticated ways. This chapter deals with the different procedures used to obtain the final high-resolution spectra.

3.1 Particle identification

The incident ^3He beam coming from the Cyclotron creates, besides the tritons, a variety of other reaction products upon hitting the target. All these particles have a different mean radius (ρ) in the spectrometer which selects the particles according to their momentum and charge. For a reaction product to reach the focal plane, its momentum and charge must satisfy the relation

$$m \frac{v^2}{\rho} = zvB \Leftrightarrow B\rho = \frac{mv}{z} \quad (3.1)$$

where mv is the momentum of the particle (mass m and velocity v) and z its atomic charge. The magnetic field B of the spectrometer can be set to detect tritons at the focal plane. However, $^3\text{He}^+$ particles produced by the pickup of an electron of the incident $^3\text{He}^{++}$ beam have nearly the same mv/z value than the produced tritons and are thus also detected at the focal plane. Since the atomic charge exchange is not a nuclear reaction, the energy of the $^3\text{He}^+$ particles is nearly the same as the incident energy of the $^3\text{He}^{++}$ particles accelerated by the Cyclotron (420 MeV) and they are thus expected to hit the high momentum side of the focal plane detectors. However, they can be eliminated from the spectrum through a particle identification procedure, using

¹meaning that to accomplish anything, about three years of preparation and perseverance are required (it takes three years sitting on a stone to make it warm).

the different energy loss of the charged ${}^3\text{He}^+$ and the tritons in the plastic scintillators (PS1 and PS2) behind the vertical drift chambers (VDC). This energy loss is mainly due to scattering on the electrons of the target, which is described by the Bethe formula [Bet30]

$$-\frac{dE_{kin}}{dx} = \frac{4\pi}{m_e c^2} \frac{n z^2}{\beta^2} \left(\frac{e^2}{4\pi\epsilon_0} \right)^2 \cdot \left[\ln \left(\frac{2m_e c^2 \beta^2}{I(1-\beta^2)} \right) - \beta^2 \right] \quad (3.2)$$

where m_e is the rest mass of the electron, and n the electron density, $n = \frac{N_A Z \rho}{A}$ (Avogadro number N_A , material density ρ , Z and A atomic number and mass number of the target material) and $\beta = \frac{v}{c}$ (where v is the projectile velocity), ze the charge of the projectile and x the distance travelled by the projectile particle. I is the mean excitation potential of the target material, which is material-dependent [Ogi88]. Note that the energy loss does not depend on the mass of the projectile, only on its velocity and charge. However in our case (see eq. 3.1) the velocity of the particle is depending on its mass and charge. Since ${}^3\text{H}^+$ and ${}^3\text{He}^+$ have the same mass and charge, their energy losses in the scintillators should be equal. However, the overwhelming part of the incident ${}^3\text{He}^+$ ions loses its electron immediately upon entering the scintillator material and becomes ${}^3\text{He}^{++}$, thus having a four times larger energy loss than the tritons. This can be seen in fig. 3.1, where the energy loss is plotted against the x_{fp} coordinate.

The energy loss itself is obtained from the scintillators through the photomultiplier tubes (PMT) attached on both sides of them. The scintillation photons produced by the ionizing particles are attenuated in the scintillator material through absorption and the photon intensity is observed in the PMTs depending on the position of the incident ion as

$$I(x) = I_0 e^{-\frac{x}{l}} \quad (3.3)$$

where I_0 is the initial photon intensity and l a characteristic attenuation length of the scintillator material. If the total length of the scintillator is L , then the output of the left and right PMT (P_L and P_R) are proportional to $I(x)$ and $I(L-x)$, respectively. The geometrical mean of both values (P_m) then becomes independent of the position x and directly proportional to I_0 , which is itself proportional to ΔE :

$$P_m = \sqrt{P_L \cdot P_R} \propto \sqrt{I(x) \cdot I(L-x)} = I_0 e^{-\frac{L}{2l}} \quad (3.4)$$

The result of this procedure is shown exemplarily for a run of the ${}^9\text{Be}({}^3\text{He}, t){}^9\text{B}$ experiment in fig. 3.2. Subsequently all spectra were gated to include only the triton events.

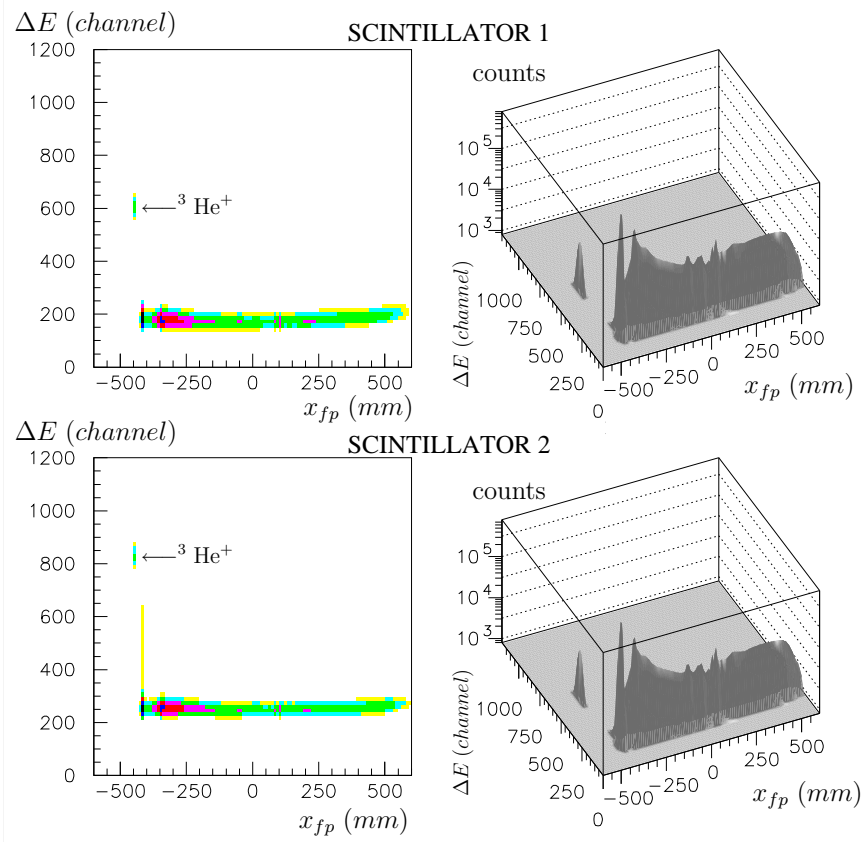


Figure 3.1: Energy loss in the plastic scintillators 1 and 2 plotted against the x_{fp} coordinate detected in the MWDC's. The $^3\text{He}^+$ events are clearly separated from the triton events.

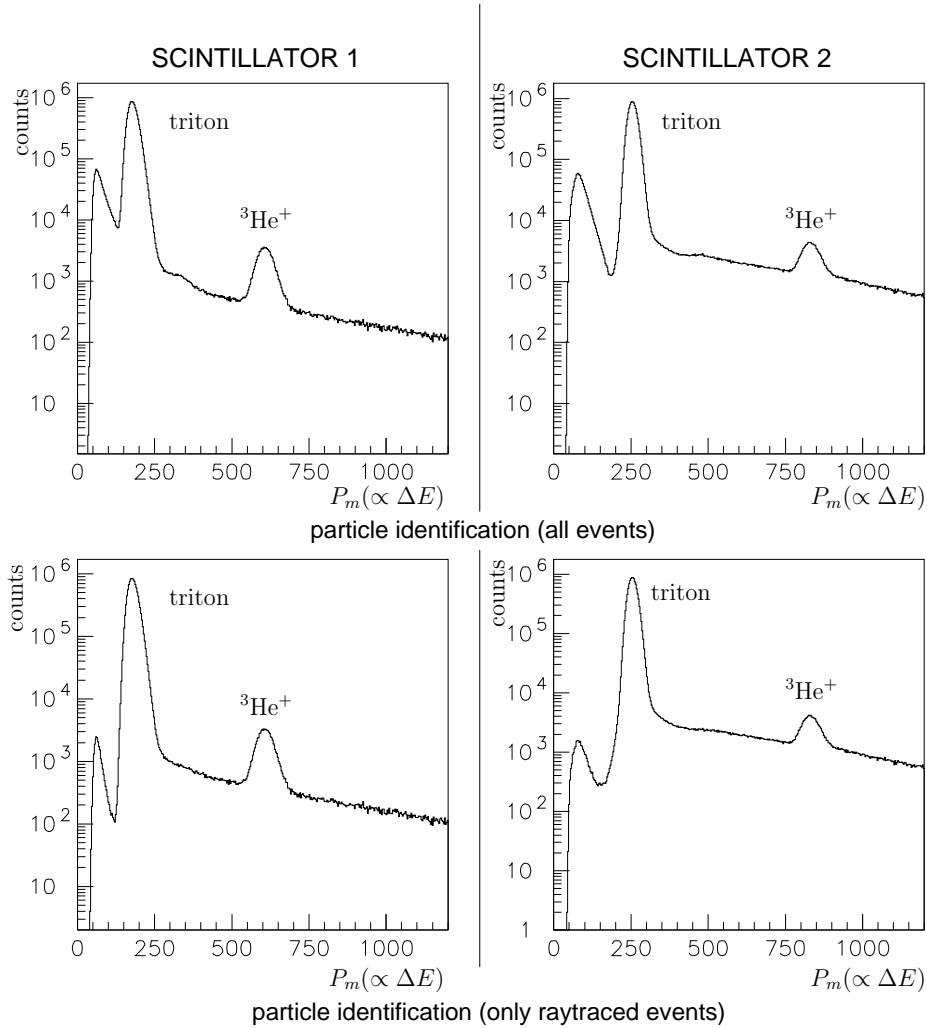


Figure 3.2: Total energy loss in the plastic scintillators 1 and 2. The absciss is the square root of the product of the respective left and right pulse height measured by the PMTs. The first row includes all detected events, the second row only the events that could be raytraced in the MWDCs.

3.2 Track reconstruction in the multiwire drift chambers

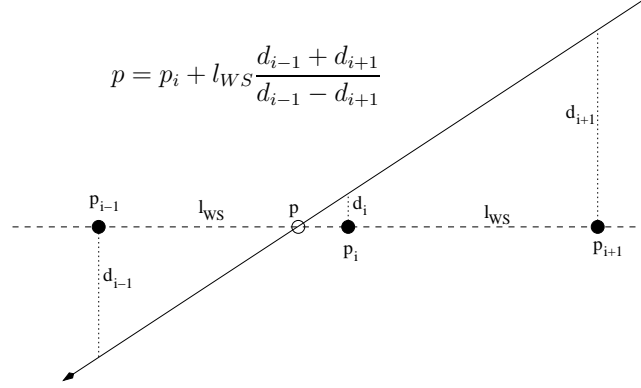


Figure 3.3: *Position determination in the MWDCs using the drift information derived from multiple sense wires.*

As shown schematically in fig. 2.4, the position(s) (i.e. trajectories) of charged particles entering the focal plane are determined by the MWDCs. The position p at which a particle hits the focal plane is determined by the drift lengths $d_{i-1}, d_i, d_{i+1}, \dots$ of at least more than two wires within the same cluster. Since X- and γ -rays mostly only cause the firing of one wire, background events by photons can generally be excluded by requiring the firing of several wires. If d_i is the minimum drift length in an event causing the firing of three wires, the position p can then be determined (see also fig. 3.3 as:

$$\begin{aligned}
 \frac{d_{i+1}}{l_{WS} + p_i - p} &= -\frac{d_{i-1}}{p - p_{i-1}} \\
 \Leftrightarrow \frac{p - p_i}{l_{WS} + p_i - p} &= -\frac{d_{i-1}}{d_{i+1}} \\
 \Leftrightarrow p - p_{i-1} &= -\frac{d_{i-1}}{d_{i+1}}(l_{WS} + p_i - p) \\
 \Leftrightarrow p \left(1 - \frac{d_{i-1}}{d_{i+1}}\right) &= -\frac{d_{i-1}}{d_{i+1}}(l_{WS} + p_i) + p_{i-1} \\
 \Leftrightarrow p &= \frac{-d_{i-1}(l_{WS} + p_i)}{d_{i+1} - d_{i-1}} + \frac{d_{i+1}p_{i-1}}{d_{i+1} - d_{i-1}} \\
 \Leftrightarrow p &= \frac{-d_{i-1}(l_{WS} + p_i) + d_{i+1}(p_i - l_{WS})}{d_{i+1} - d_{i-1}} \\
 \Leftrightarrow p &= p_i + l_{WS} \frac{d_{i-1} + d_{i+1}}{d_{i-1} - d_{i+1}} \tag{3.5}
 \end{aligned}$$

where p_{i-1} and p_i are the positions of the i th and $(i-1)$ th sense wire, l_{WS} is the wire spacing and the d_i 's are the various drift lengths as seen in fig. 3.3. The signs of d_{i-1} and d_{i+1} are opposite since the electrons moving to the $(i-1)$ th and the $(i+1)$ th wire drift in opposite directions. In the standard setting of the GRAND RAIDEN spectrometer, particles having correct trajectories usually cause more than three sense wires to fire,

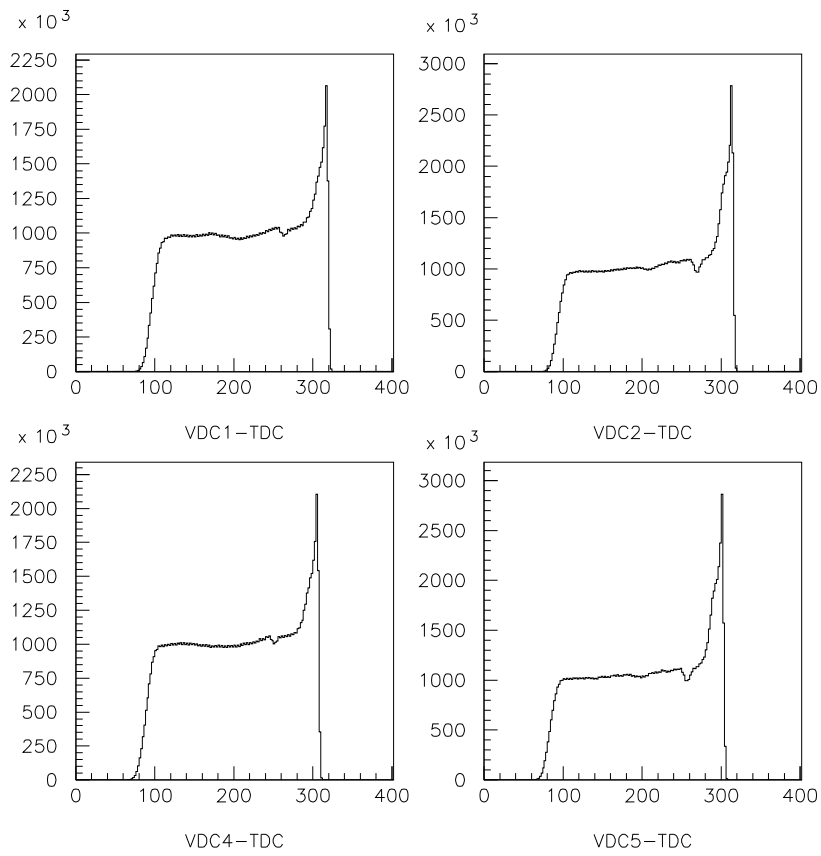


Figure 3.4: *TDC spectra of the MWDCs for X- and U-plane wires. The X-axis is an arbitrary channel number. The drift velocity changes considerably in the vicinity of the sense wires.*

except for particles with small scattering angles in the low-momentum region of the focal plane.

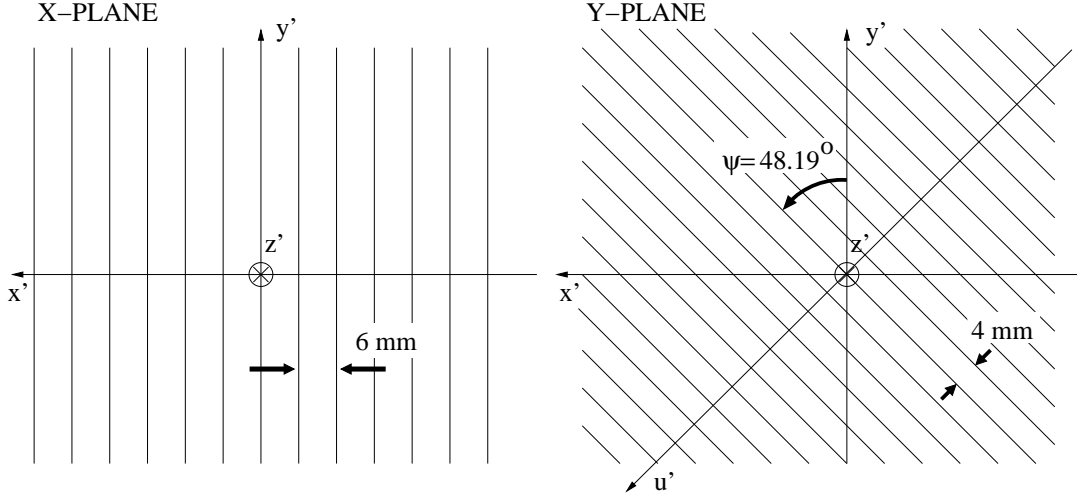


Figure 3.5: Wire configurations of the X-plane and the U-plane of the MWDCs. The U-plane wires have an inclination angle of 48.19° relative to the X-plane wires. The wire spacing is 6mm in the X-plane and 4mm in the U-plane.

Four anode planes in two MWDCs are used to determine the three-dimensional trajectory of the charged particles. Each VDC has two anode planes, an X-plane and an U-plane. The wire configurations of these planes are shown in fig. 3.5. The wires in the U-plane have an inclination angle relative to the X-plane wires of $\psi=48.19^\circ$. The sense wire spacing is 6mm in the X-plane and 4mm in the U-plane (see 2.3).

The coordinate system in the MWDCs is given as in fig. 3.5 and is labeled x', y', z' . The z' axis is perpendicular to the anode planes (X and U) of the MWDCs. The MWDC coordinate systems are different from the central ray coordinates (x, y, z) , where the z -axis is the momentum direction of the central ray.

The positions p_{x1}, p_{x2}, p_{u1} and p_{u2} , determined as in equation (3.5), represent the incident ray positions in the drift chambers. The angles of the incident ray relative to the z' axis in the MWDCs system are denoted by θ'_x, θ'_y and θ'_u . Using the distance of the two MWDCs, $L = z'_{x2} - z'_{x1} = z'_{u2} - z'_{u1}$, the angles can be determined as

$$\tan \theta'_x = \frac{p_{x2} - p_{x1}}{L} \quad (3.6)$$

$$\tan \theta'_u = \frac{p_{u2} - p_{u1}}{L} \quad (3.7)$$

$$\tan \theta'_y = \frac{\tan \theta'_x}{\tan \psi} - \frac{\tan \theta'_u}{\sin \psi} \quad (3.8)$$

and the x'_0, y'_0 and u'_0 positions (the horizontal, vertical and u-direction position at the $z'=0$ plane) in the MWDC coordinate system can be determined by (see fig. 3.6)

$$x_0' = p_{x1} \quad (3.9)$$

$$u_0' = p_{u1} - z_{u1} \cdot \tan \theta_u' \quad (3.10)$$

$$y'_0 = \frac{x'_0}{\tan \psi} - \frac{u'_0}{\sin \psi} \quad (3.11)$$

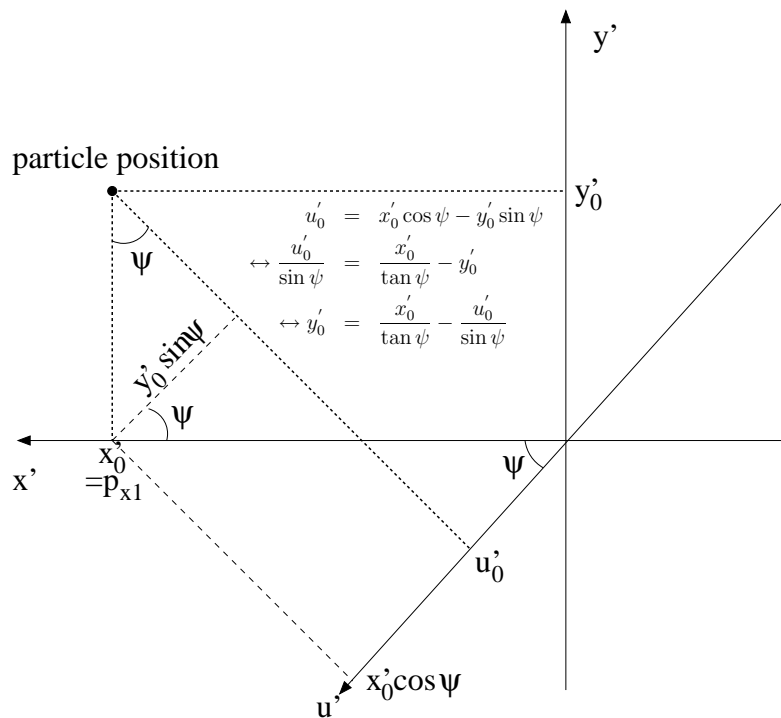


Figure 3.6: Illustration of the coordinates x'_0, y'_0 and u'_0 and the relation to the u -Plane tilting angle ψ .

For the GRAND RAIDEN spectrometer, the distance between the two drift chambers is $L=250$ mm. The horizontal and vertical angles in the MWDC coordinates can be converted back into the central ray coordinate system by using (see fig. 3.7)

$$\theta_x = \theta'_x - \Theta_{\text{VDC}} \quad (3.12)$$

$$\tan \theta_y = \tan \theta'_y \cos \Theta_{\text{VDC}} \quad (3.13)$$

with Θ_{VDC} being the the angle at which the MWDCs are positioned relative to the central ray. For the GRAND RAIDEN setup, $\Theta_{\text{VDC}}=45^\circ$. The setup of the two MWDCs is shown in fig. 3.7. The central ray coordinate angles θ_x and θ_y as determined by equations (3.12) and (3.13) can be traced back to the scattering angles at the target. This will be described in the next section.

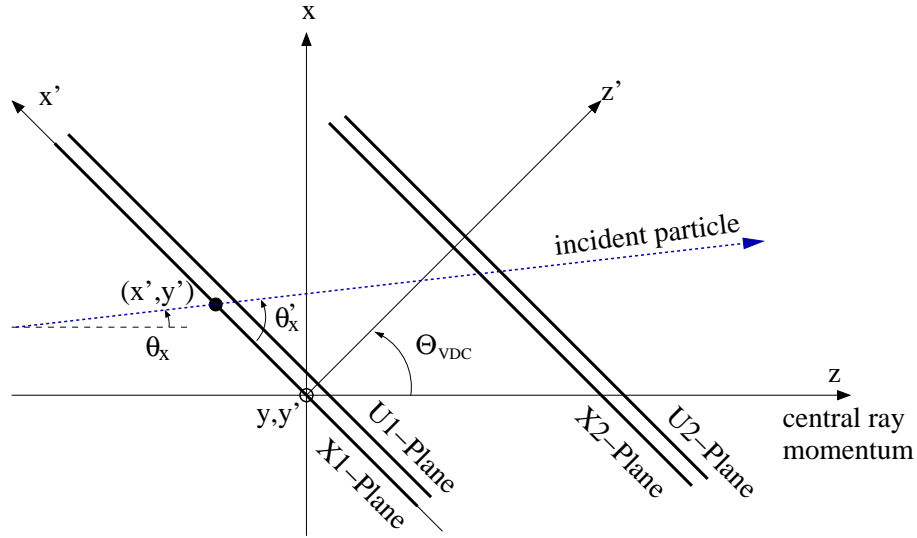


Figure 3.7: Illustration of the coordinates x' and z' and the setup of the MWDCs at the GRAND RAIDEN experiment.

3.3 Reconstruction of the scattering angle

In order to obtain a high-resolution spectrum for the reaction at 0° scattering angle, the scattering angles θ_{tgt} and ϕ_{tgt} at the target have to be reconstructed from the focal plane observables θ_{fp} and y_{fp} . A good way to achieve this is the *sieve slit technique* using the *over-focus mode* of the Grand Raiden spectrometer (see 2.4.3 and [Fuj01]). A multi-hole slit with well-known metrics as shown in fig. 3.8 is placed behind the target and a spectrum is recorded. The deformed image (see fig. 3.9) of the sieve slit is then used to obtain the correct scattering angles for the raytraced events. The procedure is explained in detail in the appendix B. The multi-hole slit (sieve) was installed 605.5 mm behind the target. An example of the focal plane image of the sieve in θ_{fp} and y_{fp} (overfocus) coordinates for two different excitation energy regions (x_{fp} coordinates) is shown in fig. 3.9. A $70 \mu\text{m}$ $^{13}\text{CH}_2$ target was used for the angle calibration runs. Two spectra were recorded for a total of 50 min. For the reconstruction of the scattering angles, the dependence of the horizontal and vertical scattering angles at the target were assumed to be polynomial functions of the scattering angles at the focal plane and the position at the focal plane, as follows:

$$\phi_{tgt} = \phi_{tgt}(y_{fp}, \theta_{fp}, x_{fp}) = \sum_{i=0}^3 \sum_{j=0}^3 \sum_{k=0}^1 a_{ijk} x_{fp}^i \theta_{fp}^j y_{fp}^k \quad (3.14)$$

$$\theta_{tgt} = \theta_{tgt}(y_{fp}, \theta_{fp}, x_{fp}) = \sum_{i=0}^2 \sum_{j=0}^4 \sum_{k=0}^2 b_{ijk} x_{fp}^i y_{fp}^j \theta_{fp}^k \quad (3.15)$$

which requires 77 parameters in total to reconstruct the scattering angles (32 parameters for the vertical scattering angle and 45 parameters for the horizontal scattering angle). The determination of these parameters is explained and shown in the appendix. The result of the scattering angle reconstruction is shown in B.1.3.

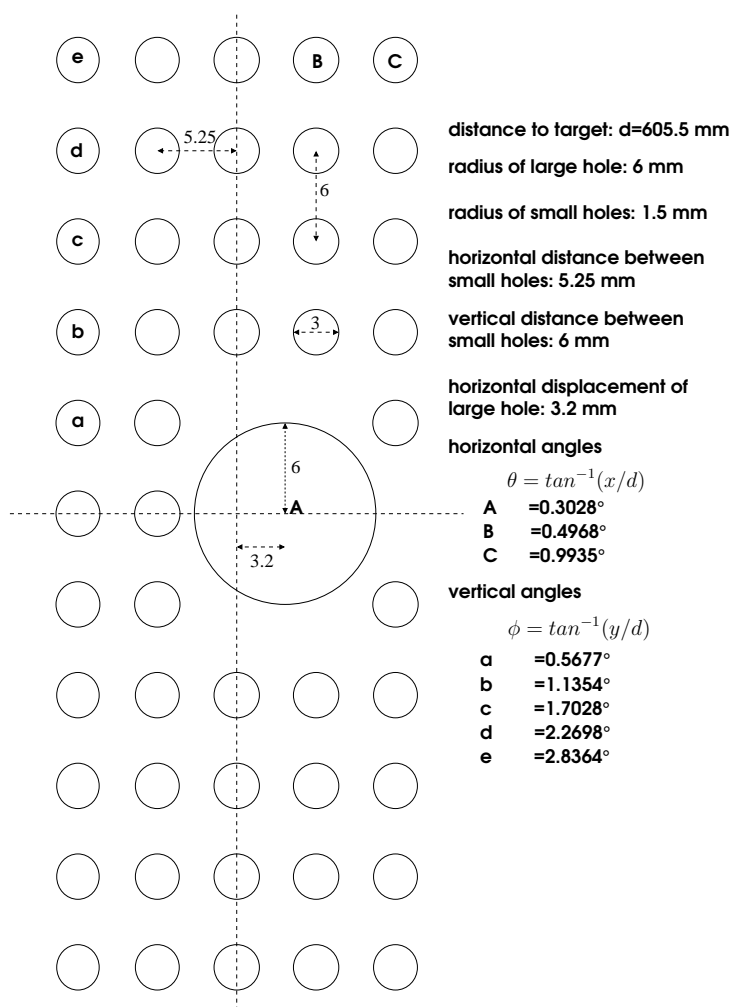
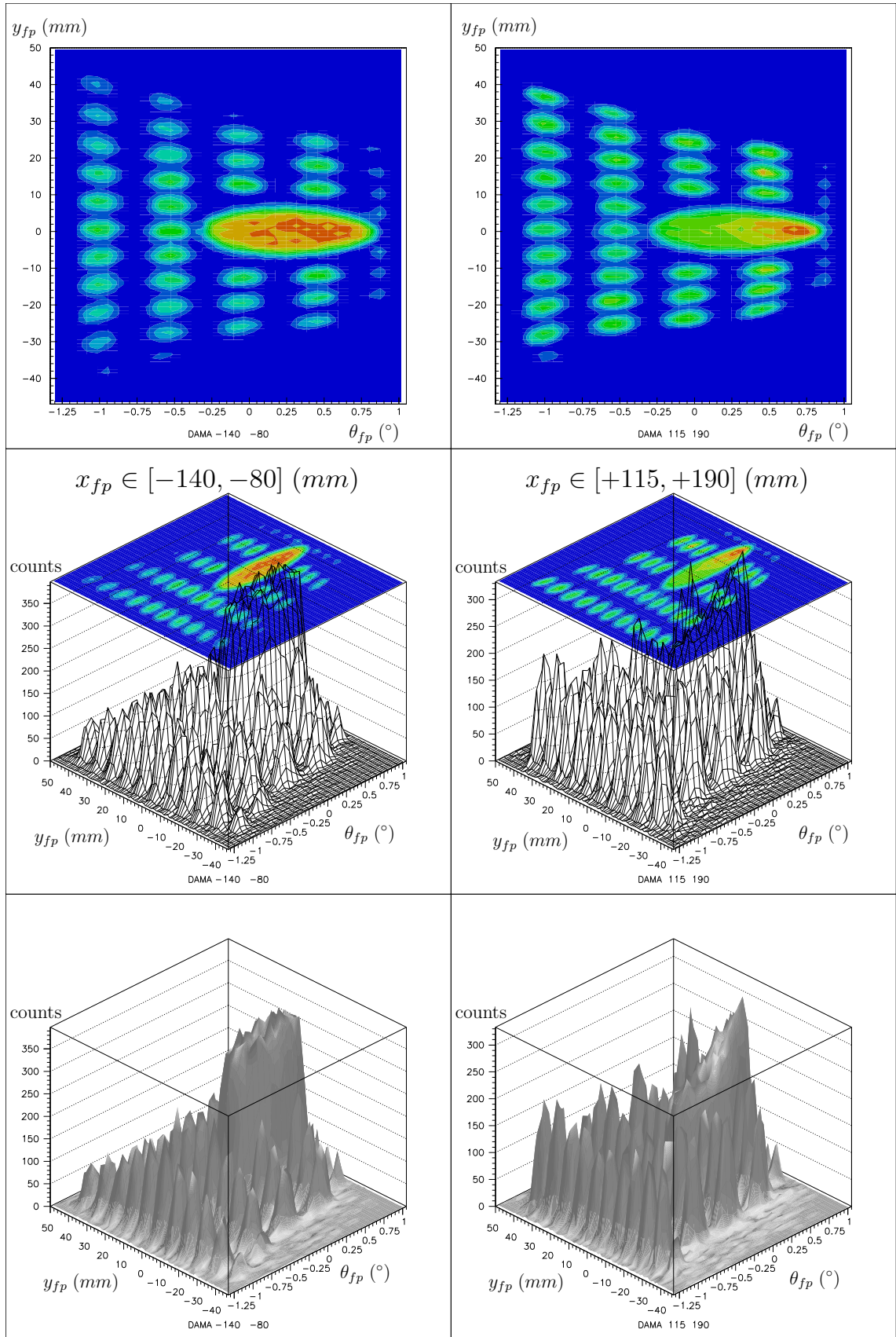


Figure 3.8: The multi-hole slit used for the angle calibration.

Figure 3.9: Sieve slit images at the focal plane for two different x_{fp} gates

3.4 Correction of ϕ and θ -aberrations

After the sieve slit correction and the reconstruction of the target scattering angles θ_{tgt} and ϕ_{tgt} , higher-order aberrations are still present in the spectra. They manifest themselves in distorted peak lines in the $x_{fp} - \theta_{tgt}$ and $x_{fp} - \phi_{tgt}$ spectra. If the scattered particles were correctly focused, the peaks would be seen as straight lines. The defocusing is mainly due to the saturation of the dipole magnets of GRAND RAIDEN at the high magnetic field of 1.7 T.

This aberration has important consequences for the energy resolution of projected spectra. Since a spectrum obtained by making a cut in $\theta - \phi$ space includes a range of θ or ϕ coordinates, the distortion of the peak line severely worsens the resolution.

To treat these higher-order aberrations, the peak lines were corrected by software using spline and polynomial interpolation. The novel procedure used to treat these aberrations and the software codes developed for this purpose are discussed in detail in the appendix B.2.

After the treatment of the ϕ and θ aberrations, the triton spectra have the desired high resolution needed for a detailed determination of B(GT) values.

Figure 3.10 shows the results obtained after each step of the offline correction for a sample peak (the ground state of ^{13}N). In the first row of the figure, only the sieve slit angle calibration has been carried out. Aberrations in θ and ϕ are clearly present and affect the projected spectra. The spectrum shown is the smallest angle cut, obviously the effect of the aberration on the resolution is even worse at larger angles.

The second row shows the result obtained after correcting the θ -aberration with the procedures outlined in B.2. The $x_{fp} - \theta_{tgt}$ spectrum is corrected so that a straight line is obtained, while the $x_{fp} - \phi_{tgt}$ spectrum is still distorted. The resolution already becomes much better since the θ -aberration has a larger effect than the ϕ -aberration on the resolution.

After treating the ϕ -aberration as well, the last row is obtained, which shows straight lines in the x - ϕ and x - θ spectra. After both aberrations have been treated, the final spectra have the highest possible resolution of around 30 keV and can be further analyzed.

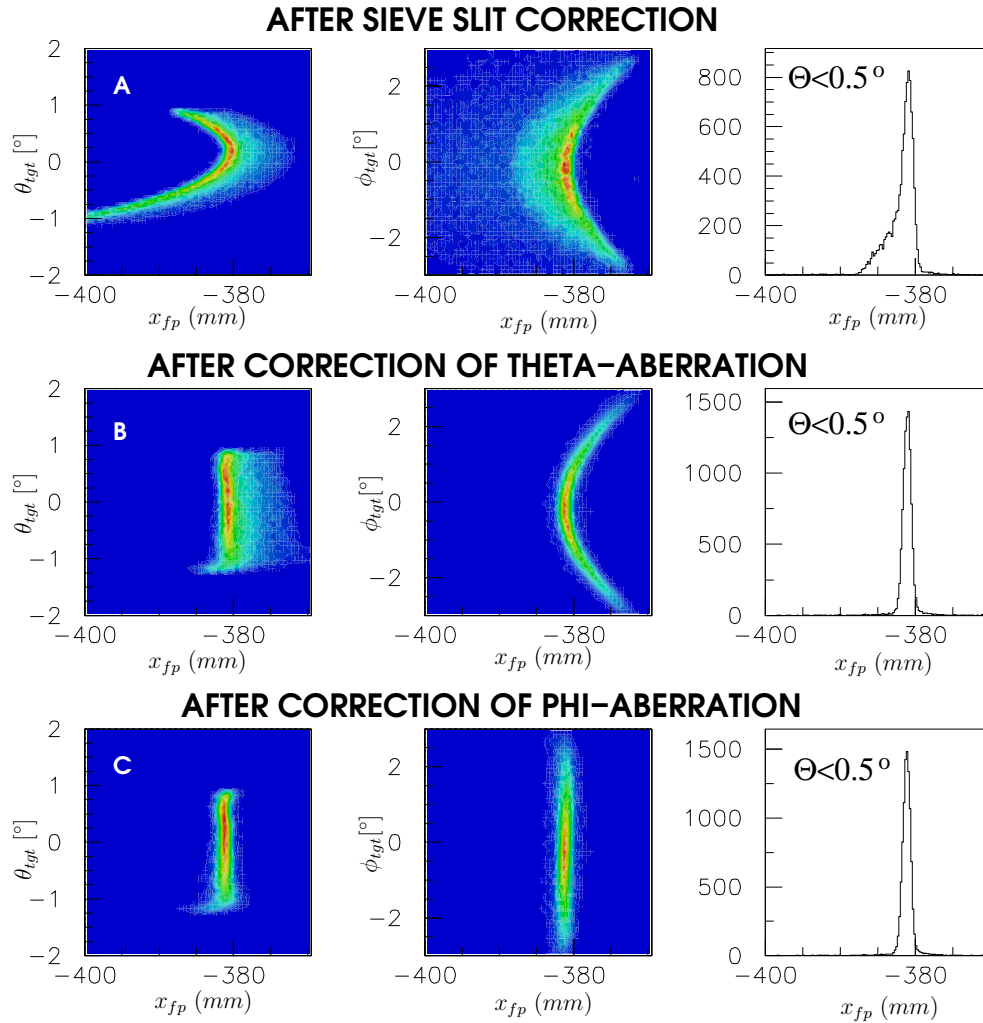


Figure 3.10: *Illustration of the effect of aberration corrections on the resolution of the final spectrum. The first column shows the $x_{fp} - \theta_{tgt}$ spectrum, the second column the $x_{fp} - \phi_{tgt}$ spectrum, and the final column the spectrum obtained by projection of events with $\Theta = \sqrt{\theta_{tgt}^2 + \phi_{tgt}^2} \leq 0.5^\circ$. All plots show the ground state of ^{13}N obtained after various corrections.*

The first row (A) shows the spectra obtained after the sieve slit correction. The aberrations in θ and ϕ can be clearly seen. Even in a projection with $\Theta \leq 0.5^\circ$, the effect on the energy spectrum are significant.

The second row (B) shows the spectra obtained after a correction of the θ -aberration. The $x_{fp} - \theta_{tgt}$ spectrum now has the form of a straight line, while the $x_{fp} - \phi_{tgt}$ spectrum is still distorted.

The third row (C) shows the final spectrum after both the θ and the ϕ aberrations have been treated. The peak in the energy spectrum now has the best possible resolution of around 30 keV.

Chapter 4

Data Analysis

4.1 Projections of 2D Spectra and calibration

Spectra for various scattering angle regions were obtained by projecting events within these regions onto the x-axis of the focal plane (see e.g. fig 4.18). Spectra for scattering angles between 0° and 0.50° are of main interest for the determination of Gamow-Teller strengths, while higher angle cuts were used to identify $\Delta L=0$ transitions, which have a pronounced forward-peaking in their angular distributions. Especially the difference spectra between 0° and 2° are very sensitive to $\Delta L=0$ contributions [Jän93]. Using several bins of scattering angles, the angular distribution can be extrapolated to the differential cross section at zero degrees, which is used to obtain the Gamow-Teller strength.

4.2 Peak fitting

The spectra were analyzed using the computer code `SFIT` [Fuj] by H. Fujita. The program allows to deconvolute peaks using a Lorentzian or gaussian peak shape, as well as a custom reference shape and its convolution with a Lorentzian peak shape. Even with the high resolution of around 30 keV, some peaks still overlap, especially with broader states, making deconvolution absolutely mandatory. The peaks in the spectra generally have a Lorentzian distribution, however this is affected by the beam condition, the fine-tuning of the ion optics by hardware and the off-line spectrum reconstruction process. Therefore, it is useful to use an isolated peak (preferably with no natural width) as a reference shape for the peak fitting procedure.

For both the ${}^9\text{Be}({}^3\text{He},t){}^9\text{B}$ and the ${}^{13}\text{C}({}^3\text{He},t){}^{13}\text{N}$ reaction, the ground state peak was used as a reference peak. The peaks were sampled from a low-angle cut spectrum and smoothed by spline interpolation to obtain a reference function for the peak shape. The form of the peak shapes can be seen in figs. 4.1 and 4.2. Both reference peaks have a FWHM value of roughly 5 channels (4.75 chn for ${}^9\text{B}$, 5.2 chn for ${}^{13}\text{N}$), the excitation

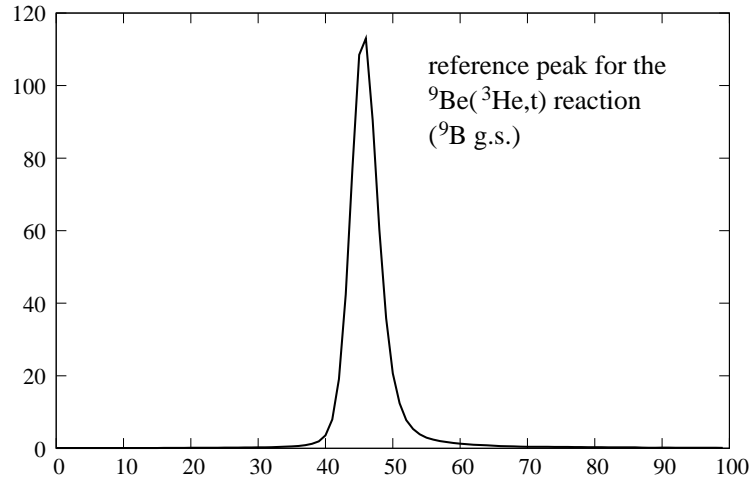


Figure 4.1: The reference peak shape for the ${}^9\text{Be}({}^3\text{He},t){}^9\text{B}$ reaction used in the deconvolution of the spectra. The x -axis represents channel numbers, the y -axis the intensity in arbitrary units.

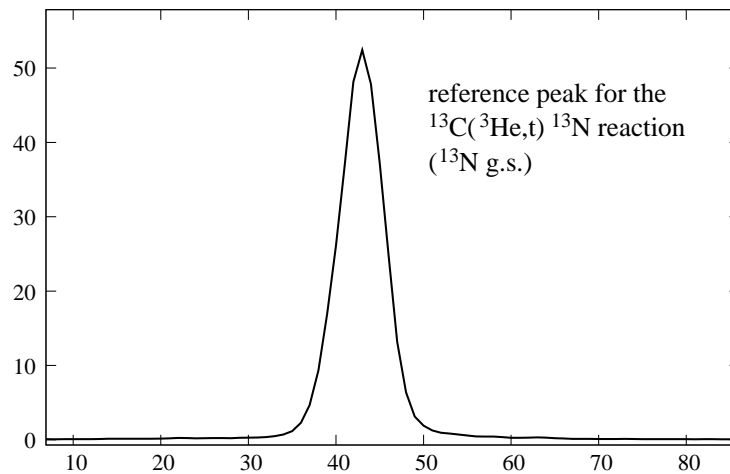


Figure 4.2: The reference peak shape for the ${}^{13}\text{C}({}^3\text{He},t){}^{13}\text{N}$ reaction used in the deconvolution of the spectra. The x -axis represents channel numbers, the y -axis the intensity in arbitrary units.

energy being roughly 6.5 keV/chn¹; this means the resolution achieved is around 30 keV. The ground states of ⁹B and ¹³N have only very small decay widths. The ground state of ¹³N has a half-life of 9.965(4) min which gives a decay width in the order of 10⁻²¹ keV², and the ground state of ⁹B has a decay width of 0.54(21) keV. The spectra were fitted using channels as position variables. The position and width information resulting from the fits as well as their respective errors (see next section) were subsequently converted into excitation energy using the energy calibration functions obtained as described in Appendix C.

4.3 Determination of errors

The program SFIT produces position, peak volume (intensity) and width information of the deconvoluted peaks. However, it does not automatically generate error estimates for these outputs. Nevertheless, it gives a χ^2 value of the obtained fit. In order to estimate the fitting error, a procedure suggested by P.R. Bevington [Bev69] was used. Approximating by expansion the χ^2 hypersurface, one finds that for a variation of σ_i^2 in one parameter a_i and an optimization of all other parameters $a_{i \neq j}$, the new value of χ^2 will be greater than the old value by 1:

$$\chi^2(a_i + \sigma_i^2) = \chi^2(a_i) + 1 \quad (4.1)$$

The errors of fits were determined using this approximation, which can be considered reasonable for the definition of the uncertainty σ_i for linear and non-linear fitting [Bev69].

4.4 Identification of contaminant peaks

It has to be taken into account that states originating from target impurities can appear in the obtained spectra. There are no isotopic impurities in the Beryllium target case, since the natural abundance of ⁹Be is nearly 100%, with only trace amounts of ¹⁰Be. A small amount of carbon contamination must have existed in the target or the vacuum container since the strong ¹²N ground state peak can be observed in the spectra (see figs. 4.13 and 4.14). Fortunately, due to the high resolution of the spectrometer, this state can be separated from the ⁹B states in the spectra. In the case of the ¹³C target, the target has a 99% enrichment in ¹³C (natural abundance 1.109%), thus contains 1% of the naturally more abundant (98.89%) ¹²C isotope. The ¹²N ground state (which is the most prominent state in the ¹²C(³He,t)¹²N reaction, see Appendix C) is thus observed in the spectra. Incidentally, the tritons being produced by an excitation of the ground state of ¹²N have nearly the same magnetic rigidity value Br within the spectrometer as the $T=3/2$, 15064.6(4) keV, $J^\pi=3/2^-$ state in ¹³N. The separation of the cross-section of this peak from the contaminant cross-section is thus more difficult, but can nevertheless be achieved because of the high resolution of the spectrometer and by using the fitting

¹See Appendix C

² $\Gamma = \frac{\hbar \ln 2}{597.9s} = 4.6 \cdot 10^{-18} \text{eV}$

program (see 4.2). The difference of 0.4 kG·cm in magnetic rigidity corresponds to 58 keV excitation energy difference, which is just at the limit of the resolving power of the spectrometer. This state will later be discussed in more detail. The spectra did not contain other contaminants or impurities.

4.5 The $^{13}\text{C}(^3\text{He},t)^{13}\text{N}$ spectrum

Figure 4.3 shows the full $^{13}\text{C}(^3\text{He},t)^{13}\text{N}$ spectrum recorded at 420 MeV beam energy for scattering angle $\Theta_{lab} < 0.5^\circ$. In the following sections, the features of the spectrum (mainly the excitation energies and widths of excited states in ^{13}N) will be analyzed in more detail.

4.5.1 Excitation energies from 0 to 6.5 MeV

The $^{13}\text{C}(^3\text{He},t)^{13}\text{N}$ spectrum from 0-6.5 MeV in excitation energy, for $\Theta_{lab} < 0.5^\circ$ is shown in fig. 4.4, with a cut-off around 1000 counts, chosen to show the weakly excited states. The dominant peaks in this region are the $J^\pi = 1/2^-$ ground state and the 3.5 MeV, $3/2^-$ state of ^{13}N . The $1/2^+$ state at 2.36 MeV and the $5/2^+$ state at 6.36 MeV can be weakly observed.

Since the proton-separation energy of ^{13}N is very low ($S_p = 1.9435$ MeV), all excited states have intrinsic natural decay widths. Thus, Lorentzian shapes were employed in fitting the peaks of the discrete states. When the energy resolution of around 30 keV was not negligibly small compared to the width of a discrete state, the Lorentzian shapes (BW) were folded with the reference peak shape shown in fig. 4.2 (RB) when possible. The obtained energies, decay widths and the triton yield in the $\Theta < 0.5^\circ$ angular cut are presented in table 4.1. There is good agreement with the compiled data from the nuclear data sheets (NDS) by F. Ajzenberg-Selove [AS91]. There is a state at 3.55 MeV ($J^\pi = 5/2^+$) which cannot be separated from the state at 3.5 MeV. The transition to the 3.55 MeV state is not of Fermi or Gamow-Teller nature ($\Delta L \neq 0$), and therefore is not expected to have a significant cross-section. If its cross-section were significant, it would drastically alter the angular distribution of the 3.5 MeV, $3/2^-$ state, since its angular distribution would have a minimum at zero degrees and a maximum at finite angle. This is not the case, as will be seen later.

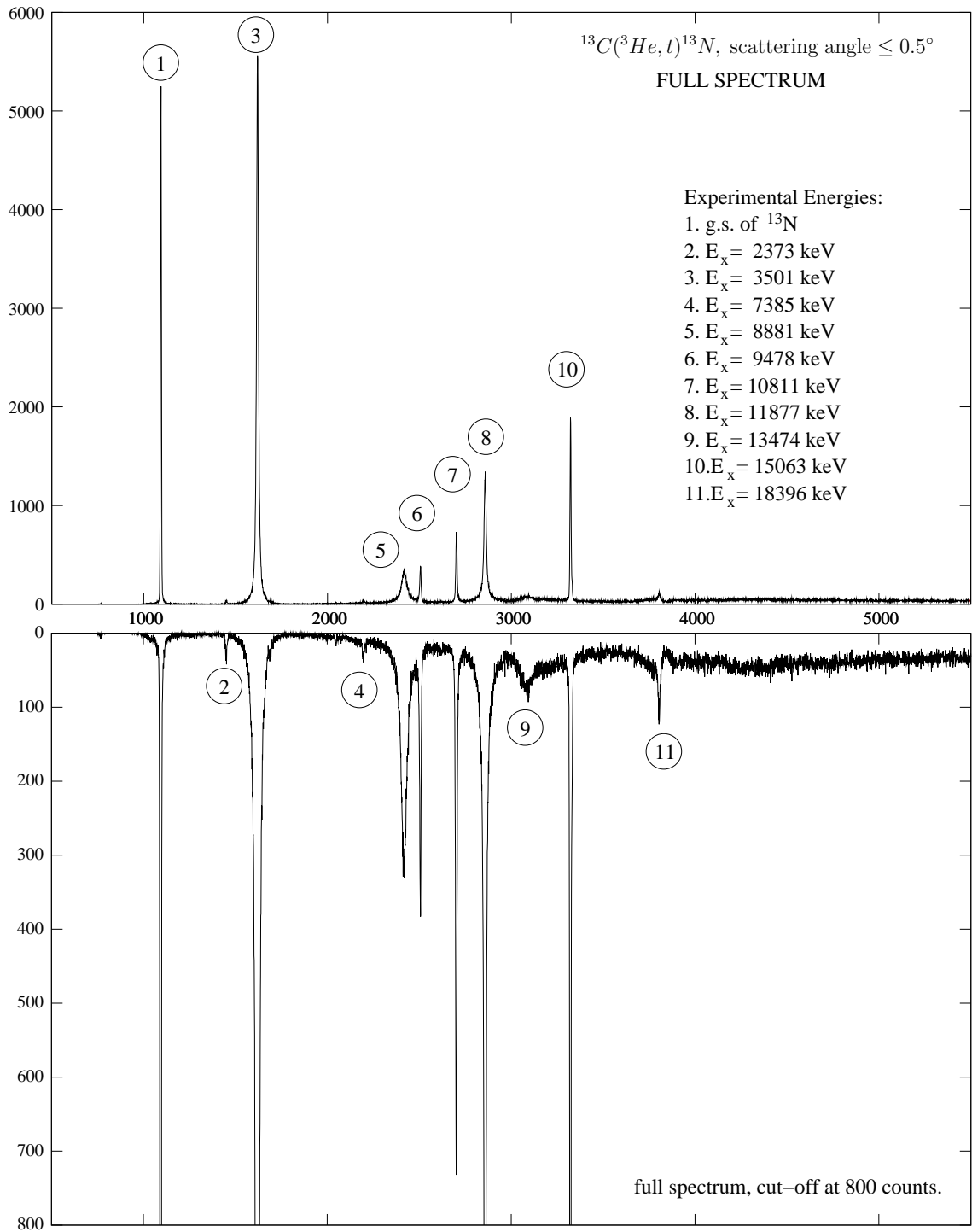


Figure 4.3: Full spectrum of the $^{13}\text{C}(^3\text{He},t)^{13}\text{N}$ reaction at 420 MeV beam energy. In the lower part of the picture, the spectrum has been cut off in order to make weakly excited states visible.

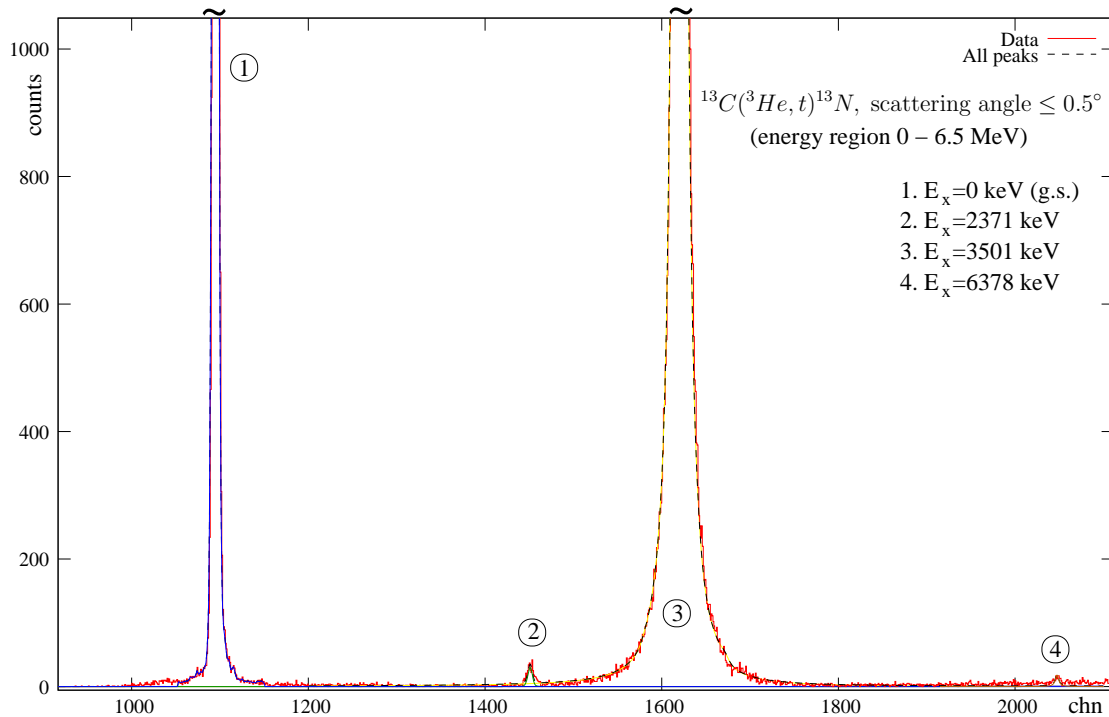
Table 4.1: Summary of the spectrum deconvolution for excitation energies 0-6.5 MeV.

(a) peak shape is the response function folded with a Breit-Wigner (Lorentzian) distribution

(b) peak shape is a Breit-Wigner (Lorentzian) distribution only

(c) $\tau_{1/2}=9.965(4)$ min [AS91](d) the natural width was determined from the width Γ_{BW} of the fitted peak using the energy resolution from the response function for ^{13}N of 33.8 keV: $\Gamma_{c.m.}=\sqrt{\Gamma_{BW}^2 - 33.8^2}$

Peak shape	$E_x^{(EXP)}$ [keV]	$E_x^{(NDS)}$ [keV]	J^π (NDS)	$\Gamma_{c.m.}^{(EXP)}$ [keV]	$\Gamma_{c.m.}^{(NDS)}$ [keV]	N_{triton}
RB ^(a)	1.2(34)	0	1/2-	0 ⁺	0 ^(c)	34826(849)
RB	2373.1 ^{+25.5} _{-20.9}	2364.9(6)	1/2+	23(3)	31.7(8)	328(54)
RB	3501.2 ^{+3.4} _{-3.6}	3502(2)	3/2-	52.5 ^{+7.4} _{-6.8}	62(4)	94238(2534)
-	-	3547(4)	5/2+	-	47(7)	-
BW ^(b)	6363.3(34)	6364(9)	5/2+	15(7) ^(d)	11	69(12)

Figure 4.4: Deconvolution of the spectrum for scattering angle less than 0.5° of the $^{13}\text{C}(^3\text{He},t)^{13}\text{N}$ reaction for excitation energies 0-6.5 MeV.

4.5.2 Excitation energies from 6 to 16 MeV

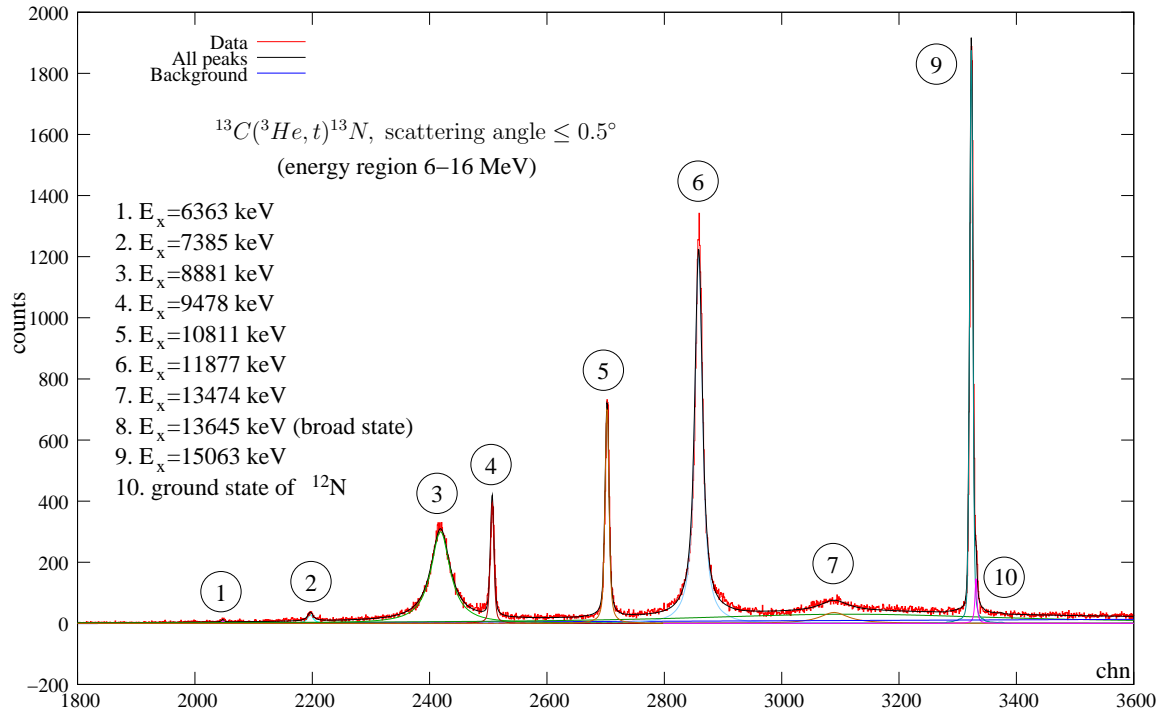


Figure 4.5: Deconvolution of the spectrum for scattering angle less than 0.5° of the $^{13}\text{C}(^3\text{He},t)^{13}\text{N}$ reaction for excitation energies 6–16 MeV.

The $^{13}\text{C}(^3\text{He},t)^{13}\text{N}$ spectrum from 6–16 MeV in excitation energy (for $\Theta_{lab} < 0.5^\circ$) is shown in fig. 4.5, while fig. 4.6 shows the same spectrum with a y-axis cut-off at 750 counts, for a better visibility of the weakly excited states. The excitation energy and decay width of eight states in total were determined for this scattering angle region using SFIT. The results are summarized in table 4.2 and compared to the compiled values [AS91].

As expected, mainly states with $J^\pi = 1/2^-$ and $3/2^-$ ($\Delta L = 0$) are excited at zero degrees in the $(^3\text{He},t)$ reaction. These are the prominent states in the spectrum for this energy region, at 8.9 MeV ($1/2^-$), 9.5 MeV ($3/2^-$), 10.8 MeV ($1/2^-$), 11.9 MeV ($3/2^-$) and 15.1 MeV ($3/2^-$).

The state at 11877(7) keV excitation energy (with $\Gamma_{c.m.} = 82(5)$ keV) in the spectrum is strongly excited, and its angular distribution clearly supports a $\Delta L = 0$ assignment. The compilation, however, lists a state at 11860(40) as being a $1/2^+$ state with a width of 380(50) keV, both of which are not supported by the present experimental evidence. The 11860(40), $1/2^+$ level was observed by Meyer and Plattner [Mey73] in 1973 from proton scattering on ^{12}C , who only found a $3/2^-$ state at 11.7 MeV with a width of 530 keV. A similar study from 1972 by Wienhard, Clausnitzer and Hartmann [Wie72] found no evidence for the $1/2^+$ state found by Meyer and Plattner, which was inside the energy range of their analysis. Wienhard *et al.* found a $3/2^-$ state at $E_x = 11.67$ MeV (a level which they felt was not identical with the 11.88 level seen in pick-up and two-nucleon transfer reactions, see below) and a $3/2^+$ state at 11.82 MeV, deduced from a strong

Table 4.2: Summary of the spectrum deconvolution for excitation energies 6.5-16 MeV.

^(a) the natural width was determined from the width Γ_{BW} of the fitted peak using the energy resolution from the response function for ^{13}N of 33.8 keV: $\Gamma_{c.m.} = \sqrt{\Gamma_{\text{BW}}^2 - 33.8^2}$

^(b) The angular distribution as well as observations by other experimentators are strongly supporting the $3/2^-$ assignment, see discussion in text or [Fuj04a]

^(c) The existence of a $3/2^-$ state at 11.8 MeV has been confirmed by many other transfer reactions, see text.

Peak shape	$E_x^{(EXP)}$ [keV]	$E_x^{(NDS)}$ [keV]	J^π (NDS)	$\Gamma_{c.m.}^{(EXP)}$ [keV]	$\Gamma_{c.m.}^{(NDS)}$ [keV]
BW	7385.2(68)	7376(9)	5/2-	66.2(74) ^(a)	75(5)
RB	8881(27)	8918(11)	1/2-	243(14)	230
RB	9478(11)	9476(8)	3/2-	25(2)	30
RB	10811.3(45)	10833(9)	1/2-	20(2)	
RB	11876.9(65)	11860(40) or 11740(50), 11.88 MeV ^(c) [Fuj04a]	1/2+ or 3/2- ^(b) 3/2-	82(5)	380(50) or 530(80) 98 [Fuj04a]
BW	13474(48)	12937(24) or 13.5 MeV [Nag61]		438(27)	>400 500 [Nag61]
BW	13645	13500(200)	3/2+	4565	≈6500
RB	15062.6(25)	15064.6(4)	3/2-	5.0 ^{+5.8} _{-5.0}	0.86(12)

destructive interference observed in the $^{12}\text{C}(p,\gamma_0)^{13}\text{N}$ reaction at 90° indicating a level with positive parity ($1/2^+$ or $3/2^+$) at 11.8 MeV.

An 11.8 MeV, $3/2^-$, $\Gamma=115$ keV state had already been observed in many transfer reactions in the 1960s, by Kozub *et al.* [Koz67], Bachelier *et al.* [Bac66], Hinterberger *et al.* [Hin68], Fleming *et al.* [Fle68] and Ball *et al.* [Bal69]. More recently (2004), Fujimura *et al.* [Fuj04a] have also studied the $(^3\text{He},t)$ reaction on ^{13}C at 450 MeV and found this $3/2^-$ state at $E_x=11.88$ MeV with a width of 98 keV, which is in agreement with the observations in the present study. It seems the elastic proton scattering is not sensitive to this level, which is clearly seen as a strongly excited state in both (p,n) and $(^3\text{He},t)$ reactions. This $3/2^-$ state was also observed in $^{11}\text{B}(^3\text{He},n)$ at 11878(12) keV, $^{14}\text{N}(p,d)$ at 11.86 MeV and $^{14}\text{N}(d,t)$ at 11.8 MeV [AS91]. The (p,n) reaction does not offer sufficient energy resolution to choose between 11.74 and 11.88 MeV, the recent experiment by Wang *et al.* [Wan01] with an energy resolution of 200 keV gives the compiled energy of 11.74 MeV.

The analog $3/2^-$ state in ^{13}C is given at 11.748(10) MeV with a width of $\Gamma=110(15)$ keV, while a level at 11.848(4) MeV with a width of 68(4) keV is assigned $J^\pi=7/2^+$ [AS91]. A $^{12}\text{C}(d,p)^{13}\text{C}$ experiment by Goss *et al.* [Gos73] saw both levels in the proton spectra at 11.748(10) MeV ($\Gamma=107(14)$) and 11.851(5) MeV ($\Gamma=68(4)$). The $3/2^-$ spin assignment for the 11.75 MeV level in ^{13}C is the result of a neutron inelastic scattering study ($^{12}\text{C}(n,n)^{12}\text{C}$) by Knox and Lane [Kno82], who acknowledge that the “*proposed structure in this region is less certain than that at lower energies due to the difficulties in fitting the experimental data in this region*”.

The excitation energies and decay widths of all other negative parity states observed are in agreement with the compiled data.

The $T=3/2$, $J^\pi=3/2^-$ state at 15.1 MeV is important for the analysis of GT strengths for calibration purposes, as it has two analog β -decay transitions ($^{13}\text{B}(\beta^-)^{13}\text{C}$ and $^{13}\text{O}(\beta^+)^{13}\text{N}$), whose lifetimes, and thus $B(\text{GT})$ values are known from experiments.

In the $(^3\text{He},t)$ experiment on a carbon target, a difficulty arises since the 15.1 MeV state in ^{13}N is nearly inseparable from the ground state of ^{12}N excited by the charge-exchange reaction on ^{12}C , especially if a target with low enrichment in ^{13}C is used. At 420 MeV and zero degrees, *relkin* [Phi67, Poi68, Dav69] gives a magnetic rigidity value of 5193.45 kG·cm for the 15.1 MeV state in ^{13}N and 5193.05 kG·cm for the ground state of ^{12}N . This difference of 0.4 kG·cm corresponds to an energy difference of 58 keV³, which means the separation of both states is just at the limit of the resolving power of GRAND RAIDEN (both states have negligible intrinsic decay widths). Previous experiments, like the $(^3\text{He},t)$ experiment on an enriched ^{13}C target by Fujimura *et al.* [Fuj04a], with a lower energy resolution (about 300 keV), were not able to separate both states and had to estimate the influence of the ^{12}N ground state cross-section on the ^{13}N $T=3/2, J^\pi=3/2^-$ state cross-section at 15.1 MeV excitation energy.

In the present work, it was possible to separate both states in the deconvolution analysis using SFIT and the reference peak shapes. The deconvolution for $\Theta_{lab}<0.5^\circ$ is shown in fig. 4.7. In this spectrum (and for the used target which had 99% enrichment in

³See Appendix C

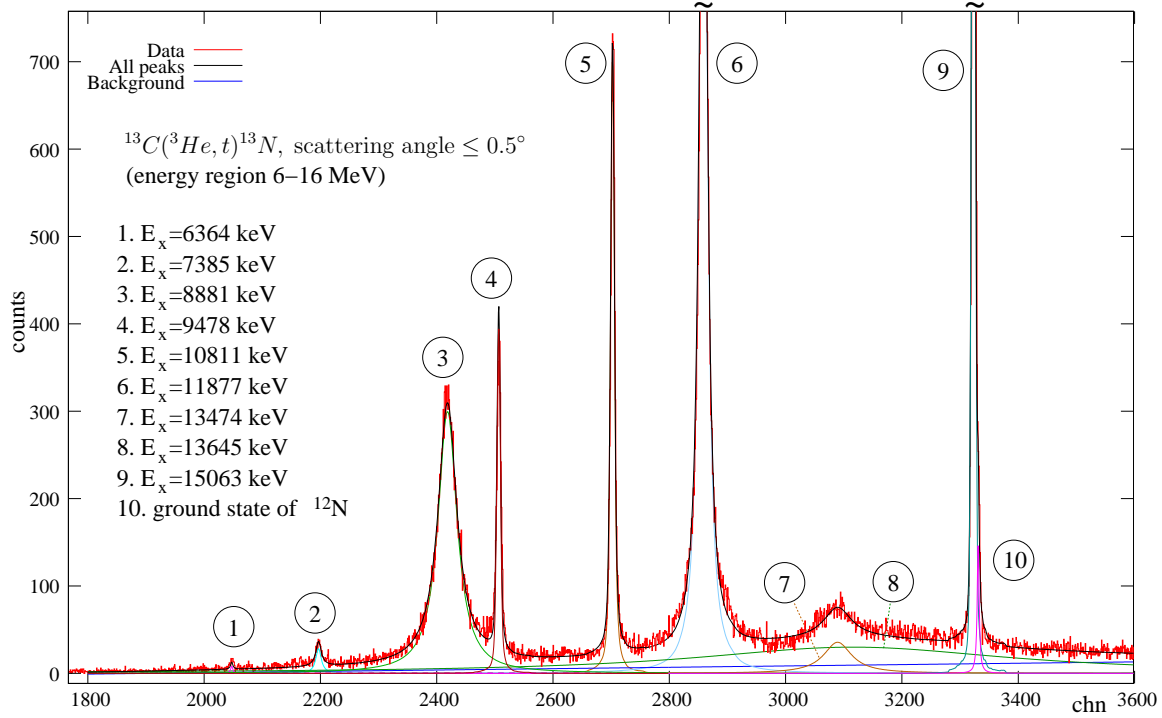


Figure 4.6: Deconvolution of the spectrum for scattering angle less than 0.5° of the $^{13}\text{C}(^3\text{He},t)^{13}\text{N}$ reaction for excitation energies 6-16 MeV. The spectrum is scaled for better visibility.

^{13}C), the ^{12}N ground state cross-section corresponds to around 6.5% of the cross-section of the ^{13}N state at 15.1 MeV.

Another feature of the recorded spectrum is the presence of a broad state which peaks at around 13.6 MeV. The data compilation quotes a state at 13.5(2) MeV with a width of ≈ 6.5 MeV. There are two references for this level, a $^{nat}\text{C}(p,\gamma)$ reaction at 9-24 MeV proton energy by D. F. Measday, M. Hasinoff and D. L. Johnson [Mea73] which gives the 6.5 MeV width, and an elastic proton scattering experiment by Nagahara [Nag61], who obtained $E_x=13.5$ MeV and $\Gamma=500$ keV. The present experimental study seems to reflect both results. A state at 13.5 MeV can clearly be seen (we obtain 13474(48) keV), and the width of 438(27) is comparable to the width obtained by Nagahara. On the other hand, there is also evidence for a broad underlying structure in the region between 10 and 16 MeV in excitation energy. The state at 13645 keV presented in table 4.2 was obtained by holding all other peak positions and widths at their previously fitted positions, and fitting a broad Lorentzian shape with free width and position. The best χ^2 was obtained for $E_x=13645$ and $\Gamma=4565$, which is close to the value of Measday *et al.* [Mea73]. It is difficult to give error estimates for these broad states from the fit, but the position can vary by at least 100 keV and the width by several hundred keV.

At higher scattering angle, the cross-section of states excited via $\Delta L \geq 1$ gradually increases. This can be seen in fig. 4.8, where the spectra obtained for different scattering angle regions are plotted, adjusted for the solid angle size (see 4.8). The spectra are plotted with a small y-offset of 25 units per spectrum for better visibility. Since the

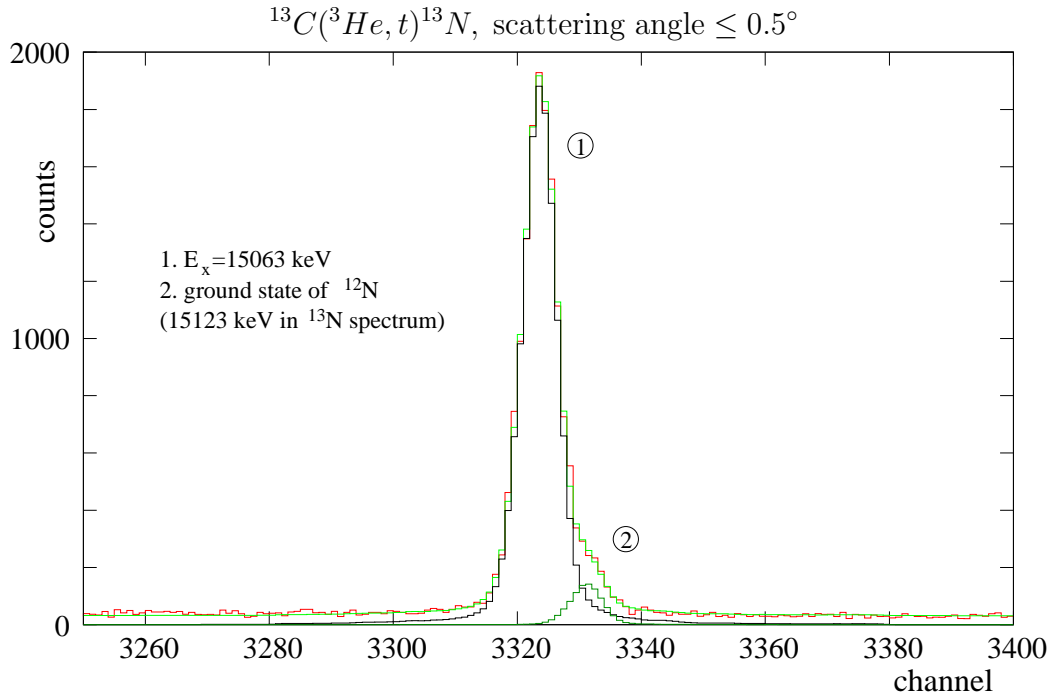


Figure 4.7: Separation of the ^{12}N ground state and the ^{13}N $T=3/2$ state at 15.1 MeV in the deconvolution analysis with SFIT.

spectra have been adjusted for the solid angle, the y-axis is directly proportional to the differential cross-section.

Small peaks that appear at higher scattering angle can clearly be distinguished. Peaks at 6950 keV (most likely corresponding to the 6886(8) keV, $3/2^+$ state in the compilation [AS91]) and 7170 keV (most likely corresponding to the 7155(5), $7/2^+$ state in the compilation) can be observed below 8 MeV. Another state not present in the zero degree spectrum is found at 10.29 MeV (most likely corresponding to the 10.25(15), $(1/2^+)$ state in the compilation).

4.5.3 Excitation energies from 17 to 30 MeV

At higher excitation energy, beyond the 15.1 MeV $T=3/2$ state, there is anecdotal evidence for a state around 15.9 MeV which could either correspond to the 15.3(2) MeV, $(3/2^+)$ or to the 15.99(3) MeV, $7/2^+$ state in the compilation. There is also indication for one or more broad state(s) at around 18 MeV, and there are two possible candidates in the compilation: 18.15(3), $3/2^+$ and 18.17(2), $1/2^-$. The states observed in fig. 4.9 at 17.8 MeV and 18.2 MeV can be better distinguished at higher angle, since the cross-section of the 17.8 MeV state increases with higher scattering angle.

The state observed at 18.4 MeV clearly has $\Delta L=0$ nature, however the compilation quotes a state with $E_x=18.406(5)$ MeV and $J^\pi=3/2^+$, observed in proton scattering on ^{12}C . The situation here could be similar to the one encountered at the 11.8 MeV level, as the (p,n) reaction does not have sufficient energy resolution to distinguish between

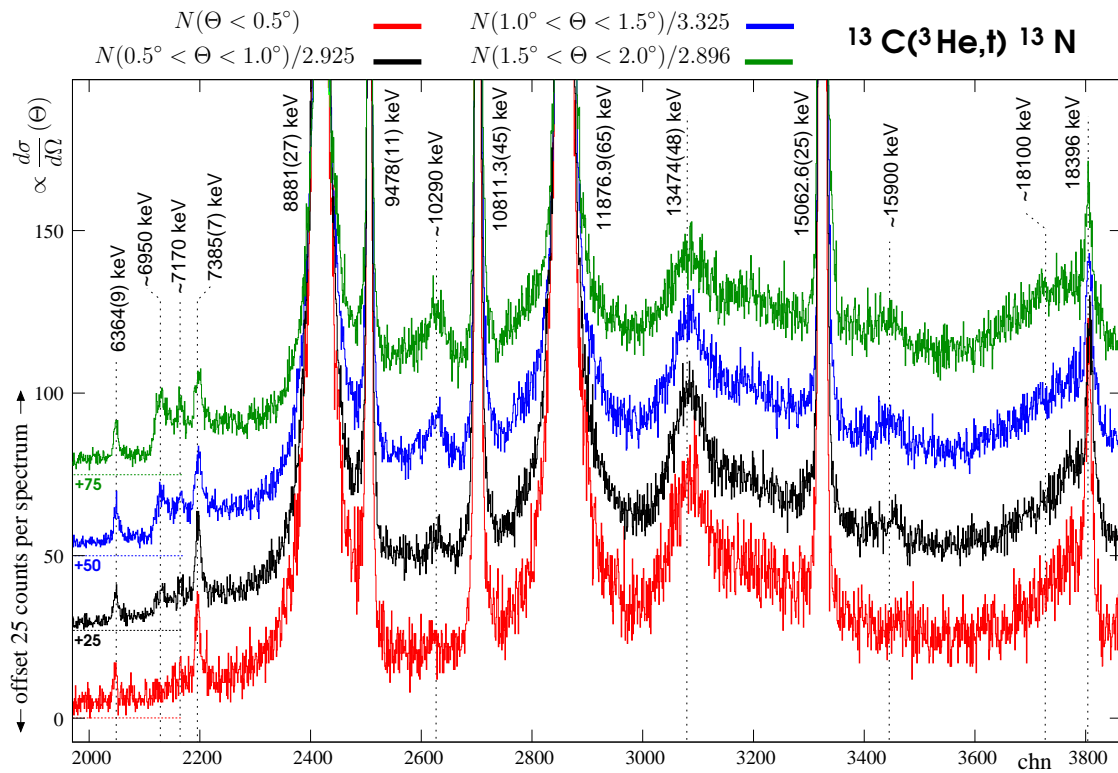


Figure 4.8: Spectra of the $^{13}\text{C}(^3\text{He},t)^{13}\text{N}$ reaction for excitation energies 6-19 MeV at different scattering angles. The spectra are offset by 25 counts to each other for better visibility, and have been scaled with their respective solid angle adjustment factors (Ω_i/Ω_1) so that the y-axis is directly proportional to the differential cross-section. The lowest spectrum (red) shows the data obtained for $\Theta < 0.5^\circ$, the next spectrum (black) the data for $0.5^\circ < \Theta < 1.0^\circ$, the spectrum with +50 counts offset (blue) shows the data for $1.0^\circ < \Theta < 1.5^\circ$ and the last spectrum (green) shows the data for $1.5^\circ < \Theta < 2.0^\circ$. It is evident in the green and blue spectra that states excited with $\Delta L \geq 1$ appear at higher scattering angle.

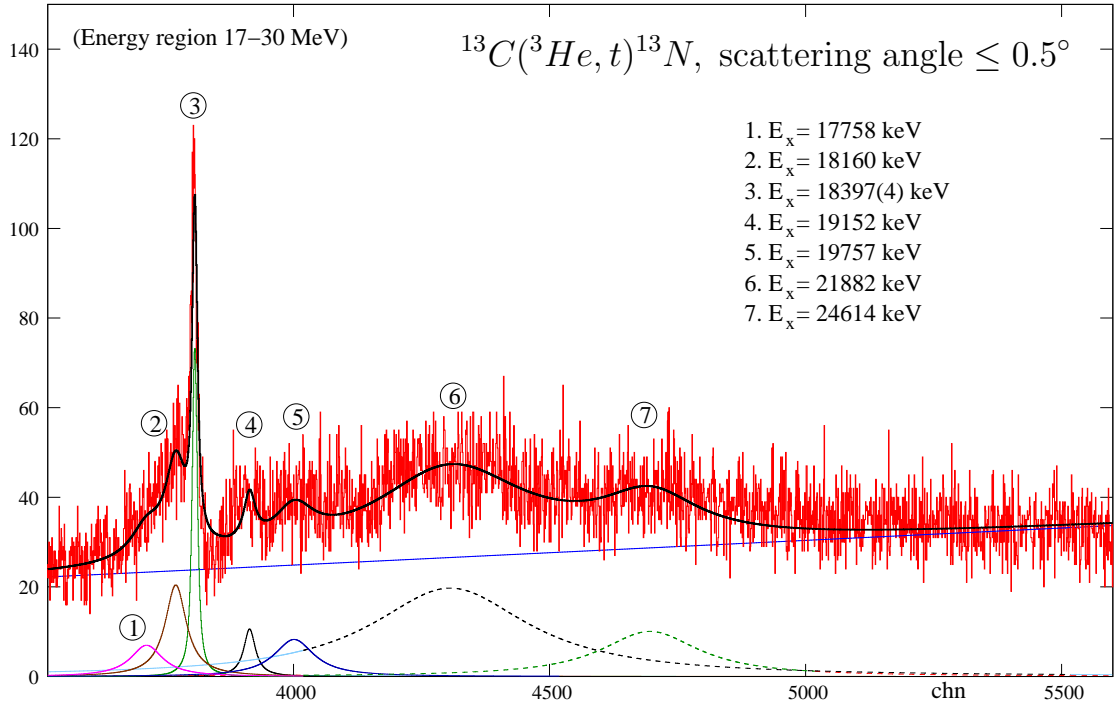


Figure 4.9: Deconvolution of the spectrum for scattering angle less than 0.5° of the $^{13}\text{C}(^3\text{He}, t)^{13}\text{N}$ reaction for excitation energies 17–30 MeV.

18.2 and 18.4 MeV (Wang *et al.* give the 18.17 MeV value for the $3/2^-$ level). Fujimura *et al.* [Fuj04a] (who also noted the difficulty to find one-to-one correspondence with the compiled data) also observed this level, they found it at 18.37(1) MeV with a width of 23 keV (fixed, corresponding to the compiled width of the 18.96(1), $(3/2^-, 7/2^+)$ state), which is in agreement with the present study. The two smaller states at 17.8 MeV and 18.2 MeV were found by Fujimura *et al.* [Fuj04a] at 17.68(3) MeV and 18.12(2) MeV respectively.

There are more states at higher excitation energy, but no $\Delta L=0$ nature can evidently be attributed to them. Since this work is restricted to rather small scattering angles, not much can be said about the states beyond 19 MeV. The work of Fujimura *et al.* [Fuj04a] also studied higher scattering angles of up to 6.25° , and analyzed the region 16–30 MeV excitation energy in great detail. Of the states found in [Fuj04a], the states at 19.15 MeV (19.11(1) MeV in [Fuj04a]), 19.76 MeV (19.83(2) MeV in [Fuj04a]), 21.9 MeV (22.14(1) MeV in [Fuj04a]) and 24.6 MeV (24.50(4) MeV in [Fuj04a]) were observed as well.

4.6 The ${}^9\text{Be}({}^3\text{He},t){}^9\text{B}$ spectrum

Figure 4.10 shows the full ${}^9\text{Be}({}^3\text{He},t){}^9\text{B}$ spectrum recorded at 420 MeV beam energy for scattering angle $\Theta_{lab} < 0.5^\circ$. The nucleus ${}^9\text{Be}$ has the smallest neutron separation energy among stable nuclei ($S_n = 1665.4(4)$ keV) [Til04], and the mass difference between ${}^9\text{B}$ and ${}^9\text{Be}$ being smaller than the mass difference between proton and neutron gives a negative proton separation energy for ${}^9\text{B}$ ($S_p = -185.6(10)$ keV), which means all states in ${}^9\text{B}$ are above the proton threshold and particle-unbound.

In the following sections, the features of the spectrum (mainly the excitation energies and widths of excited states in ${}^9\text{B}$) will be analyzed in more detail.

4.6.1 Excitation energies from 0 to 10 MeV

The excited states in ${}^9\text{B}$ below 10 MeV, with exception of the ground state, are overlapping with large widths, which makes the identification of individual states rather difficult. All states below 10 MeV are $T=1/2$ states. The deconvolution of the spectrum was attempted based on the compiled information from Tilley *et al.* [Til04]⁴. The obtained excitation energies and widths for states below 10 MeV are summarized in table 4.3 and compared to the previous evaluations. The deconvolution of the spectrum is shown in the figures 4.11 and 4.12.

The first excited state in ${}^9\text{B}$ is deemed to be the analog of the 1.68 MeV, $J^\pi=1/2^+$ state of ${}^9\text{Be}$. The search for this state has yielded a wide range of possible energies and widths in previous experimental studies. Since $1/2^+$ states are only weakly excited in the $({}^3\text{He},t)$ reaction at forward angle, this state would be buried under the very large bump-like structure arising from the overlapping of the higher excited states with large widths. The present deconvolution attempt yields a value for the excitation energy of 1.85(13) MeV for this state, and a decay width of 700^{+270}_{-200} keV. This is broadly in line with previous studies, especially the recent $({}^3\text{He},t)$ deconvolution analysis by Akimune *et al.* [Aki01]. The next state is the strongly excited $5/2^-$ state at 2.358(7) MeV (the second-strongest after the ground state), whose excitation energy and width is well confirmed in the present study.

The study by Akimune *et al.* [Aki01] from 2001, using the same $({}^3\text{He},t)$ reaction at a slightly higher beam energy of $E/A=150$ MeV, furthermore found compelling evidence for a state at excitation energy of 3.8 MeV, which is also clearly seen in the present experiment. The angular distribution also supports a $\Delta L=0$ character, and the obtained decay width also agrees with the value obtained by Akimune *et al.*

The spectrum of the present experiment also contains a rather strongly excited state with $\Delta L=0$ character around 2.7 MeV. Akimune *et al.* observed this state as well, but fixed the excitation energy at 2.788 MeV, which corresponds to a state assigned $5/2^+$ [Til04]. The evaluation cites a state at 2.75(30) MeV with $J^\pi=1/2^-$ (analog to the 2.78 MeV state in ${}^9\text{Be}$) which would better correspond to the observed angular

⁴The most current data can be found on the TUNL nuclear data evaluation website, <http://www.tunl.duke.edu/nucldata/>

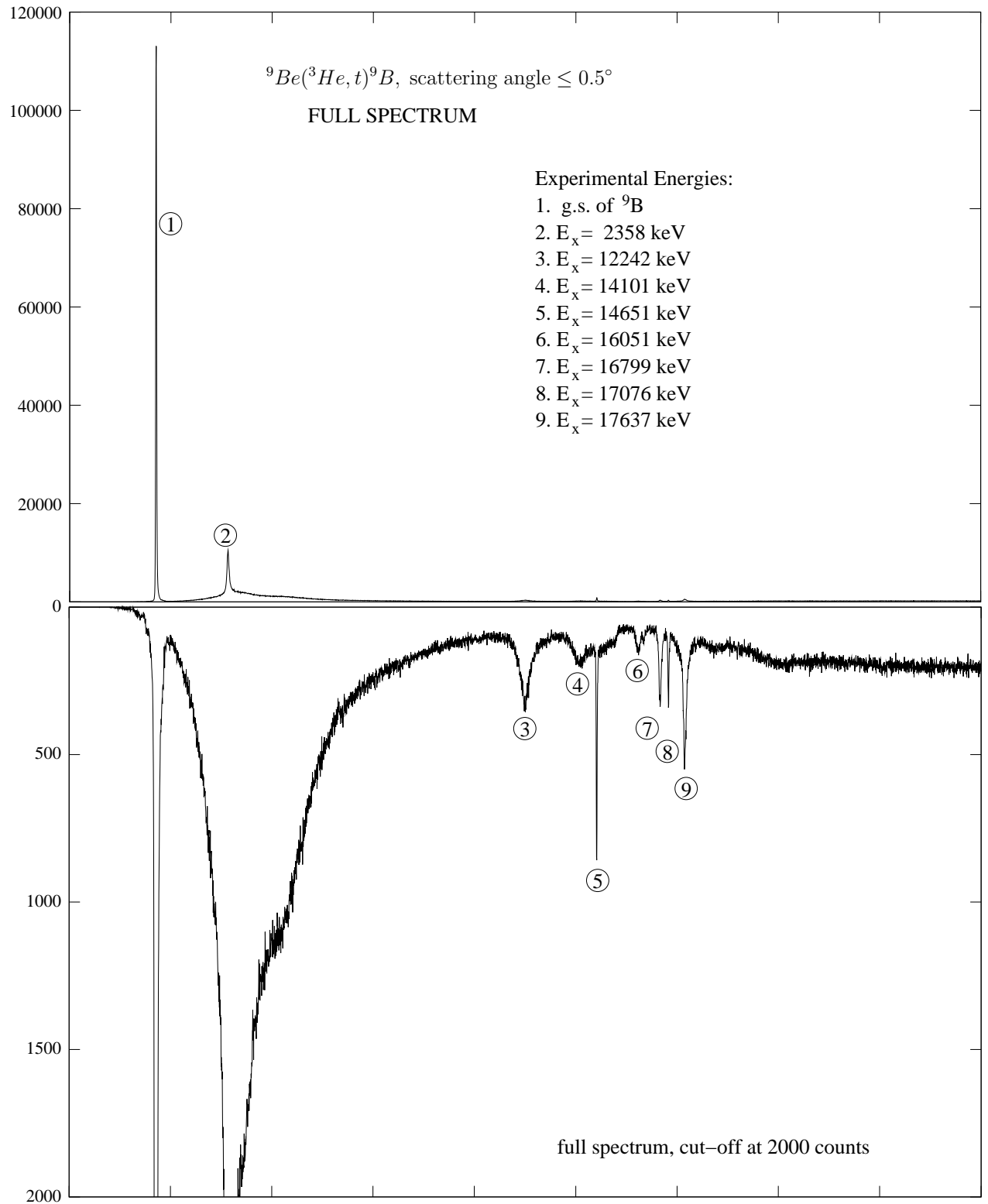


Figure 4.10: Full spectrum of the ${}^9\text{Be}({}^3\text{He}, t){}^9\text{B}$ reaction at 420 MeV beam energy. In the lower part of the picture, the spectrum has been cut off in order to make weakly excited states visible.

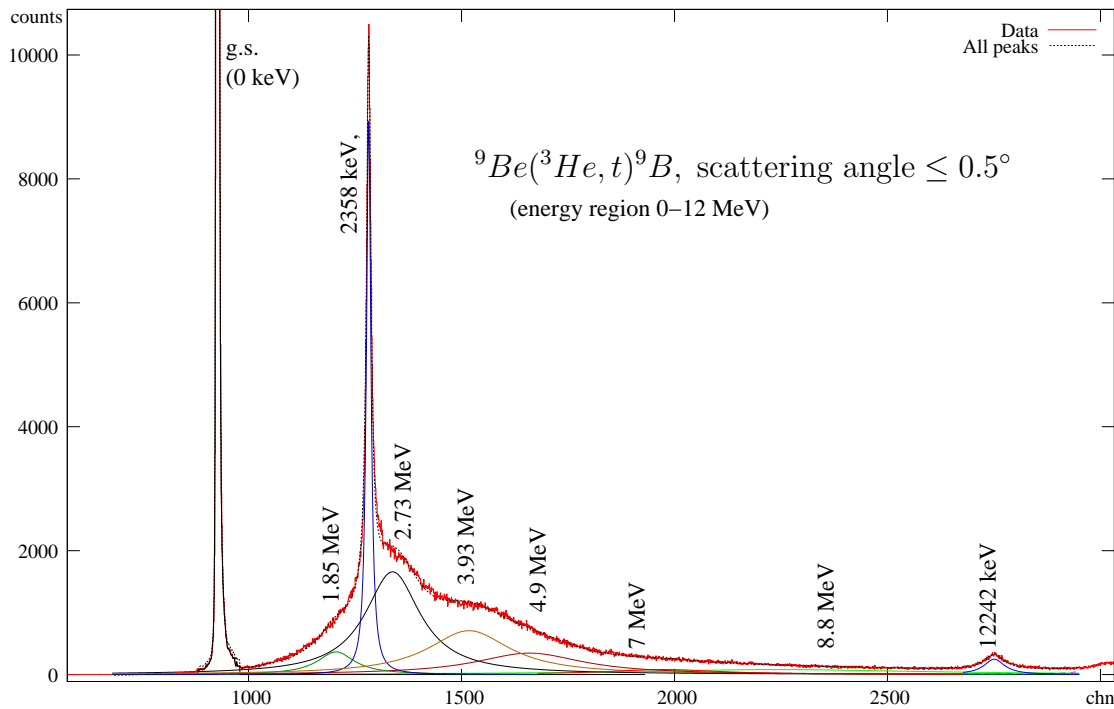


Figure 4.11: Deconvolution of the lower part of the spectrum for scattering angle less than 0.5° of the ${}^9\text{Be}({}^3\text{He},t){}^9\text{B}$ reaction. The spectrum is scaled to the height of the 2.3 MeV peak for better visibility (the ground state peak has $1.13 \cdot 10^5$ maximum counts).

distribution and excitation strength. However, the decay width cited in the compilation (3.13(20) MeV) is larger than the value obtained from the deconvolution (1.0(2) MeV). It does however agree with the value obtained in [Aki01].

The states given in the compilation at 4.8 MeV and 7.0 MeV are not strongly excited and also do not exhibit $\Delta L=0$ character in their angular distribution. Their positions have been kept fixed for the deconvolution. Although the presence of further strongly excited states in the spectrum can be ruled out, there is some evidence pointing to the presence of one (or more) state(s) with a large decay width around 8 MeV excitation energy. It is however very difficult to give an exact position or width for this hypothetical state because of the weak excitation and large ambiguity in the fitting procedure. A good fit is obtained for $E_x \approx 8.8$ MeV and $\Gamma \approx 6$ MeV.

Table 4.3: Summary of the spectrum deconvolution for excitation energies 0-10 MeV. The observables presented in columns indicated with a (NDS) superscript denote values from the evaluation by Tilley *et al.* [Til04], unless another citation is given.

^(a) this value has been kept fixed for the deconvolution

^(b) A wide range of excitation energies and widths have been given from searches for the analog of the 1.68 MeV $1/2^+$ state of ${}^9\text{Be}$ [Til04]. The values obtained by Akimune *et al.* [Aki01] for the excitation energy and width of this state closely coincide to the values obtained in the present study.

^(c) A $5/2^+$ and a $1/2^-$ state have been reported in this energy range [Til04]. Akimune *et al.* chose to fix the position of this state in the spectrum at 2788 keV, but acknowledged the angular distribution does not follow the expected $L=1$ behaviour for a $5/2^+$ state. The width, however, matches the reported value. The excitation energy obtained in the present study agrees with both energy values, but not the quoted widths. It agrees with the width obtained in [Aki01], and the angular distribution shows a clear $\Delta L=0$ character.

^(d) This state is not present in the previous evaluations. The deconvolution of the spectrum supports the presence of an additional very broad peak within this energy range.

$E_x^{(EXP)}$ [keV]	$E_x^{(NDS)}$ [keV]	J^π (NDS)	$\Gamma_{c.m.}^{(EXP)}$ [keV]	$\Gamma_{c.m.}^{(NDS)}$ [keV]
0.0(3)	g.s.	3/2-	$0.0^{+0.5}$	0.54(21)
1850(130)	$\approx 1600^{(b)}$ 1800^{+220}_{-160} [Aki01]		700^{+270}_{-200}	≈ 700 600^{+300}_{-270} [Aki01]
2358(7)	2361(5)	5/2-	84(7)	81(5)
2730(70)	$2750(300)^{(c)}$ $2788(30)^{(c)}$	$1/2^-$ $5/2^+$	1000(200)	3130(200) 550(40) 810^{+340}_{-310} keV [Aki01]
3930(100)	3820^{+230}_{-220} [Aki01]		1570(250)	1330^{+620}_{-360} [Aki01]
4900 ^(a)	4800(100)		2000(500)	1200(200)
7000 ^(a)	6985(50)	7/2-	2190 ^(a)	2180(150)
8800 ^(d)				≈ 6000

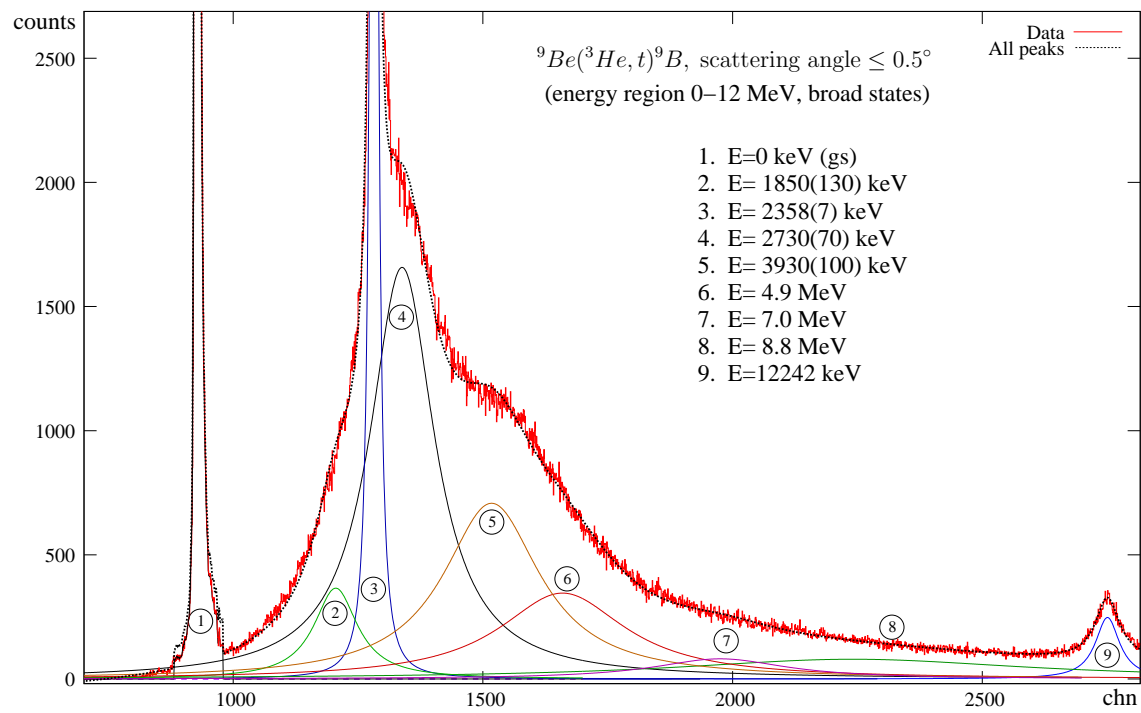


Figure 4.12: Deconvolution of the lower part of the spectrum for scattering angle less than 0.5° of the ${}^9\text{Be}({}^3\text{He}, t){}^9\text{B}$ reaction. The spectrum is scaled to the height of the 2.73 MeV peak for better visibility of the broad states making up the “bump”-like structure of the spectrum between 1-10 MeV excitation energy.

4.6.2 Excitation energies from 10 to 16 MeV

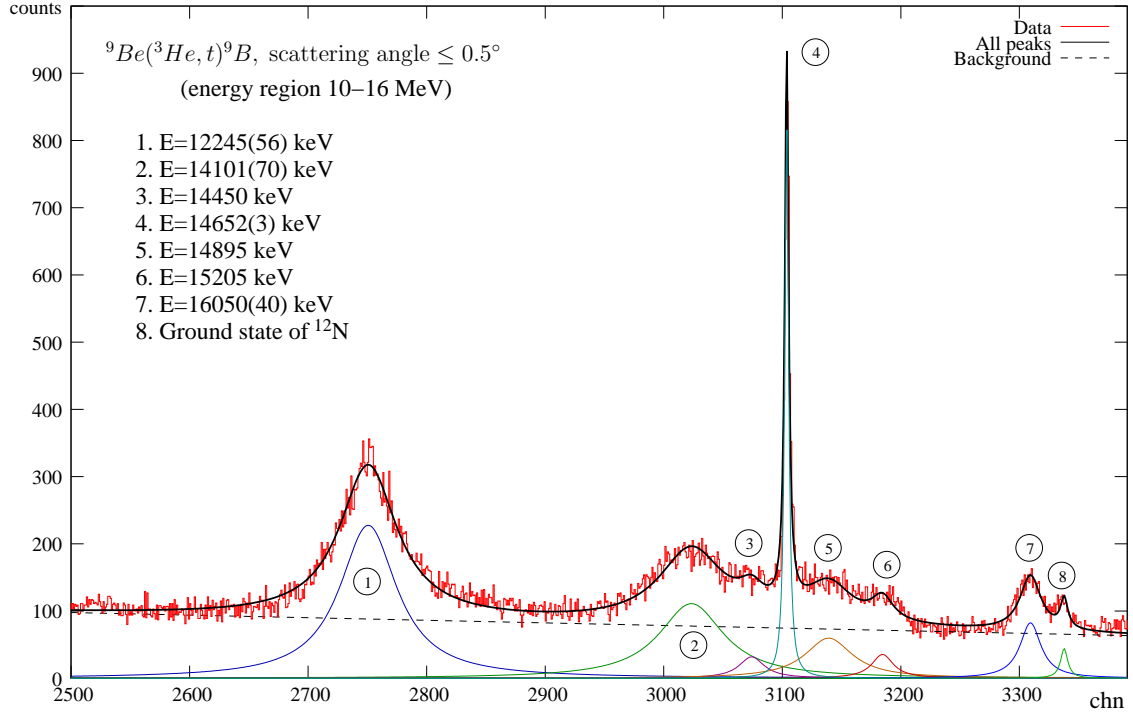


Figure 4.13: Deconvolution of the spectrum for scattering angle less than 0.5° of the ${}^9\text{Be}({}^3\text{He},t){}^9\text{B}$ reaction for excitation energies 10-16 MeV.

More easily separable peaks appear in the spectrum starting with the 12.245(56) MeV, $5/2^-$ state. The deconvolution of the spectrum in the excitation energy region 10-16 MeV is shown in fig. 4.13, and the obtained energies and widths are presented in table 4.4 and compared to the compiled data.

The observed excitation energy of the 12.2 MeV state agrees with the compilation, however we find a somewhat smaller decay width of 376(20) keV ($\Gamma^{(NDS)}=450(20)$ keV).

A bump-like structure can be seen in the spectrum between 13.8 and 15.3 MeV. It contains the well-separated 14101^{+50}_{-90} keV state (its energy and width agree with the compilation, and the angular distribution supports a $\Delta L=0$ assignment, which gives the spin/parity assignment possibilities $J^\pi=(1/2,3/2,5/2)^-$), and the $T=3/2$ analog state to the ${}^9\text{C}$ ground state ($J^\pi=3/2^-$) at 14.65 MeV.

The remaining strength is given by the compilation as a state with $E_x=14.70(18)$ MeV and $\Gamma=1.35(20)$ MeV. The deconvolution of the spectrum cannot be achieved in a satisfactory way assuming the existence of such a state. Especially the sharp drop of the spectrum at around 15.3 MeV rules out a significant strength with large decay width. The deconvolution attempt of the present spectrum uses three states which the best fit places at 14.45, 14.90 and 15.2 MeV, with decay widths of 175, 330 and 150 keV, respectively. The angular distribution of the whole “bump” shows no significant $\Delta L \geq 1$ contribution, so that it can be assumed that the whole structure could have GT nature (the $(5/2)^-$ assignment in the compilation is thus not contradicted). However, since it

seems that a decomposition in several smaller states is required in order to reproduce the total structure, it cannot be ruled out that strength arising from higher L transfer is present in the structure. It will therefore not be attempted to extract a GT strength from the three extra states derived from the deconvolution, but rather an upper limit for the GT strength that can be derived from the zero degree cross-section of the whole structure will be given.

The spectrum contains a further state, near the contaminant ^{12}N ground state peak, but well-separated, at 16050(40) keV, which agrees with the compiled value of 16024(25) keV (the obtained width agrees as well). This state does not have a spin/parity assignment, but the angular distribution supports a $\Delta L=0$ character for this state. It can thus be assigned $J^\pi=(1/2^-, 3/2^-, 5/2^-)$.

Table 4.4: Summary of the spectrum deconvolution for excitation energies 10-16 MeV. The observables presented in columns indicated with a (NDS) superscript denote values from the evaluation by Tilley *et al.* [Til04], unless another citation is given.

^(a) The bump-like structure between 13.8 and 15.3 MeV was deconvoluted using the clearly separated peaks at 14.1 MeV and 14.65 MeV. The compilation [Til04] only gives one very broad state ($\Gamma=1.35(20)$ MeV) at an energy degenerate with the $T=3/2$ peak at 14.65 MeV. The present spectrum can not be deconvoluted using such a state. Instead, it was found that rather three states are needed to correctly reproduce the observed spectrum. They are given here with the fitted positions and width, without errors. The state at the edge of the bump, at $E_x=15.2$ MeV might correspond to the 15.3 MeV state in the compilation.

$E_x^{(EXP)}$ [keV]	$E_x^{(NDS)}$ [keV]	J^π (NDS)	$\Gamma_{c.m.}^{(EXP)}$ [keV]	$\Gamma_{c.m.}^{(NDS)}$ [keV]
12245(56)	12190(40)	5/2-	376(20)	450(20)
14101^{+50}_{-90}	14010(70)	$\pi = -$	454(35)	390(110)
14652(3)	14655(3)	3/2-, T=3/2	$0.0^{+7.0}$	0.395(42)
14450 ^(a)			175	
14895 ^(a)	14700(180)	(5/2-)	330	1350(200)
15205 ^(a)	15290(40)		150	
16050(40)	16024(25)		155(20)	180(16)

4.6.3 Excitation energies from 16 to 25 MeV

The deconvolution of the spectrum for the excitation energy region 16-25 MeV is shown in fig. 4.14, and the obtained energies and decay widths are summarized in table 4.5, and compared with previously compiled data.

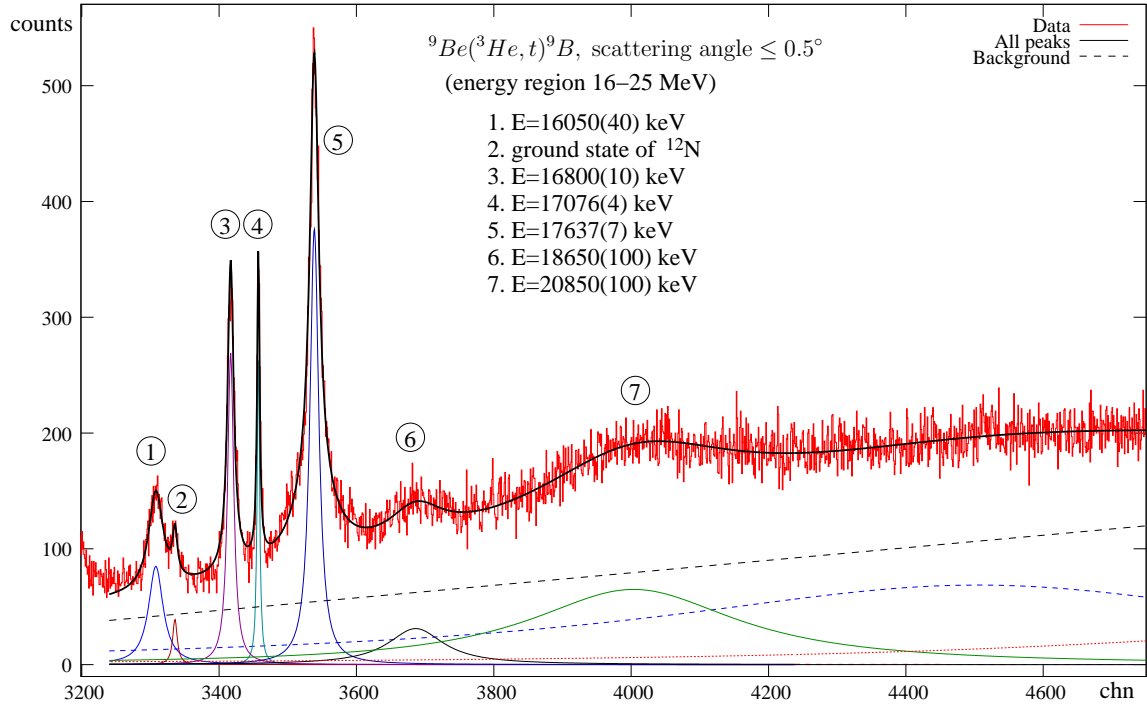


Figure 4.14: Deconvolution of the spectrum for scattering angle less than 0.5° of the ${}^9\text{Be}({}^3\text{He},t){}^9\text{B}$ reaction for excitation energies 16–25 MeV.

The ${}^9\text{B}$ nucleus has a second $T=3/2$ state (the analog of the first $1/2^-$ state in ${}^9\text{Li}$ and ${}^9\text{C}$) at 17.1 MeV, which is seen as a sharp state in the $({}^3\text{He},t)$ spectrum. Its level energy is known with good accuracy from its γ -decay to the ground state.

Some 300 keV lower there is a state identified at 16.71(10) MeV in the compilation [Til04], from unpublished work [Pug85, Faz82] on ${}^9\text{Be}(p,n)$. Dixit *et al.* [Dix91] observed the analog state in ${}^9\text{Be}$ at 16.671(8) MeV, which is assigned $J^\pi=5/2^+$, which would not be contradicted by the observed angular distribution ($\Delta L \geq 1$). The level energy assigned in the present study ($E_x=16.800(10)$ MeV) is much more precise than the compiled value, since the state can be well separated from the $T=3/2$ state owing to the high resolution.

The width of this state has not been given before, we obtain 81(5) keV in the present study.

The next observed peak is seen at 17.637(7) MeV in the present study. There are two levels in the compilation which correspond to this energy, and it might well be the case that both levels are not distinct [Til04]. One is given as 17.54(10) MeV ($7/2^+$) from unpublished ${}^9\text{Be}(p,n)$ work [Pug85, Faz82] and is thought to be the analog of the ${}^9\text{Be}$ $7/2^+$ state at 17.49 MeV. Dixit *et al.* observed this level at 17.490(9) and assigned $J^\pi=7/2^+$. The other compiled state is given at 17.638(10) MeV, with a decay width of 71(8) keV. The energy assigned in the present study ($E_x=17.637(7)$ MeV) agrees well with the second data point, however the width obtained is a little larger ($\Gamma=102(18)$ keV). The decay width from the compilation is the average of 71(8) keV obtained from a ${}^7\text{Be}(d,n)$ experiment and 70(20) keV from a ${}^6\text{Li}({}^3\text{He},\alpha)$ study [Til04]. The angular

distribution of this peak does not have $\Delta L=0$ character.

There are only two more levels compiled above 18 MeV excitation energy in ^9B , both are broad and lie near to the neutron and triton separation energies. The level given as $E_x=18.6(3)$ MeV, $\Gamma=1$ MeV is observed at 18.65(10) MeV with a somewhat smaller width of 680(140) keV. The $^8\text{B}+n$ separation threshold lies at 18.577 MeV.

The last compiled state is given at $E_x=20.7(5)$ MeV, $\Gamma=1.6(3)$ MeV. We observe this level at 20.85(10) MeV with a larger width of 2.56(22) MeV. The $^6\text{Be}+t$ separation threshold lies at 20.909 MeV.

Table 4.5: Summary of the spectrum deconvolution for excitation energies 16-25 MeV. The observables presented in columns indicated with a (NDS) superscript denote values from the evaluation by Tilley *et al.* [Til04], unless an other citation is given.

^(a) level from unpublished work on $^9\text{Be}(p,n)$ [Pug85, Faz82], which might not be distinct from the 17.637(10) MeV level [Til04]. The J^π assignment of the analog state in ^9Be was determined from a proton scattering experiment at 180 MeV by Dixit *et al.* [Dix91], who placed this level at 17.490(9) MeV. The present study cannot distinguish these states. The angular distribution of the observed 17.637(7) MeV peak does not have $\Delta L=0$ character.

$E_x^{(EXP)}$ [keV]	$E_x^{(NDS)}$ [keV]	J^π (NDS)	$\Gamma_{c.m.}^{(EXP)}$ [keV]	$\Gamma_{c.m.}^{(NDS)}$ [keV]
16800(10)	16710(100)	(5/2+)	81(5)	
17076(4)	17076(4)	1/2-, T=3/2	22.5(35)	22(5)
17637(7)	17638(10) 17540(100) ^(a)	(7/2+) [Dix91]	102(18)	71(8)
18650(100)	18600(300)		680(140)	1000
20850(100)	20700(500)		2560(220)	1600(300)

4.7 Identification of $\Delta L=0$ states in the ($^3\text{He},t$) reaction

Gamow-Teller transitions occur upon the action of the $\sigma\tau$ operator on the nuclear wavefunction, where τ changes the isospin, and the operator σ can cause a change $\Delta S=0$ or 1 in the spin part of the nuclear wavefunction, but no change in L . In Fermi transitions, there is no change in orbital or spin angular momentum. The orbital angular momentum L is not always a good quantum number, however if the nuclear wavefunction is decomposed in its various components, it can be seen that Gamow-Teller or Fermi transitions can only occur between those parts of the wavefunction where the orbital momentum L of the considered components does not change (the wavefunctions of the initial and final states have components with the same values of L). The ($^3\text{He},t$) reaction at zero degrees mainly excites states via $\Delta L=0$, which is desired since Gamow-Teller (and Fermi) excitations are the subject of this analysis. However, states with higher angular momentum transfer can be weakly observed as well, and their cross-section increases with the scattering angle. The $\Delta L=0$ cross-section has a strong forward-peaking with maximum at zero scattering angle, while the cross-section for states excited via $\Delta L \geq 1$ increases as the momentum transfer q gets larger. The cross-sections of these states peak at finite angle. Figure 4.15 shows the typical angular distribution of cross-sections obtained for different ΔL transfer in a ($^3\text{He},t$) reaction. The angular distributions were calculated using the DWBA code FOLD by J. Cook and J.A. Carr [Coo] in an updated version.

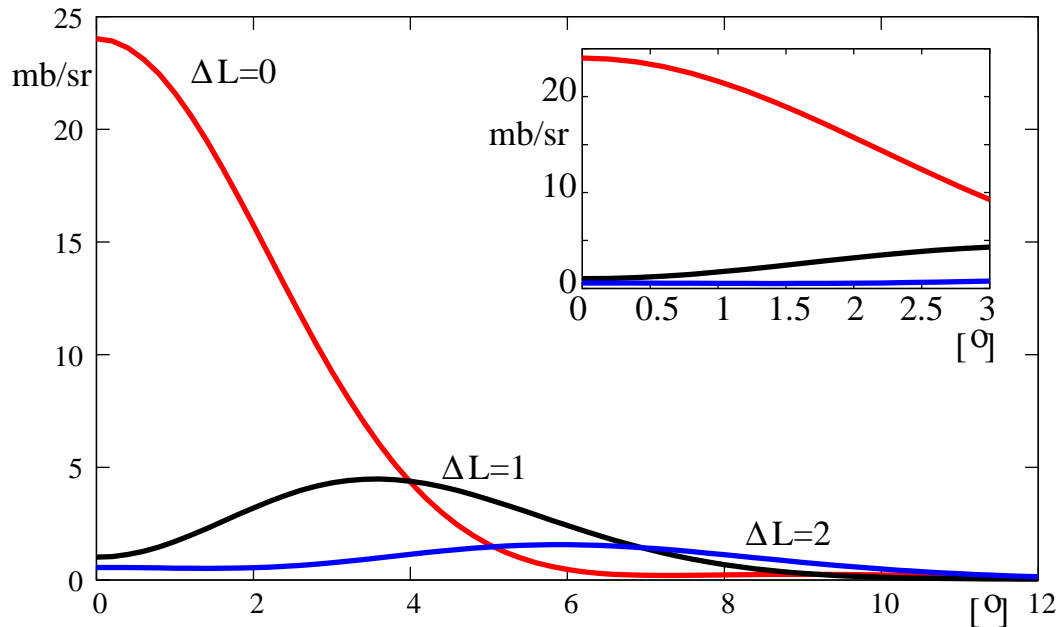


Figure 4.15: Angular distribution of differential cross-sections depending on the angular momentum transfer ΔL for a typical ($^3\text{He},t$) reaction. Calculated with FOLD [Coo]. The insert shows the detail of the angular distribution from 0° to 3° , which is the region of interest in the zero-degrees scattering experiment.

There are various ways to identify the states that are excited in the ($^3\text{He},t$) reaction via $\Delta L=0$. One way would be to take the intensity ratio of states around zero degrees

and at finite angle, and to normalize it with respect to a known $\Delta L=0$ transition. States exhibiting the same behaviour as this transition could then be classified as $\Delta L=0$, while states showing a higher ratio would be classified as $\Delta L \geq 1$.

Another method would be to analyze the angular distribution of the respective cross-sections in detail. The angular distribution of cross-sections can be compared to a DWBA calculation to analyze the L-transfer character. This is the most exhaustive method and should be used if the first, rather crude method is inconclusive. The rough method of considering intensity ratios of zero degree and finite scattering angles is, however, in most cases sufficient to distinguish $\Delta L=0$ from $\Delta L \geq 1$ states.

The figures 4.16 and 4.17 show a plot of the normalized ratio of counts obtained from the deconvolution of the spectrum with scattering angle less than 0.5° to the spectrum with scattering angle $1.5^\circ \leq \Theta \leq 2.0^\circ$ for both analyzed nuclei. The ratio is normalized so that the average of the ratio obtained from the ground state transition and the transition to a highly excited $T=3/2$ state is unity. It can be seen that in both cases, the normalized ratio of states with dominant $\Delta L=0$ character does not deviate more than 25% from unity.

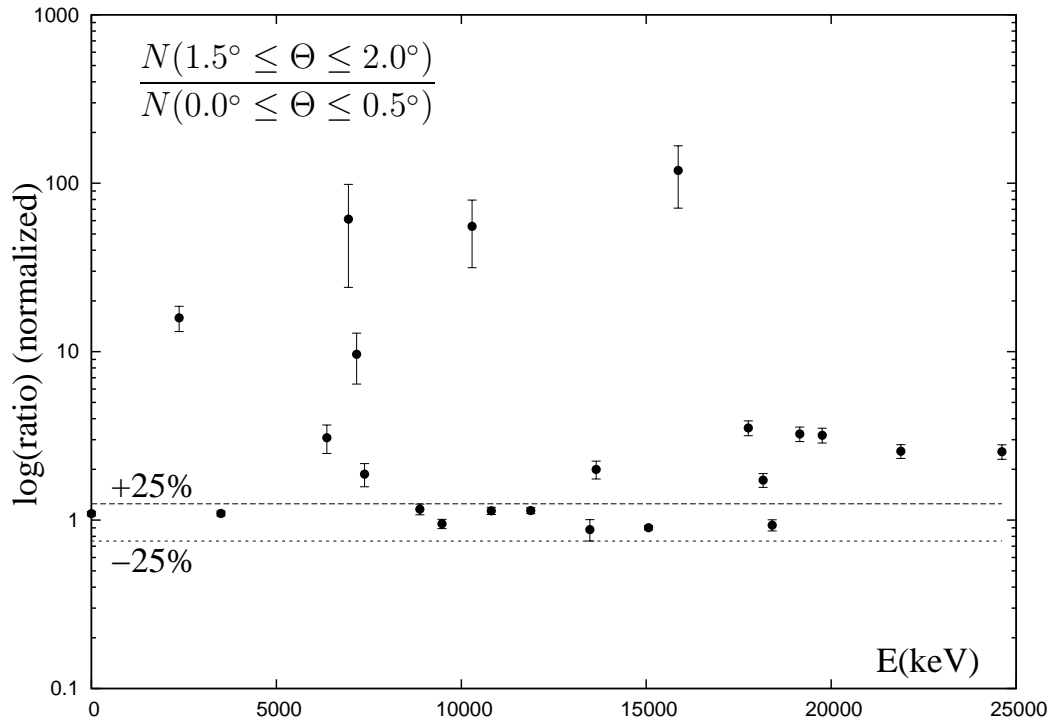


Figure 4.16: Identification of $\Delta L=0$ states in the $^{13}\text{C}(^3\text{He},t)^{13}\text{N}$ reaction. The ratio of the counts obtained in the $1.5^\circ \leq \Theta \leq 2.0^\circ$ spectrum to the counts obtained in the $0.0^\circ \leq \Theta \leq 0.5^\circ$ spectrum can be used as a tool to identify these states. The ratio was normalized to the average value of the ratio for the ground state and the 15.1 MeV state. The lines show variations of 25% from unity. States within the lines have a dominant $\Delta L=0$ nature. The ratio is plotted on a logarithmic scale.

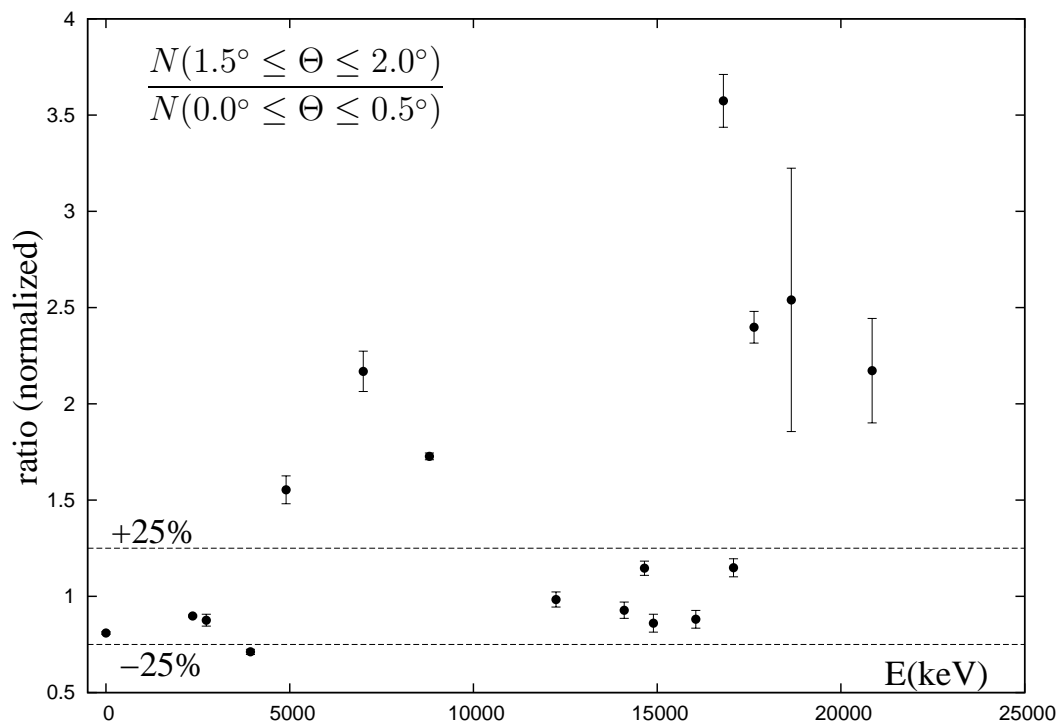


Figure 4.17: Identification of $\Delta L=0$ states in the ${}^9\text{Be}({}^3\text{He},t){}^9\text{B}$ reaction. The ratio of the counts obtained in the $1.5^\circ \leq \Theta \leq 2.0^\circ$ spectrum to the counts obtained in the $0.0^\circ \leq \Theta \leq 0.5^\circ$ spectrum can be used as a tool to identify these states. The ratio was normalized to the average value of the ratio for the ground state and the 17.1 MeV state. The lines show variations of 25% from unity. States within the lines have a dominant $\Delta L=0$ nature.

4.8 Determination of Cross-sections

This section describes the experimental procedures used to derive absolute differential cross-sections for the experiments. The analysis of the angular distributions of cross-sections (the experimental results) will be considered in detail in the next chapter, as the extrapolated differential cross-section at zero degrees is used to determine the B(GT) strength.

The scattering angles were divided into four bins of 0.5° (8.7 mrad) (See figs. 4.18 and 4.19) in the laboratory frame, up to a total of 2° (34.9 mrad) in scattering angle. In the center of mass frame, 2° in the lab frame correspond to around 2.52° for the carbon target and 2.74° for the beryllium target⁵. The solid angle Ω_i ($i=1,2,3,4$) is

$$\Omega_i = \int_{\Phi=0}^{2\pi} \int_{\Theta=\theta_i}^{\theta_{i+1}} \sin \Theta d\Theta d\Phi \quad (4.2)$$

where Θ and Φ are the regular spherical coordinates, while the scattering angles derived from the experimental data are the horizontal (θ) and vertical (ϕ) scattering angles. However, since the involved angles are small (horizontal displacement angle (θ) and vertical displacement angle (ϕ) are smaller than 2°), the surface of the circle inscribed in the θ - ϕ plane as in fig. 4.18 and 4.19 can also be used as a good approximation to obtain the relevant solid angle. This surface is much easier to calculate, especially if the angles are limited by the spectrometer acceptance:

$$\Omega_{r,a,b} \simeq 2 \cdot I_r(a,b) = 2 \cdot \int_a^b \sqrt{r^2 - \theta^2} d\theta = \left(\theta \sqrt{r^2 - \theta^2} + r^2 \arcsin \frac{\theta}{r} \right) \Big|_a^b \quad (4.3)$$

For example, in the case of Ω_1 , the difference is $8 \cdot 10^{-4}\%$ (0.8 pcm):

$$\Omega_1 = \int_{\Phi=0}^{2\pi} \int_{\Theta=0}^{\frac{\pi}{360}} \sin \Theta d\Theta d\Phi = 0.000239244 \text{ sr} \quad (4.4)$$

$$\simeq \Omega_{0.5^\circ, -0.5^\circ, 0.5^\circ} = 2 \cdot \int_{-\frac{\pi}{360}}^{\frac{\pi}{360}} \sqrt{r^2 - \theta^2} d\theta = 0.000239246 \text{ sr} \quad (4.5)$$

The solid angles Ω_i ($i=1,2,3,4$) can thus be approximated (depending on the acceptance,

⁵Calculated with CATKIN [Cat04]

which is different for the ^9Be and the ^{13}C target) as

$$\begin{aligned}\Omega_1 &\simeq \Omega_{0.5^\circ, -0.5^\circ, 0.5^\circ} \\ &= 0.000239246 \text{ sr}\end{aligned}\quad (4.6)$$

$$\begin{aligned}\Omega_2^{(^{13}\text{C})} &\simeq \Omega_{1.0^\circ, -1.0^\circ, 0.9^\circ} - \Omega_{0.5^\circ, -0.5^\circ, 0.5^\circ} \\ &= 0.000939095 - 0.000239246 = 6.99849 \cdot 10^{-4} \text{ sr} \text{ } (^{13}\text{C target})\end{aligned}\quad (4.7)$$

$$\begin{aligned}\Omega_2^{(^9\text{Be})} &\simeq \Omega_{1.0^\circ, -1.0^\circ, 0.6^\circ} - \Omega_{0.5^\circ, -0.5^\circ, 0.5^\circ} \\ &= 0.00082073 - 0.000239246 = 5.81484 \cdot 10^{-4} \text{ sr} \text{ } (^9\text{Be target})\end{aligned}\quad (4.8)$$

$$\begin{aligned}\Omega_3^{(^{13}\text{C})} &\simeq \Omega_{1.5^\circ, -1.2^\circ, 0.9^\circ} - \Omega_{1.0^\circ, -1.0^\circ, 0.9^\circ} \\ &= 0.00173458 - 0.000939095 = 7.95485 \cdot 10^{-4} \text{ sr} \text{ } (^{13}\text{C target})\end{aligned}\quad (4.9)$$

$$\begin{aligned}\Omega_3^{(^9\text{Be})} &\simeq \Omega_{1.5^\circ, -1.5^\circ, 0.6^\circ} - \Omega_{1.0^\circ, -1.0^\circ, 0.6^\circ} \\ &= 0.00160992 - 0.00082073 = 7.8919 \cdot 10^{-4} \text{ sr} \text{ } (^9\text{Be target})\end{aligned}\quad (4.10)$$

$$\begin{aligned}\Omega_4^{(^{13}\text{C})} &\simeq \Omega_{2.0^\circ, -1.2^\circ, 0.9^\circ} - \Omega_{1.5^\circ, -1.2^\circ, 0.9^\circ} \\ &= 0.00242735 - 0.00173458 = 6.9277 \cdot 10^{-4} \text{ sr} \text{ } (^{13}\text{C target})\end{aligned}\quad (4.11)$$

$$\begin{aligned}\Omega_4^{(^9\text{Be})} &\simeq \Omega_{2.0^\circ, -1.6^\circ, 0.6^\circ} - \Omega_{1.5^\circ, -1.5^\circ, 0.6^\circ} \\ &= 0.00243471 - 0.00160992 = 8.2479 \cdot 10^{-4} \text{ sr} \text{ } (^9\text{Be target})\end{aligned}\quad (4.12)$$

In the case of the outer angular bins ($\Omega_2, \Omega_3, \Omega_4$), the limits of integration are constrained by the angular acceptance of the spectrometer (see fig. 4.18 and 4.19), and angles $\theta > 0.9$ and $\theta < -1.2$ (for the ^{13}C target) and $\theta > 0.6$ and $\theta < -1.6$ (for the ^9Be target) have to be excluded from the integration. The opening solid angles in the laboratory frame are listed in table 4.6 for each scattering angle region and target.

Table 4.6: Laboratory scattering angle ranges and corresponding opening angles.

^{13}C target			
i	Θ -range $[\circ]$	Ω_i [sr]	Ω_i/Ω_1
1	[0.0, 0.5)	$0.239246 \cdot 10^{-3}$	1.000
2	[0.5, 1.0)	$0.699849 \cdot 10^{-3}$	2.925
3	[1.0, 1.5)	$0.795485 \cdot 10^{-3}$	3.325
4	[1.5, 2.0)	$0.69277 \cdot 10^{-3}$	2.896
^9Be target			
i	Θ -range $[\circ]$	Ω_i [sr]	Ω_i/Ω_1
1	[0.0, 0.5)	$0.239246 \cdot 10^{-3}$	1.000
2	[0.5, 1.0)	$0.581484 \cdot 10^{-3}$	2.430
3	[1.0, 1.5)	$0.78919 \cdot 10^{-3}$	3.299
4	[1.5, 2.0)	$0.82479 \cdot 10^{-3}$	3.447

For each opening angle Ω_i , the absolute differential cross-section in the center of mass frame $\frac{d\sigma(\Theta)}{d\Omega_{c.m.}}$ is given by

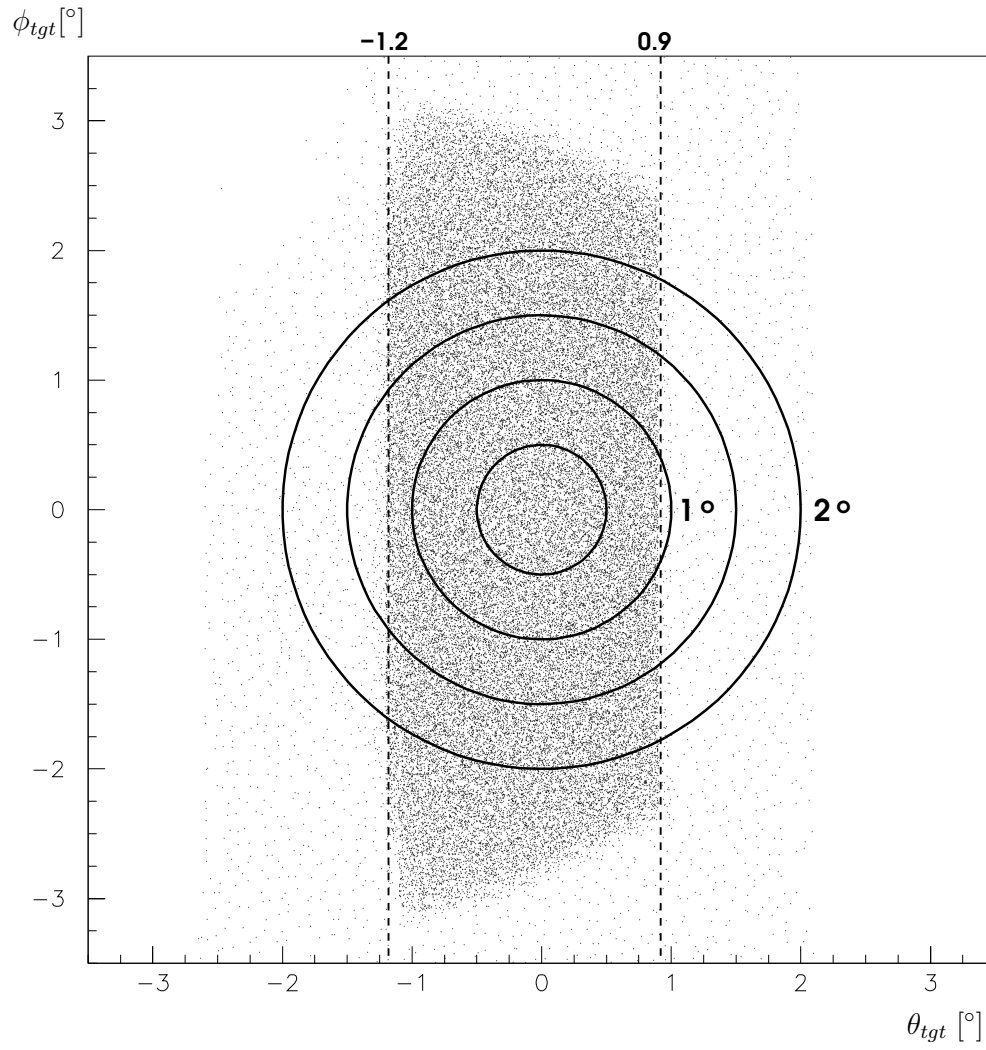


Figure 4.18: Angular aperture and integration surfaces for the experiment with ^{13}C target.

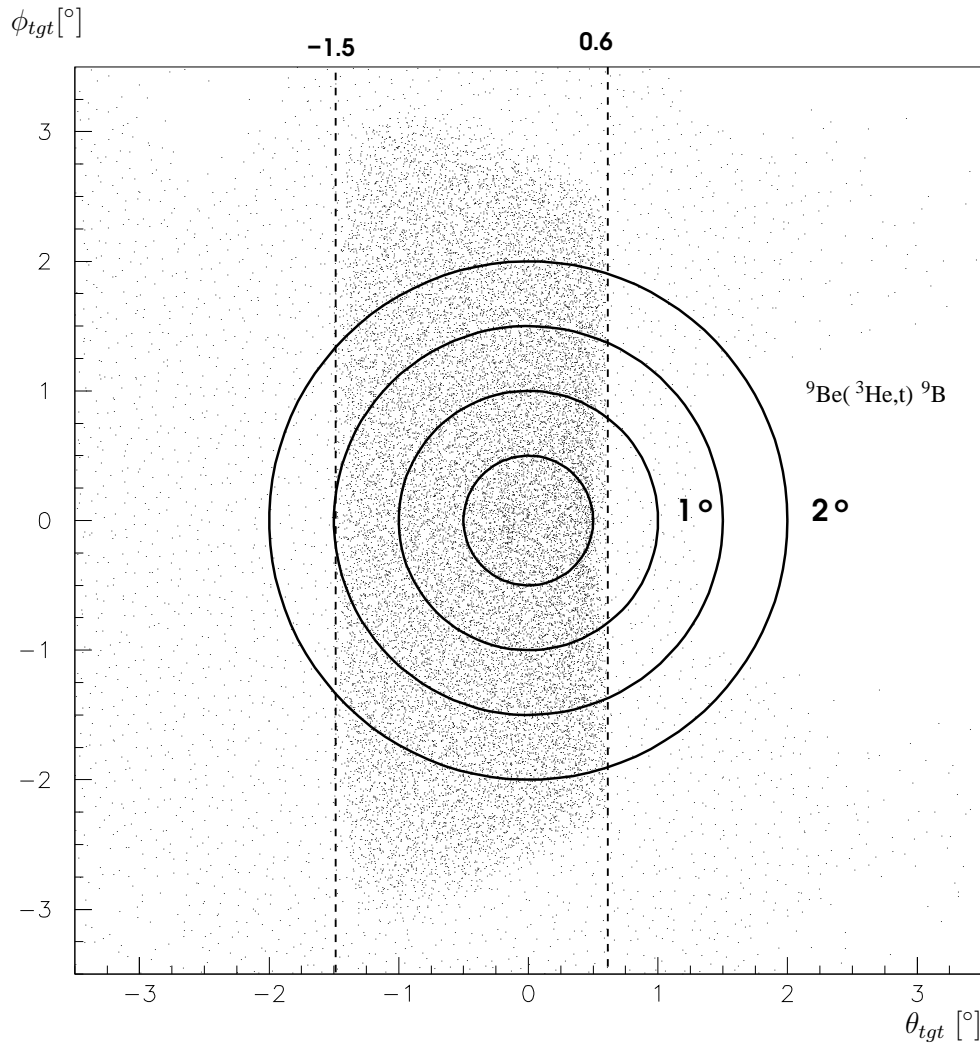


Figure 4.19: Angular aperture and integration surfaces for the experiment with ${}^9\text{Be}$ target.

$$\frac{d\sigma(\Theta_i)}{d\Omega_{c.m.}} = \frac{1}{f^2\Omega_i} \cdot \frac{N_{\text{triton}}(\Theta_i)}{n_{\text{target}} \cdot N_{^3\text{He}}}, \quad (4.13)$$

where $N_{\text{triton}}(\Theta_i)$ is the number of tritons in the focal plane at angle Θ_i (i.e. in the corresponding scattering angle bin) that can be attributed to the charge-exchange reaction for a given number of incident ^3He particles ($N_{^3\text{He}}$) on the target, and where n_{target} gives the number of target nuclei per unit area. The solid angle in the laboratory frame (Ω_i) is transformed into the solid angle $\Omega_{c.m.}$ in the center of mass frame via the factor f which connects both frames. The factor f can be calculated relativistically and is $f = 1.372$ for the beryllium target and $f = 1.260$ for the carbon target. The average angle Θ_i (laboratory frame) used to represent each bin was calculated in way such that it would halve the surface of the corresponding circle in the $\theta - \phi$ plane, by the formula

$$\Theta_i = \sqrt{\frac{\theta_i^2 + \theta_{i+1}^2}{2}}, \quad (4.14)$$

which gives the values presented in table 4.7. This table also contains the conversion of the lab frame angles to the respective center of mass angles, which is useful for the angular distributions.

Table 4.7: Scattering angles in the center of mass and the laboratory frame.

	Laboratory frame [mrad]	c.m. frame [mrad] (^9Be target)	c.m. frame [mrad] (^{13}C target)
Θ_1	6.17	8.38	7.85
Θ_2	13.80	19.02	17.45
Θ_3	22.25	30.54	28.10
Θ_4	30.85	42.41	38.92

The determination of the zero degree cross section gives rise to a statistical error, which is caused by the fitting of the angular distribution with four angular bins and then extrapolating to zero degrees, as well as by the fitting of the respective spectra to determine $N_{\text{triton}}(\Theta_i)$, and a systematic error which is due to the uncertainty in the overall normalization of the ^3He beam. The ^3He beam intensity is normalized using the scattered ^3He particles collected in the D1 Faraday cup of the GRAND RAIDEN spectrometer.

Absolute cross-sections of states excited by the ($^3\text{He},t$) reaction can be deduced from the experiments by determining the number of tritons $N_{\text{triton}}(\Theta_i)$ scattered from the target under the scattering angle Θ_i at various energies. The number of tritons is determined as discussed in 4.2 by fitting the spectra obtained for each scattering angle bin.

The number of incident ^3He particles from the beam was determined in the experiment from a Faraday cup installed inside the inner bend of the first dipole (D1) magnet

of GRAND RAIDEN. The charge accumulated in the Faraday cup was counted by a scaler/integrator with a sampling frequency of 1kHz. At various *full scale current* settings of the scaler, the total amount of charge (in nanocoulomb) accumulated during a run can be determined by

$$Q [\text{nC}] = \text{scaler counts} \times \frac{\text{full scale current} [\text{nA}]}{1000 \text{ Hz}} \quad (4.15)$$

For the charge-exchange reaction with the ^9Be target, the full scale current of the integrator was set at 20 nA. The total amount of incident ^3He beam particles can thus be determined by dividing the total collected charge by two elementary charges.

$$N_{^3\text{He}} = \frac{Q_{\text{total}}}{2e} \quad (4.16)$$

The data of the various experimental runs is shown in table 4.8. For the $^9\text{Be}(^3\text{He},t)^9\text{B}$ reaction, $5.09 \cdot 10^{14}$ particles were collected in total in the Faraday cup during 4.86h of runtime, corresponding to an average beam current of 9.3 nA. The live time of the spectrometer was approximately 94%. As was noted during the experiment, the transmission to the D1 Faraday cup was not 100%. Beam current measurements at the scattering chamber Faraday cup and the beam stopper BS3 indicate approximately 20% loss. Therefore the total amount of incident ^3He particles was corrected by a factor 1.25.

Table 4.8: Intensity of the ^3He beam (^9Be target).

run	1129	1130	1131	Total
time [s]	6857	6922	3734	17513
beam intensity [scaler]	3113167	3269962	1764286	8147415
accumulated charge [nC]	62263.34	65399.24	35285.72	162948.3
^3He particles	$1.9431 \cdot 10^{14}$	$2.0409 \cdot 10^{14}$	$1.1012 \cdot 10^{14}$	$5.0852 \cdot 10^{14}$
corrected for D1FC loss				$6.3565 \cdot 10^{14}$
GR event request	14944083	15736677	8427357	39108117
GR events after veto	13981196	14727892	7897833	36606921
ratio	93.56%	93.59%	93.72%	93.60%
GR clock request	65962240	66560741	35922201	168445182
GR clock after veto	62294519	62696908	33850612	158842039
ratio	94.44%	94.20%	94.23%	94.30%

If eq. (4.13) is rewritten, the differential cross-section for the $^9\text{Be}(^3\text{He},t)^9\text{B}$ reaction becomes

$$\begin{aligned}
\frac{d\sigma(\Theta_i \in \Omega_i)}{d\Omega_{c.m.}} &= \frac{1}{f^2\Omega_1} \cdot \frac{1}{n_{\text{target}}} \cdot \frac{1}{N_{\text{He}}} \cdot \frac{N_{\text{triton}}(\Theta_i)}{\Omega_i/\Omega_1} \\
&= \frac{1}{(1.372)^2(0.239246 \cdot 10^{-3} \text{ sr})(6.3565 \cdot 10^{14})} \times \\
&\quad \times \frac{9.012 \cdot 10^3 \text{ g} \cdot \text{mol}^{-1} \cdot 10^{27} \text{ mb} \cdot \text{cm}^{-2}}{1.0 \cdot 1.73 \text{ g} \cdot \text{cm}^{-2} \cdot 6.022 \cdot 10^{23} \text{ mol}^{-1}} \cdot \frac{N_{\text{triton}}(\Theta_i)}{\Omega_i/\Omega_1} \\
&= (3.02176 \cdot 10^{-5} \text{ mb/sr}) \cdot \frac{N_{\text{triton}}(\Theta_i)}{\Omega_i/\Omega_1} \tag{4.17}
\end{aligned}$$

where the relativistic angle scaling factor $f = 1.372$, the target thickness of 1.73 mg/cm^2 , the Avogadro constant $N_A = 6.022 \cdot 10^{23} \text{ mol}^{-1}$, the target enrichment of 100%, the molar mass of ^9Be ($9.012 \text{ g} \cdot \text{mol}^{-1}$) and the definition of millibarn ($1 \text{ mb} = 10^{-27} \text{ cm}^2$) were used.

Table 4.9: Efficiency of the MWDCs (^9Be target).

efficiency of the X_1 plane	99.80%
efficiency of the U_1 plane	99.83%
efficiency of the X_2 plane	99.67%
efficiency of the U_2 plane	99.82%
total efficiency	99.12%

Table 4.10: Efficiency of the MWDCs (^{13}C target).

efficiency of the X_1 plane	99.52%
efficiency of the U_1 plane	99.75%
efficiency of the X_2 plane	99.51%
efficiency of the U_2 plane	99.75%
total efficiency	98.54%

The number of triton counts $N_{\text{triton}}(\Theta_i)$ has to be corrected for the dead time of the data acquisition system of the spectrometer (GR dead time, see table 4.8) and the detection efficiency of the MWDCs. To assess the efficiency of the drift chambers, the raytracing information provided by the analyzer program [Yos01] (see table D.1 in the appendix) was used. The efficiency of each plane is defined as

$$\epsilon_{X_1} = \frac{N_{X_1 \cap U_1 \cap X_2 \cap U_2}}{N_{X_1 \cap U_1 \cap X_2 \cap U_2} + N_{U_1 \cap X_2 \cap U_2}} \quad (4.18)$$

$$\epsilon_{U_1} = \frac{N_{X_1 \cap U_1 \cap X_2 \cap U_2}}{N_{X_1 \cap U_1 \cap X_2 \cap U_2} + N_{X_1 \cap X_2 \cap U_2}} \quad (4.19)$$

$$\epsilon_{X_2} = \frac{N_{X_1 \cap U_1 \cap X_2 \cap U_2}}{N_{X_1 \cap U_1 \cap X_2 \cap U_2} + N_{X_1 \cap U_1 \cap U_2}} \quad (4.20)$$

$$\epsilon_{U_2} = \frac{N_{X_1 \cap U_1 \cap X_2 \cap U_2}}{N_{X_1 \cap U_1 \cap X_2 \cap U_2} + N_{X_1 \cap U_1 \cap X_2}} \quad (4.21)$$

Where $N_{X_1 \cap U_1 \cap X_2 \cap U_2}$ is the number of events for which the raytracing was successful (position determined in all four planes, RAY-ID=1), and $N_{i \cap j \cap k}$ is the number of events for which the position could only be determined in the planes i, j and k (i.e. the position could not be determined for one plane, RAY-ID=1,2,4,5). These numbers are in principle dependant on the triton energy, and the time-difference spectra from the trigger scintillators can be used as a gate to roughly estimate the position (i.e. excitation energy) dependence. The position dependence of the efficiency is negligible in the present experiments. Efficiencies of 98-99% were obtained for all planes (see table 4.9 and table 4.10) and the overall efficiency is 99.12% for the experiment with ^9Be target and 98.54% for the experiment with ^{13}C target.

Let us now consider the $^{13}\text{C}(^3\text{He}, t)^{13}\text{N}$ experiment. As for the $^9\text{Be}(^3\text{He}, t)^9\text{B}$ cross-sections, ^3He beam particles were collected in the Faraday cup inside the D1 magnet. For the charge determination using the integrator, the full scale current was set to 60 nA. The data from the experimental runs is shown in table 4.11, and the total result for all runs in table 4.12. A total of $2.87 \cdot 10^{14}$ particles were gathered within 3.3h of runtime, corresponding to an average beam current of 7.68 nA. The live time of the spectrometer was approximately 99%.

If eq. (4.13) is rewritten as for the ^9Be target, the differential cross-section for the $^{13}\text{C}(^3\text{He}, t)^{13}\text{N}$ reaction becomes

$$\begin{aligned} \frac{d\sigma(\Theta_i \in \Omega_i)}{d\Omega_{c.m.}} &= \frac{1}{f^2 \Omega_1} \cdot \frac{1}{n_{\text{target}}} \cdot \frac{1}{N_{^3\text{He}}} \cdot \frac{N_{\text{triton}}(\Theta_i)}{\Omega_i / \Omega_1} \\ &= \frac{1}{(1.26)^2 (0.239246 \cdot 10^{-3} \text{ sr}) (3.592 \cdot 10^{14})} \times \\ &\quad \times \frac{13.00335 \cdot 10^3 \text{ g} \cdot \text{mol}^{-1} \cdot 10^{27} \text{ mb} \cdot \text{cm}^{-2}}{0.99 \cdot 0.5 \text{ g} \cdot \text{cm}^{-2} \cdot 6.022 \cdot 10^{23} \text{ mol}^{-1}} \cdot \frac{N_{\text{triton}}(\Theta_i)}{\Omega_i / \Omega_1} \\ &= (3.19736 \cdot 10^{-4} \text{ mb/sr}) \cdot \frac{N_{\text{triton}}(\Theta_i)}{\Omega_i / \Omega_1} \end{aligned} \quad (4.22)$$

where the relativistic angle scaling factor $f = 1.26$, the target thickness of 0.5 mg/cm^2 , the Avogadro constant $N_A = 6.022 \cdot 10^{23} \text{ mol}^{-1}$, the target enrichment of 99%, the molar mass of ^{13}C ($13.00335 \text{ g} \cdot \text{mol}^{-1}$) and the definition of millibarn ($1 \text{ mb} = 10^{-27} \text{ cm}^2$) were used.

Table 4.11: Intensities of the ^3He beam (^{13}C target).

run	1024	1025	1026	1027
time [s]	3622	905	1198	148
beam intensity [scaler]	471475	130318	151338	12485
accumulated charge [nC]	28288.5	7819.08	9080.28	749.1
^3He particles	$8.8281 \cdot 10^{13}$	$2.4401 \cdot 10^{13}$	$2.8337 \cdot 10^{13}$	$2.3378 \cdot 10^{12}$
GR event request	1814747	530521	603085	52683
GR events after veto	1788315	521232	593483	51830
ratio	98.54%	98.25%	98.41%	98.38%
GR clock request	34842170	8708076	11527972	1424196
GR clock after veto	34394036	8576953	11378802	1411138
ratio	98.71%	98.49%	98.71%	99.08%
run	1028	1029	1030	1031
time [s]	1487	1514	1578	1542
beam intensity [scaler]	194826	196734	189508	188013
accumulated charge [nC]	11689.56	11804.04	11370.48	11280.78
^3He particles	$3.6480 \cdot 10^{13}$	$3.6838 \cdot 10^{13}$	$3.5484 \cdot 10^{13}$	$3.5205 \cdot 10^{13}$
GR event request	796305	792071	775721	783083
GR events after veto	782603	778415	762220	769927
ratio	98.28%	98.28%	98.26%	98.32%
GR clock request	14296363	14567326	15182528	14830824
GR clock after veto	14099483	14371718	14990915	14637079
ratio	98.62%	98.66%	98.74%	98.69%

Table 4.12: Intensity of the ^3He beam (^{13}C target, total of all runs).

run numbers	1024-1031
time [s]	11994
beam intensity [scaler]	1534697
accumulated charge [nC]	92081.82
^3He particles	$2.8736 \cdot 10^{14}$
corrected for D1FC loss	$3.592 \cdot 10^{14}$
GR event request	6148216
GR event after veto	6048025
ratio	98.37%
GR clock request	115379455
GR clock after veto	113860124
ratio	98.68%

Chapter 5

Extraction of Gamow-Teller strengths

This chapter deals with the extraction of the $B(\text{GT})$ strengths from the ${}^9\text{Be}({}^3\text{He}, \text{t}){}^9\text{B}$ and the ${}^{13}\text{C}({}^3\text{He}, \text{t}){}^{13}\text{N}$ reactions, by using the proportionality relation (5.1) between the $B(\text{GT})$ strength and the cross-section at momentum transfer $q=0$.

5.1 DWBA calculations

The following section analyzes the dependence of the cross section distribution as a function of momentum transfer q and energy loss ω . In the proportionality relationship

$$\frac{d\sigma}{d\Omega} = \hat{\sigma}_\alpha(E_p, A) F_\alpha(q, \omega) B(\alpha) \quad (5.1)$$

the factor $F(q, \omega)$ describes the shape of the cross-section distribution as a function of q and $\omega = E_x - Q$ and goes to unity in the limit of zero momentum transfer and energy loss. If the reaction is fixed, this factor depends only on the scattering angle and excitation energy $F = F(\theta_{\text{lab}}, E_x)$. Since we are mainly interested in the cross-section at zero degrees, what should be examined is the dependence of the cross section distribution on the excitation energy. The determination of the energy dependence of the F -factor is crucial to extract $B(\text{GT})$ values from the measured differential cross-sections. For these reasons, $F(\Theta = 0^\circ, E_x)$ was studied by DWBA (*distorted wave Born approximation*) calculations. The code DW81 by J.R. Comfort [Com], whose formalism is detailed in [Ray67], was used to perform these calculations.

5.1.1 Q-values

To compute the excitation energies for the considered reactions, their respective Q-values have to be determined. The Q-value of the ${}^A_Z\text{X}({}^3\text{He}, \text{t}){}^A_{Z+1}\text{Y}$ reaction is

$$Q = m_X + m_{{}^3\text{He}} - m_Y - m_{\text{t}}. \quad (5.2)$$

The Q-values of the analyzed reactions were calculated using masses from the *Atomic Mass Evaluation* [Aud03] as given in table 5.1.

Table 5.1: Masses (from [Aud03]) and corresponding reaction Q-values.

Nucleus	Mass [keV]	Reaction Q-value [keV]
t	14949.8060(23)	
^3He	14931.2148(24)	
^9Be	11347.6(4)	
^9B	12415.7(10)	$Q(^9\text{Be}(^3\text{He}, t)^9\text{B}) = -1086.7(10)$
^{13}C	3125.0113(9)	
^{13}N	5345.48(27)	$Q(^{13}\text{C}(^3\text{He}, t)^{13}\text{N}) = -2239.06(27)$

5.1.2 DWBA calculation parameters

The DWBA calculation requires parameters for the optical potential (entrance and exit channel) and the interaction, single particle energies and transition densities.

Optical potential parameters for ^{12}C are available for ^3He beams of 450 MeV (*Yamagata et al.*) [Yam95] and 443 MeV (*Kamiya et al.*) [Kam03]. These parameters (given in table 5.2) were used in the DWBA calculations for the $^9\text{Be}(^3\text{He}, t)$ and $^{13}\text{C}(^3\text{He}, t)$ reactions.

Table 5.2: Optical potential parameters for ^{12}C from ^3He elastic scattering by *Yamagata et al.* [Yam95] and *Kamiya et al.* [Kam03].

ref.	$E_{^3\text{He}}$	V_R [MeV]	r_R [fm]	a_R [fm]	W_I [MeV]	r_I [fm]	a_I [fm]
[Yam95]	450	30.4	1.49	0.73	11.2	1.15	1.37
[Kam03]	443	19.73	1.592	0.705	37.76	0.989	0.868

The effective ^3He - N interaction $V_{^3\text{He}N}$ was used in the DWBA calculations. The interaction parameters, represented by a Yukawa potential, were $V_\tau = 0.75$ MeV, $V_{\sigma\tau} = -2.5$ MeV and $V_{T\tau} = -2.1$ MeV [Zeg03]. For the outgoing triton channel, by following the arguments given by *van der Werf et al.* [vdW89], the well depths were multiplied by a factor of 0.85 without changing the geometrical parameters of the optical potential.

The single-particle energies for the $p_{3/2}$ and $p_{1/2}$ orbits were taken from fig.5.1: $E_{p_{3/2}} = -9.75$ MeV for $A=9$ and -18 MeV for $A=13$, $E_{p_{1/2}} = -3.5$ MeV for $A=9$ and -13 MeV for $A=13$. These values can be obtained in more detail, e.g. in [Sch08] (see 5.3), but the more precise values (different for proton and neutron orbits) have only marginal influence on $F(0^\circ, \omega)$.

For the one-body transition densities (OBTD), various scenarios were considered. As it is shown in fig. 5.2, in the $A=9$ case, ($p_{3/2}p_{3/2}^{-1}$) and ($p_{1/2}p_{3/2}^{-1}$) transitions were con-

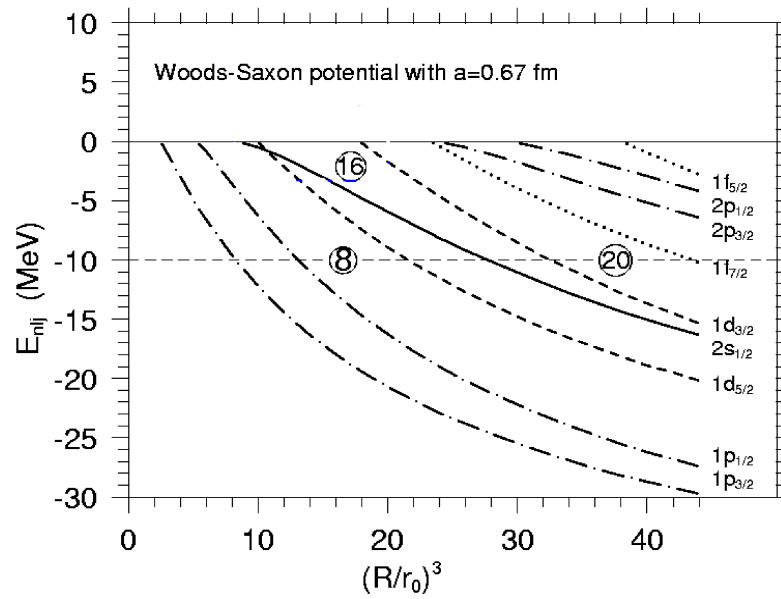


Figure 5.1: Single particle energies for light nuclei in the shell model. Energies of neutron orbits in Wood-Saxon potentials. $r_0=1.27$ fm, $V_{WS}=-51$ MeV, $R=r_0A^{1/3}$.

sidered, whereas in the $A=13$ case, $(p_{1/2}p_{3/2}^{-1})$ and $(p_{1/2}p_{1/2}^{-1})$ transitions were considered. Only pure transitions (OBTD=1) were considered for all cases to derive the behaviour of the $F(0^\circ, \omega)$ -factor. As it can be seen in fig. 5.3 and 5.4, the energy-dependent behaviour of the F-factor at zero degrees is robust against changes in the parameters of the optical potential as well as a change in the shells considered for the transition. The decrease in GT strength obtained via the differential cross-section is about 20% at 18 MeV reaction Q-value. A detailed table of the calculated values shown in figs. 5.3 and 5.4 can be found in the appendix (tables E.1 and E.2).

5.2 Angular distribution of cross-sections

The differential cross-sections obtained from the data analysis were fitted to angular distributions calculated using a distorted wave Born approximation (DWBA) with the program FOLD [Coo]. This code uses the Love-Franey nucleon-nucleon interaction [Lov81, Fra85], double-folded over the projectile-ejectile and target-residue transition densities. A short-range approximation [Lov81] is used for the exchange terms in the potential. Radial wave functions were calculated using the Woods-Saxon potential (parameters from [Sch08]) with the code WSAW, a part of the FOLD package¹. Optical potential parameters were used as described in the previous sections. For the outgoing triton channel, by following the arguments given by *van der Werf et al.* [vdW89], the well depths were multiplied by a factor of 0.85 without changing the geometrical parameters of the optical potential (radii and diffuseness).

¹The FOLD program package can be downloaded from Remco Zegers' website at <http://www.nsl.msu.edu/~zegers/fold.html>

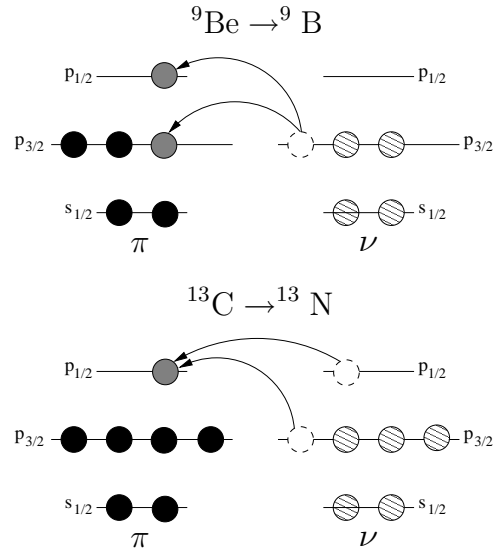


Figure 5.2: Possible configurations (not exhaustive) resulting from β^- -type transitions ($\Delta J=0,1$) ${}^9\text{Be} \rightarrow {}^9\text{B}$ and ${}^{13}\text{C} \rightarrow {}^{13}\text{N}$. The most simple shell structure is assumed. The filling of protons (π) and neutrons (ν) is shown with filled black and striped circles, respectively. The particles and holes newly created by the transitions are shown in filled grey and dotted circles, the arrows indicate the direction of the charge-exchange reaction.

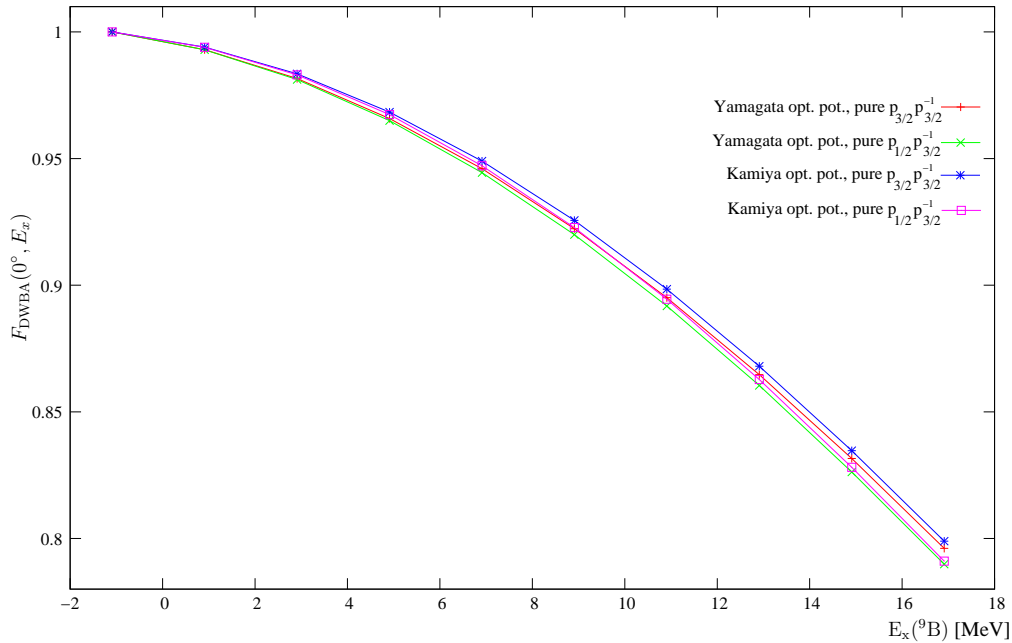


Figure 5.3: Evolution of the relative cross section of ${}^9\text{Be}({}^3\text{He}, t){}^9\text{B}$ calculated with DWBA. The cross section is normalized to zero energy loss and zero momentum transfer, where the factor $F(0^\circ, E_x)$ goes to unity (data from table E.1 is used). The energy-dependent behaviour of F is robust against different parametrizations of the optical potential and the choice of shell configurations.

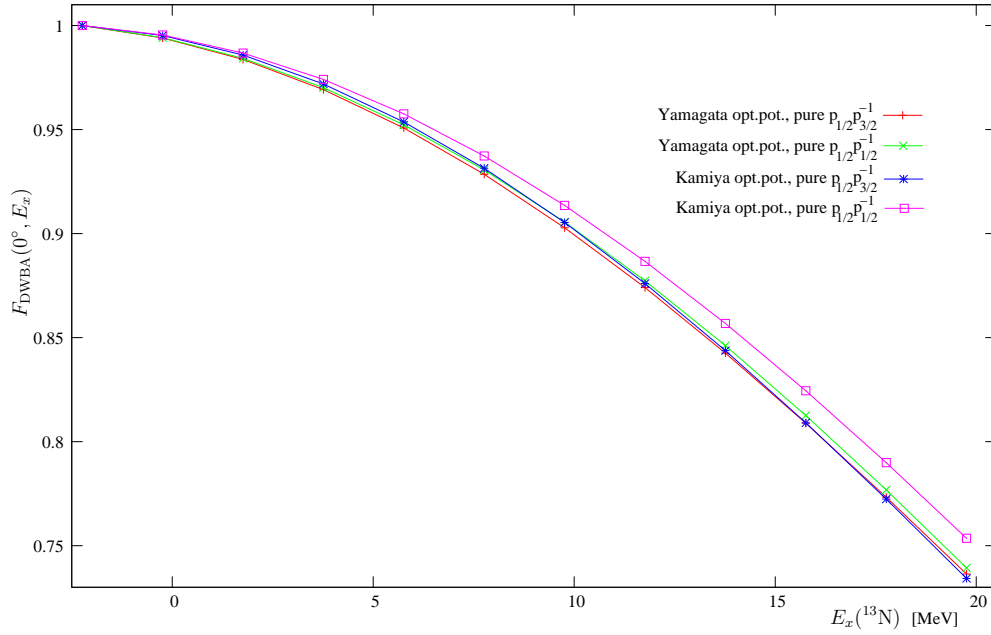


Figure 5.4: Evolution of the relative cross-section of $^{13}\text{C}(^3\text{He},t)^{13}\text{N}$ calculated with DWBA. The cross-section is normalized to zero energy loss and zero momentum transfer, where the factor $F(0^\circ, E_x)$ goes to unity (data from table E.2 is used).

5.3 Cross-sections of the $^{13}\text{C}(^3\text{He},t)^{13}\text{N}$ reaction

For the $^{13}\text{C}(^3\text{He},t)^{13}\text{N}$ reaction, the absolute differential cross-sections shown in table 5.4 were determined for four angular bins, as described in 4.8. The angular distributions of states with $\Delta L=0$ character ($1/2^-$ and $3/2^-$) were compared to angular distributions calculated in DWBA as described in 5.2. The calculated distributions were fitted to the obtained data by using a single scaling parameter, using the program TOPFIT [Wie]. The fit to these calculated distributions allows to extrapolate the cross section at zero degrees scattering angle, $\frac{d\sigma}{d\Omega}(\Theta_{c.m.} = 0)$ which is shown in table 5.3 for all states with $\Delta L=0$ character.

In principle, the analysis of $\Delta J^\pi=1^+$ states requires a fit in which the $\Delta L=0$ and the $\Delta L=2$ parts are separately fitted². The DWBA analysis shows that incoherent $\Delta L=2$ contributions to the cross section are very small at forward scattering angles in the case of ^{13}N (less than 1%, thus negligible when considering the cross-section uncertainties [Zeg08]).

The values obtained for the zero-degrees cross-section of observed GT states are summarized in table 5.3 and in the logarithmic plot of angular distributions in fig. 5.5. These cross-sections can then be used to calculate the cross-section at momentum transfer $q=0$ by dividing by the factor $F(0^\circ, \omega)$ calculated in 5.1. The cross section at zero degrees and zero momentum transfer can then be used to determine the Gamow-Teller strength of the corresponding state.

²A $\Delta J^\pi=1^+$ can be obtained via $\Delta L=0, \Delta S=1$ and $\Delta L=2, \Delta S=1$, where only the first possibility is physically relevant for the B(GT) strength.

Table 5.3: Extrapolated absolute differential cross-sections for ^{13}N levels with $\Delta L=0$ character from fits to calculated DWBA angular distribution.

$E_x^{(exp)}$	$\left[\frac{d\sigma}{d\Omega}(0^\circ)\right]^{(exp)}$ (mb/sr)
0 keV	11.89(11)
3501(4) keV	31.63(31)
8881(27) keV	5.32(10)
9478(11) keV	1.25(2)
10811(5) keV	2.53(4)
11877(7) keV	8.98(10)
13474(48) keV	0.77(2)
15063(3) keV	4.75(5)
18397(4) keV	0.50(1)

The individual angular distributions $\frac{d\sigma}{d\Omega}(\Theta_{c.m.})$ together with the fitted DWBA curves are shown in figs. 5.6-5.11. The errorbars shown in the plots only reflect the statistical error arising from the deconvolution of the spectrum, and do not account for systematic errors (mainly the beam intensity and target thickness) which would have the effect of scaling the entire set of derived cross sections by a single scaling factor (see 4.8).

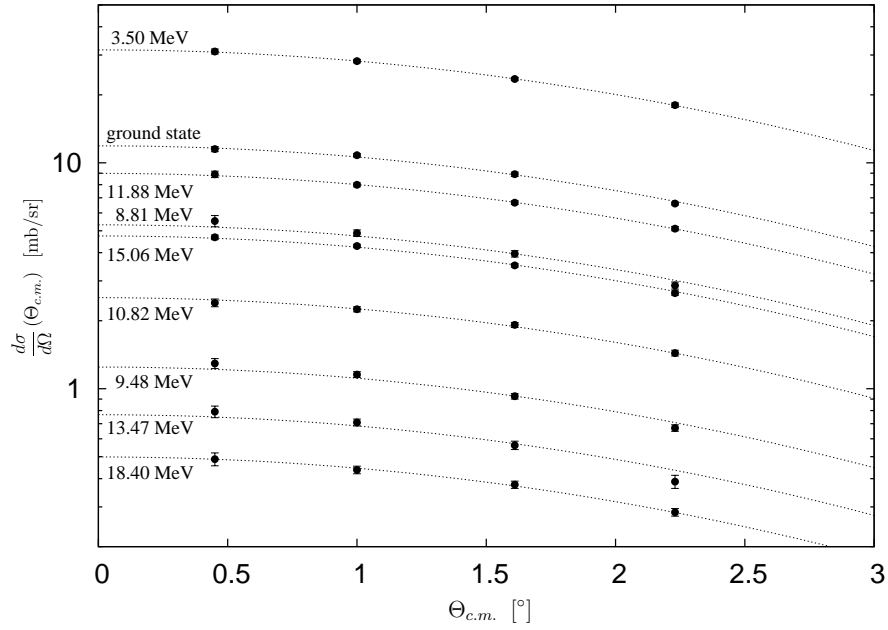


Figure 5.5: Summary of angular distributions of cross-sections for $1/2^-$ and $3/2^-$ states in ^{13}N (logarithmic plot). The data are fitted to the calculated angular distribution for $\Delta L=0$, $\Delta S=1$ with a single scaling factor.

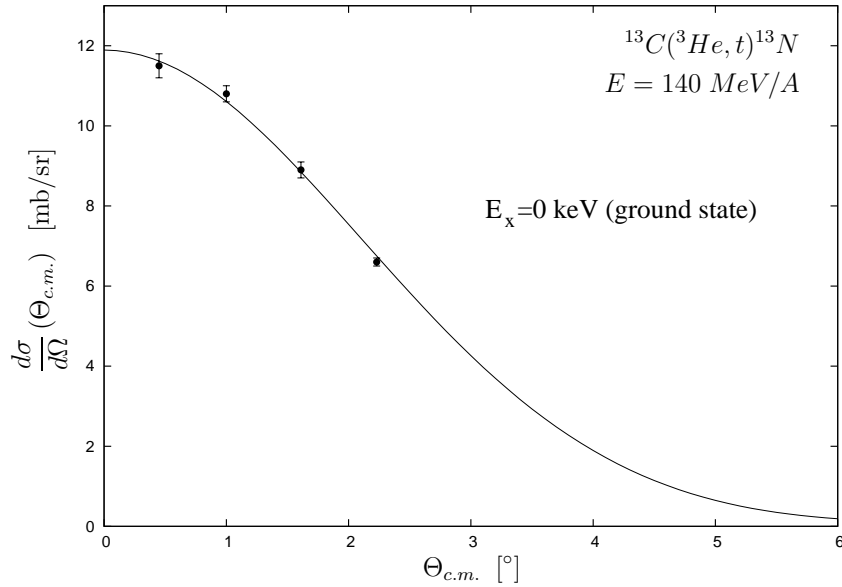


Figure 5.6: Angular distribution of the cross-section of the ^{13}N $1/2^-$ ground state excited by the $(^3\text{He},t)$ reaction at 140 MeV/A beam energy. The solid curve is the calculated angular distribution for $\Delta L=0$, $\Delta S=1$, scaled to fit the data with a single scaling factor ($\chi^2_{red.} = 0.75$).

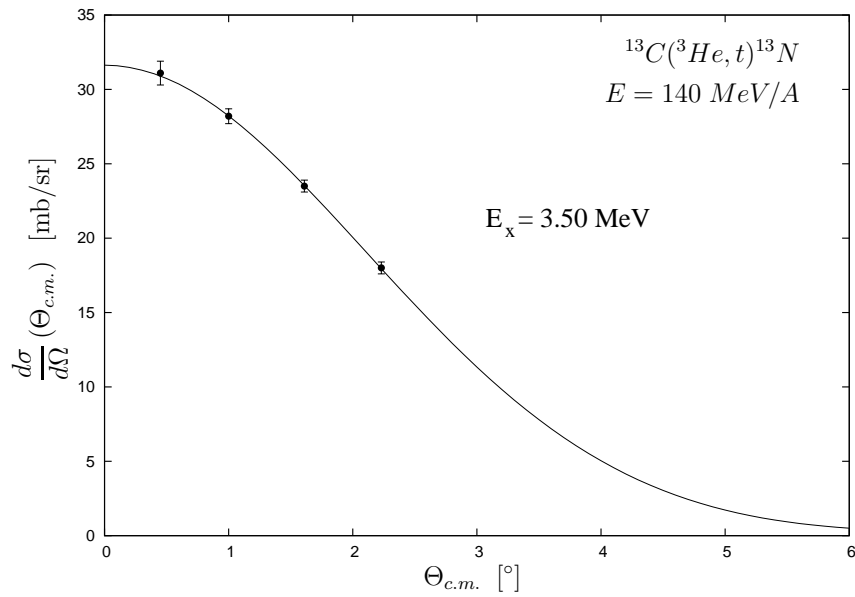


Figure 5.7: Angular distribution of the cross-section of the $^{13}\text{N } 3/2^-$ state at 3.50 MeV excited by the $(^3\text{He},t)$ reaction at 140 MeV/A beam energy. The solid curve is the calculated angular distribution for $\Delta L=0, \Delta S=1$, scaled to fit the data with a single scaling factor ($\chi^2_{red.}=0.03$).

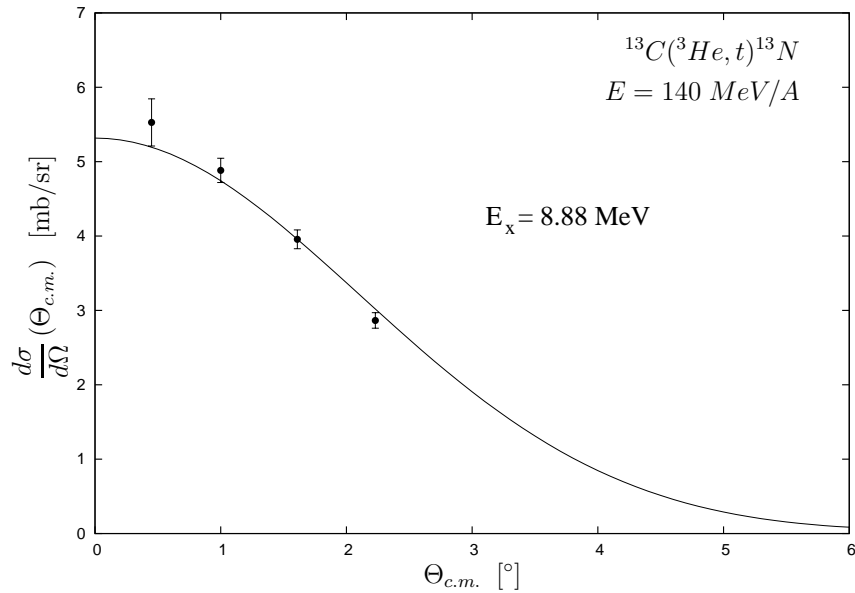


Figure 5.8: Angular distribution of the cross-section of the $^{13}\text{N } 1/2^-$ state at 8.88 MeV excited by the $(^3\text{He},t)$ reaction at 140 MeV/A beam energy. The solid curve is the calculated angular distribution for $\Delta L=0, \Delta S=1$, scaled to fit the data with a single scaling factor ($\chi^2_{red.}=1.32$).

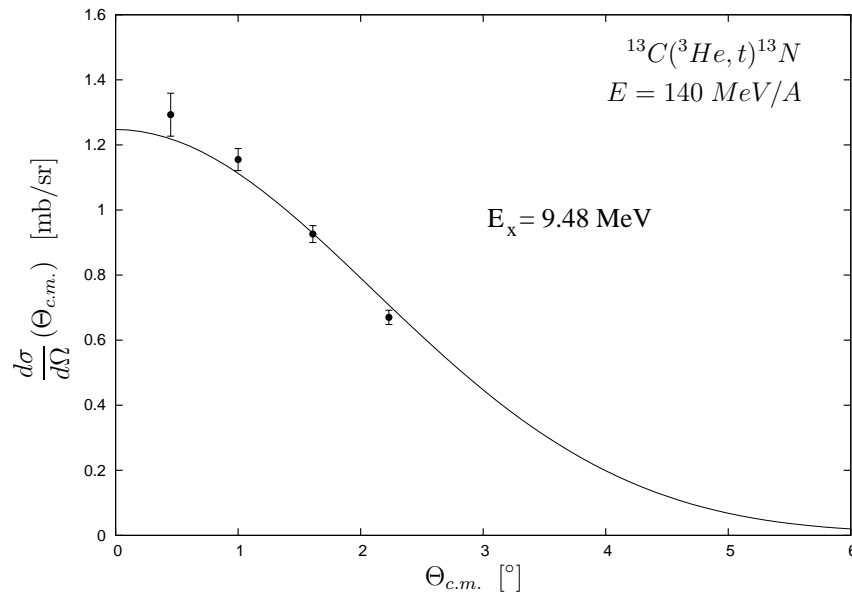


Figure 5.9: Angular distribution of the cross-section of the $^{13}\text{N } 3/2^-$ state at 9.48 MeV excited by the $(^3\text{He},t)$ reaction at 140 MeV/A beam energy. The solid curve is the calculated angular distribution for $\Delta L=0$, $\Delta S=1$, scaled to fit the data with a single scaling factor ($\chi^2_{red.}=1.98$).

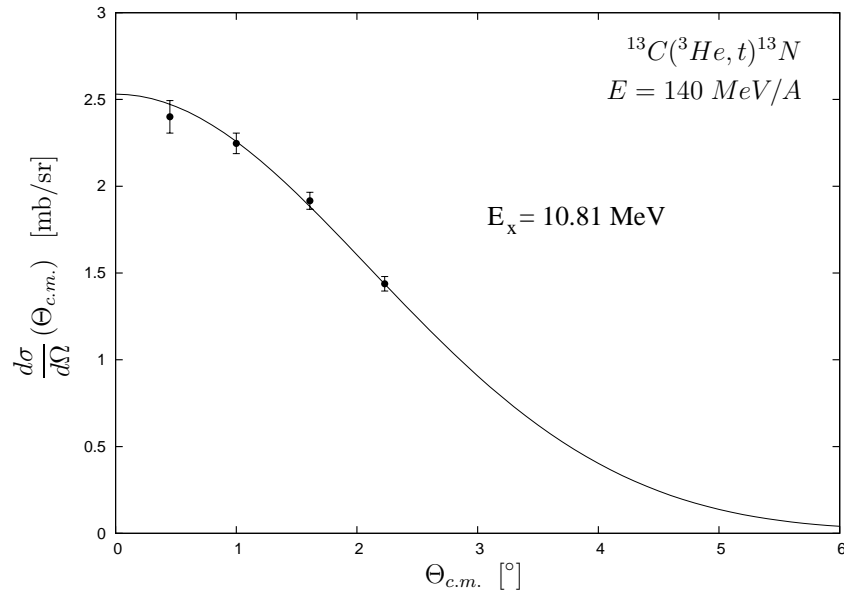


Figure 5.10: Angular distribution of the cross-section of the $^{13}\text{N } 1/2^-$ state at 10.81 MeV excited by the $(^3\text{He},t)$ reaction at 140 MeV/A beam energy. The solid curve is the calculated angular distribution for $\Delta L=0$, $\Delta S=1$, scaled to fit the data with a single scaling factor ($\chi^2_{red.}=0.36$).

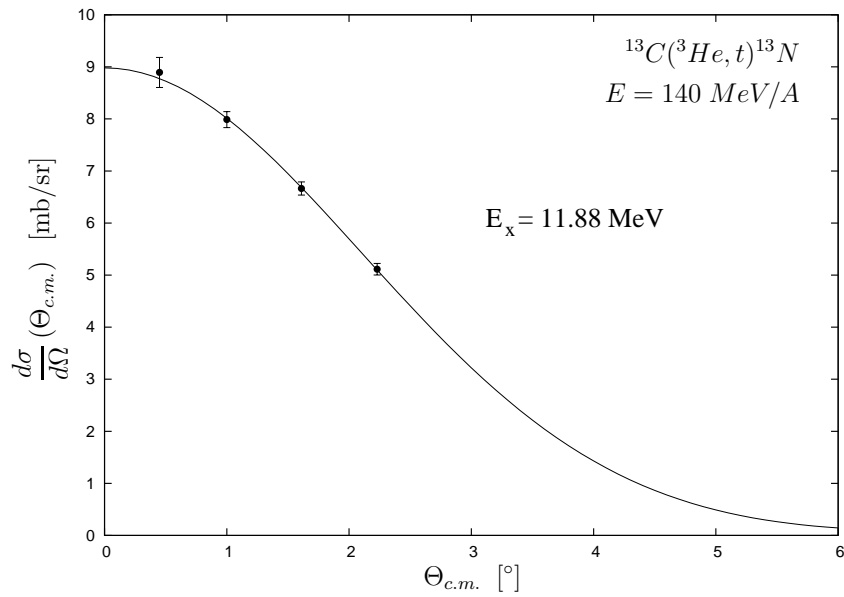


Figure 5.11: Angular distribution of the cross-section of the $^{13}\text{N} (1/2^-, 3/2^-)$ state at 11.88 MeV excited by the $(^3\text{He}, t)$ reaction at 140 MeV/A beam energy. The solid curve is the calculated angular distribution for $\Delta L=0, \Delta S=1$, scaled to fit the data with a single scaling factor ($\chi^2_{red.}=0.08$).

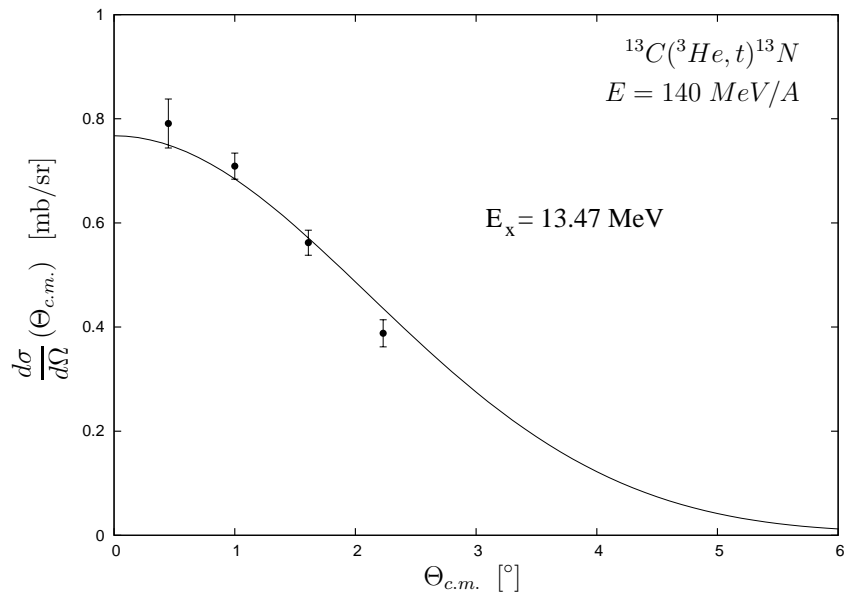


Figure 5.12: Angular distribution of the cross-section of the $^{13}\text{N} (1/2^-, 3/2^-)$ state at 13.47 MeV excited by the $(^3\text{He}, t)$ reaction at 140 MeV/A beam energy. The solid curve is the calculated angular distribution for $\Delta L=0, \Delta S=1$, scaled to fit the data with a single scaling factor ($\chi^2_{red.}=1.71$).

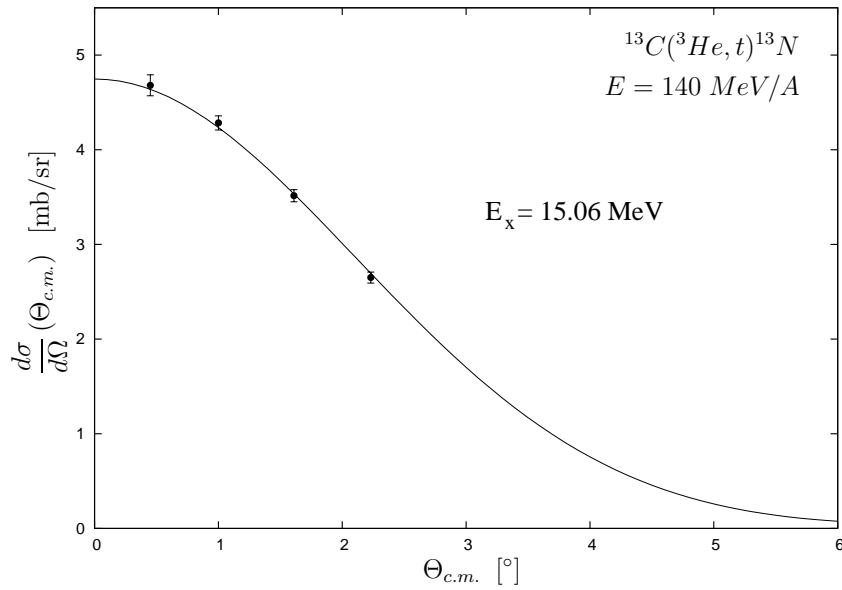


Figure 5.13: Angular distribution of the cross-section of the ^{13}N $3/2^-$, $T=3/2$ state at 15.06 MeV excited by the $(^3\text{He},t)$ reaction at 140 MeV/A beam energy. The solid curve is the calculated angular distribution for $\Delta L=0$, $\Delta S=1$, scaled to fit the data with a single scaling factor ($\chi^2_{red.}=0.38$).

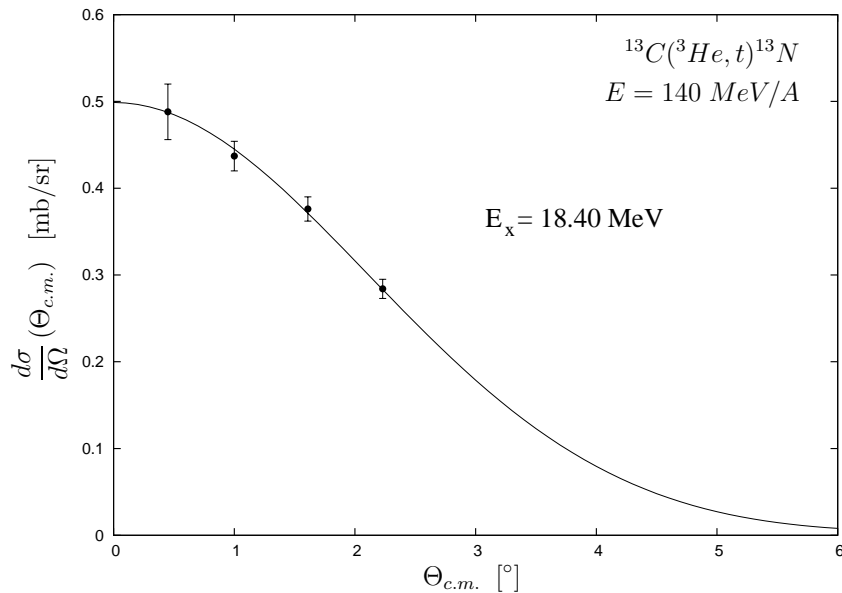


Figure 5.14: Angular distribution of the cross-section of the ^{13}N $(1/2^-, 3/2^-)$ state at 18.40 MeV excited by the $(^3\text{He},t)$ reaction at 140 MeV/A beam energy. The solid curve is the calculated angular distribution for $\Delta L=0$, $\Delta S=1$, scaled to fit the data with a single scaling factor ($\chi^2_{red.}=0.12$).

Table 5.4: Absolute differential cross-sections for ^{13}N levels. $\Delta \frac{d\sigma}{d\Omega}^{stat.}$ indicates the statistical error from the fitting of the angular distribution and the triton spectra. $\Delta \frac{d\sigma}{d\Omega}^{tot.}$ includes the errors from the target thickness and the ^3He beam intensity, both of which are assumed at 10%.

$\Theta_{c.m.}$ [°]	$\frac{d\sigma}{d\Omega}(\Theta_{c.m.})$ mb/sr	$\Delta \frac{d\sigma}{d\Omega}^{stat.}$ mb/sr	$\Delta \frac{d\sigma}{d\Omega}^{tot.}$ mb/sr	$\Theta_{c.m.}$ [°]	$\frac{d\sigma}{d\Omega}(\Theta_{c.m.})$ mb/sr	$\Delta \frac{d\sigma}{d\Omega}^{stat.}$ mb/sr	$\Delta \frac{d\sigma}{d\Omega}^{tot.}$ mb/sr
$E_x^{(exp)}=0$ keV $J^\pi=1/2^-$				$E_x^{(exp)}=2373^{+26}_{-21}$ keV $J^\pi=1/2^+$			
0.45	11.5	0.3	1.6	0.45	0.11	0.02	0.02
1.00	10.8	0.2	1.5	1.00	0.30	0.02	0.05
1.61	8.9	0.2	1.3	1.61	0.59	0.03	0.09
2.23	6.6	0.1	0.9	2.23	0.91	0.05	0.14
$E_x^{(exp)}=3501.2^{+3.4}_{-3.6}$ keV $J^\pi=3/2^-$				$E_x^{(exp)}=6363.3(34)$ keV $J^\pi=5/2^+$			
0.45	31.1	0.8	4.5	0.45	0.021	0.004	0.005
1.00	28.2	0.5	4.0	1.00	0.028	0.003	0.005
1.61	23.5	0.4	3.3	1.61	0.038	0.003	0.006
2.23	18.0	0.4	2.6	2.23	0.052	0.003	0.008
$E_x^{(exp)}=7385(7)$ keV $J^\pi=5/2^-$				$E_x^{(exp)}=8881(27)$ keV $J^\pi=1/2^-$			
$\Theta_{c.m.}$ [°]	$\frac{d\sigma}{d\Omega}(\Theta_{c.m.})$ mb/sr	$\Delta \frac{d\sigma}{d\Omega}^{stat.}$ mb/sr	$\Delta \frac{d\sigma}{d\Omega}^{tot.}$ mb/sr	$\Theta_{c.m.}$ [°]	$\frac{d\sigma}{d\Omega}(\Theta_{c.m.})$ mb/sr	$\Delta \frac{d\sigma}{d\Omega}^{stat.}$ mb/sr	$\Delta \frac{d\sigma}{d\Omega}^{tot.}$ mb/sr
0.45	0.130	0.016	0.024	0.45	5.53	0.32	0.84
1.00	0.170	0.016	0.029	1.00	4.88	0.16	0.71
1.61	0.148	0.013	0.025	1.61	3.96	0.13	0.57
2.23	0.128	0.013	0.022	2.23	2.87	0.10	0.42
$E_x^{(exp)}=9478(11)$ keV $J^\pi=3/2^-$				$E_x^{(exp)}=10811(5)$ keV $J^\pi=1/2^-$			
0.45	1.29	0.07	0.19	0.45	2.40	0.09	0.35
1.00	1.16	0.03	0.17	1.00	2.25	0.06	0.32
1.61	0.93	0.03	0.13	1.61	1.92	0.05	0.28
2.23	0.67	0.02	0.10	2.23	1.44	0.04	0.21
$E_x^{(exp)}=11877(7)$ keV $J^\pi=(3/2^-;1/2^-)$				$E_x^{(exp)}=13474(48)$ keV $J^\pi=(3/2^-;1/2^-)$			
$\Theta_{c.m.}$ [°]	$\frac{d\sigma}{d\Omega}(\Theta_{c.m.})$ mb/sr	$\Delta \frac{d\sigma}{d\Omega}^{stat.}$ mb/sr	$\Delta \frac{d\sigma}{d\Omega}^{tot.}$ mb/sr	$\Theta_{c.m.}$ [°]	$\frac{d\sigma}{d\Omega}(\Theta_{c.m.})$ mb/sr	$\Delta \frac{d\sigma}{d\Omega}^{stat.}$ mb/sr	$\Delta \frac{d\sigma}{d\Omega}^{tot.}$ mb/sr
0.45	8.9	0.3	1.3	0.45	0.79	0.05	0.12
1.00	8.0	0.2	1.1	1.00	0.71	0.03	0.10
1.61	6.7	0.1	1.0	1.61	0.56	0.02	0.08
2.23	5.1	0.1	0.7	2.23	0.39	0.03	0.06
$E_x^{(exp)}=15062.6(25)$ keV $J^\pi=3/2^-$				$E_x^{(exp)}=18397(4)$ keV $J^\pi=(3/2^-;1/2^-)$			
0.45	4.68	0.11	0.67	0.45	0.49	0.03	0.08
1.00	4.28	0.08	0.64	1.00	0.44	0.02	0.06
1.61	3.52	0.06	0.54	1.61	0.38	0.01	0.06
2.23	2.65	0.06	0.41	2.23	0.28	0.01	0.04

5.4 Cross-sections of the ${}^9\text{Be}({}^3\text{He},t){}^9\text{B}$ reaction

For the ${}^9\text{Be}({}^3\text{He},t){}^9\text{B}$ reaction, the absolute differential cross-sections shown in table 5.6 were determined for four angular bins, as described in 4.8. The angular distributions of states with $\Delta L=0$ character ($1/2^-$, $3/2^-$, $5/2^-$) were compared to angular distributions calculated in DWBA as described in 5.2. The calculated distributions were fitted to the obtained data by using a single scaling parameter, using the program TOPFIT [Wie]. The fit to these calculated distributions allows to extrapolate the cross-section at zero degrees scattering angle, $\frac{d\sigma}{d\Omega}(\Theta_{c.m.}=0)$ which is shown in table 5.5 for all states with $\Delta L=0$ character.

Table 5.5: Extrapolated absolute differential cross-sections for ${}^9\text{B}$ levels with $\Delta L=0$ character from fits to calculated DWBA angular distribution.

$E_x^{(exp)}$	$[\frac{d\sigma}{d\Omega}(0^\circ)]^{(exp)}$ (mb/sr)
0.0(3)	24.53(6)
2358(7)	6.29(1)
2730(70)	18.71(20)
3930(100)	9.31(5)
12245(56)	0.732(9)
14101^{+50}_{-90}	0.461(6)
14652(3)	0.135(1)
14895	0.494(7)
16050(40)	0.065(1)
17076(4)	0.0705(8)

The detailed DWBA fit for ${}^9\text{B}$ is difficult as optical potentials are only known for much lower beam energies, and the angle region of the experiment is not large enough to allow a detailed determination of all parameters. We will assume in the following that the incoherent $\Delta L=2$ contribution to the cross-section at zero degrees scattering angle is small.

The values obtained for the zero-degrees cross-section of observed GT states are summarized in table 5.5. These cross-sections can then be used to calculate the cross-section at momentum transfer $q=0$ by dividing by the factor $F(0^\circ, \omega)$ calculated in 5.1. The cross section at zero degrees and zero momentum transfer can then be used to determine the Gamow-Teller strength of the corresponding state.

The individual angular distributions $\frac{d\sigma}{d\Omega}(\Theta_{c.m.})$ together with the fitted DWBA curves are shown in figs. 5.15-5.24. The errorbars shown in the plots only reflect the statistical error arising from the deconvolution of the spectrum, and do not account for systematic errors (mainly the beam intensity and target thickness) which would have the effect of scaling the entire set of derived cross-sections by a single scaling factor (see 4.8).

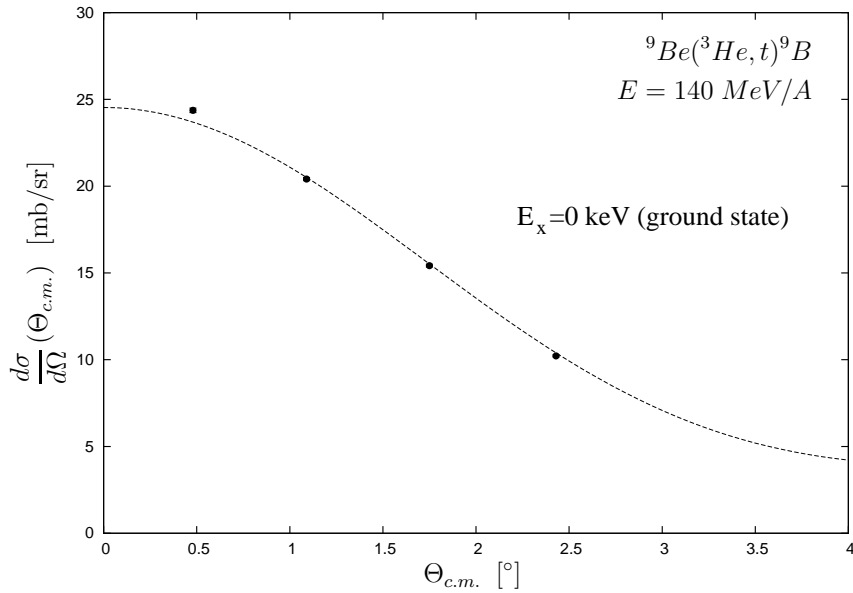


Figure 5.15: Angular distribution of the cross-section of the ${}^9\text{B}$ $3/2^-$ ground state excited by the $({}^3\text{He}, t)$ reaction at 140 MeV/A beam energy. The solid curve is the calculated angular distribution for $\Delta L=0, \Delta S=1$, scaled to fit the data with a single scaling factor.

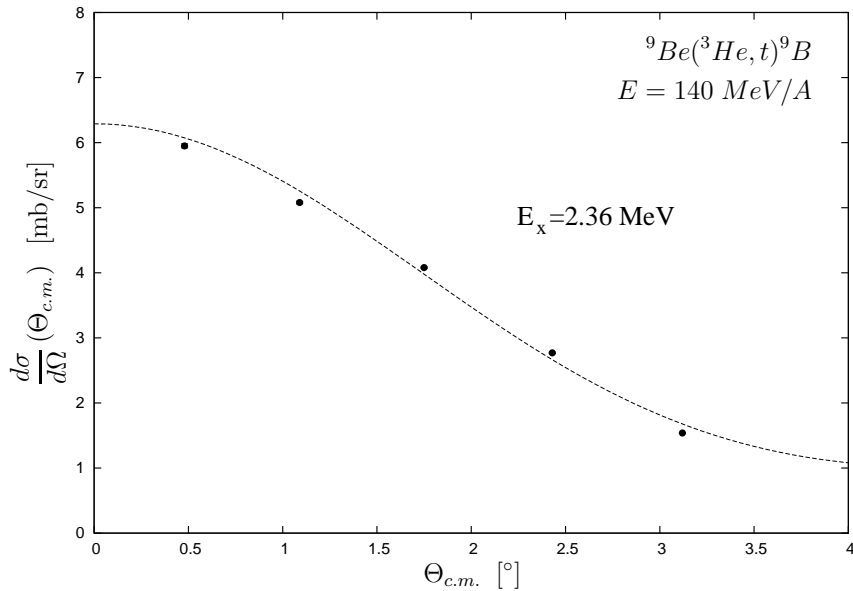


Figure 5.16: Angular distribution of the cross-section of the ${}^9\text{B}$ $5/2^-$ state at 2358(7) keV, excited by the $({}^3\text{He}, t)$ reaction at 140 MeV/A beam energy. The solid curve is the calculated angular distribution for $\Delta L=0, \Delta S=1$, scaled to fit the data with a single scaling factor.

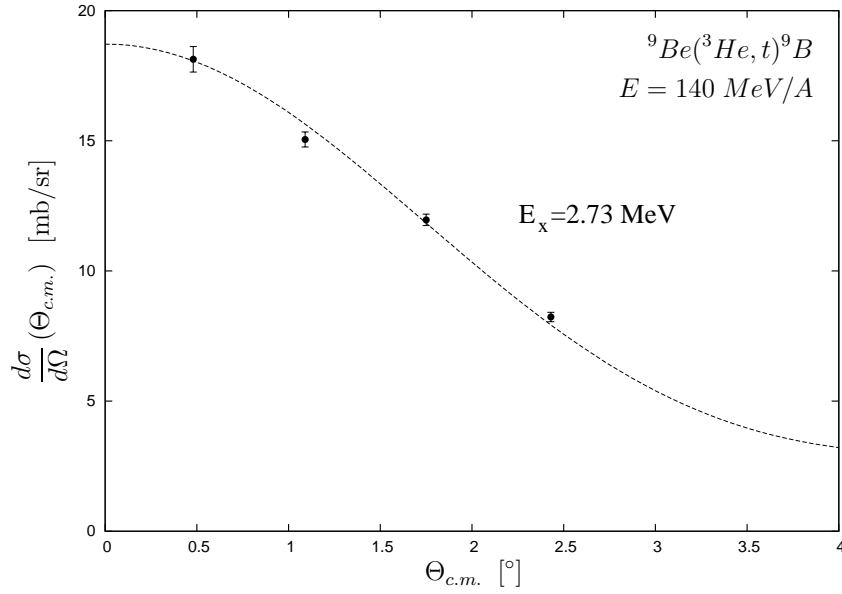


Figure 5.17: Angular distribution of the cross-section of the ${}^9\text{B}$ $1/2^-$ state at 2730(70) keV excited by the $({}^3\text{He},t)$ reaction at 140 MeV/A beam energy. The solid curve is the calculated angular distribution for $\Delta L=0, \Delta S=1$, scaled to fit the data with a single scaling factor.

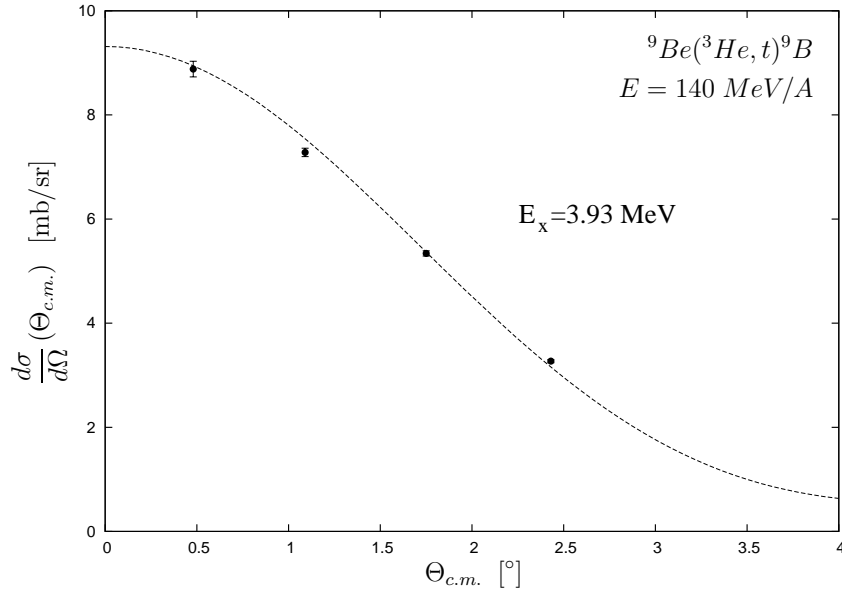


Figure 5.18: Angular distribution of the cross-section of the ${}^9\text{B}$ $(\frac{1}{2}^-, \frac{3}{2}^-, \frac{5}{2}^-)$ state at 3930(100) keV excited by the $({}^3\text{He},t)$ reaction at 140 MeV/A beam energy. The solid curve is the calculated angular distribution for $\Delta L=0, \Delta S=1$, scaled to fit the data with a single scaling factor.

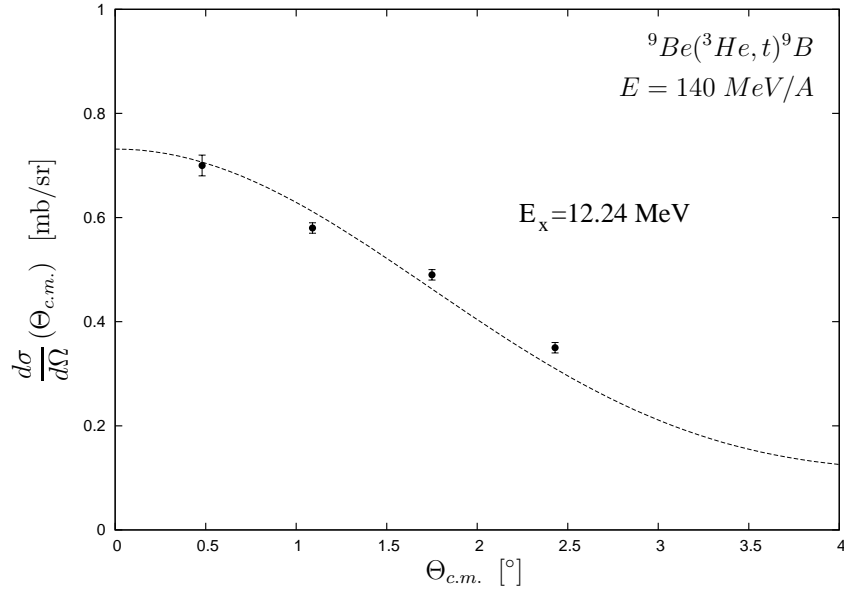


Figure 5.19: Angular distribution of the cross-section of the ${}^9\text{B}$ $5/2^-$ state at 12245(56) keV excited by the $({}^3\text{He}, t)$ reaction at 140 MeV/A beam energy. The solid curve is the calculated angular distribution for $\Delta L=0, \Delta S=1$, scaled to fit the data with a single scaling factor.

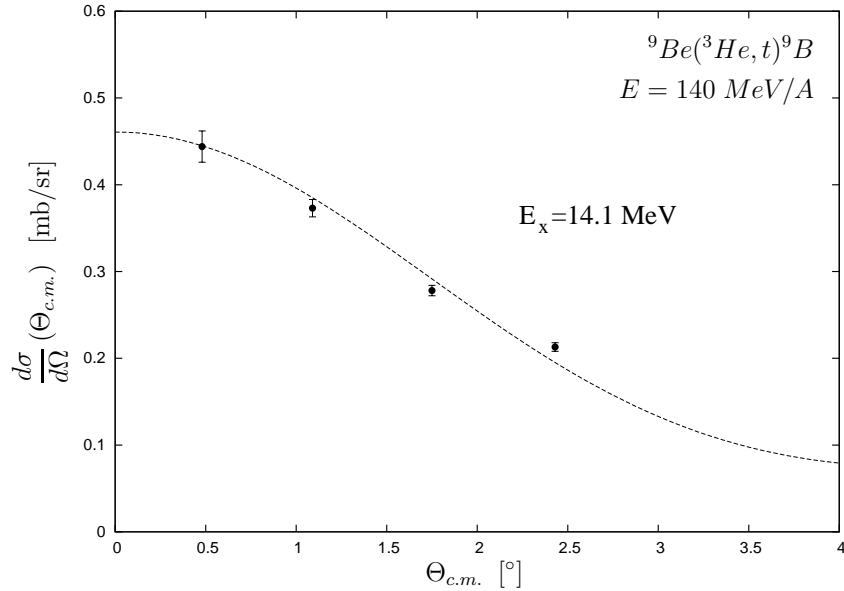


Figure 5.20: Angular distribution of the cross-section of the ${}^9\text{B}$ $(\frac{1}{2}^-, \frac{3}{2}^-, \frac{5}{2}^-)$ state at 14101^{+50}_{-90} keV excited by the $({}^3\text{He}, t)$ reaction at 140 MeV/A beam energy. The solid curve is the calculated angular distribution for $\Delta L=0, \Delta S=1$, scaled to fit the data with a single scaling factor.

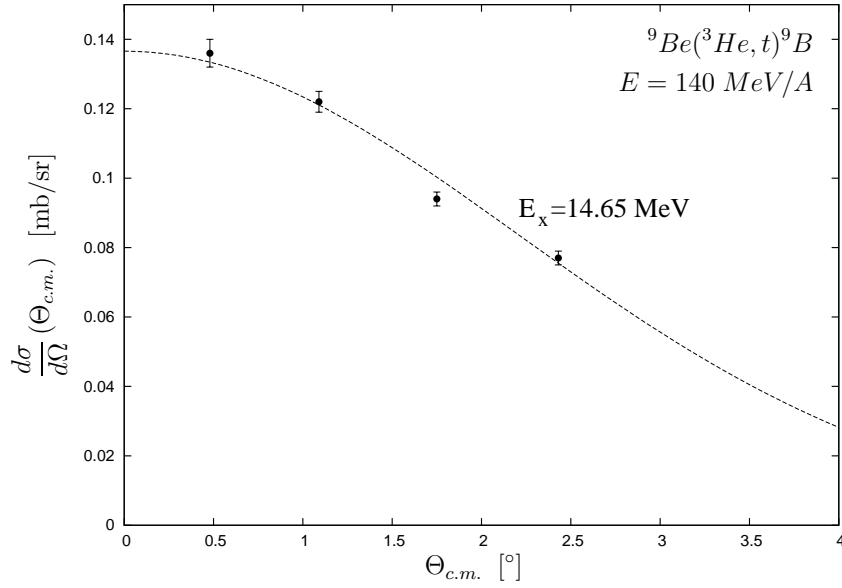


Figure 5.21: Angular distribution of the cross-section of the ${}^9\text{B}$ $3/2^-$, $T=3/2$ state at 14652(3) keV excited by the $({}^3\text{He},t)$ reaction at 140 MeV/A beam energy. The solid curve is the calculated angular distribution for $\Delta L=0$, $\Delta S=1$, scaled to fit the data with a single scaling factor.

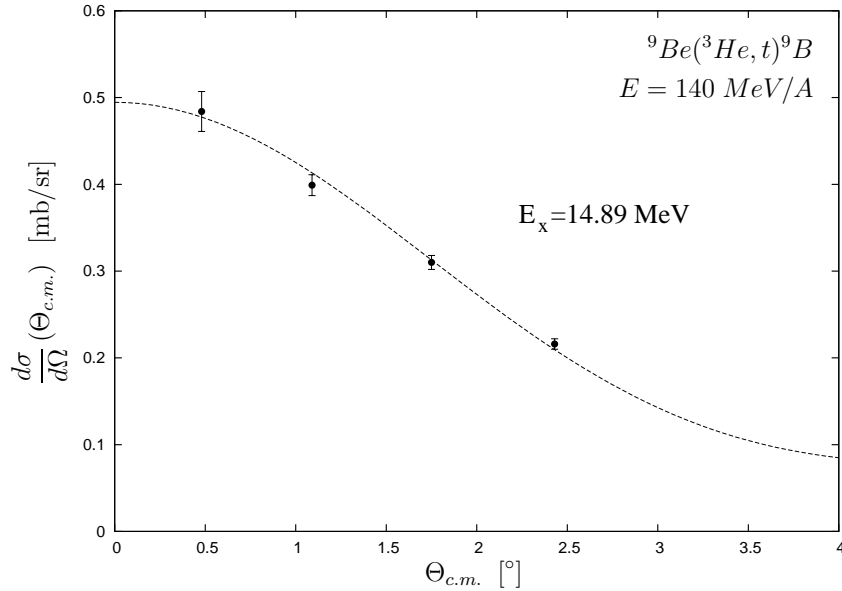


Figure 5.22: Angular distribution of the cross-section of the ${}^9\text{B}$ $(\frac{1}{2}^-, \frac{3}{2}^-, \frac{5}{2}^-)$ state(s) around 14895 keV excited by the $({}^3\text{He},t)$ reaction at 140 MeV/A beam energy. The solid curve is the calculated angular distribution for $\Delta L=0$, $\Delta S=1$, scaled to fit the data with a single scaling factor.

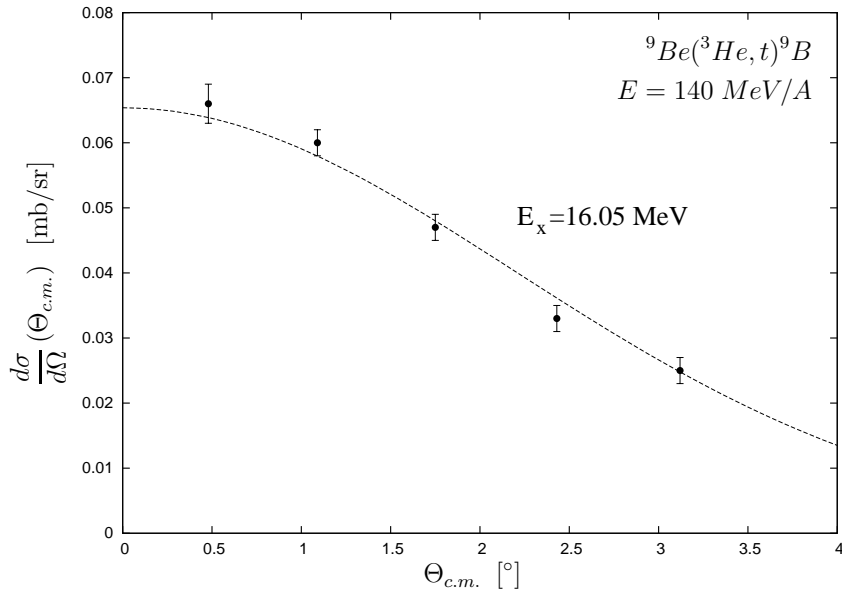


Figure 5.23: Angular distribution of the cross-section of the ${}^9\text{B}$ ($\frac{1}{2}^-$, $\frac{3}{2}^-$, $\frac{5}{2}^-$) state at 16050(40) keV excited by the $({}^3\text{He}, t)$ reaction at 140 MeV/A beam energy. The solid curve is the calculated angular distribution for $\Delta L=0, \Delta S=1$, scaled to fit the data with a single scaling factor.

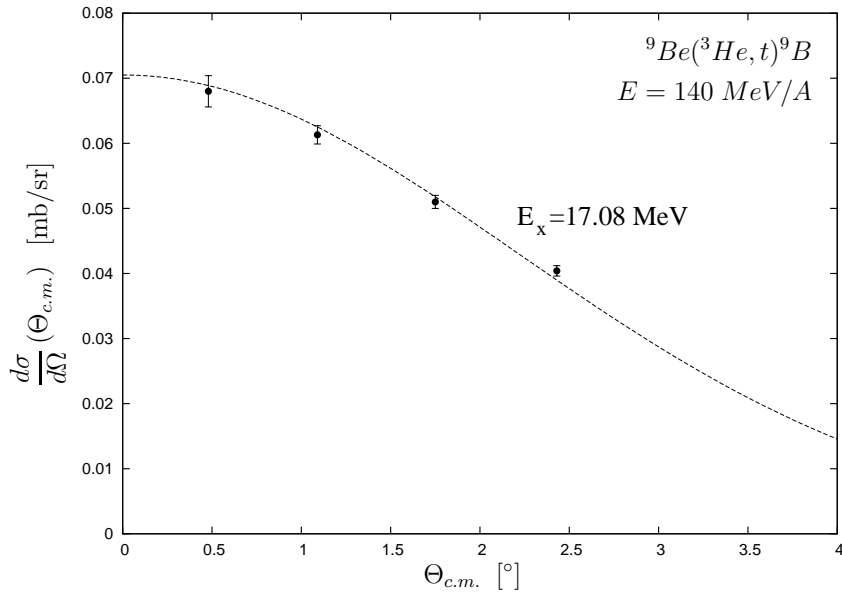


Figure 5.24: Angular distribution of the cross-section of the ${}^9\text{B}$ $1/2^-$, $T=3/2$ state at 17076(4) keV excited by the $({}^3\text{He}, t)$ reaction at 140 MeV/A beam energy. The solid curve is the calculated angular distribution for $\Delta L=0, \Delta S=1$, scaled to fit the data with a single scaling factor.

Table 5.6: Absolute differential cross-sections for ${}^9\text{B}$ levels. $\Delta \frac{d\sigma}{d\Omega}^{stat.}$ indicates the statistical error from the fitting of the angular distribution and the triton spectra. $\Delta \frac{d\sigma}{d\Omega}^{tot.}$ includes the errors from the target thickness and the ${}^3\text{He}$ beam intensity, both are assumed to be at 10%.

$\Theta_{c.m.}$ [°]	$\frac{d\sigma}{d\Omega}(\Theta_{c.m.})$ mb/sr	$\Delta \frac{d\sigma}{d\Omega}^{stat.}$ mb/sr	$\Delta \frac{d\sigma}{d\Omega}^{tot.}$ mb/sr	$\Theta_{c.m.}$ [°]	$\frac{d\sigma}{d\Omega}(\Theta_{c.m.})$ mb/sr	$\Delta \frac{d\sigma}{d\Omega}^{stat.}$ mb/sr	$\Delta \frac{d\sigma}{d\Omega}^{tot.}$ mb/sr
$E_x^{(exp)} = 0.0(3)$ keV $J^\pi = 3/2^-$				$E_x^{(exp)} = 2358(7)$ keV $J^\pi = 5/2^-$			
0.48	24.37	0.13	3.45	0.48	5.95	0.03	0.84
1.09	20.41	0.09	2.89	1.09	5.08	0.02	0.72
1.75	15.42	0.08	2.18	1.75	4.08	0.01	0.58
2.43	10.22	0.06	1.45	2.43	2.77	0.01	0.39
$E_x^{(exp)} = 2730(70)$ keV $J^\pi = 1/2^-$				$E_x^{(exp)} = 3930(100)$ keV $J^\pi = (\frac{1}{2}^-, \frac{3}{2}^-, \frac{5}{2}^-)$			
0.48	18.13	0.49	2.61	0.48	8.88	0.15	1.26
1.09	15.05	0.29	2.15	1.09	7.28	0.08	1.03
1.75	11.96	0.22	1.71	1.75	5.34	0.05	0.76
2.43	8.23	0.18	1.18	2.43	3.27	0.03	0.46
$E_x^{(exp)} = 12245(56)$ keV $J^\pi = 5/2^-$				$E_x^{(exp)} = 14101^{+50}_{-90}$ keV $J^\pi = (\frac{1}{2}^-, \frac{3}{2}^-, \frac{5}{2}^-)$			
0.48	0.696	0.024	0.101	0.48	0.444	0.018	0.065
1.09	0.584	0.013	0.084	1.09	0.373	0.010	0.054
1.75	0.492	0.010	0.070	1.75	0.278	0.006	0.040
2.43	0.355	0.007	0.051	2.43	0.213	0.005	0.031
$E_x^{(exp)} = 14652(3)$ keV $J^\pi = 3/2^-$				$E_x^{(exp)} = 14895$ keV $J^\pi = (5/2^-)$			
0.48	0.136	0.004	0.020	0.48	0.484	0.023	0.072
1.09	0.122	0.003	0.017	1.09	0.399	0.012	0.058
1.75	0.094	0.002	0.013	1.75	0.310	0.008	0.045
2.43	0.077	0.002	0.011	2.43	0.216	0.006	0.031
$E_x^{(exp)} = 16050(40)$ keV $J^\pi = (\frac{1}{2}^-, \frac{3}{2}^-, \frac{5}{2}^-)$				$E_x^{(exp)} = 17076(4)$ keV $J^\pi = 1/2^-$			
0.48	0.066	0.003	0.010	0.48	0.0680	0.0024	0.0099
1.09	0.060	0.002	0.009	1.09	0.0613	0.0014	0.0088
1.75	0.047	0.002	0.007	1.75	0.0510	0.0010	0.0073
2.43	0.003	0.002	0.005	2.43	0.0404	0.0008	0.0058

5.5 Gamow-Teller strengths for the ^{13}C target

The extrapolated cross-sections at zero degree scattering angle determined in 5.3 allow to determine the corresponding GT strength by using the proportionality relation [Tad87]

$$\left. \frac{d\sigma}{d\Omega} \right|_{q=0} = \hat{\sigma}_{GT} B(GT) \quad (5.3)$$

for Gamow-Teller states, and

$$\left. \frac{d\sigma}{d\Omega} \right|_{q=0} = \hat{\sigma}_F B(F) + \hat{\sigma}_{GT} B(GT) \quad (5.4)$$

for the isobaric analog state (IAS), where the factors $\hat{\sigma}_{F,GT}$ are the *unit cross-sections* for the Fermi- and Gamow-Teller transitions. The unit cross-sections can be obtained by calibrating the experimental cross-section with a known lifetime from beta-decay, or by carefully using the systematics across a wide range of nuclear masses [Zeg07].

For the ($^3\text{He}, t$) reaction at 420 MeV beam energy, the empirical relations

$$\hat{\sigma}_F = 72 \cdot A^{-1.06} \text{ mb/sr} \quad (5.5)$$

$$\hat{\sigma}_{GT} = 109 \cdot A^{-0.65} \text{ mb/sr} \quad (5.6)$$

give unit cross-sections $\hat{\sigma}_F=4.75$ mb/sr and $\hat{\sigma}_{GT}=20.6$ mb/sr for $A=13$. Furthermore, the transition to the $3/2^-, T=3/2$ state at 15.06 MeV in ^{13}N can be used to calibrate the GT unit cross-section, since the lifetimes of the analog transitions $^{13}\text{B}(\beta^-)^{13}\text{C}$ and $^{13}\text{O}(\beta^+)^{13}\text{N}$ are known from beta-decay measurements.

Using the ft values from beta-decay, the $B(GT)$ value can be obtained (see introduction) using

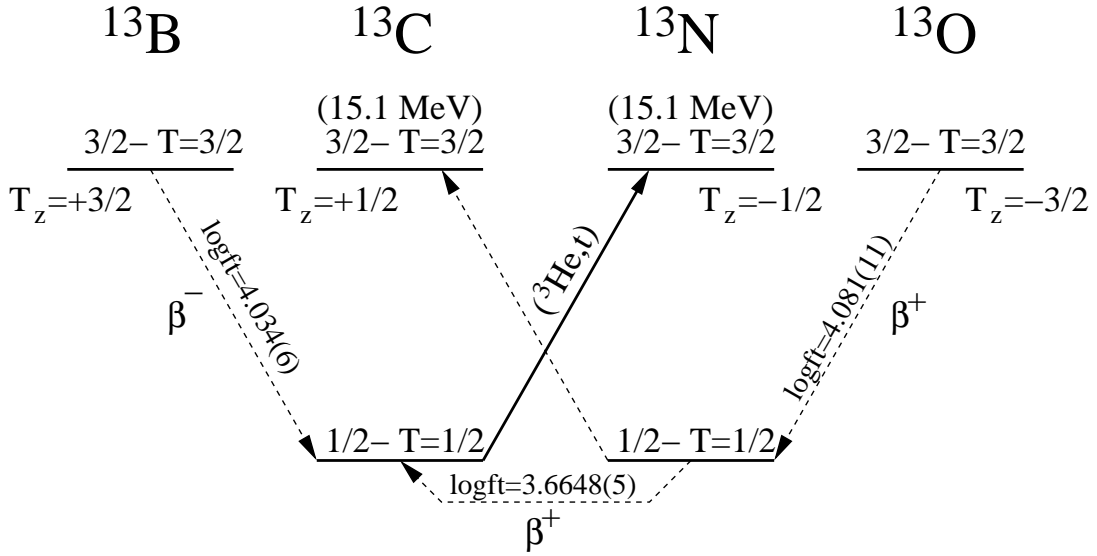
$$B(F) + \left(\frac{g_A}{g_V} \right)^2 B(GT) = \frac{K}{g_V^2 \cdot ft}, \quad (5.7)$$

where $K/g_V^2=6147(7)$ s [Har09] and $g_A/g_V=-1.2695(29)$ [Har06]. The GT strength of the ground state transition can be found by assuming that the Fermi strength $B(F)$ exhausts the full Fermi sum rule [Ost92]

$$\Sigma B(F) = (N - Z) = 1, \quad (5.8)$$

an assumption that is valid on the level of 0.15(9)% [Orm95], and gives (using the $\log ft$ value of the ^{13}N to ^{13}C ground state to ground state beta-decay of 3.6648(5))

$$\begin{aligned} B(GT) &= \frac{1}{(g_A/g_V)^2} \left(\frac{K}{g_V^2 \cdot ft} - 1 \right) \\ &= \frac{1}{(1.2695(29))^2} \left(\frac{6147(7)}{4621(5)} - 1 \right) = 0.205(2) \end{aligned} \quad (5.9)$$

Figure 5.25: β -decays and analog transitions for $A=13$

However, this value is not suited to accurately calibrate the GT unit cross-section [Zeg08, Zeg07, Wan01] since the Fermi unit cross-section has to be known with good accuracy.

There is no Fermi part in the beta decay of the ^{13}O $3/2^-$ ground state to the ^{13}N $1/2^-$ ground state, and in the ^{13}B $3/2^-$ ground state to the ^{13}C $1/2^-$ ground state. The lifetimes of these decays can be used to calibrate the GT unit cross-section. The $\log ft$ value of the $^{13}\text{O} \rightarrow ^{13}\text{N}$ transition is 4.081(11), which gives $ft=12050(305)\text{s}$. Thus we obtain for the $B(\text{GT})$ value of this transition

$$B(\text{GT}; ^{13}\text{O}(\text{g.s.}) \rightarrow ^{13}\text{N}(\text{g.s.})) = 0.317(2). \quad (5.10)$$

To obtain the $B(\text{GT})$ value of the $^{13}\text{C}(\text{g.s.}) \rightarrow ^{13}\text{N}(E_x=15.1 \text{ MeV})$ transition, one has to adjust for the different spin and isospin factors, while the reduced matrix element M_{GT} is the same for both transitions. The relation between $B(\text{GT})$ and the reduced matrix element of the $\sigma\tau$ operator is

$$B(\text{GT}) = \frac{1}{2(2J_i + 1)} \frac{\langle T_i T_{zi} \Delta T \Delta T_z | T_f T_{zf} \rangle^2}{2T_f + 1} M_{\text{GT}}^2 \quad (5.11)$$

where J_i and J_f are the total angular momentum of the initial and final states, T_i and T_f the initial and final isospin values, and T_z the z-projection of Isospin. Since

$$B(\text{GT}; ^{13}\text{O}(\text{g.s.}) \rightarrow ^{13}\text{N}(\text{g.s.})) = 0.317(2) = \frac{1}{8} \cdot \frac{1}{2} \cdot \left\langle \frac{3}{2}; -\frac{3}{2}; 1; 1 \left| \frac{1}{2}; -\frac{1}{2} \right. \right\rangle^2 M_{\text{GT}}^2 \quad (5.12)$$

and

$$B(\text{GT}; ^{13}\text{C}(\text{g.s.}) \rightarrow ^{13}\text{N}(15.1 \text{ MeV})) = \frac{1}{4} \cdot \frac{1}{4} \cdot \left\langle \frac{1}{2}; +\frac{1}{2}; 1; -1 \left| \frac{3}{2}; -\frac{1}{2} \right. \right\rangle^2 M_{\text{GT}}^2 \quad (5.13)$$

the $B(\text{GT})$ value for this transition can be obtained by combining both expressions, to

obtain

$$\begin{aligned}
 B(GT; {}^{13}\text{C}_{(\frac{1}{2}^-, \frac{1}{2}, +\frac{1}{2})} \rightarrow {}^{13}\text{N}_{(\frac{3}{2}^-, \frac{3}{2}, -\frac{1}{2})}) &= \frac{\langle \frac{1}{2}; +\frac{1}{2}; 1; -1 | \frac{3}{2}; -\frac{1}{2} \rangle^2}{\langle \frac{3}{2}; -\frac{3}{2}; 1; 1 | \frac{1}{2}; -\frac{1}{2} \rangle^2} \cdot 0.317(2) \\
 &= \frac{2}{3} \cdot 0.317(2) = 0.211(1) \quad (5.14)
 \end{aligned}$$

A similar calculation for the ${}^{13}\text{B}(\text{g.s.}) \rightarrow {}^{13}\text{C}(\text{g.s.})$ ($\log ft = 4.034(6)$) yields $B(GT) = 0.353(3)$ for this transition and thus $B(GT) = 0.235(2)$ for the transition from the ${}^{13}\text{C}$ ground state to the $T = 3/2$ state at 15.1 MeV in ${}^{13}\text{N}$. The difference between both values is due to the breaking of the isospin by the Coulomb interaction. The $B(GT)$ value for the considered transition should be between those two values. Rather than taking an average of both values, Taddeucci *et al.* used the ${}^{13}\text{B}(\beta^-)$ value and the asymmetry parameter for $A = 12$, by which they obtained $B(GT) = 0.23(1)$ with the larger error accounting for the uncertainty arising from the asymmetry [Tad87]. We shall use this value for our considerations as well.

Using this transition to calibrate the GT unit cross-section has the disadvantage that the Q -value for this beta-decay is rather large (~ 17 MeV), which means that the momentum transfer for this transition is relatively large. The value of the cross-section at zero momentum transfer has to be extrapolated (see 5.1) using the factor $F(\omega, 0^\circ)$. The uncertainty arising from this extrapolation is however smaller than using the ground state transition which contains the Fermi part.

Using $F(\omega = 17.3 \text{ MeV}, 0^\circ) = 0.82$ and the zero-degrees cross-section extrapolated from the data (4.75(5) mb/sr), one obtains

$$\left. \frac{d\sigma}{d\Omega} \right|_{q=0, \Theta=0} = 5.79(6) \text{ mb/sr}. \quad (5.15)$$

Using this value and $B(GT) = 0.23(1)$ to calibrate, the GT unit cross-section is 25(1) mb/sr, which is not consistent with the value of 20.6 mb/sr obtained from the systematics³. It should however be remembered that the errors do not include the systematic errors stemming from the beam normalization and the target thickness, both of which are significant. The deviation in the GT unit cross-section from systematics does also not affect the derived $B(GT)$ values using the calibration, as the systematic errors affect all determined cross-sections by the same magnitude.

The $B(GT)$ strengths in ${}^{13}\text{N}$ obtained by using this GT unit cross-section are given in table 5.7 in the fifth column. They are compared to $B(GT)$ values obtained from a (p,n) reaction by Wang *et al.* [Wan01] in 2001.

Wang *et al.* used a different method to obtain the GT unit cross-section (in this case for the (p,n) reaction at 197 MeV), namely calculating it using the ground state transition $B(GT)$ derived from the known beta-decay ft value ($B(GT) = 0.205(2)$) and extracting the $\hat{\sigma}_{GT}$ unit cross-section by using the empirical ratio $R^2 = \hat{\sigma}_{GT} / \hat{\sigma}_F$ obtained from mass-number systematics (in this case, from the (p,n) reaction on even targets, see [Tad87]).

³Zegers *et al.* [Zeg08] obtained a unit cross-section of 20(1) mb/sr in their (${}^3\text{He}, t$) experiment

If we use a similar approach, following [Zeg07], we would obtain a value (see equations (5.5) and (5.6))

$$R_{(A=13)}^2 = \frac{\hat{\sigma}_{GT}(A=13)}{\hat{\sigma}_F(A=13)} = \frac{109}{72} 13^{0.41} = 4.33(69) \quad (5.16)$$

where the error is obtained by the error of the systematics indicated in [Zeg07] (5% for $\hat{\sigma}_{GT}$ and 15% for $\hat{\sigma}_F$). Using this R^2 value together with the ground state transition $B(GT)=0.205(2)$ yields

$$\begin{aligned} \hat{\sigma}_{GT} &= \frac{\left. \frac{d\sigma}{d\Omega}(E_x=0) \right|_{q=0, \Theta=0}}{B(GT) + \frac{1}{R^2} B(F)} \\ &= \frac{11.98(11)}{0.205(2) + \frac{1}{4.33(69)}} = 27(2) \text{ mb/sr} \end{aligned} \quad (5.17)$$

which agrees with the value of 25(1) mb/sr which results from using the 15.06 MeV transition (25(1) mb/sr), but has larger uncertainty. Its absolute value is about 10% higher, which agrees with the works of Watson [Wat01, Wat85] and Zegers [Zeg08] regarding the issue of using the ground state transition for calibration purposes (see discussion in 6.1). The $B(GT)$ values derived using this method (analog to the one used by Wang *et al.*) are shown in table 5.7 in the sixth column.

The distribution of $B(GT)$ strength obtained in this study is compared to the (p,n) values from by Wang *et al.* in figure 5.26.

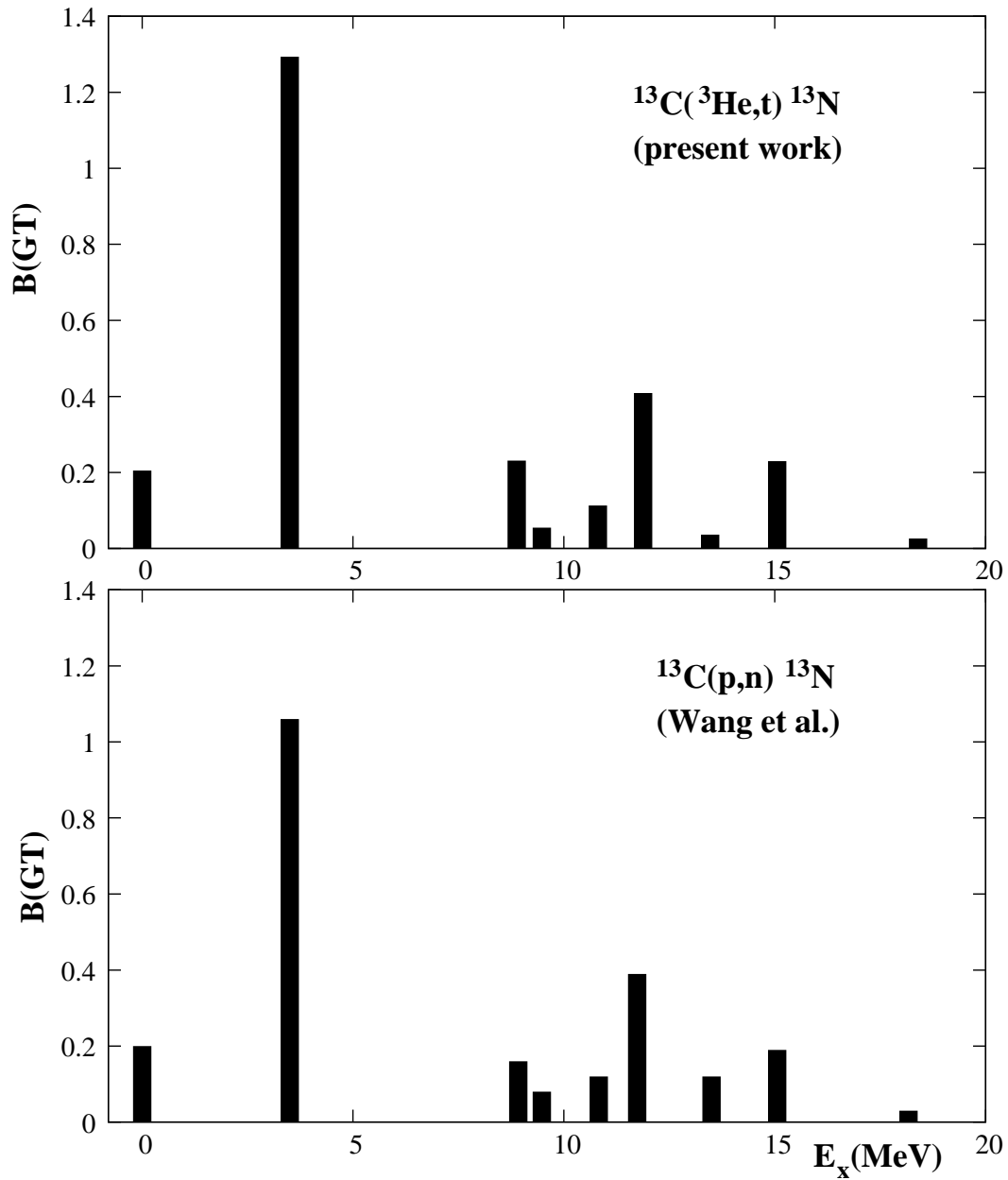


Figure 5.26: Distribution of the $B(GT)$ strengths in ^{13}N obtained in the present work (using the 15.1 MeV transition calibration), compared with the results from $^{13}\text{C}(p,n)$ by Wang et al. [Wan01].

Table 5.7: $B(\text{GT})$ values for $^{13}\text{C}(\text{g.s.}) \rightarrow ^{13}\text{N}(E_x)$ calculated using the GT unit cross-section obtained by calibrating with the $T=3/2$ beta-decay values. The errors are only statistical (arising from the fitting of the triton spectra). $B(\text{GT})$ values obtained from (p,n) [Wan01] are shown as comparison.

^(a) Obtained by using the ft value for the 15.06 MeV transition to determine the GT unit cross-section

^(b) Obtained by using the ground state transition and R^2 mass number systematics to extract the GT unit cross-section

^(c) Wang *et al.* calculated $\hat{\sigma}_{GT}$ by normalizing to the Fermi transition and using the empirical ratio $R^2 = \hat{\sigma}_{GT}/\hat{\sigma}_F$ obtained with even targets in the (p,n) reaction.

^(d) Value derived from the $^{13}\text{N}(\beta^+)$ decay, see discussion regarding the Fermi unit cross-section in the text

^(e) calibration value for $\hat{\sigma}_{GT}$ used in the present work

E_x [MeV]	$F(0^\circ, \omega)$	$\frac{d\sigma}{d\Omega}(0^\circ)$ [mb/sr]	$\frac{d\sigma}{d\Omega}(q=0)$ [mb/sr]	B(GT) present data ^(a)	B(GT) present data ^(b)	B(GT) [Wan01] ^(c)
0.00	0.99	11.89(11)	11.98(11)	0.205(2) ^(d)	0.205(2) ^(d)	0.20 ^(d)
3.50	0.97	31.63(31)	32.56(32)	1.29(6)	1.19(10)	1.06
8.88	0.91	5.32(10)	5.82(11)	0.23(1)	0.21(2)	0.16
9.48	0.91	1.25(2)	1.38(2)	0.055(3)	0.050(4)	0.08
10.81	0.89	2.53(4)	2.85(5)	0.113(5)	0.104(9)	0.12
11.88	0.87	8.98(10)	10.30(11)	0.41(2)	0.37(3)	0.39
13.47	0.85	0.77(2)	0.91(2)	0.036(2)	0.033(3)	0.12
15.06	0.82	4.75(5)	5.79(6)	0.23(1) ^(e)	0.21(2)	0.19
18.40	0.76	0.50(1)	0.66(1)	0.026(1)	0.024(2)	0.03
Σ				2.60(6)	2.40(11)	2.35

5.6 Gamow-Teller strengths for the ${}^9\text{Be}$ target

The extrapolated cross-sections at zero degree scattering angle determined in 5.4 can be used along with the proportionality relations (5.3),(5.4) to determine the $B(\text{GT})$ strength for the ${}^9\text{Be}$ target. Equations (5.5) and (5.6) give unit cross-sections $\hat{\sigma}_F=7.01$ mb/sr and $\hat{\sigma}_{GT}=26.13$ mb/sr for $A=9$ ($R^2=3.73$). In this case, however, there is no beta-decay from ${}^9\text{B}$ that can be used for calibration purposes.

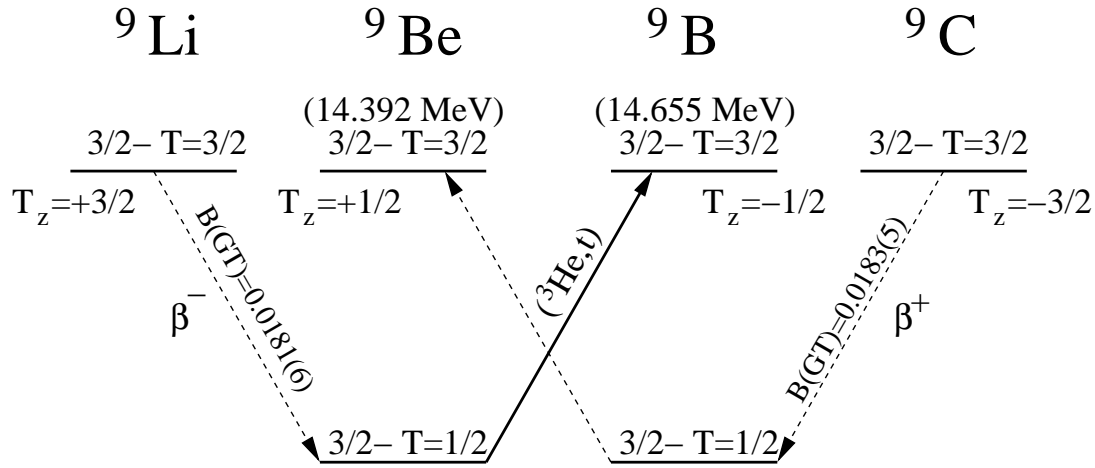


Figure 5.27: β -decays and analog transitions for $A=9$.

The Gamow-Teller unit cross-section can be calibrated as in the ${}^{13}\text{C}$ case by using the analog beta decays from ${}^9\text{Li}$ and ${}^9\text{C}$ (see fig. 5.27):

$$B(\text{GT}; {}^9\text{C}(\text{g.s.}) \rightarrow {}^9\text{B}(\text{g.s.})) = 0.0183(5) \quad (5.18)$$

$$B(\text{GT}; {}^9\text{Li}(\text{g.s.}) \rightarrow {}^9\text{Be}(\text{g.s.})) = 0.0181(6) \quad (5.19)$$

These values were taken from the compilation by Tilley *et al.* [Til04]. Recent studies of the ${}^9\text{C}(\beta^+)$ decay were carried out by Buchmann *et al.* [Buc01], Bergmann *et al.* [Ber01] and Mikolas *et al.* [Mik88]. Recent studies of the ${}^9\text{Li}(\beta^-)$ decay include the works of Nyman *et al.* [Nym90] and Prezado *et al.* [Pre03]. Regarding the Gamow-Teller strength, the experimental work of Dangtip *et al.* [Dan00] using the ${}^9\text{Be}(\text{n,p}){}^9\text{Li}$ reaction should also be mentioned. Although large asymmetries have been observed in the $A=9$ system for decays to excited states [Pre03], the decays to the ground states of ${}^9\text{Be}$ and ${}^9\text{B}$ exhibit no asymmetry. Adjusting for the different spin and isospin character of the ${}^9\text{Be}(\text{g.s.}) \rightarrow {}^9\text{B}(E_x=14.655 \text{ MeV})$ transition (using eq. (5.11) and the same procedure as outlined for the $A=13$ case), we obtain

$$\begin{aligned} B(\text{GT}; {}^9\text{Be}_{(\frac{3}{2}^-, \frac{1}{2}, +\frac{1}{2})} \rightarrow {}^9\text{B}_{(\frac{3}{2}^-, \frac{3}{2}, -\frac{1}{2})}) &= \frac{1}{2} \frac{\langle \frac{1}{2}; +\frac{1}{2}; 1; -1 | \frac{3}{2}; -\frac{1}{2} \rangle^2}{\langle \frac{3}{2}; -\frac{3}{2}; 1; 1 | \frac{1}{2}; -\frac{1}{2} \rangle^2} \cdot 0.0183(5) \\ &= \frac{1}{3} \cdot 0.0183(5) = 0.0061(2) \end{aligned} \quad (5.20)$$

using the ${}^9\text{C}(\beta^+)$ decay and $B(\text{GT})=0.0060(2)$ taking the ${}^9\text{Li}(\beta^-)$ decay value. In the present study, we shall use the value $B(\text{GT}; {}^9\text{Be}_{\text{g.s.}} \rightarrow {}^9\text{B}_{14.6 \text{ MeV}})=0.00607(18)$ as the calibration value for the Gamow-Teller unit cross-section.

As for the $A=13$ case, using this transition to calibrate the GT unit cross-section has the disadvantage that the Q -value for this beta-decay is rather large (~ 16 MeV) which means that the momentum transfer for this transition is relatively large. The value of the cross-section at zero momentum transfer has to be extrapolated (see 5.1) using the factor $F(\omega, 0^\circ)$. This is however the only practicable way since there is no ground state beta-decay of ${}^9\text{B}$.

Using $F(\omega=15.74 \text{ MeV}, 0^\circ)=0.836$ and the zero-degrees cross-section extrapolated from the data ($0.135(1) \text{ mb/sr}$), one obtains

$$\left. \frac{d\sigma}{d\Omega} \right|_{q=0, \Theta=0} (E_x = 14.655 \text{ MeV}) = 0.161(2) \text{ mb/sr}. \quad (5.21)$$

Using this value and $B(\text{GT})=0.00607(18)$ to calibrate, the GT unit cross-section is $26.5(8) \text{ mb/sr}$, which is consistent with the value of 26.13 mb/sr obtained from the systematics. The errors do not include the systematic errors stemming from the beam normalization and the target thickness, both of which are significant. Using the $R^2=3.73(59)$ value from the systematics⁴, the Fermi unit cross-section obtained is

$$\hat{\sigma}_F = \frac{26.5(8)}{3.7(6)} = 7(1) \text{ mb/sr}. \quad (5.22)$$

The Fermi unit cross-section derived from the R^2 systematics can be used to extract the $B(\text{GT})$ strength in the ground state transition (${}^9\text{Be}_{g.s.} \rightarrow {}^9\text{B}_{g.s.}$). Following eq. (5.4), we obtain (assuming once more that the total $B(\text{F})=N-Z=1$ strength is concentrated in the IAS)

$$\begin{aligned} \left. \frac{d\sigma}{d\Omega} (E_x = 0) \right|_{q=0, \Theta=0} &= \hat{\sigma}_F \cdot 1 + \hat{\sigma}_{GT} \cdot B(\text{GT}; {}^9\text{Be}_{g.s.} \rightarrow {}^9\text{B}_{g.s.}) \\ \Leftrightarrow B(\text{GT}; {}^9\text{Be}_{g.s.} \rightarrow {}^9\text{B}_{g.s.}) &= \frac{1}{R^2} \left(\frac{\left. \frac{d\sigma}{d\Omega} (E_x = 0) \right|_{q=0, \Theta=0}}{\hat{\sigma}_F} - 1 \right) \\ &= 0.66(18) \end{aligned} \quad (5.23)$$

All other $B(\text{GT})$ strengths in ${}^9\text{B}$ were obtained by dividing the extrapolated zero-degrees, $q=0$ cross-section by the determined $\hat{\sigma}_{GT}$. The results are summarized in table 5.8 and the $B(\text{GT})$ strength distribution is shown in fig. 5.28.

⁴The error is derived from the error of the systematics indicated in [Zeg07] (5% for $\hat{\sigma}_{GT}$ and 15% for $\hat{\sigma}_F$), $\Delta R^2 = \sqrt{(0.05 \cdot R^2)^2 + (0.15 \cdot R^2)^2}$

Table 5.8: $B(\text{GT})$ values for ${}^9\text{Be}(\text{g.s.}) \rightarrow {}^9\text{B}(E_x)$ calculated using the GT unit cross-section obtained by calibrating with the $T=3/2$ beta-decay values. The errors are only statistical (arising from the fitting of the triton spectra).

^(a) Obtained by using the $B(\text{GT})$ values from the ${}^9\text{Li}(\beta^-)$ and ${}^9\text{C}(\beta^+)$ decays to determine the GT unit cross-section (see text)

^(b) Obtained using R^2 from systematics (see text)

^(c) as discussed in section 4.6, the bump-like structure around 14.9 MeV most probably consists of several states, all of which may not be GT states. The analysis of the angular distribution supports an overall $\Delta L=0$ character, but as a precaution the $B(\text{GT})$ value is given as an upper limit. This value was included in the total sum of $B(\text{GT})$ strength.

E_x [keV]	$F(0^\circ, \omega)$	$\frac{d\sigma}{d\Omega}(0^\circ)$ [mb/sr]	$\frac{d\sigma}{d\Omega}(q=0)$ [mb/sr]	$B(\text{GT})$ present data ^(a)
0.0(3)	0.997	24.53(6)	24.61(6)	0.66(18) ^(b)
2358(7)	0.985	6.29(1)	6.38(1)	0.241(8)
2730(70)	0.983	18.71(20)	19.0(2)	0.718(24)
3930(100)	0.974	9.31(5)	9.56(5)	0.360(12)
12245(56)	0.875	0.732(9)	0.836(10)	0.0315(11)
14101 ⁺⁵⁰ ₋₉₀	0.845	0.461(6)	0.545(7)	0.0205(7)
14652(3)	0.836	0.135(1)	0.161(2)	0.0061(2)
14895	0.832	0.494(7)	0.594(9)	$\leq 0.0224(8)$ ^(c)
16050(40)	0.812	0.065(1)	0.0806(18)	0.00304(12)
17076(4)	0.793	0.0705(8)	0.0889(1)	0.00335(11)
Σ				2.07(18)

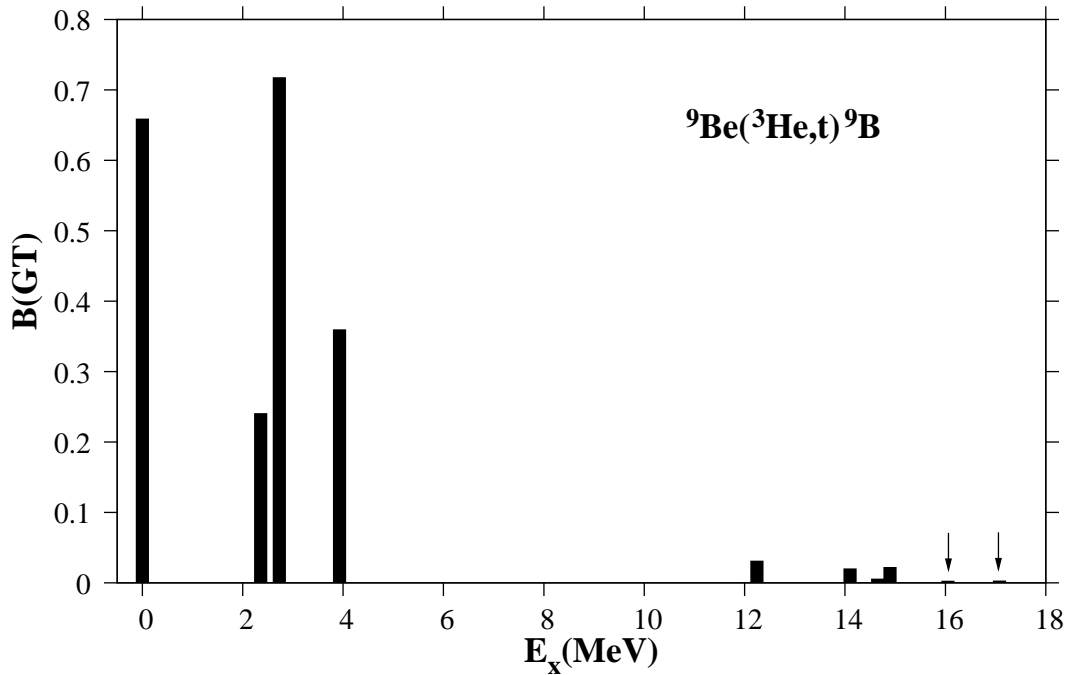


Figure 5.28: Distribution of $B(\text{GT})$ strength in ${}^9\text{B}$ obtained from the ${}^9\text{Be}({}^3\text{He}, t){}^9\text{B}$ experiment. The arrows indicate the very weak strengths at 16.05 and 17.08 MeV.

Chapter 6

Interpretation of the obtained results and comparison with previous studies

6.1 GT strength in ^{13}N

The $B(\text{GT})$ strengths obtained in the present $^{13}\text{C}(^3\text{He},t)^{13}\text{N}$ experiment were already given in table 5.7, and compared to the results obtained by Wang *et al.* in [Wan01]. We will now compare these results in more detail.

It has been known for some time, especially from the works of Watson *et al.* [Wat01, Wat85], that there are anomalies in the conversion of CE cross-sections to GT strength when considering the ground state to ground state transitions in odd-A nuclei (especially for the targets ^{13}C , ^{15}N and ^{39}K). Charge-exchange measurements using the (p,n) reaction [Wat01] found that the Gamow-Teller fraction $f_{\text{GT}} = \sigma_{\text{GT}}/(\sigma_{\text{F}} + \sigma_{\text{GT}})$ in the ground state transitions is typically 10% larger than predicted from beta-decay matrix elements and the systematics of even-A (p,n) results.

Both the studies of Watson *et al.* [Wat01, Wat85] and the more recent studies of Zegers *et al.* [Zeg07, Zeg08] conclude that this effect is due to an interference between $\Delta L=0$ and $\Delta L=2$ amplitudes which breaks the general proportionality between the beta-decay strength and the experimental cross-section. While Watson *et al.* speculate that this is due to Δ -isobar admixtures in the reaction mechanism [Wat85], Zegers *et al.* found [Zeg07, Col06, Zeg08] that a theoretical description of the cross-section using DWBA with the effective interaction of Love and Franey yields values consistent with systematics when the effect of the tensor- τ (V_{τ}^T) part of the interaction is accounted for. The consequences of both descriptions are similar (interference of $\Delta L=0$ and $\Delta L=2$ amplitudes that break the proportionality for ground state to ground state transitions for odd-A target nuclei).

This causes the unit cross-sections derived from charge-exchange experiments on these nuclei (when using odd-A systematics) to deviate by about 10-15% from the proportionality. Zegers *et al.* [Zeg08] found that the contribution from the tensor- τ part

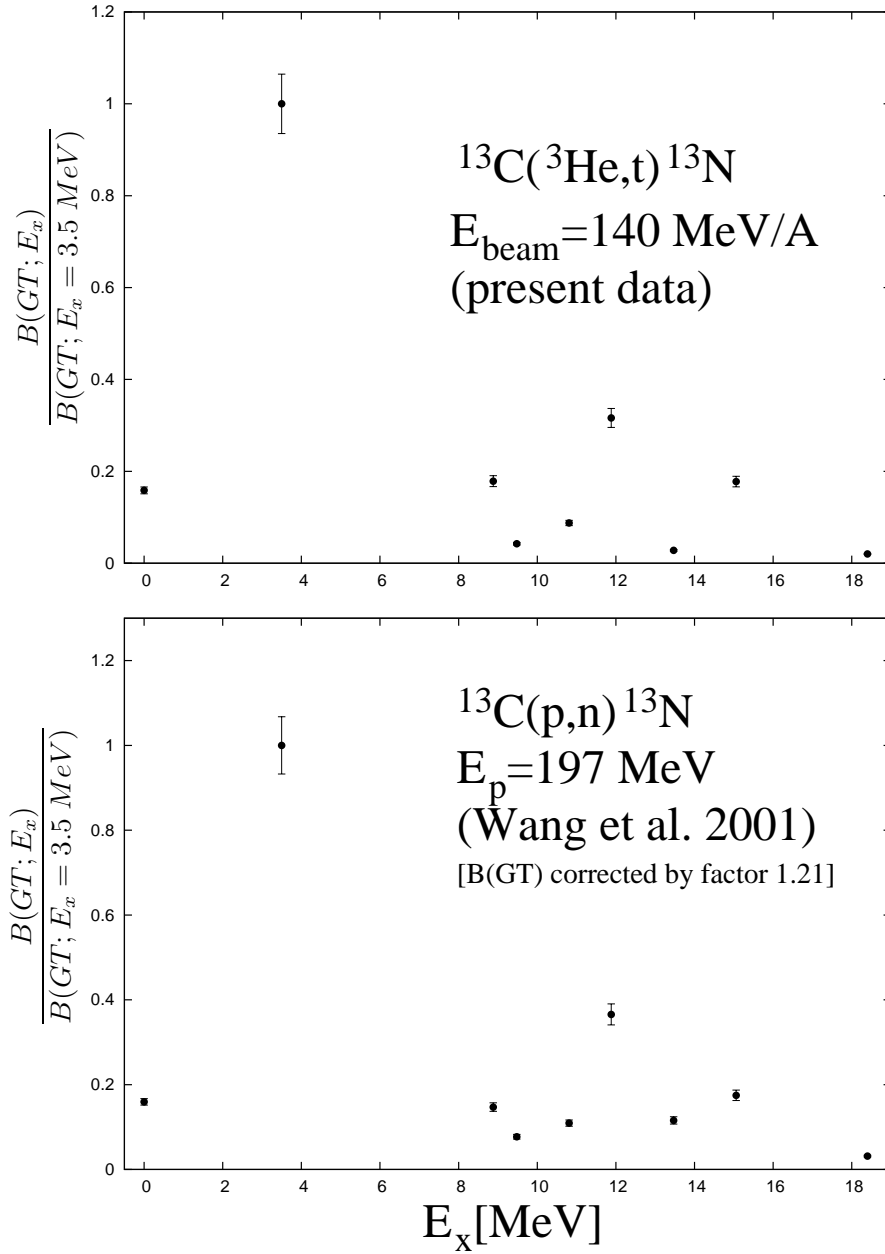


Figure 6.1: Comparison of the ratios of the $B(\text{GT})$ strength of excited states in ^{13}N with respect to the 3.5 MeV $B(\text{GT})$ strength. The data of Wang et al. [Wan01] was re-calibrated to the 15.1 MeV transition (see text).

of the effective interaction increases the Fermi part of the ground state cross-section by about 16% (from 5.1(5) mb/sr to 5.9(5) mb/sr) while it decreases the GT part of the ground state cross-section by 16% (from 5.0(2) mb/sr to 4.2(2) mb/sr). The $\hat{\sigma}_{GT}$ values derived from the systematics are thus too large when calibrating with the ground state transitions, and all B(GT) values for higher excited states obtained from the proportionality relation are thus smaller than they should be. A calibration with a transition where such interferences are not significant (e.g. pure GT transitions like the 15 MeV beta-decay of ^{13}O to ^{13}N) is thus the better choice and offers a way to empirically test the proportionality breaking when a ground-state beta-decay is available, such as for the ^{13}N case.

In the case of ^{13}N , the problems were compounded by the fact that the 15.1 MeV state is contaminated by the ground state of ^{12}N which has nearly the same Q-value. Charge-exchange measurements using the (p,n) probe were unable to separate both states, which is one of the main reasons Wang *et al.* [Wan01] chose to determine B(GT) values from their (p,n) experiment by relying on the systematics of unit cross-sections. If their B(GT) value of $B(\text{GT}, E_x=15.1 \text{ MeV})=0.19$ were taken as reference value, all their B(GT) values would have to be increased by about 21%, which would e.g. bring the B(GT) value of the 3.5 MeV transition ($1.06(5) \cdot 1.21 = 1.28(7)$) in-line with the result of ($^3\text{He}, t$) studies (1.37(7) [Zeg08], and 1.29(6) (present work)) and shell-model results (1.50 with the CKI interaction with 67%-quenching [Zeg08] and 1.34 with the WBT interaction [Wan01]). The results obtained are shown in table 6.1 and compared to the results of Wang *et al.* if recalculated using the 15.1 MeV state cross-section as a reference. The B(GT) ratios obtained by dividing the B(GT) strength of an excited state by the strength of the 3.5 MeV state are shown in figure 6.1 and figure 6.2.

While the results for the states with rather large cross-sections agree quite well, those with smaller cross-sections clearly do not. This is most certainly a result of the higher sensitivity and resolution of the ($^3\text{He}, t$) reaction compared to the (p,n) experiment.

The B(GT) values for the strong and well-separated 3.5 MeV state agree if the calibration is made with the 15.1 MeV state. The states at 8.88 and 9.48 MeV cannot be well separated in the (p,n) reaction, while the ($^3\text{He}, t$) reaction clearly separates them. While the present study obtains a higher B(GT) for the 8.88 MeV state (0.23(1) vs 0.19(1) in (p,n)), it also obtains a lower value (0.055(3) vs 0.099(5)) for the 9.48 MeV state. If both strengths are added together, the present study obtains $B(\text{GT}, 8.88+9.48 \text{ MeV})=0.285$ while Wang *et al.* would obtain 0.288 (if calibrating with the 15.1 MeV state). The B(GT) of the 10.81 MeV and 11.88 MeV states, which are separated in the spectra, agree with the results of [Wan01], however they are smaller than the results obtained if the (p,n) data is calibrated with the 15.1 MeV state.

The most important deviation (by about a factor of four) is observed for the GT strength of the 13.47 MeV state. As has been discussed in 4.5, the present experimental study distinguishes two separate states around this excitation energy. The B(GT) strength of 0.036(2) given represents the strength of the sharper state with width of 440 keV. The present study assumes that the broader state ($\Gamma \approx 4.5 \text{ MeV}$) is not a GT state and thus its cross-section does not result in a corresponding GT strength. The (p,n) reaction is certainly unable to distinguish both states (see spectrum shown in [Wan01])

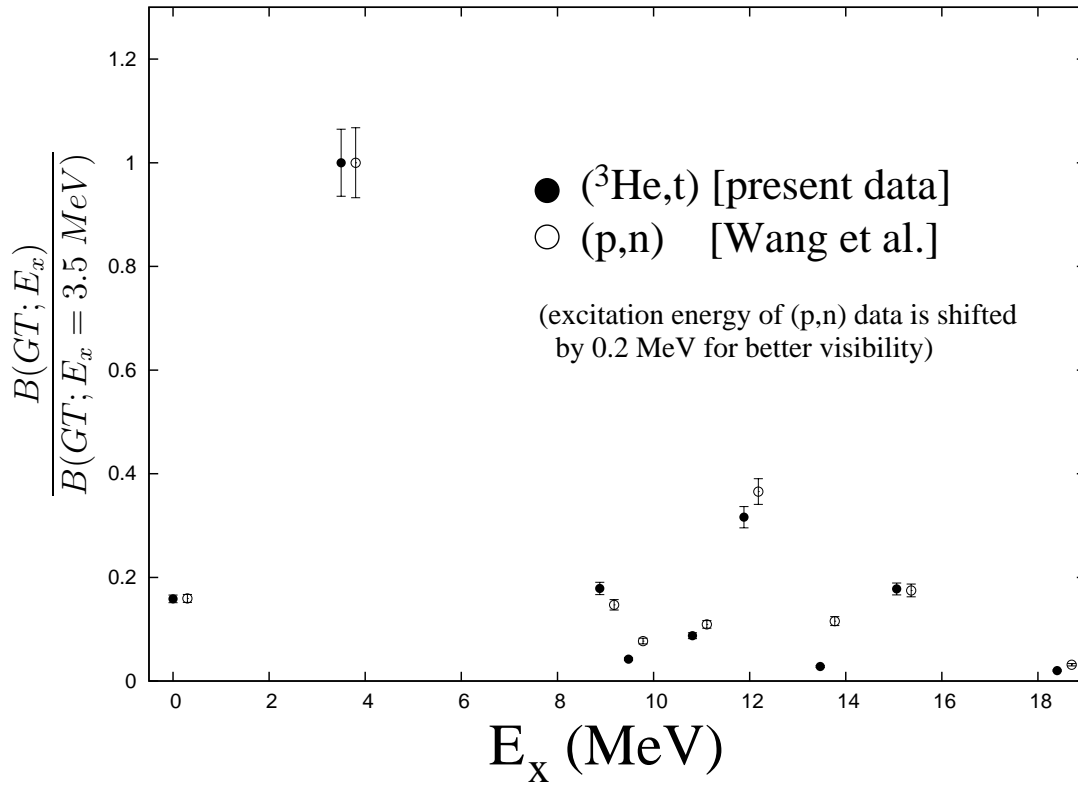


Figure 6.2: Comparison of the ratios of the $B(GT)$ strength of excited states in ^{13}N with respect to the 3.5 MeV $B(GT)$ strength. The data of Wang et al. [Wan01] (empty circles) was re-calibrated to the 15.1 MeV transition (see text), and the excitation energies of the (p,n) data are shifted upwards by 200 keV for better visibility.

compared to fig. 4.6 in this work).

The same effect is most probably playing into the 50% larger B(GT) value determined in (p,n) for the 18.4 MeV state. As can be seen in fig. 4.9, the (p,n) reaction cross-section certainly has a large admixture of strength resulting from the states at 17.8 and 18.2 MeV which do not have $\Delta L=0$ nature and should thus not give rise to any B(GT) strength.

Table 6.1: B(GT) values for $^{13}\text{C}(\text{g.s.}) \rightarrow ^{13}\text{N}(E_x)$ by various authors. B(GT) values from [Wan01] were obtained from (p,n), B(GT) values from [Zeg08] from ($^3\text{He,t}$).

^(a) Obtained by using the ft value for the 15.06 MeV transition to determine the GT unit cross-section

^(b) Obtained by using the ground state transition and using R^2 mass number systematics to extract the GT unit cross-section

^(c) Wang *et al.* calculated $\hat{\sigma}_{GT}$ by normalizing to the Fermi transition and using the empirical ratio $R^2 = \hat{\sigma}_{GT}/\hat{\sigma}_F$ obtained with even targets in the (p,n) reaction. The values were recalculated from the cross-sections indicated in [Wan01] using the indicated statistical errors.

^(d) Values that would be obtained from the (p,n) data of Wang *et al.* if they had calibrated with the 15.1 MeV state, and the indicated 15.1 MeV cross-section is indeed the $^{13}\text{C}(\text{p,n})$ cross-section.

^(e) Zegers *et al.* [Zeg08] obtained B(GT)=1.37(7) for this state in their ($^3\text{He,t}$) study.

^(f) The results obtained from the shell model calculations both include the phenomenological quenching of about 0.67 for the Gamow-Teller strength. The values from [Zeg08] were derived using the CKII interaction, while the values from [Wan01] were derived from the WBT interaction.

^(g) Value derived from the $^{13}\text{N}(\beta^+)$ decay

^(h) calibration value for $\hat{\sigma}_{GT}$ used in the present work and in [Zeg08], also used for column 5.

E_x [MeV]	B(GT) ^(a) present work	B(GT) ^(b) present work	B(GT) ^(c) [Wan01]	B(GT) ^(d) ($\times 1.21$)	B(GT) _{SM} ^(f) [Zeg08]	B(GT) _{SM} ^(f) [Wan01]
0	0.205(2) ^(g)	0.205(2)	0.2	0.2 ^(g)	0.19	0.17
3.5	1.29(6) ^(e)	1.19(10)	1.06(5)	1.29(6)	1.5	1.34
8.88	0.23(1)	0.21(2)	0.156(8)	0.189(9)		
9.48	0.055(3)	0.050(4)	0.082(4)	0.099(5)		
10.81	0.113(5)	0.104(9)	0.116(6)	0.141(7)		
11.88	0.41(2)	0.37(3)	0.39(2)	0.47(2)		
13.47	0.036(2)	0.033(3)	0.123(7)	0.149(8)		
15.06	0.23(1) ^(h)	0.21(2)	0.19(1)	0.22(1)	0.23	0.29
18.4	0.026(1)	0.024(2)	0.033(2)	0.040(2)		

6.2 B(GT) strengths in ^9B

Previous charge-exchange studies of ^9B include the $^9\text{Be}(\text{p,n})^9\text{B}$ reaction at $E_p=135$ MeV studies by B.G. Pugh in his Ph.D. thesis at MIT [Pug85, Faz82]. While Pugh was not able to give B(GT) values due to the lack of beta-decay data (and the difficulty to resolve the weakly excited state at 14.6 MeV), differential cross-section values for the excited states in ^9B are given in his thesis.

These cross-sections can be used to obtain a comparison to the present ($^3\text{He,t}$) data

Table 6.2: Comparison of the ratio obtained by dividing the B(GT) strength of an excited state by the B(GT) strength of the state at 3.5 MeV for the present data and the (p,n) data of Wang *et al.* [Wan01]. The (p,n) data has been recalibrated to the 15.1 MeV state (see text). The data is compared graphically in figure 6.2

E_x [MeV]	$\frac{B(GT;E_x)}{B(GT;3.5)}$ (present data)	$\frac{B(GT;E_x)}{B(GT;3.5)}$ (Wang <i>et al.</i> [Wan01], recalibrated)
0	0.159(7)	0.159(7)
3.5	1.00(6)	1.00(7)
8.88	0.18(1)	0.15(1)
9.48	0.042(3)	0.077(6)
10.81	0.088(6)	0.109(7)
11.88	0.32(2)	0.37(2)
13.47	0.028(2)	0.116(9)
15.06	0.18(1)	0.17(1)
18.4	0.020(1)	0.031(2)

by converting them to B(GT) values using the present results. It would not be wise to calibrate the (p,n) data using the 14.6 MeV $T=3/2$ state, as the resolution and sensitivity of the (p,n) reaction is not good enough to isolate the strength of this state (see spectrum in [Pug85]). Instead a calibration by using the strongest pure GT state, the $5/2^-$ state at $E_x=2.36$ MeV was made. The calibration value used was $B(GT)=0.241(8)$ taken from the present high-resolution ($^3\text{He},t$) experiment (see table 5.8 in 5.6). The results of the determination of B(GT) values derived from the (p,n) cross-sections is shown in table 6.3, and the B(GT) ratios obtained by dividing the B(GT) strength of an excited state by the strength of the 2.36 MeV state are shown in fig. 6.3. The zero-degree cross-sections obtained by Pugh were converted to $q=0$ cross-sections by calculating the $F(\omega)$ factor in DWBA, using the proton bombarding energy of $E_p=135$, and the optical potential parameters Pugh used for the fitting of cross-sections in his experiment ($V_R=16.2$ MeV, $r_R=1.2$ fm, $a_R=0.66$ fm, $W_I=11.1$ MeV, $r_I=1.28$ fm and $a_I=0.63$ fm [Pug85]). The calibration to the B(GT) strength of the 2.36 MeV state yields a GT unit cross-section of

$$\hat{\sigma}_{GT}^{(p,n)} = \frac{2.13(4) \text{ mb/sr}}{0.241(8)} = 8.85(34) \text{ mb/sr} \quad (6.1)$$

which agrees well with the systematic trend of the (p,n) GT unit cross-sections (see fig. 1.3 in the introduction). All $q=0$ cross-sections (except for the ground state) were then divided by $\hat{\sigma}_{GT}^{(p,n)}$ to obtain the corresponding B(GT) strength. The ground state was treated using eq. (5.23) since there is no beta-decay data available. The Fermi to Gamow-Teller unit cross-section ratio was taken from the systematics for (p,n) experiments [Tad87], assuming a 10% error:

$$R^2 = \left(\frac{E_p(\text{MeV})}{55} \right)^2 = 6.0(6) \quad (6.2)$$

The B(GT) value for the ground state transition obtained in this way is $B(GT, E_x=0) =$

0.91(15), which agrees with the value of 0.66(18) obtained from the ($^3\text{He},t$) data within the errorbars.

Table 6.3: B(GT) values for $^9\text{Be}(\text{g.s.}) \rightarrow ^9\text{B}(E_x)$ calculated from the cross-section data obtained by Pugh in his $^9\text{Be}(p,n)$ experiment [Pug85, Faz82]. Like in the comparison with (p,n) data for the ^{13}C target, the B(GT) values of strong and well-separated GT states agree with the ($^3\text{He},t$) results, while weaker states and states that are near to other $\Delta L \geq 1$ states that cannot be resolved in the (p,n) reaction result in much higher B(GT) values since the $\Delta L \geq 1$ often cannot be properly separated in the (p,n) experiment due to lower resolution.

(a) The F-Factor was determined by DWBA using the bombarding proton energy of 135 MeV and the optical potential parameters used by Pugh in his thesis [Pug85]

(b) The B(GT) values were derived from the zero-degree cross-sections given by Pugh in his thesis [Pug85], using the 2.36 MeV state as a calibration value since it is the strongest pure GT state. The reference value used was $B(\text{GT})=0.241(8)$ obtained from the present ($^3\text{He},t$) study.

(c) The ground state B(GT) was calculated using the equation (5.23), and using the R^2 value obtained from (p,n) systematics: $R^2 = \left(\frac{E_p(\text{MeV})}{55} \right)^2$ [Tad87]

E_x [MeV]	$F(0^\circ, \omega)^{(a)}$	$\frac{d\sigma}{d\Omega}(0^\circ)$ [mb/sr]	$\frac{d\sigma}{d\Omega}(q=0)$ [mb/sr]	B(GT) derived from [Pug85] ^(b)
0	0.995	9.52(4)	9.56(4)	0.91(15) ^(c)
2.36	0.98	2.09(4)	2.13(4)	0.24(1) ^(b)
2.71	0.977	2.83(36)	2.9(4)	0.33(4)
2.75	0.977	9.73(29)	10.0(3)	1.13(5)
4.3	0.962	2.41(6)	2.50(6)	0.28(1)
12.2	0.848	0.230(14)	0.27(2)	0.031(2)
14	0.814	0.0657(22)	0.081(3)	0.0091(5)
14.6	0.802	0.213(25)	0.27(3)	0.030(4)
15.9	0.775	0.0578(59)	0.075(8)	0.0084(9)
16.7	0.759	0.0441(50)	0.058(7)	0.0066(8)
Σ				2.98(16)

Generally, like in the case of the ^{13}C target, the B(GT) obtained for the strong states that can be resolved in the (p,n) reaction agree with the ($^3\text{He},t$) results. In ^9B this can only be said for the ground state, the 2.36 MeV state (which was used for calibration), and the 12.2 MeV state. Remarkably, the B(GT) value for the 12.2 MeV state (0.031(2)), which is the strongest of the states at higher excitation energy and is also well separated from other states, agrees completely with the ($^3\text{He},t$) value (0.0315(11)).

The values for the states with higher excitation energy are all much larger than the more precise data obtained from ($^3\text{He},t$). The sharp $T=3/2$ state at 14.6 MeV (which was used for the calibration of the ($^3\text{He},t$) data) could not be separated from the “bump” strength (see 4.6) and the 14 MeV state is not clearly separated as well. Comparing the whole strength in the 14–15 MeV region gives a better result: for the (p,n) data, we obtain $\Sigma B(\text{GT})=0.0091(5) + 0.030(4) = 0.039(4)$ and for the ($^3\text{He},t$) data $\Sigma B(\text{GT})=0.049(1)$ (sum of the strengths of the 14.1 MeV state, the 14.6 MeV state and the 14.9 MeV state) which is in much better agreement than the individual B(GT) strengths.

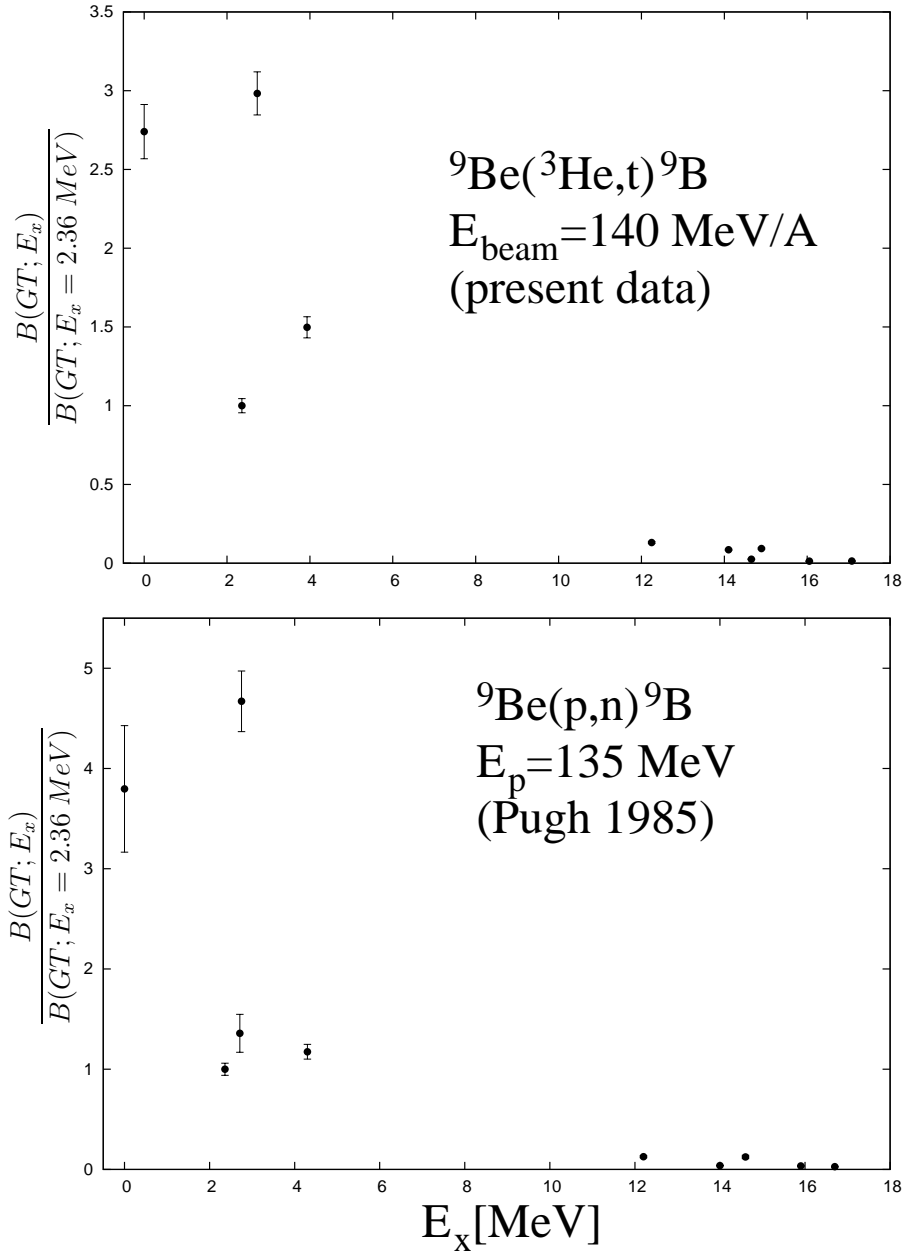


Figure 6.3: Comparison of the ratios of the $B(GT)$ strength of excited states in ${}^9\text{B}$ with respect to the 2.36 MeV $B(GT)$ strength. The data derived (see text) from the cross-sections obtained in Pugh's (p,n) experiment [Pug85] are shown in comparison.

The same separation problem exists for the states given at 15.9 MeV and 16.7 MeV in Pugh's thesis. Both states are near to the 16.8 MeV state and the 17.6 MeV state, both of which have $\Delta L \geq 1$ character and have a significant cross-section. The B(GT) values of both states being larger by a factor of two in the (p,n) results is therefore not suprising.

The most important difference (which also makes the biggest contribution to the larger total B(GT) strength) comes from the treatment of the broad states at 2-3 MeV excitation energy. Here, Pugh gives two cross-sections, for a 2.71 MeV state and a 2.75 MeV state, which yield a total B(GT) value of 1.46, while the B(GT) value from ($^3\text{He},t$) for the 2.73 MeV state is only 0.718(24). The 2.75 MeV state shown in the spectrum fits in [Pug85] has a very unusual shape and seems to be more of a residual strength required to obtain a good fit. Pugh assumed that the broad "bump" around 3 MeV was mainly the result of a single broad peak, which he assumed was the 2.75 MeV state. From ($^3\text{He},t$) results with higher resolution, like the study of Akimune *et al.* [Aki01], we now know that the bump is made up of several states with different character. It is therefore understandable that (while it still can not be ruled out that there are still some weak GT states present in the spectrum in the region 5-9 MeV) the strength obtained from the (p,n) data is far too large.

Table 6.4: Comparison of the ratio obtained by dividing the B(GT) strength of an excited state by the B(GT) strength of the state at 2.36 MeV for the present data and the data extracted from the (p,n) cross-sections obtained by Pugh [Pug85]. The data is compared graphically in figure 6.3.

E_x [MeV]	$\frac{B(GT;E_x)}{B(GT;3.5)}$ (present data)	E_x [MeV]	$\frac{B(GT;E_x)}{B(GT;3.5)}$ (derived from Pugh [Pug85])
0	2.7(2)	0	3.8(6)
2.358	1.00(4)	2.36	1.00(6)
2.73	3.0(1)	2.71	1.4(2)
		2.75	4.7(3)
3.93	1.50(7)	4.3	1.17(7)
12.245	0.131(6)	12.2	0.13(1)
14.101	0.085(4)	14	0.038(3)
14.652	0.025(1)	14.6	0.12(2)
14.895	0.093(4)		
16.05	0.0126(6)	15.9	0.035(4)
17.076	0.0139(6)	16.7	0.027(3)

6.3 Clusters, the NCSM and beta-decay

Studies of B(GT) strength in light nuclei are an important testing ground for theoretical nuclear structure calculations, as has been shown *e.g.* for the nucleus ^{11}B [Fuj04b].

The B(GT) transition strengths are an important observable that state-of-the art nuclear structure calculations like *ab initio* calculations (no core shell model, NCSM) or cluster calculations (antisymmetrized molecular dynamics (AMD) or fermionic molecular dynamics (FMD)) must be able to reproduce. The B(GT) strengths also give some insight into the nuclear structure. This will be illustrated here for the ${}^9\text{B}$ case.

Table 6.5: Shell model predictions for the lowest levels in ${}^9\text{B}$. The values are taken from the work of Mikolas *et al.* [Mik88]. Four interactions were considered and are given in this order in the table: Cohen-Kurath CK-2BME [Coh65], Millener [Mik88], Kumar [Kum74] and Cohen-Kurath CK-POT [Coh65].

J^π	$E_x(\text{SM})$ [MeV]	$B(\text{GT}; E_x)$ (SM)	Experiment (present work)
3/2-	0	0.647	B(GT)=0.66(18) $E_x=0$ $J^\pi=3/2-$
	0	0.617	
	0	0.569	
	0	0.603	
5/2-	2.64	0.145	B(GT)=0.241(8) $E_x=2358(7)$ $J^\pi=5/2-$
	3.03	0.177	
	2.43	0.145	
	2.95	0.181	
1/2-	3.02	0.655	B(GT)=0.718(24) $E_x=2730(70)$ $J^\pi=1/2-$
	2.75	0.653	
	3.25	0.651	
	1.79	0.638	
3/2-	5.09	0.243	B(GT)=0.360(12) $E_x=3930(100)$ $J^\pi=(1/2-, 3/2-, 5/2-)$
	4.87	0.292	
	5.49	0.303	
	4.66	0.300	

An immediately obvious feature of the B(GT) strength distribution in ${}^9\text{B}$ (fig. 5.28) is that the B(GT) strengths above 12 MeV excitation energy are one order of magnitude smaller (even two orders of magnitude smaller starting from 14.6 MeV) than the B(GT) strengths of the states with excitation energy 0-4 MeV.

To understand this, it must be remembered that the B(GT) strength is an expression of the action of the $\sigma\tau$ operator, which by its simple form cannot change the spatial shape of the nucleus. The fact that B(GT) strengths to the higher excited energies are strongly suppressed therefore suggests that the states lying in the excitation energy range of the ground states of the $T_z=\pm 3/2$ nuclei ${}^9\text{Li}$ and ${}^9\text{C}$ and above have a different spatial structure. A similar behaviour can be observed in the beta-decays of these $T_z=\pm 3/2$ nuclei to the $T_z=\pm 1/2$ nuclei ${}^9\text{Be}$ and ${}^9\text{B}$ (see figure 6.4). Recent high-precision beta-decay measurements of ${}^9\text{C}(\beta^+){}^9\text{B}$ [Ber01, Pre03, Buc01] and ${}^9\text{Li}(\beta^-){}^9\text{Be}$ [Nym90] clearly show that the transitions from the ground state of these nuclei to the ground states of ${}^9\text{Be}$ and ${}^9\text{B}$ have very weak B(GT) strengths, while transitions to the highly excited

states have very large $B(GT)$ strengths. This is the same effect as the one observed in the $(^3\text{He},t)$ charge exchange reaction, where the transitions between the ground states and states with low excitation energy have large $B(GT)$ strengths whereas the $B(GT)$ strength to states with higher excitation energy above 14 MeV are strongly suppressed. This fact is illustrated in figure 6.5.

The description of states with different spatial structures is a big challenge for the shell model. While standard shell model calculations (see table 6.5) are able to predict quite well the excitation energy and $B(GT)$ strengths of the lowest levels, the higher excitation energies and $B(GT)$ values could not be reproduced.

Recent *ab initio* shell model calculations using a three-body interaction (TNI) [Nav07, For05] have been quite successful in the description of higher excited states in light nuclei. Navratil *et al.* report a $B(GT)$ value for the sharp $T=3/2$ states that is in agreement with our experimental results while the excitation energies only differ by about 800 keV [Nav] (the older shell model calculations underpredicted the excitation energies of these states by around 2 MeV [Mik88]).

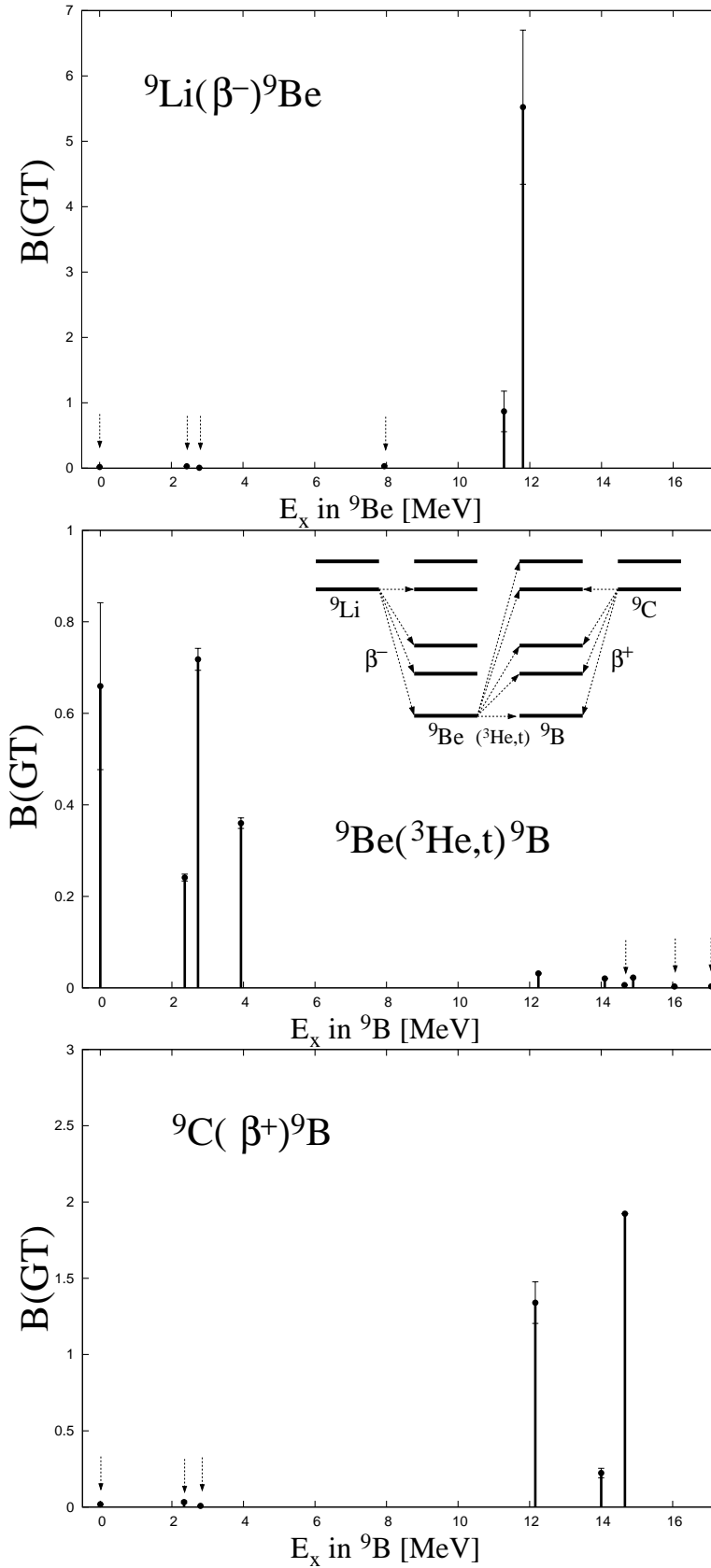


Figure 6.4: Comparison of the $B(\text{GT})$ strengths obtained from ${}^9\text{C}(\beta^+){}^9\text{B}$, ${}^9\text{Be}({}^3\text{He}, t){}^9\text{B}$ and ${}^9\text{Li}(\beta^-){}^9\text{Be}$. The arrows indicate very weak strengths. It can clearly be seen that the states with similar spatial structure are strongly connected by the $\sigma\tau$ operator, whereas transitions to states with different spatial structure are strongly suppressed.

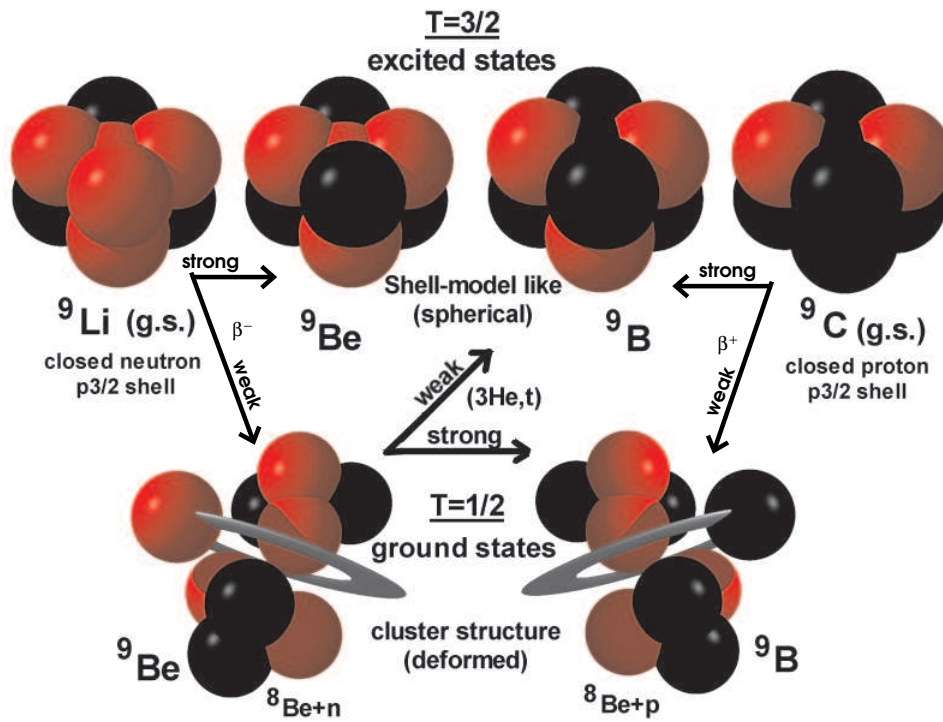


Figure 6.5: Illustration of the spatial shapes in the $A=9$ system and interpretation of the distribution of $B(GT)$ strengths in charge-exchange processes in the $A=9$ system (see fig 6.4). The ground states of ${}^9\text{Li}$ and ${}^9\text{C}$ can be considered spherical or mean-field-like, and have closed $p_{3/2}$ shells, while the ground states of ${}^9\text{Be}$ and ${}^9\text{B}$ are strongly deformed and have a $2\alpha+n$ or $2\alpha+p$ structure. The weak process, mediated by the $\sigma\tau$ operator, only very weakly connects states with different spatial structure.

Chapter 7

Summary

Excited states in the light nuclei ${}^9\text{B}$ and ${}^{13}\text{C}$ were studied using the $({}^3\text{He},t)$ charge-exchange reaction on ${}^9\text{Be}$ and ${}^{13}\text{C}$ targets. The measurements were performed at the research center for nuclear physics (RCNP) in Osaka, Japan, using the magnetic spectrometer GRAND RAIDEN and the dispersive WS course. The ${}^3\text{He}$ beam with an energy of 420 MeV was accelerated by the RCNP Ring Cyclotron.

The GRAND RAIDEN spectrometer and the WS course allow to study the $({}^3\text{He},t)$ charge-exchange reaction with an energy resolution of around 30 keV, which is one order of magnitude better than measurements with the (p,n) charge-exchange reaction. The high resolution allows to better separate individual states and to determine weak excitation strengths because of low background in the spectra. For both the ${}^9\text{Be}$ and the ${}^{13}\text{C}$ targets, excited states could be studied in the charge-exchange reaction with a precision that was previously not available. This made it possible to get more precise and complete information on excitation energies and decay widths of excited states in these nuclei. A total of 19 states in ${}^{13}\text{N}$ were studied, and a total of 20 states were observed in ${}^9\text{B}$. Of these, 9 states in ${}^{13}\text{C}$ and 10 states in ${}^9\text{B}$ were identified as being excited by a Gamow-Teller transition.

Charge-exchange reactions are related to beta-decay, and at zero momentum transfer a simple proportionality exists between the cross-section of the charge-exchange experiment and the Fermi (F) or Gamow-Teller (GT) beta-decay strength. While the Fermi strength $B(F)$ is concentrated in the transition to the isobaric analog state, the Gamow-Teller strength $B(GT)$ is scattered among the excited states. The main aim of the present study was to determine the $B(GT)$ strengths in the nuclei ${}^9\text{B}$ and ${}^{13}\text{N}$.

The only charge-exchange study of ${}^9\text{B}$ was made 30 years ago with the (p,n) reaction and a resolution of around 300-400 keV. Many states, especially at high excitation energy, could not be resolved by this study. The present work was able to separate many weakly excited states with small decay width at high excitation energies (12-19 MeV) in ${}^9\text{B}$ and determine the $B(GT)$ strength distribution by using recent high-precision beta-decay data. This was a significant improvement over the (p,n) study which was unable to discern among these states. The results point to a strong difference in spatial structure between the low-lying levels of ${}^9\text{B}$ and the levels with high excitation energy. This result is also corroborated by beta-decay measurements and theoretical calculations.

Furthermore, the decay width and excitation energy information of the highly excited states in ^9B was substantially improved.

The nucleus ^{13}N has last been studied in 2001 using the (p,n) reaction. A $(^3\text{He},t)$ experiment was also performed at the RCNP Osaka a few years ago (2004), however with a lower resolution of around 300 keV. In the present work, the $(^3\text{He},t)$ reaction with high resolution (30 keV) was used to determine the $B(\text{GT})$ strength distribution in ^{13}N . For the first time, the ^{13}N $T=3/2$ state at 15.1 MeV could be separated from the contaminant ^{12}N state which lies at nearly the same excitation energy in the spectrum, allowing a unambiguous calibration of the GT unit cross-section. This calibration allowed a precise determination of $B(\text{GT})$ strengths in ^{13}N which confirms the main results of the (p,n) analysis, but provides results going beyond the (p,n) study because some states and their cross-section could be better isolated owing to the high resolution of the $(^3\text{He},t)$ data and the high target enrichment.

Appendix A

Beam optics

This appendix chapter contains the detailed derivation of equations (2.1),(2.2),(2.3) introduced in 2.4.

A.1 Beam coordinates

A beam line can be idealized as a set of magnetic elements that are placed sequentially at intervals along an (assumed) reference trajectory. This reference trajectory (or central trajectory) is the path of a charged particle produced by the beam source with the design momentum p_0 that is passing through ideal magnets (*i.e.* with no fabrication or positioning errors). As neither the magnetic elements nor the beam source can be assumed to be perfect, a realistic beam is always broadened. The design of the beam line and the tuning of the magnetic parameters can however provide means to ensure *matching* of a dispersed and diffracted beam to the spectrometer to get optimal measuring conditions (*e.g.* a high resolving power).

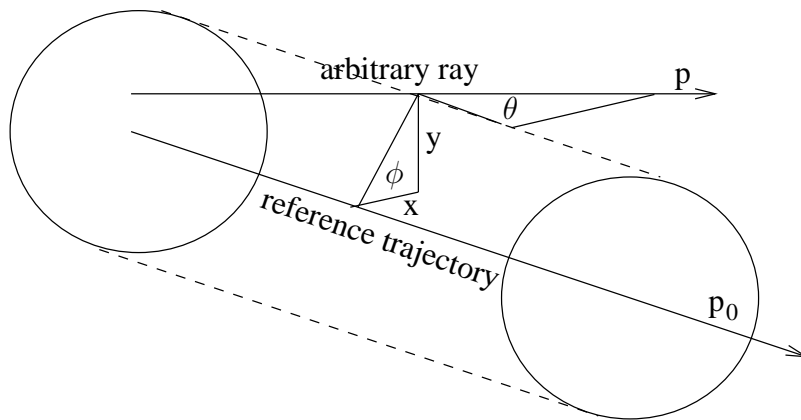


Figure A.1: Geometrical representation of the arbitrary ray with respect to the assumed central beam trajectory and the components of \vec{v} as given in eq. A.1.

For theoretical purposes, we can model the position of a charged particle in the beam

line (following the widely used notations of the computer code TRANSPORT [Car98]) as a vector \vec{v} (that will also be referred to as *ray*) with six components

$$\vec{v} = \begin{pmatrix} x \\ \theta \\ y \\ \phi \\ l \\ \delta \end{pmatrix} \quad (\text{A.1})$$

which are (see illustration in fig. A.1:

- x = the horizontal displacement of the arbitrary ray with respect to the reference trajectory
- θ = the angle between the ray and the reference trajectory in the horizontal plane (horizontal angle)
- y = the vertical displacement of the ray with respect to the reference trajectory
- ϕ = the angle between the ray and the reference trajectory in the vertical plane (vertical angle)
- l = the path length difference between the ray and the central trajectory
- $\delta = \Delta p/p_0$ is the fractional momentum deviation of the ray from the assumed central trajectory.

To be strict, θ and ϕ are not really angles but tangents of angles ($\tan \theta, \tan \phi$) but the difference between an angle and its tangent is of third order for angles close to zero so that they can be referred to as angles. The local coordinate system is shown in fig. A.2.

A.2 Beam transformation

In first order, the action of a magnetic lens on the particle coordinates can be represented by a square matrix R . Taking \vec{v}_0 as initial coordinate vector of the considered particle and \vec{v}_1 as the final (transformed) coordinate vector, the action of a magnet can be described by the equation

$$\vec{v}_1 = R\vec{v}_0 \quad (\text{A.2})$$

The same matrix R can be used for all particles going through the magnet, since they only differ in their initial coordinates \vec{v}_0 .

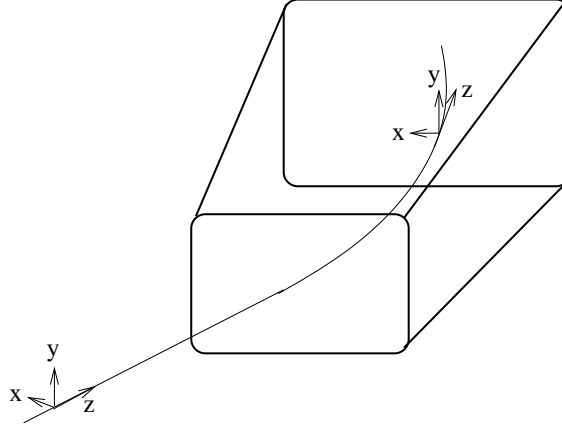


Figure A.2: The local coordinate system shown before and inside a bending magnet. The longitudinal coordinate is marked as z . The distance along the reference trajectory is usually marked as s . In a field-free region, s and z are the same. However, inside a bending magnet, the coordinate s is curvilinear and follows the central trajectory, while z remains rectilinear and is tangent to the central trajectory.

When going through a system of magnets and drift spaces (the beam line), the transforming effects can be cumulated in a single *cumulative transfer matrix* which is the product matrix of the individual transformation matrices:

$$R(t) = R(n)R(n-1) \cdots R(3)R(2)R(1) \quad (\text{A.3})$$

If we now only consider bending magnets acting on the horizontal component of the beam, the 6×6 matrices can be reduced to 3×3 square matrices if we don't consider the path length difference l in our calculations. So let us consider a beam originating from a source point at the beginning of the beam line with components x_0, θ_0, δ_0 . This beam is transported to the target and its components are transformed under the action of the beam line matrix $\hat{B} = (b_{ij})$ and just before hitting the target the ray has the components x_1, θ_1, δ_1 . The energy is not changed inside the beamline, which means that $\delta_1 = \delta_0$. Thus we can write:

$$\begin{pmatrix} x_1 \\ \theta_1 \\ \delta_1 \end{pmatrix} = \begin{pmatrix} b_{11} & b_{12} & b_{13} \\ b_{21} & b_{22} & b_{23} \\ b_{31} & b_{32} & b_{33} \end{pmatrix} \cdot \begin{pmatrix} x_0 \\ \theta_0 \\ \delta_0 \end{pmatrix} = \begin{pmatrix} b_{11} & b_{12} & b_{13} \\ b_{21} & b_{22} & b_{23} \\ 0 & 0 & 1 \end{pmatrix} \cdot \begin{pmatrix} x_0 \\ \theta_0 \\ \delta_0 \end{pmatrix} \quad (\text{A.4})$$

$$= \begin{pmatrix} b_{11}x_0 + b_{12}\theta_0 + b_{13}\delta_0 \\ b_{21}x_0 + b_{22}\theta_0 + b_{23}\delta_0 \\ \delta_0 \end{pmatrix} \quad (\text{A.5})$$

At the target, the beam particles are scattered. Assuming a scattering angle α and a target angle relative to the central ray of the beam of ϕ_T , the horizontal distance of a scattered non-central ray changes (see fig. A.3) from x_1 to x_2 and the transformation can be easily derived from the figure:

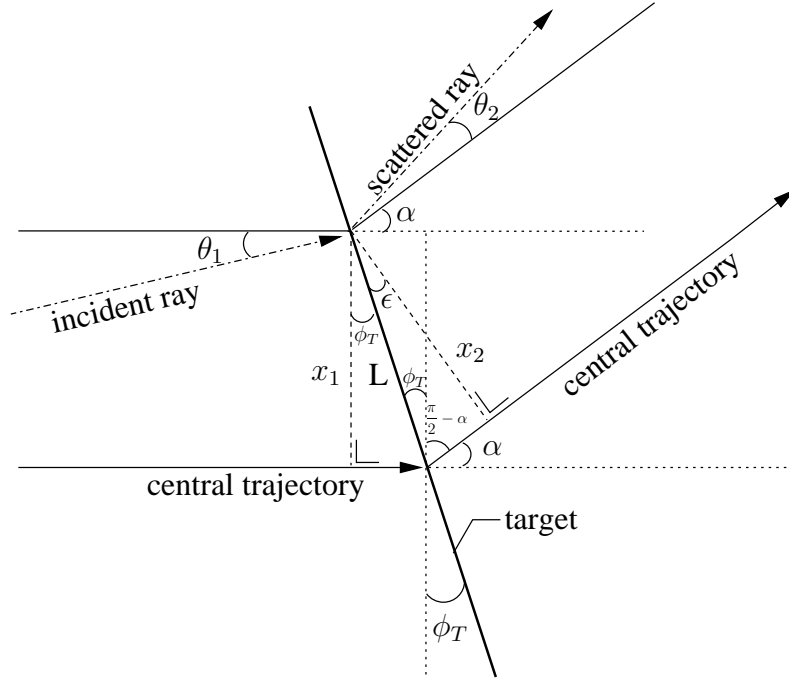


Figure A.3: *Scattering situation at the target in the horizontal plane.*

$$\begin{aligned} L &= \frac{x_1}{\cos \phi_T} = \frac{x_2}{\cos \epsilon} \implies \epsilon = \alpha - \phi_T ; x_2 = \frac{\cos(\alpha - \phi_T)}{\cos \phi_T} x_1 \\ \pi &= \frac{\pi}{2} - \alpha + \phi_T + \frac{\pi}{2} + \epsilon \end{aligned} \quad (\text{A.6})$$

The factor transforming the horizontal displacement of the ray at the target is called *target function* and will be called T . Thus, we already have the transformation of the first coordinate of the ray at the target:

$$x_2 = T \cdot x_1 = \frac{\cos(\alpha - \phi_T)}{\cos \phi_T} x_1 \quad (\text{A.7})$$

The transformation of the horizontal angle can also easily be derived from fig. A.3. The incident beam has a horizontal angle θ_1 relative to the central trajectory. The scattered particle has a relative horizontal angle θ_2 . Introducing the free parameter $\Theta = \theta_2 - \theta_1$ as "effective scattering angle" (the real scattering angle of the non-central ray would be $\alpha + \theta_2 - \theta_1$) [Fuj97], we get

$$\theta_2 = \theta_1 + \Theta \quad (\text{A.8})$$

as transformation for the horizontal angle of the particle ray. The only issue left to consider is the transformation of the fractional momentum deviation δ_1 to δ_2 . In order to calculate it, the following definition can be used:

$$\delta_2 = \frac{\Delta p_{out}}{p_{out}} \quad (\text{A.9})$$

and the differential Δp_{out} (p_{out} depends on the scattering angle α and the incident momentum p_{in}) can then be calculated as

$$\Delta p_{out} = \frac{\partial p_{out}}{\partial \alpha} \Delta \alpha + \frac{\partial p_{out}}{\partial p_{in}} \Delta p_{in} \quad (\text{A.10})$$

Further using the relations $\Delta \alpha = \theta_2 - \theta_1 = \Theta$ (the horizontal angle difference between the scattering angle of the central trajectory and the scattering angle of the non-central ray) and $\Delta p_{in} = p_{in} \cdot \delta_1$ (see eq. A.9) we obtain

$$\delta_2 = \frac{1}{p_{out}} \left(\frac{\partial p_{out}}{\partial \alpha} \Theta + \frac{\partial p_{out}}{\partial p_{in}} p_{in} \delta_1 \right) \quad (\text{A.11})$$

where $\delta_1 = \delta_0$ (eq. A.4). Introducing the *kinematic factor* K and the *relative momentum ratio* C defined as

$$K = \frac{1}{p_{out}} \frac{\partial p_{out}}{\partial \alpha} \quad (\text{A.12})$$

$$C = \frac{p_{in}}{p_{out}} \frac{\partial p_{out}}{\partial p_{in}} \quad (\text{A.13})$$

we can rewrite eq. A.11 as

$$\delta_2 = K\Theta + C\delta_1 \quad (\text{A.14})$$

We now have the transformations for all three components of the ray, and can thus write down the ray components directly after the scattering as a function of the initial coordinates x_0, θ_0, δ_0 :

$$\begin{pmatrix} x_2 \\ \theta_2 \\ \delta_2 \end{pmatrix} = \begin{pmatrix} Tb_{11}x_0 + Tb_{12}\theta_0 + Tb_{13}\delta_0 \\ b_{21}x_0 + b_{22}\theta_0 + b_{23}\delta_0 + \Theta \\ K\Theta + C\delta_0 \end{pmatrix} \quad (\text{A.15})$$

The last transformation is the beam trajectory inside the magnetic spectrograph, which we will describe by the matrix \hat{S} (once again the energy of the beam is not changed here, so $s_{31} = s_{32} = 0$ and $s_{33} = 1$). The end coordinates of the ray on the focal plane of the detector are defined as x, θ, δ . The transformation gives:

$$\begin{pmatrix} x \\ \theta \\ \delta \end{pmatrix} = \begin{pmatrix} s_{11} & s_{12} & s_{13} \\ s_{21} & s_{22} & s_{23} \\ 0 & 0 & 1 \end{pmatrix} \cdot \begin{pmatrix} Tb_{11}x_0 + Tb_{12}\theta_0 + Tb_{13}\delta_0 \\ b_{21}x_0 + b_{22}\theta_0 + b_{23}\delta_0 + \Theta \\ K\Theta + C\delta_0 \end{pmatrix} = \quad (\text{A.16})$$

$$\begin{pmatrix} x_0(s_{11}b_{11}T + s_{12}b_{21}) + \theta_0(s_{11}b_{12}T + s_{12}b_{22}) + \delta_0(s_{11}b_{13}T + s_{12}b_{23} + s_{13}C) + \Theta(s_{12} + s_{13}K) \\ x_0(s_{21}b_{11}T + s_{22}b_{21}) + \theta_0(s_{21}b_{12}T + s_{22}b_{22}) + \delta_0(s_{21}b_{13}T + s_{22}b_{23} + s_{23}C) + \Theta(s_{22} + s_{23}K) \\ K\Theta + C\delta_0 \end{pmatrix} \quad (\text{A.17})$$

The end result at the focal plane is thus

$$\begin{aligned}
 x_{fp} &= x_0 (s_{11}b_{11}T + s_{12}b_{21}) \\
 &+ \theta_0 (s_{11}b_{12}T + s_{12}b_{22}) \\
 &+ \delta_0 (s_{11}b_{13}T + s_{12}b_{23} + s_{13}C) \\
 &+ \Theta (s_{12} + s_{13}K)
 \end{aligned} \tag{A.18}$$

$$\begin{aligned}
 \theta_{fp} &= x_0 (s_{21}b_{11}T + s_{22}b_{21}) \\
 &+ \theta_0 (s_{21}b_{12}T + s_{22}b_{22}) \\
 &+ \delta_0 (s_{21}b_{13}T + s_{22}b_{23} + s_{23}C) \\
 &+ \Theta (s_{22} + s_{23}K)
 \end{aligned} \tag{A.19}$$

$$\delta_{fp} = \delta_2 = K\Theta + C\delta_0 \tag{A.20}$$

Appendix B

Angular calibration procedure

The following chapter describes in detail the calibration procedure to obtain a good definition of the scattering angle, as well as spectra with a high energy-resolution, which was briefly summarized in chapter 3. It is structured in two parts, which follow the chronological order of the data processing: first the reconstruction of the scattering angle using a multi-hole slit (sieve), then the correction of higher-order aberrations and the correction of the spectra.

B.1 Reconstruction of the scattering angle

In order to obtain a high-resolution spectrum for the reaction at 0° scattering angle, the scattering angles θ_{tgt} and ϕ_{tgt} at the target have to be reconstructed from the focal plane observables θ_{fp} and y_{fp} . A good way to achieve this is the *sieve slit technique* using the *over-focus mode* of the Grand Raiden spectrometer [Fuj01]. A multi-hole slit with well-known metrics is placed behind the target and a spectrum is recorded. The deformed image of the sieve slit is then used to obtain the correct scattering angles for the raytraced events. The procedure will be explained in detail in this section.

The deformation of the original sieve image is a function of several variables. The deformation depends on the x-position at the focal plane, as well as the angle coordinates θ_{fp} and y_{fp} at the focal plane. For the correction method described here, we will assume that

$$\phi_{tgt} = \phi_{tgt}(y_{fp}, \theta_{fp}, x_{fp}) = \sum_{i=0}^3 \sum_{j=0}^3 \sum_{k=0}^1 a_{ijk} x_{fp}^i \theta_{fp}^j y_{fp}^k \quad (\text{B.1})$$

$$\theta_{tgt} = \theta_{tgt}(y_{fp}, \theta_{fp}, x_{fp}) = \sum_{i=0}^2 \sum_{j=0}^4 \sum_{k=0}^2 b_{ijk} x_{fp}^i y_{fp}^j \theta_{fp}^k \quad (\text{B.2})$$

which requires 77 parameters in total to reconstruct the scattering angles (32 parameters for the vertical scattering angle and 45 parameters for the horizontal scattering

angle). This number may seem large, but consider that approximately 40 hole images of the sieve slit can be seen at the focal plane for each focal plane position. Since sieve slit images were taken for ten different regions at the focal plane, this gives a total amount of roughly 400 data points which have to be fitted in order to reconstruct the scattering angles at the target. The following sections will explain in detail how the parameters in equations (B.1) and (B.2) were derived.

The first step requires to obtain the “distorted” images of the sieve slit for various x_{fp} positions at the focal plane. Nine such images were obtained for different x-regions as shown in fig. B.1.

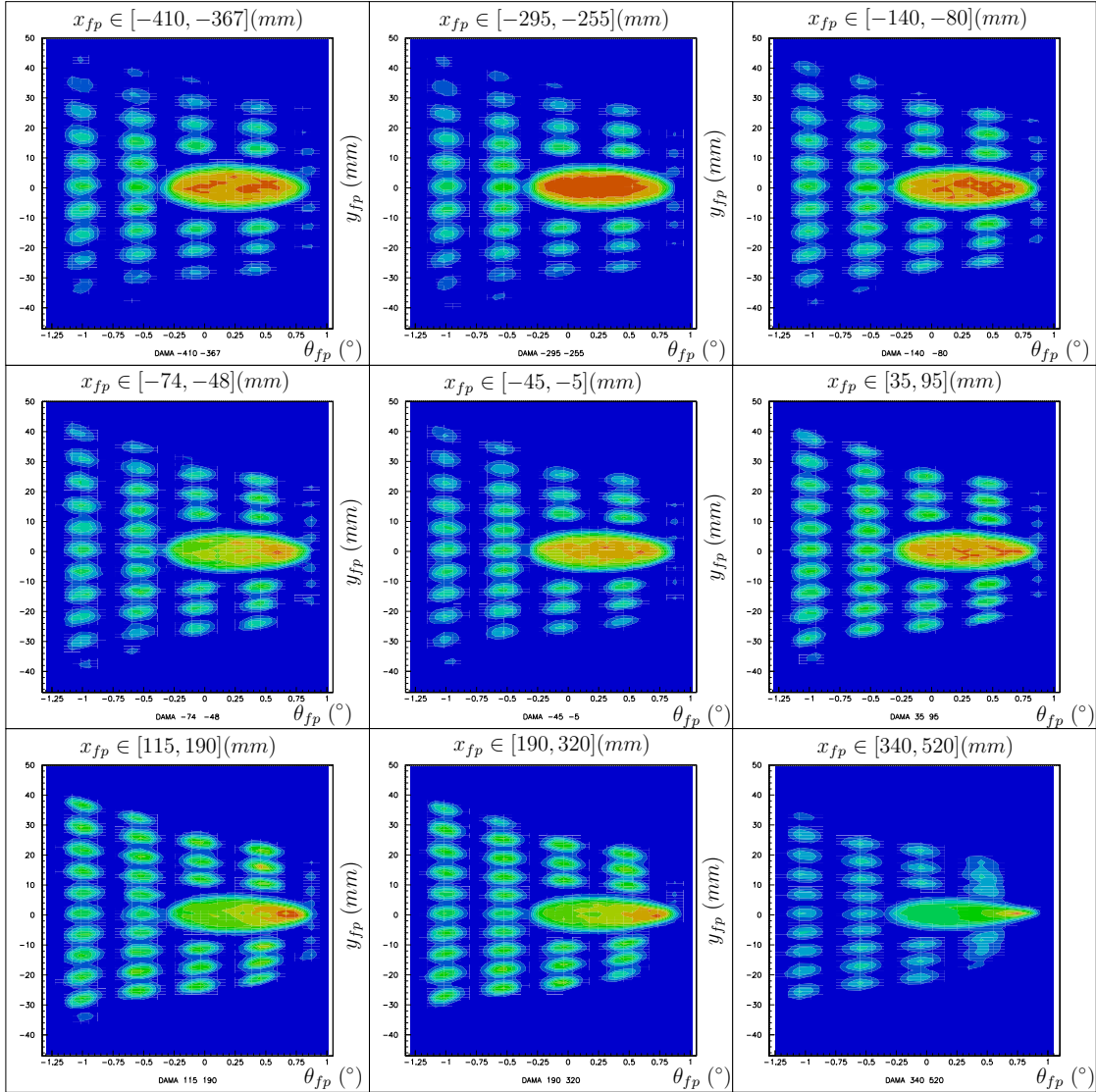


Figure B.1: Images of the sieve slit at nine different x-positions at the focal plane. These images were used to reconstruct the scattering angles θ_{tgt} and ϕ_{tgt} at the target from the focal plane observables via the known dimensions of the sieve.

These images, which show a θ_{fp} vs y_{fp} plot of triton events, can subsequently be sliced in “rows” and “columns” to determine the distorted positions of the original θ_{tgt} and ϕ_{tgt} coordinates.

B.1.1 Reconstruction of ϕ_{tgt}

ϕ_{tgt} as a linear function of y_{fp}

To determine the parameters required for the reconstruction of the ϕ_{tgt} angle, the images shown in fig. B.1 are sliced into five “columns”. For the images with the highest x_{fp} values, the fifth column could not always be seen or did not have a sufficient number of events to be used in the fitting procedure. The columns correspond to the θ_{tgt} positions given in table B.1, derived from the positions of the holes in the sieve slit and the target-slit distance of 605.5 mm. For column 5, it was assumed that observed counts only result from particles originating from the parts of the hole closest to the center of the slit, whose horizontal displacement is 9 mm (instead of 10.5 mm if the center of the hole is considered)

Table B.1: θ_{tgt} positions corresponding to the column numbers.

Column	$\theta_{tgt} [^\circ]$
Column 1	-0.993(5)
Column 2	-0.497(5)
Column 3	0.000(5)
Column 4	0.497(5)
Column 5	0.852(5)

For each of the nine x_{fp} -ranges, five columns are projected onto the y_{fp} axis, and the y_{fp} position of the respective peaks is related to the ϕ_{tgt} position corresponding to the respective hole in the sieve slit:

$$\phi_{tgt} = a(\theta_{tgt}, x_{fp})y_{fp} + b(\theta_{tgt}, x_{fp}) \quad (\text{B.3})$$

with a and b depending on the x-position and the column (i.e. the θ -position). The results of the linear fit are summarized in table B.2, and the details of the individual projections are shown in the figures B.3-B.11.

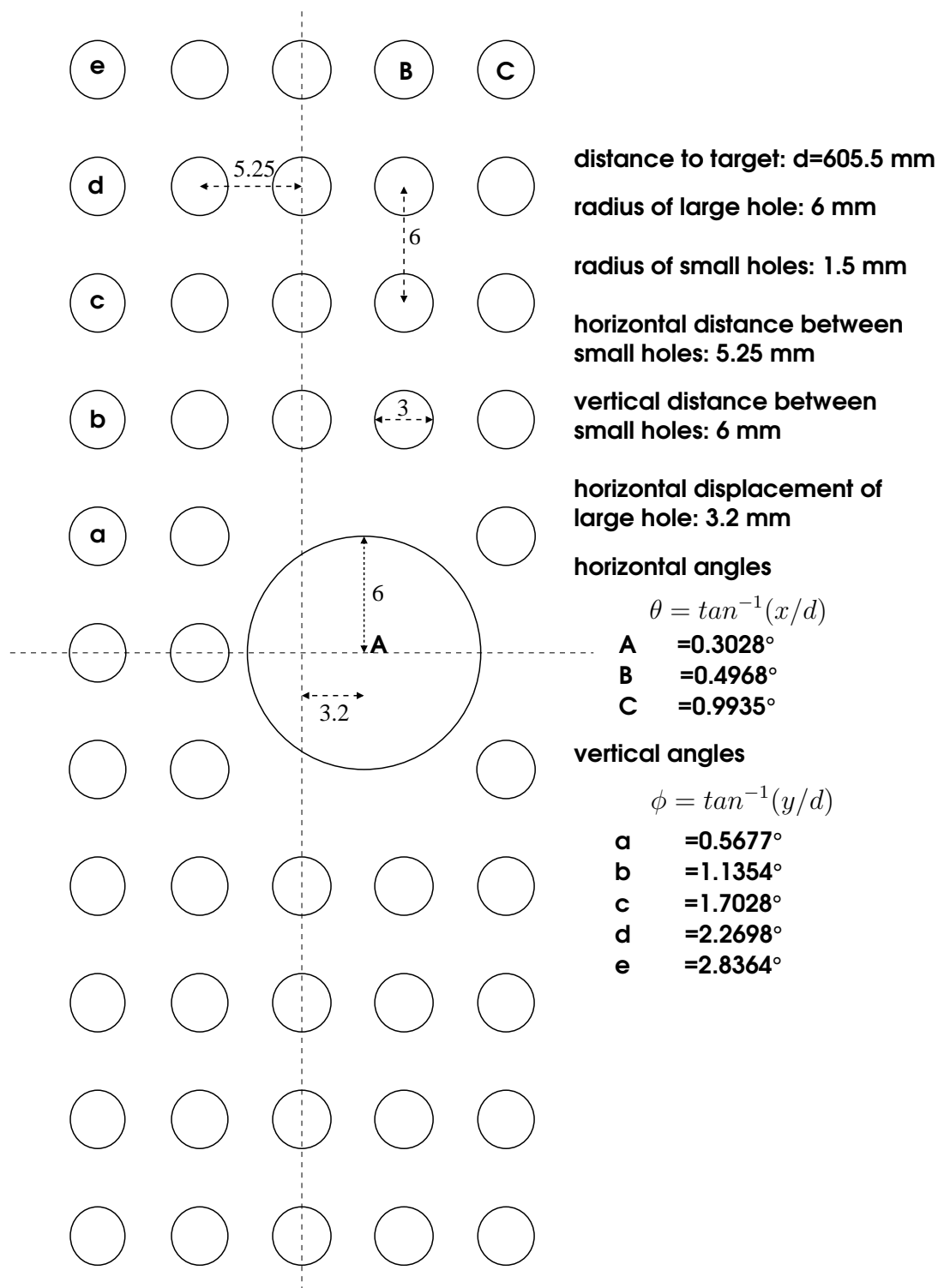


Figure B.2: Dimensions of the sieve slit. The large hole in the center is asymmetrically installed at a horizontal distance of 3.2 mm. The placement of the smaller holes is symmetric and all have the same horizontal and vertical spacing (except around the large hole). Horizontal and vertical angles resulting from a target-slit distance of 605.5 mm are given in the picture.

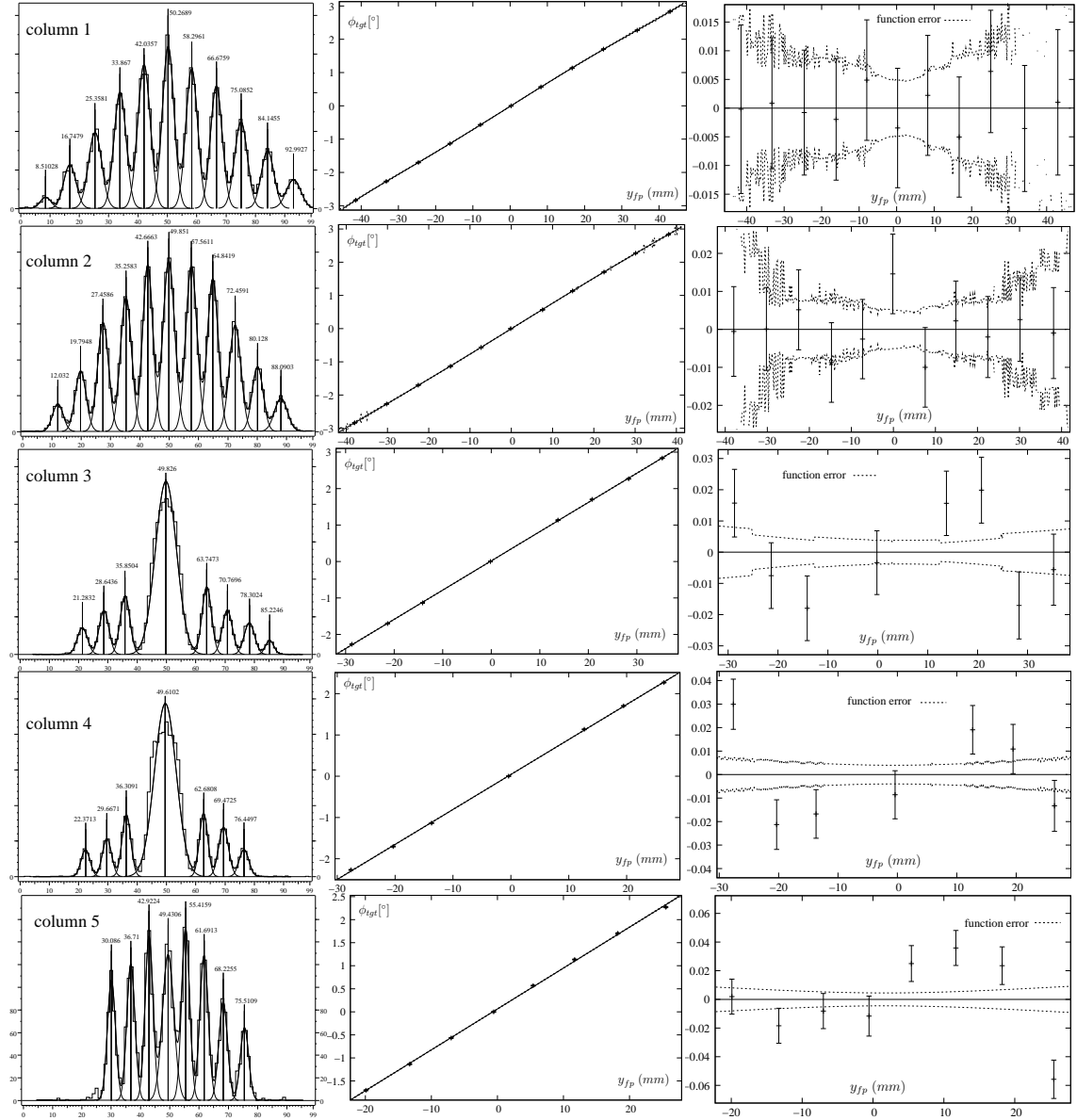


Figure B.3: Projections of all five columns for the sieve slit image at $x_{fp} \in [-410, -367]$ and determination of centroids. The centroids are fitted to their respective original ϕ_{tgt} position using a linear function. The fitted functions are shown along with the residuum of the fit.

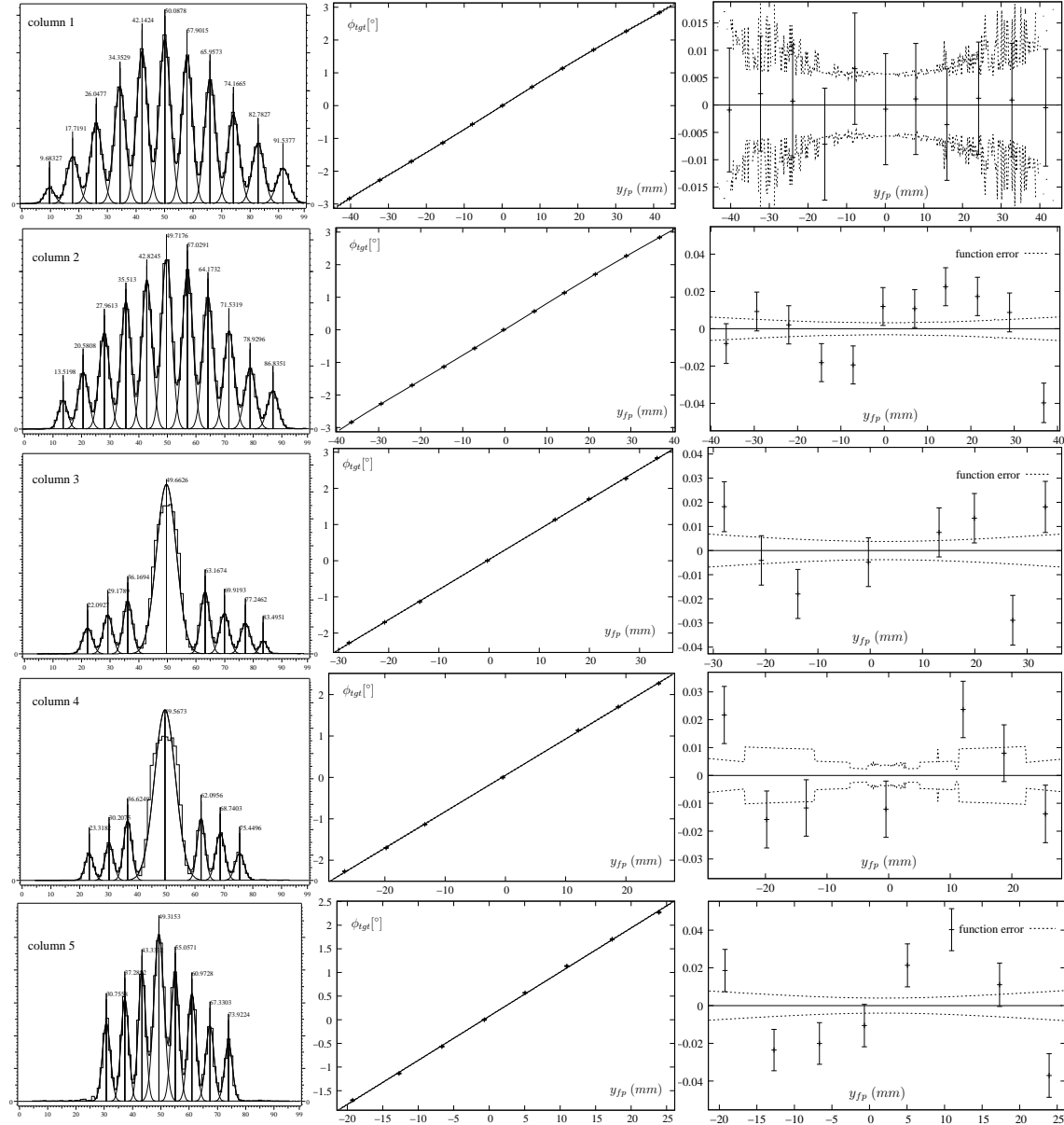


Figure B.4: Projections of all five columns for the sieve slit image at $x_{fp} \in [-295, -255]$ and determination of centroids. The centroids are fitted to their respective original ϕ_{tgt} position using a linear function. The fitted functions are shown along with the residuum of the fit.

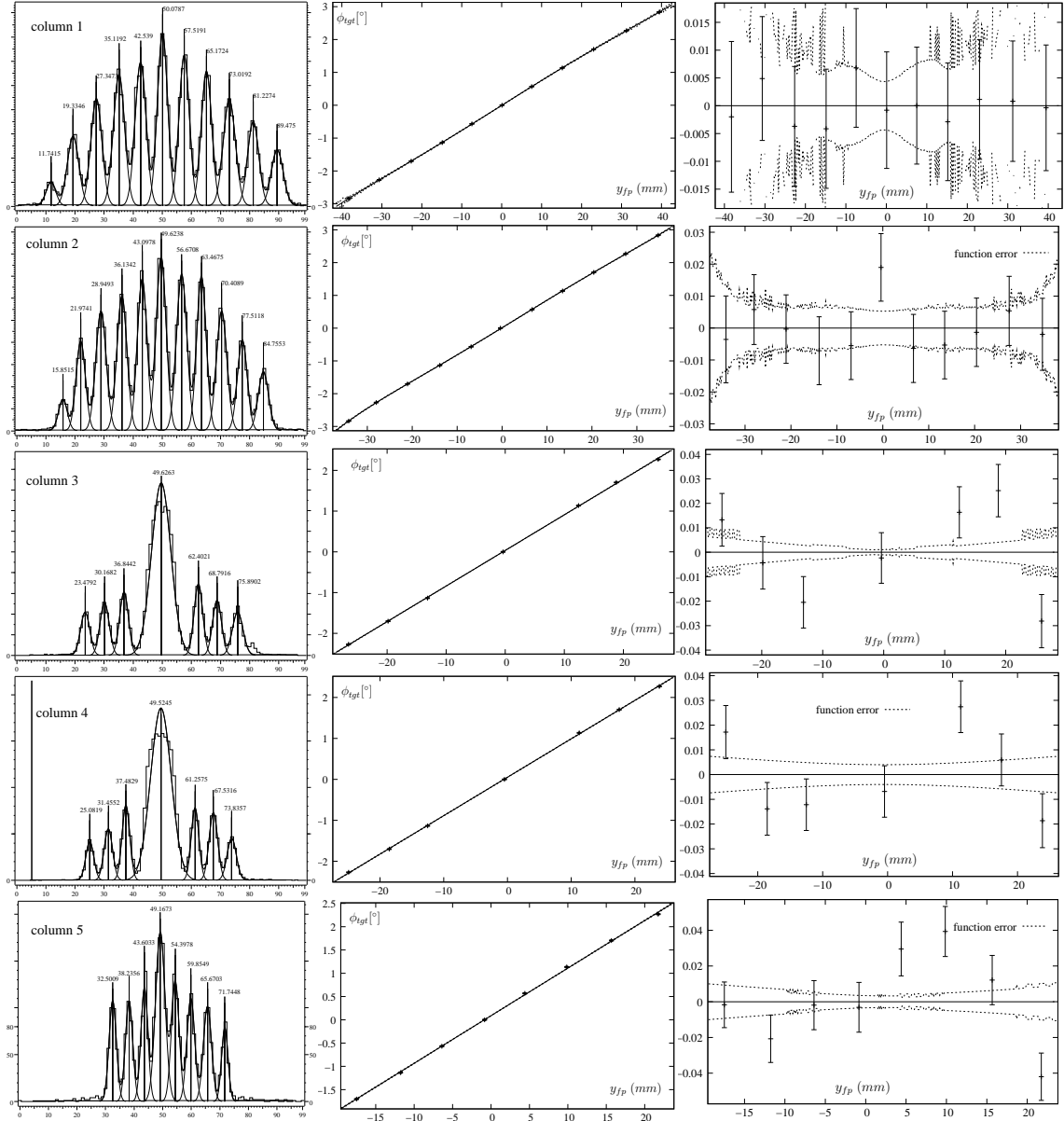


Figure B.5: Projections of all five columns for the sieve slit image at $x_{fp} \in [-140, -80]$ and determination of centroids. The centroids are fitted to their respective original ϕ_{tgt} position using a linear function. The fitted functions are shown along with the residuum of the fit.

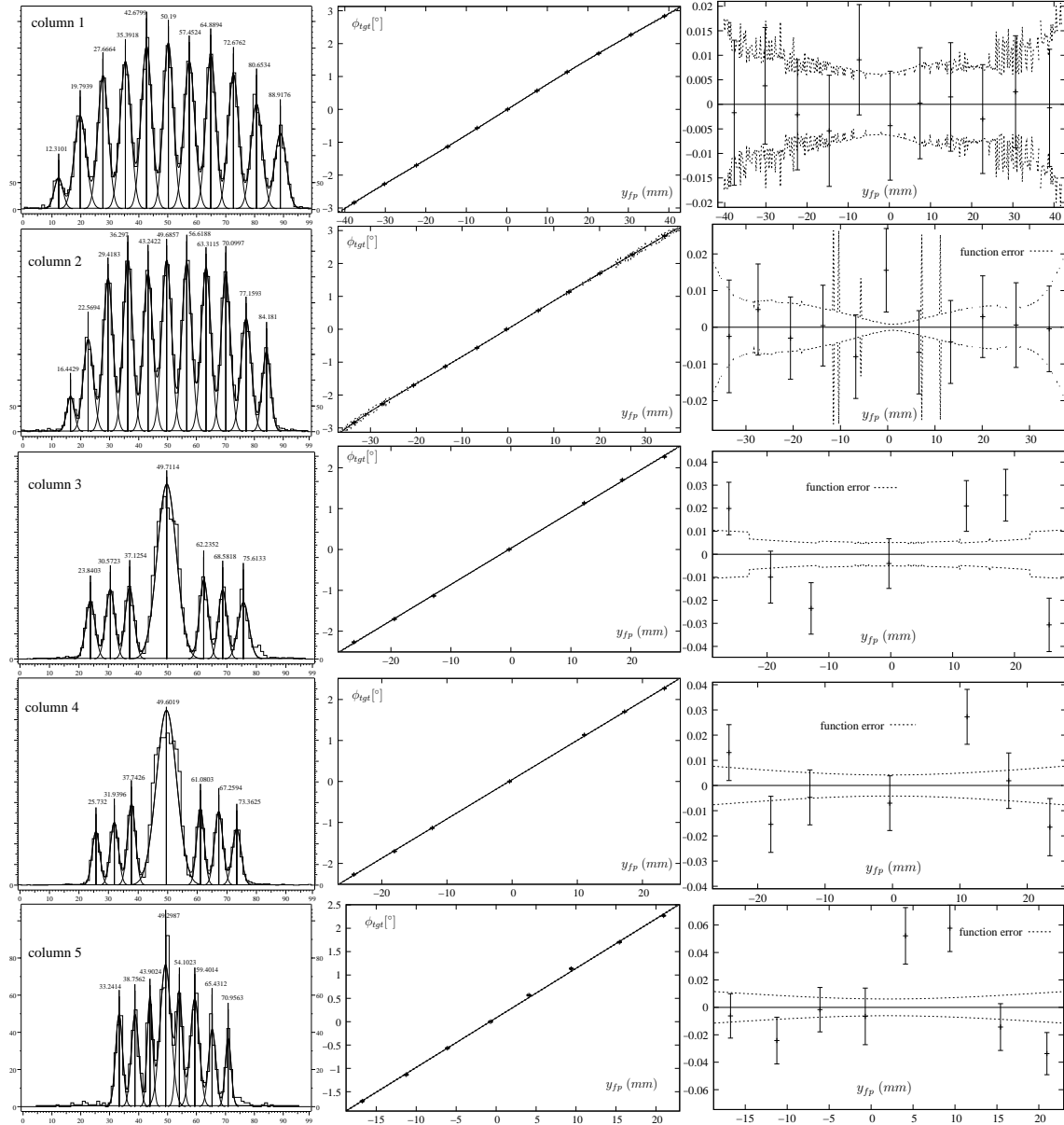


Figure B.6: Projections of all five columns for the sieve slit image at $x_{fp} \in [-74, -48]$ and determination of centroids. The centroids are fitted to their respective original ϕ_{tgt} position using a linear function. The fitted functions are shown along with the residuum of the fit.

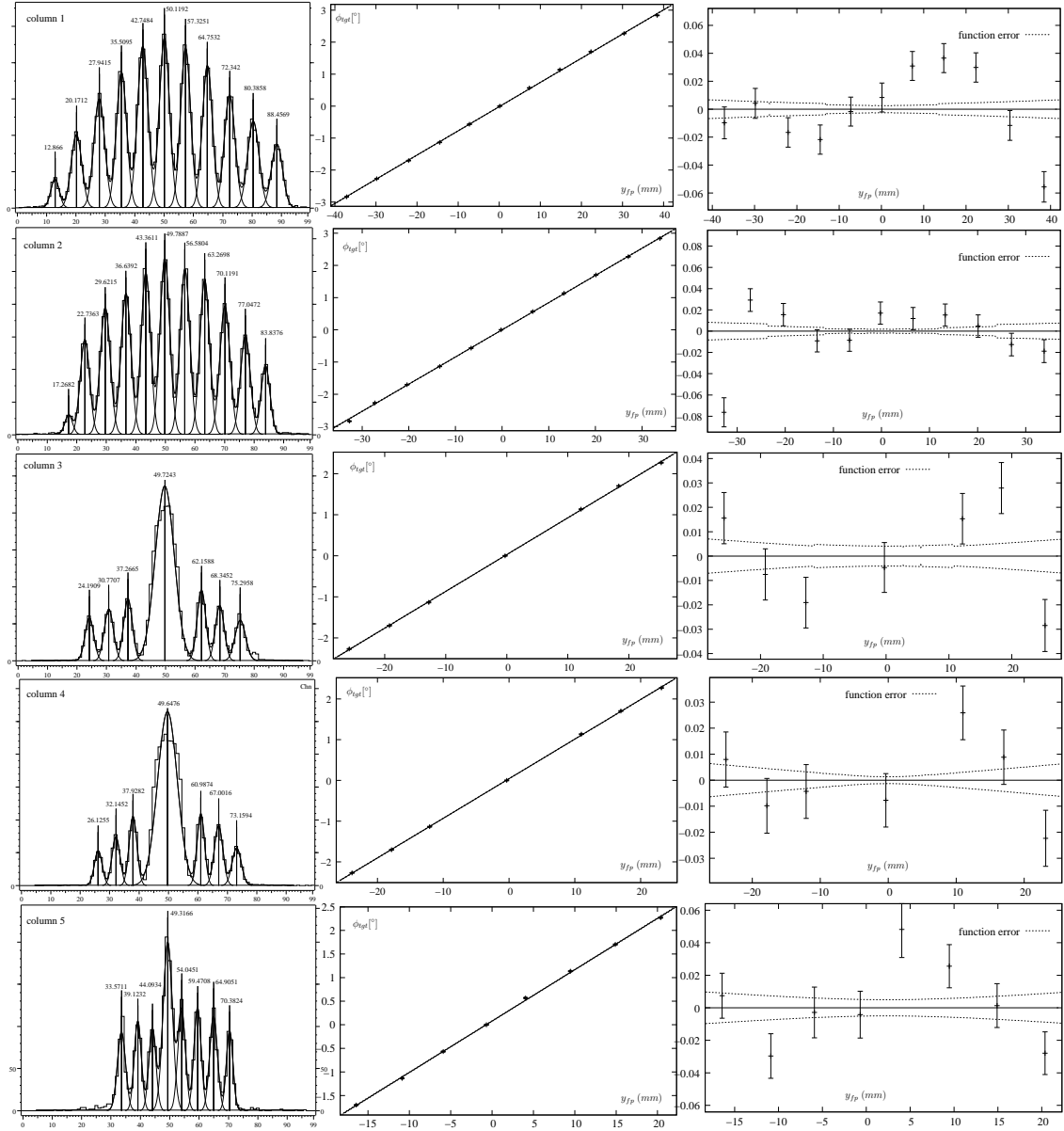


Figure B.7: Projections of all five columns for the sieve slit image at $x_{fp} \in [-45, -5]$ and determination of centroids. The centroids are fitted to their respective original ϕ_{tgt} position using a linear function. The fitted functions are shown along with the residuum of the fit.

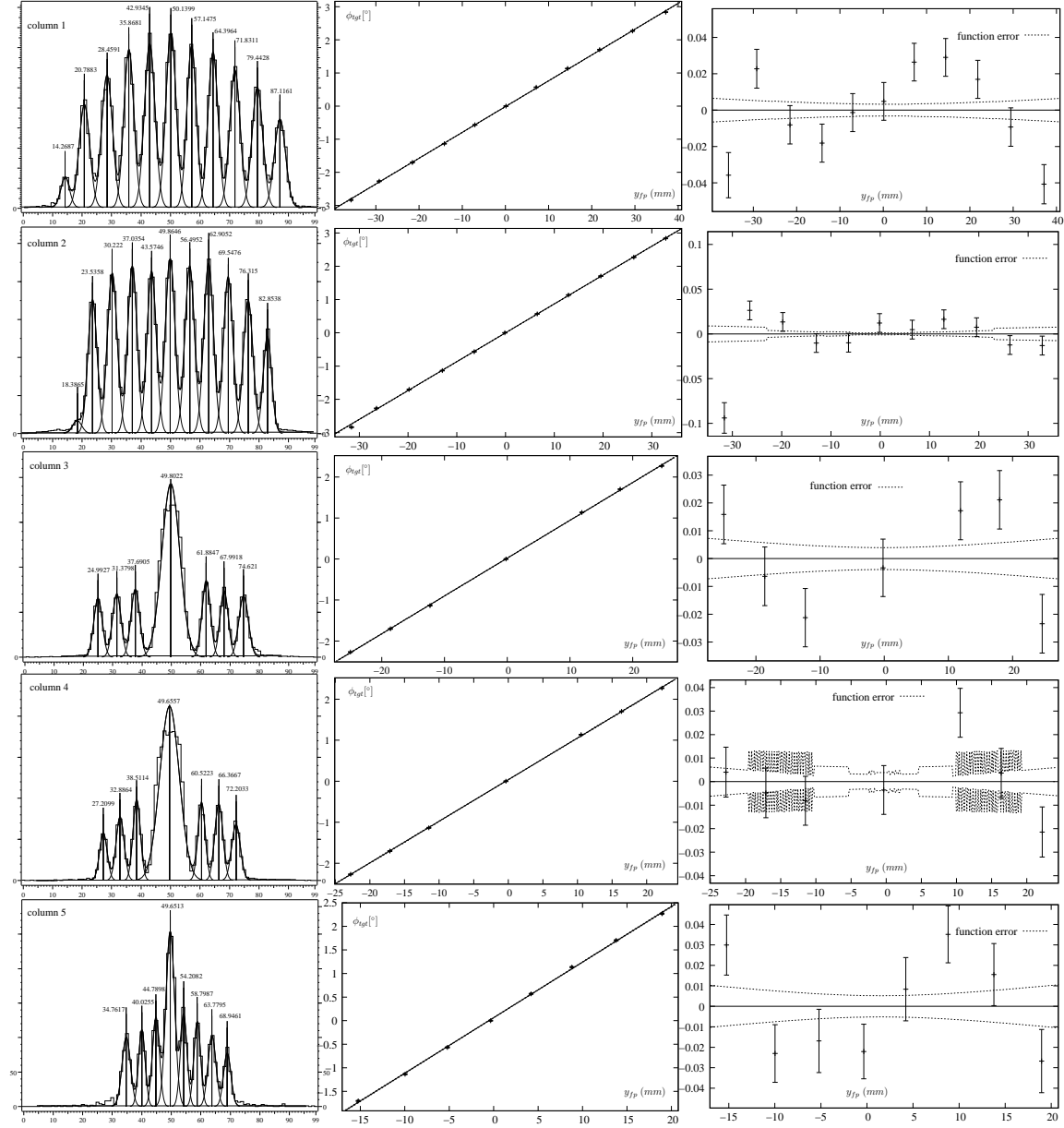


Figure B.8: Projections of all five columns for the sieve slit image at $x_{fp} \in [35, 95]$ and determination of centroids. The centroids are fitted to their respective original ϕ_{tgt} position using a linear function. The fitted functions are shown along with the residuum of the fit.

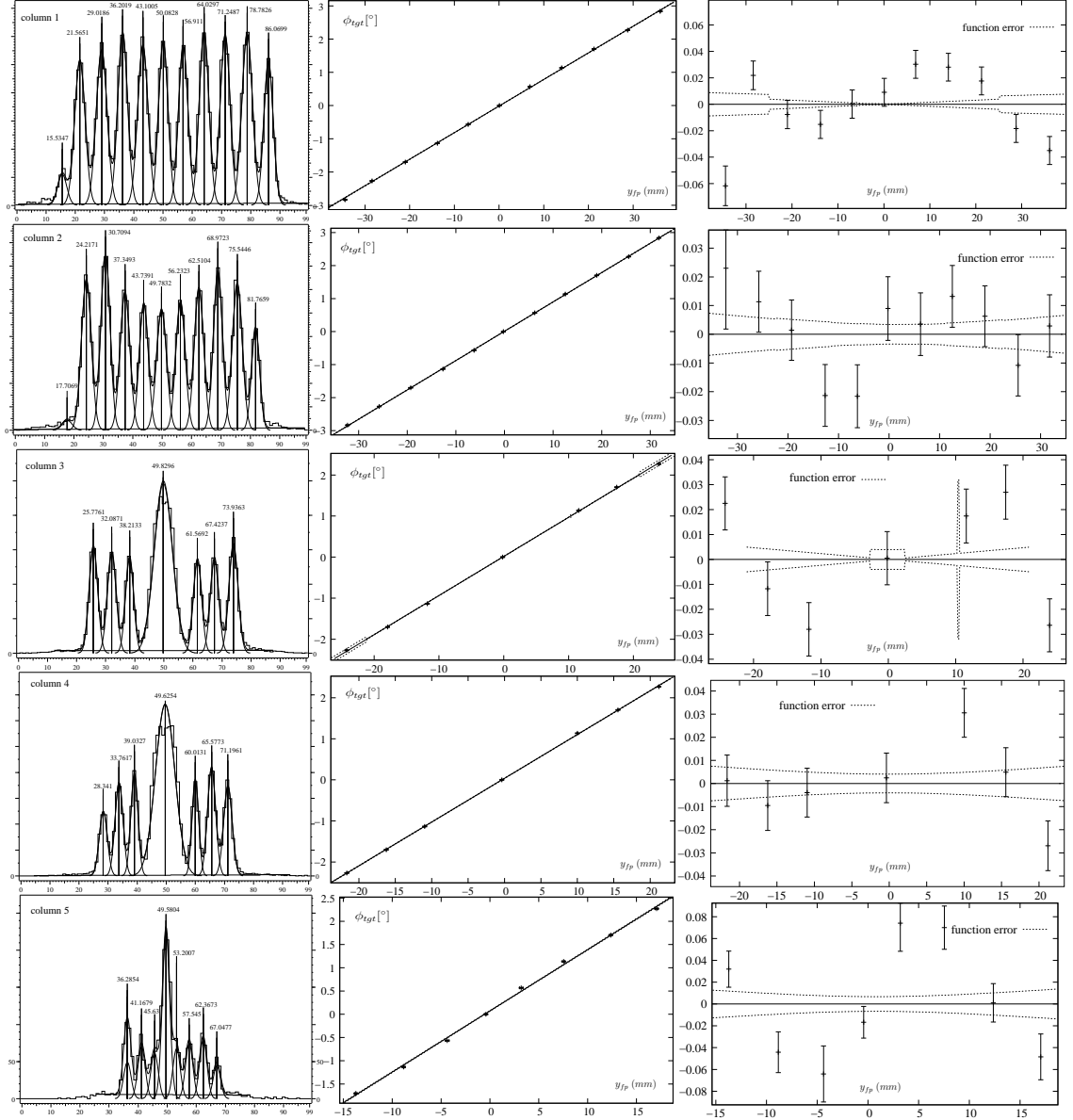


Figure B.9: Projections of all five columns for the sieve slit image at $x_{fp} \in [115, 190]$ and determination of centroids. The centroids are fitted to their respective original ϕ_{tgt} position using a linear function. The fitted functions are shown along with the residuum of the fit.

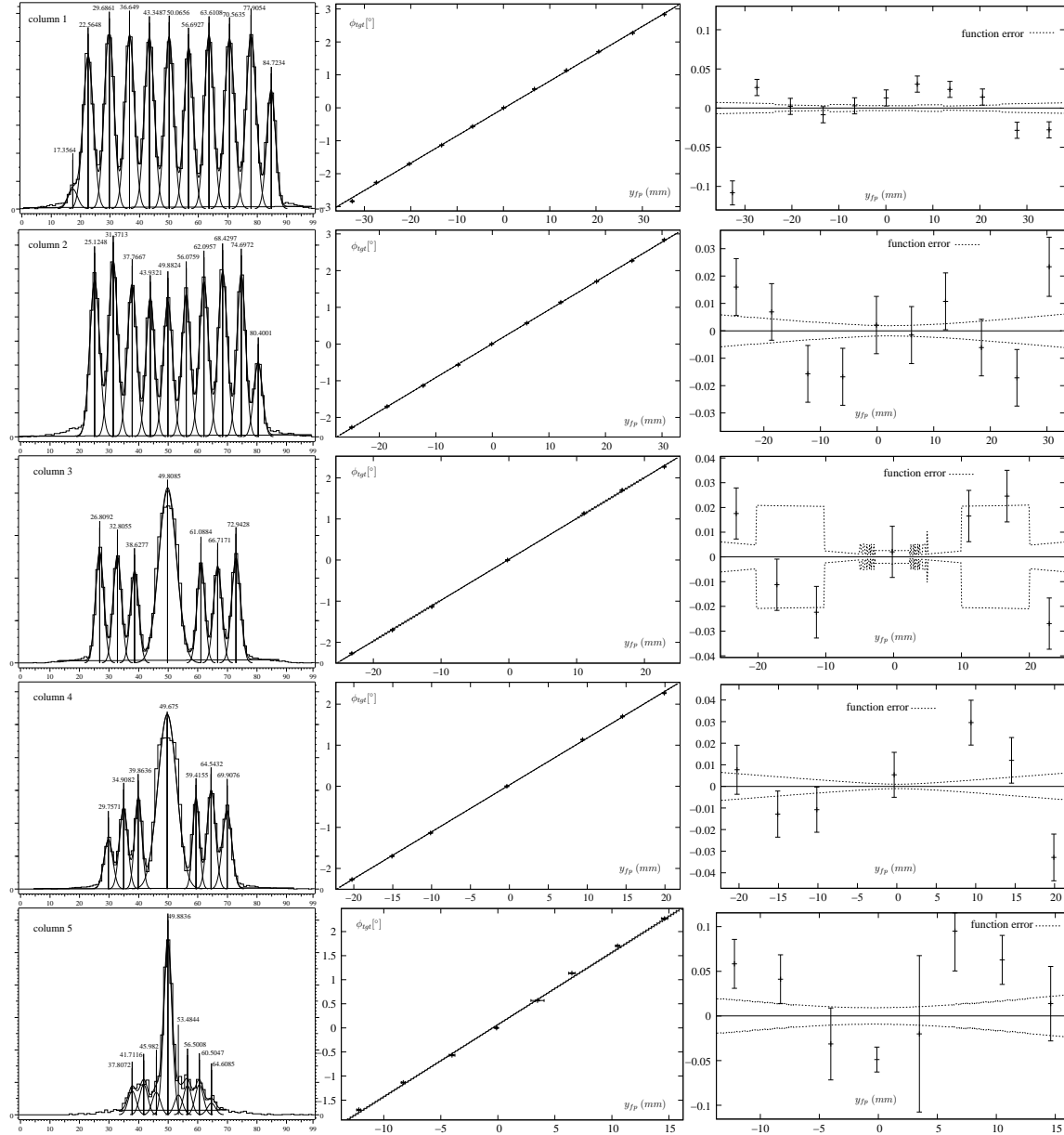


Figure B.10: Projections of all five columns for the sieve slit image at $x_{fp} \in [190, 320]$ and determination of centroids. The centroids are fitted to their respective original ϕ_{tgt} position using a linear function. The fitted functions are shown along with the residuum of the fit.

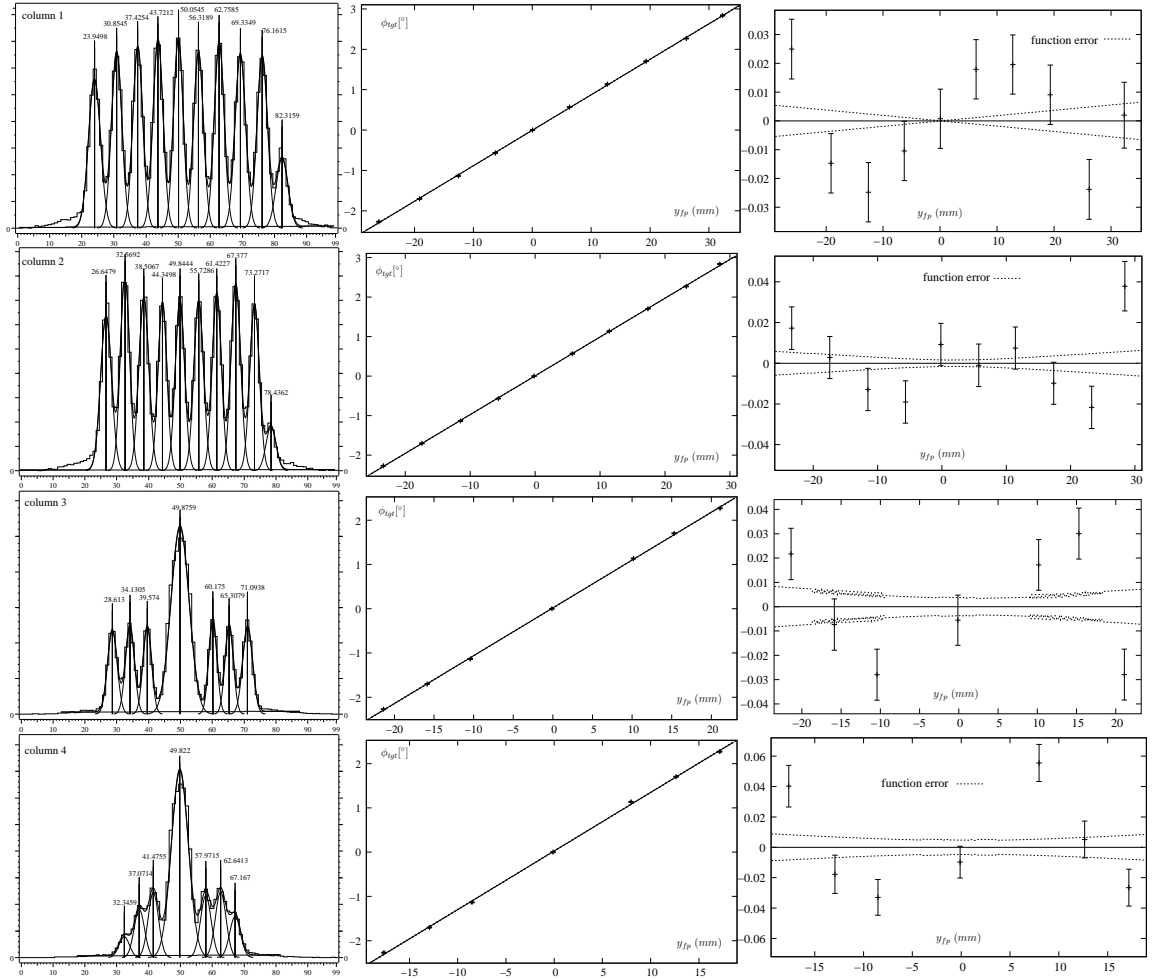


Figure B.11: Projections of the first four columns for the sieve slit image at $x_{fp} \in [340, 520]$ and determination of centroids. The centroids are fitted to their respective original ϕ_{tgt} position using a linear function. The fitted functions are shown along with the residuum of the fit.

Table B.2: Results of the linear fit connecting y_{fp} to original ϕ_{tgt} position via $\phi_{tgt} = ay_{fp} + b$.

Column		$x \in [-410, -367]$	$x \in [-295, -255]$	$x \in [-140, -80]$	$x \in [-74, -48]$	$x \in [-45, -5]$
Col.1	a	.0677(1)	.0699(1)	.0736(1)	.0748(2)	.0757(1)
	b	-.022(4)	-.014(3)	-.016(3)	-.017(3)	-.018(3)
Col.2	a	.0752(1)	.0778(1)	.0821(2)	.0835(2)	.0844(2)
	b	-.001(3)	.010(3)	.014(3)	.009(3)	.001(3)
Col.3	a	.0802(2)	.0832(2)	.0874(2)	.0887(2)	.0897(2)
	b	.017(4)	.033(4)	.035(1)	.030(4)	.029(4)
Col.4	a	.0847(2)	.0878(2)	.0938(2)	.0959(2)	.0972(2)
	b	.042(4)	.050(4)	.051(4)	.045(4)	.042(1)
Col.5	a	.0887(3)	.0933(3)	.1023(4)	.1060(5)	.1089(4)
	b	.062(5)	.074(4)	.088(3)	.081(6)	.079(5)
Column		$x \in [35, 95]$	$x \in [115, 190]$	$x \in [190, 320]$	$x \in [340, 520]$	
Col.1	a	.0779(1)	.0800(2)	.0830(2)	.0879(2)	
	b	-.016(3)	-.015(3)	-.018(3)	-.005(1)	
Col.2	a	.0889(2)	.0922(2)	.0982(2)	.0982(2)	
	b	-.000(3)	.010(2)	.009(2)	.006(2)	
Col.3	a	.0923(2)	.0953(2)	.0994(2)	.1080(3)	
	b	.022(4)	.016(4)	.017(4)	.019(4)	
Col.4	a	.1015(3)	.1066(3)	.1141(3)	.1323(4)	
	b	.039(2)	.038(4)	.032(4)	.025(1)	
Col.5	a	.1179(5)	.1227(65)	.126(9)	.140(15)	
	b	.063(5)	.05(1)	.05(1)	.05(1)	

Parameters of the linear function as a function of θ_{tgt}

The parameters $a(\theta_{tgt}, x_{fp})$ and $b(\theta_{tgt}, x_{fp})$ derived as in table B.2 were subsequently fitted for each x_{fp} region as a function of θ_{tgt} . The different columns of the sieve slit images correspond to specific θ_{tgt} values as given in table B.1. The parameters were fitted as third-order polynomial functions of θ_{tgt} :

$$a(\theta_{tgt}, x_{fp}) = \alpha_a(x_{fp}) + \beta_a(x_{fp})\theta_{tgt} + \gamma_a(x_{fp})\theta_{tgt}^2 + \delta_a(x_{fp})\theta_{tgt}^3 \quad (\text{B.4})$$

$$b(\theta_{tgt}, x_{fp}) = \alpha_b(x_{fp}) + \beta_b(x_{fp})\theta_{tgt} + \gamma_b(x_{fp})\theta_{tgt}^2 + \delta_b(x_{fp})\theta_{tgt}^3 \quad (\text{B.5})$$

where the fitted parameters $\alpha_{a,b}$, $\beta_{a,b}$, $\gamma_{a,b}$ and $\delta_{a,b}$ still depend on the focal plane position x_{fp} . The results of the fit are summarized in table B.3, and the details of the individual fits are shown in the figures B.12-B.20.

Table B.3: Results of the fit of $a(\theta_{tgt}, x_{fp})$ and $b(\theta_{tgt}, x_{fp})$ as a function of θ_{tgt} for different x_{fp} positions.

x_{fp}	α_a	β_a	γ_a	δ_a
-386(5)	0.0802(1)	0.0089(15)	-0.0010(3)	0.0026(23)
-273(4)	0.0830(2)	0.0092(3)	-0.0001(4)	0.0040(4)
-107(2)	0.0873(2)	0.0102(4)	0.0029(4)	0.0066(6)
-54(3)	0.0886(2)	0.0105(4)	0.0047(5)	0.0082(6)
-23(3)	0.0895(2)	0.0108(4)	0.0059(5)	0.0091(7)
69(5)	0.0919(2)	0.0121(5)	0.0103(5)	0.0123(7)
157(5)	0.0952(2)	0.0154(19)	0.0100(12)	0.0100(13)
274(7)	0.0994(3)	0.0187(5)	0.0152(13)	0.0130(14)
430(15)	0.1081(3)	0.0293(6)	0.0289(18)	0.0200(18)
x_{fp}	α_b	β_b	γ_b	δ_b
-386(5)	0.018(3)	0.041(7)	0.007(6)	0.007(10)
-273(4)	0.031(3)	0.038(7)	0.005(5)	0.011(9)
-107(2)	0.035(1)	0.033(7)	0.009(3)	0.028(9)
-54(3)	0.026(3)	0.032(8)	0.013(7)	0.025(11)
-23(3)	0.020(2)	0.033(5)	0.017(6)	0.023(8)
69(5)	0.018(2)	0.036(6)	0.010(6)	0.008(9)
157(5)	0.020(3)	0.019(6)	0.008(9)	0.025(1)
274(7)	0.018(3)	0.015(6)	0.005(9)	0.027(11)
430(15)	0.014(2)	0.016(4)	0.008(9)	0.011(10)

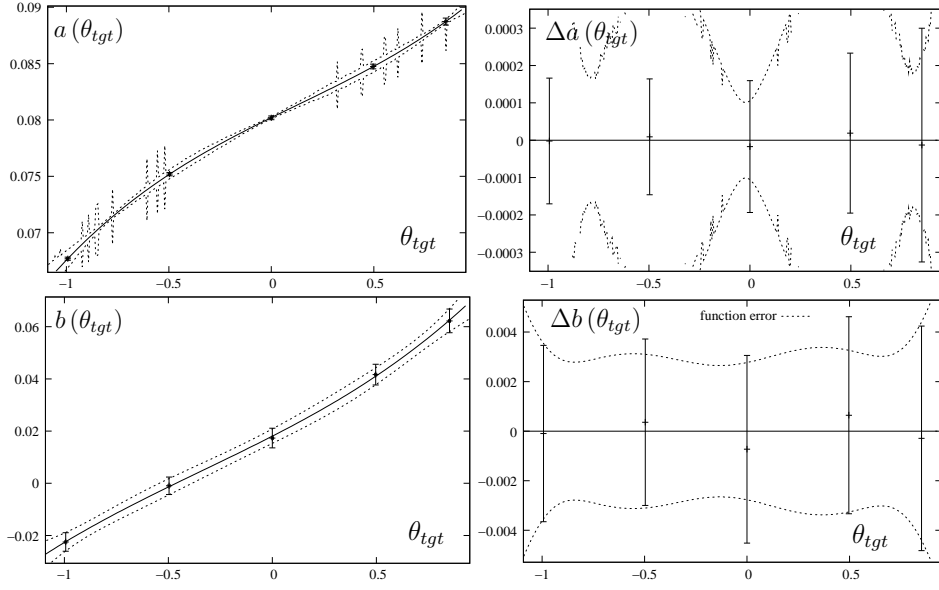


Figure B.12: Third-order polynomial fit as a function of θ for the linear parameters a and b of the $\phi_{tgt} = a y_{fp} + b$ relation for the sieve slit image at $x_{fp} \in [-410, -367]$. The fitted functions are shown along with the residuum of the fit.

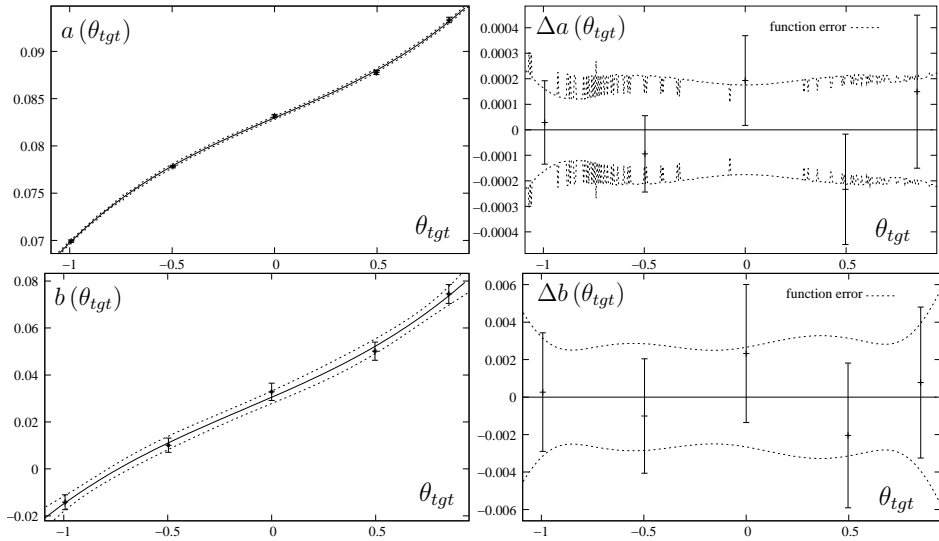


Figure B.13: Third-order polynomial fit as a function of θ for the linear parameters a and b of the $\phi_{tgt} = a y_{fp} + b$ relation for the sieve slit image at $x_{fp} \in [-295, -255]$. The fitted functions are shown along with the residuum of the fit.

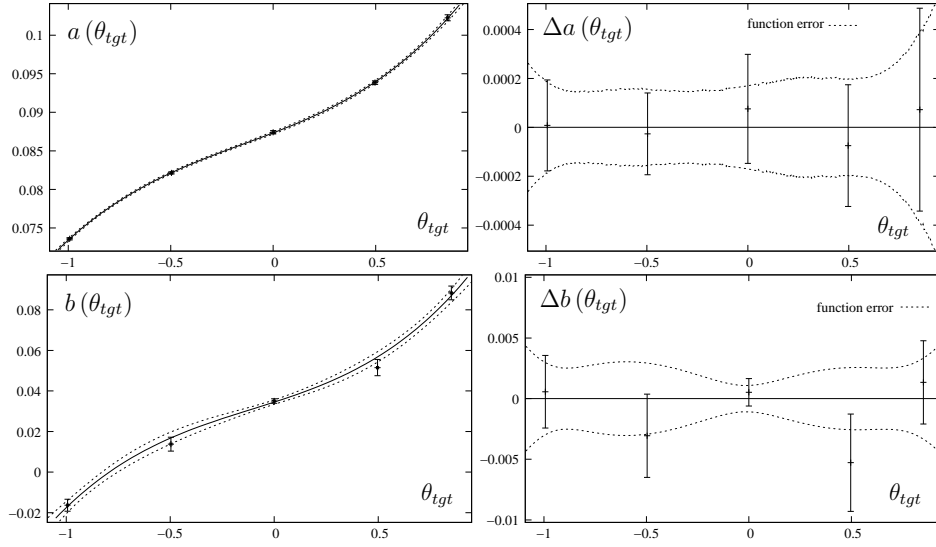


Figure B.14: Third-order polynomial fit as a function of θ for the linear parameters a and b of the $\phi_{tgt} = a y_{fp} + b$ relation for the sieve slit image at $x_{fp} \in [-140, -80]$. The fitted functions are shown along with the residuum of the fit.

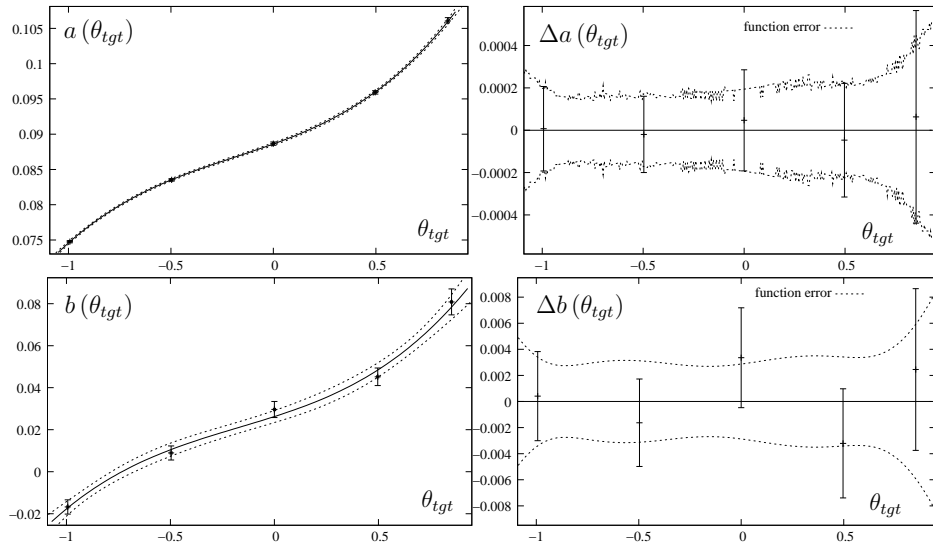


Figure B.15: Third-order polynomial fit as a function of θ for the linear parameters a and b of the $\phi_{tgt} = a y_{fp} + b$ relation for the sieve slit image at $x_{fp} \in [-74, -48]$. The fitted functions are shown along with the residuum of the fit.

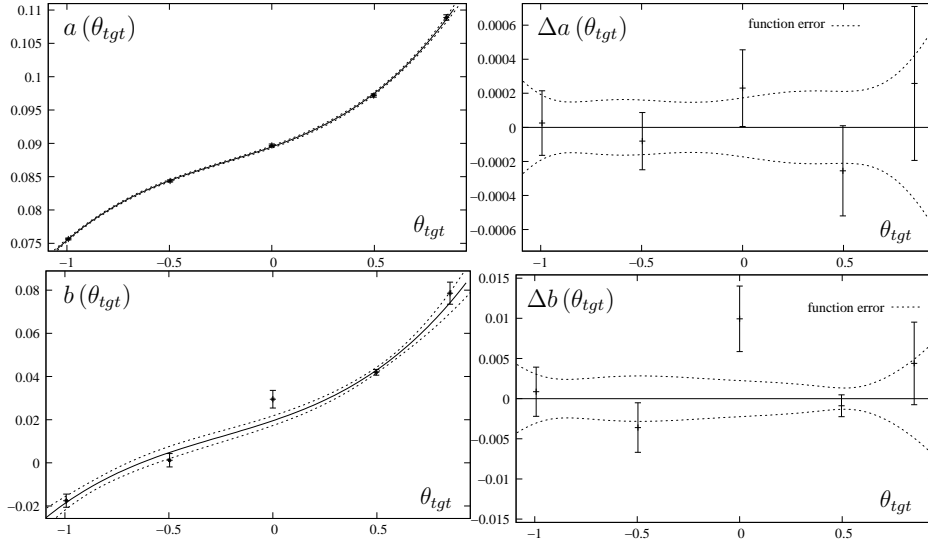


Figure B.16: Third-order polynomial fit as a function of θ for the linear parameters a and b of the $\phi_{tgt} = a y_{fp} + b$ relation for the sieve slit image at $x_{fp} \in [-45, -5]$. The fitted functions are shown along with the residuum of the fit.

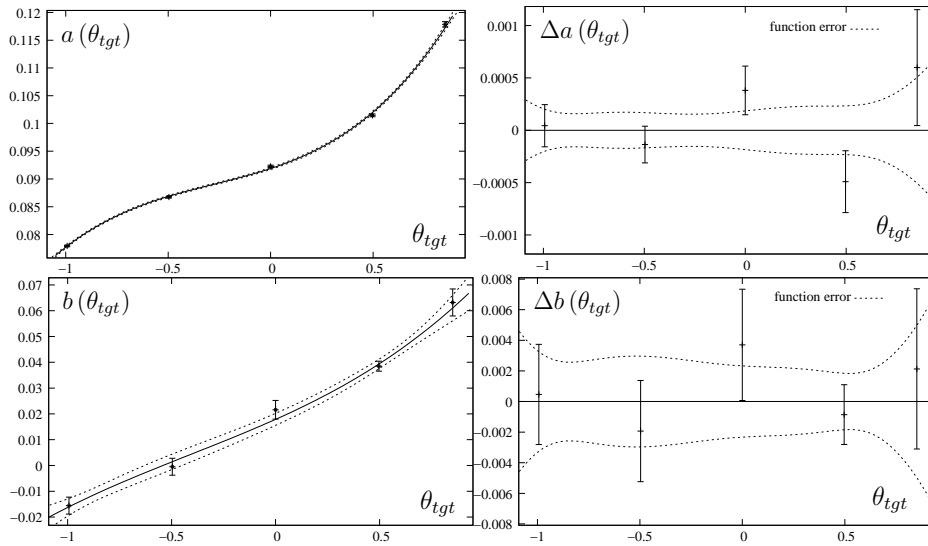


Figure B.17: Third-order polynomial fit as a function of θ for the linear parameters a and b of the $\phi_{tgt} = a y_{fp} + b$ relation for the sieve slit image at $x_{fp} \in [35, 95]$. The fitted functions are shown along with the residuum of the fit.

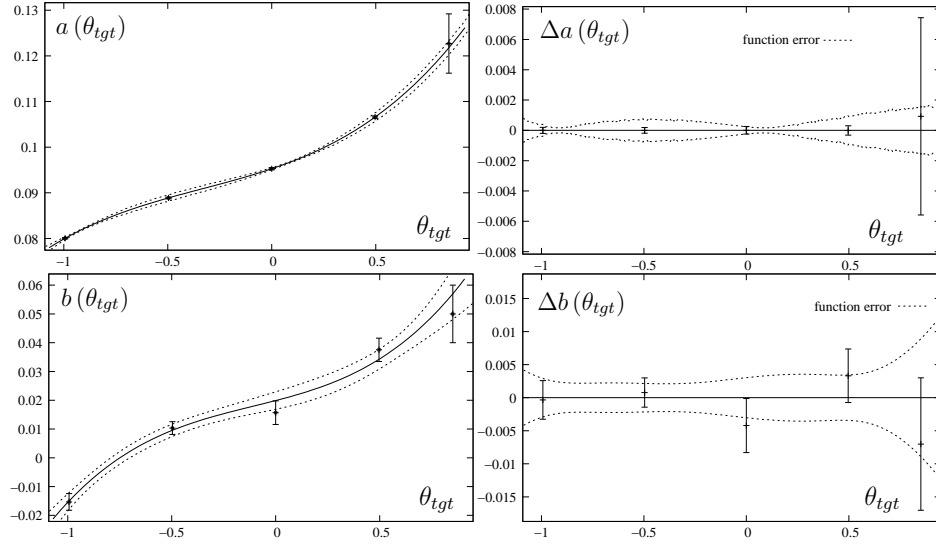


Figure B.18: Third-order polynomial fit as a function of θ for the linear parameters a and b of the $\phi_{tgt} = a y_{fp} + b$ relation for the sieve slit image at $x_{fp} \in [115, 190]$. The fitted functions are shown along with the residuum of the fit.

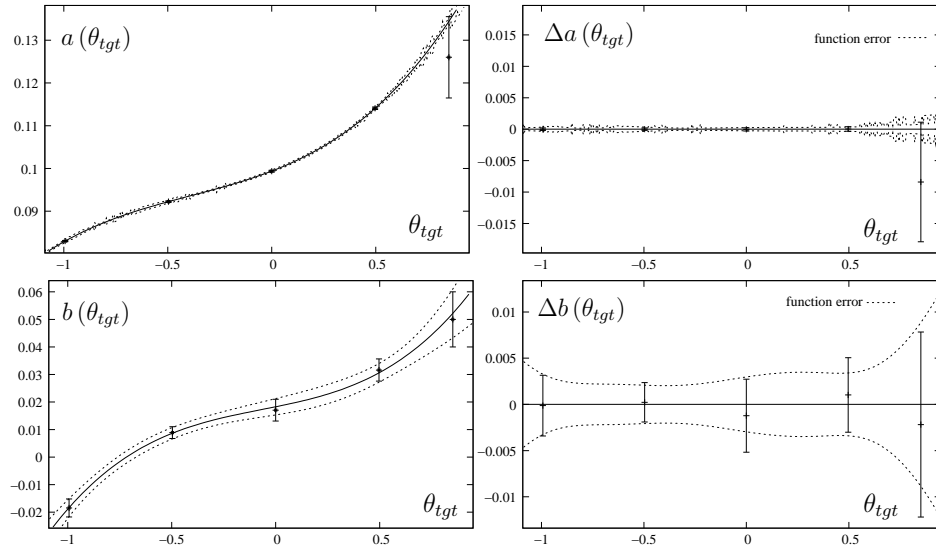


Figure B.19: Third-order polynomial fit as a function of θ for the linear parameters a and b of the $\phi_{tgt} = a y_{fp} + b$ relation for the sieve slit image at $x_{fp} \in [190, 320]$. The fitted functions are shown along with the residuum of the fit.

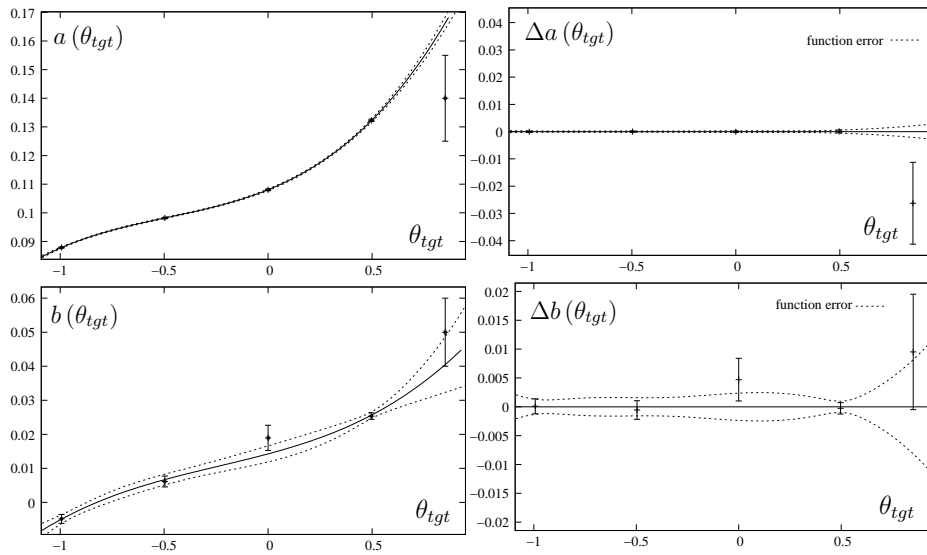


Figure B.20: Third-order polynomial fit as a function of θ for the linear parameters a and b of the $\phi_{tgt} = ay_{fp} + b$ relation for the sieve slit image at $x_{fp} \in [340, 520]$. The fitted functions are shown along with the residuum of the fit.

Determination of a_{ijk} for the reconstruction of ϕ_{tgt}

The parameters $\alpha_{a,b}$, $\beta_{a,b}$, $\gamma_{a,b}$ and $\delta_{a,b}$ as determined in table B.3 still depend on the focal plane position x_{fp} . By fitting these parameters as a function of x_{fp} up to third order one can finally obtain the coefficients a_{ijk} required to correct the vertical angle ϕ_{tgt} :

$$\alpha_a(x_{fp}) = a_{000} + a_{100}x_{fp} + a_{200}x_{fp}^2 + a_{300}x_{fp}^3 \quad (\text{B.6})$$

$$\beta_a(x_{fp}) = a_{010} + a_{110}x_{fp} + a_{210}x_{fp}^2 + a_{310}x_{fp}^3 \quad (\text{B.7})$$

$$\gamma_a(x_{fp}) = a_{020} + a_{120}x_{fp} + a_{220}x_{fp}^2 + a_{320}x_{fp}^3 \quad (\text{B.8})$$

$$\delta_a(x_{fp}) = a_{030} + a_{130}x_{fp} + a_{230}x_{fp}^2 + a_{330}x_{fp}^3 \quad (\text{B.9})$$

$$\alpha_b(x_{fp}) = a_{001} + a_{101}x_{fp} + a_{201}x_{fp}^2 + a_{301}x_{fp}^3 \quad (\text{B.10})$$

$$\beta_b(x_{fp}) = a_{011} + a_{111}x_{fp} + a_{211}x_{fp}^2 + a_{311}x_{fp}^3 \quad (\text{B.11})$$

$$\gamma_b(x_{fp}) = a_{021} + a_{121}x_{fp} + a_{221}x_{fp}^2 + a_{321}x_{fp}^3 \quad (\text{B.12})$$

$$\delta_b(x_{fp}) = a_{031} + a_{131}x_{fp} + a_{231}x_{fp}^2 + a_{331}x_{fp}^3 \quad (\text{B.13})$$

The coefficients a_{ijk} are given in table B.4, and the fits are shown in fig. B.21 and B.22.

Table B.4: Results of the fit of $\alpha_{a,b}$, $\beta_{a,b}$, $\gamma_{a,b}$ and $\delta_{a,b}$ as a function of focal plane position.

$a(\theta_{tgt}, x_{fp})$ (k=0)	a_{0j0} (i=0)	a_{1j0} (i=1)	a_{2j0} (i=2)	a_{3j0} (i=3)
α_a (j=0)	0.0901(1)	2.80(5)E-05	1.7(2)E-08	2.9(6)E-11
β_a (j=1)	0.0111(2)	1.26(21)E-05	4.0(4)E-08	6.6(19)E-11
γ_a (j=2)	0.0065(2)	3.4(2)E-05	3.3(5)E-08	-9.6(2)E-12
δ_a (j=3)	0.0093(4)	1.95(27)E-05	1.8(59)E-09	7(15)E-12
$b(\theta_{tgt}, x_{fp})$ (k=1)	a_{0j1} (i=0)	a_{1j1} (i=1)	a_{2j1} (i=2)	a_{3j1} (i=3)
α_b (j=0)	0.024(1)	-7.1(9)E-05	1.3(6)E-07	4.9(7)E-10
β_b (j=1)	0.031(3)	-5.0(24)E-05	-2.5(35)E-08	1.4(17)E-10
γ_b (j=2)	0.011(3)	5(24)E-06	-3.4(35)E-08	-2(18)E-11
δ_b (j=3)	0.022(4)	1(40)E-06	-7.7(54)E-08	6(28)E-11

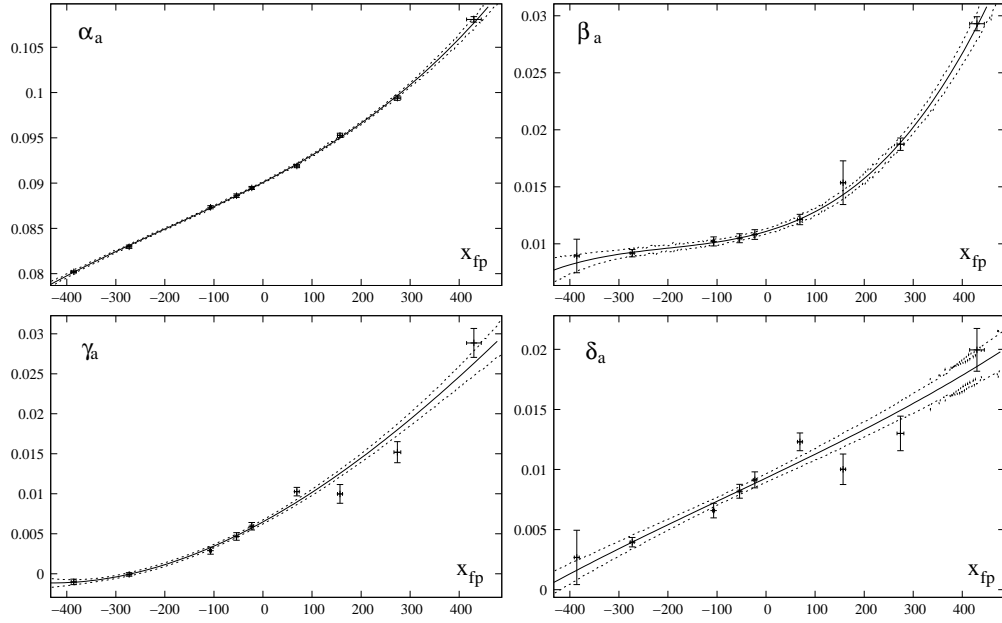


Figure B.21: *third-order polynomial fit as a function of x_{fp} for the parameters $\alpha_a, \beta_a, \gamma_a$ and δ_a .*

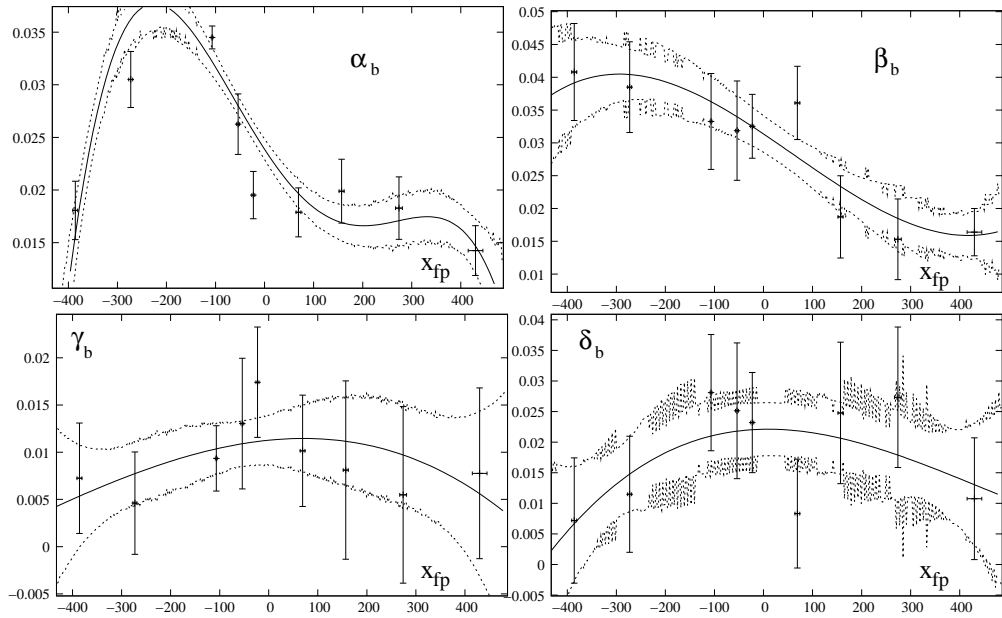


Figure B.22: *third-order polynomial fit as a function of x_{fp} for the parameters $\alpha_b, \beta_b, \gamma_b$ and δ_b .*

B.1.2 Reconstruction of θ_{tgt}

θ_{tgt} as a quadratic function of θ_{fp}

To determine the parameters required for the reconstruction of the θ_{tgt} angle, the sieve slit plots obtained after the ϕ_{tgt} correction (previous section) were sliced into seven “rows” and projected onto the θ -axis. The row numbers correspond to the rows of the multi-hole slit (see fig. B.2), counted from the lowest vertical angle (row 1, $\phi_{tgt}=-2.8364^\circ$) to the highest vertical angle (row 11, $\phi_{tgt}=+2.8364^\circ$). In order to obtain sufficient data points for a fit, the rows 5-7, which contain the large hole, were consolidated into one (row 6 would only have three anchor points, while rows 5 and 7 would only contain data about the fringe of the large hole). The θ_{fp} position was determined by fitting the obtained spectra. In order to reconstruct the horizontal angle at the target, it was assumed that

$$\theta_{tgt} = a(\phi_{tgt}, x_{fp}) + b(\phi_{tgt}, x_{fp})\theta_{fp} + c(\phi_{tgt}, x_{fp})\theta_{fp}^2 \quad (\text{B.14})$$

with the parameters a, b and c to be determined by fitting the positions obtained by fitting the row projections to the sieve position. The results are shown in table B.5, and the details of the fits (projections of the rows and fit-functions) can be found in the figures B.24-B.37.

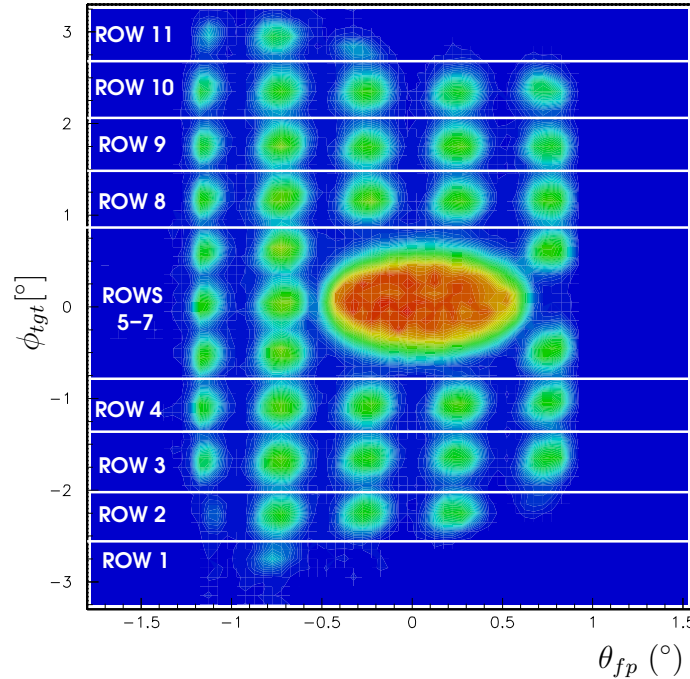


Figure B.23: A sieve slit image after the reconstruction of ϕ_{tgt} . To obtain the row projections on the θ_{fp} axis, the image is sliced into rows on the ϕ_{tgt} axis as shown in the picture.

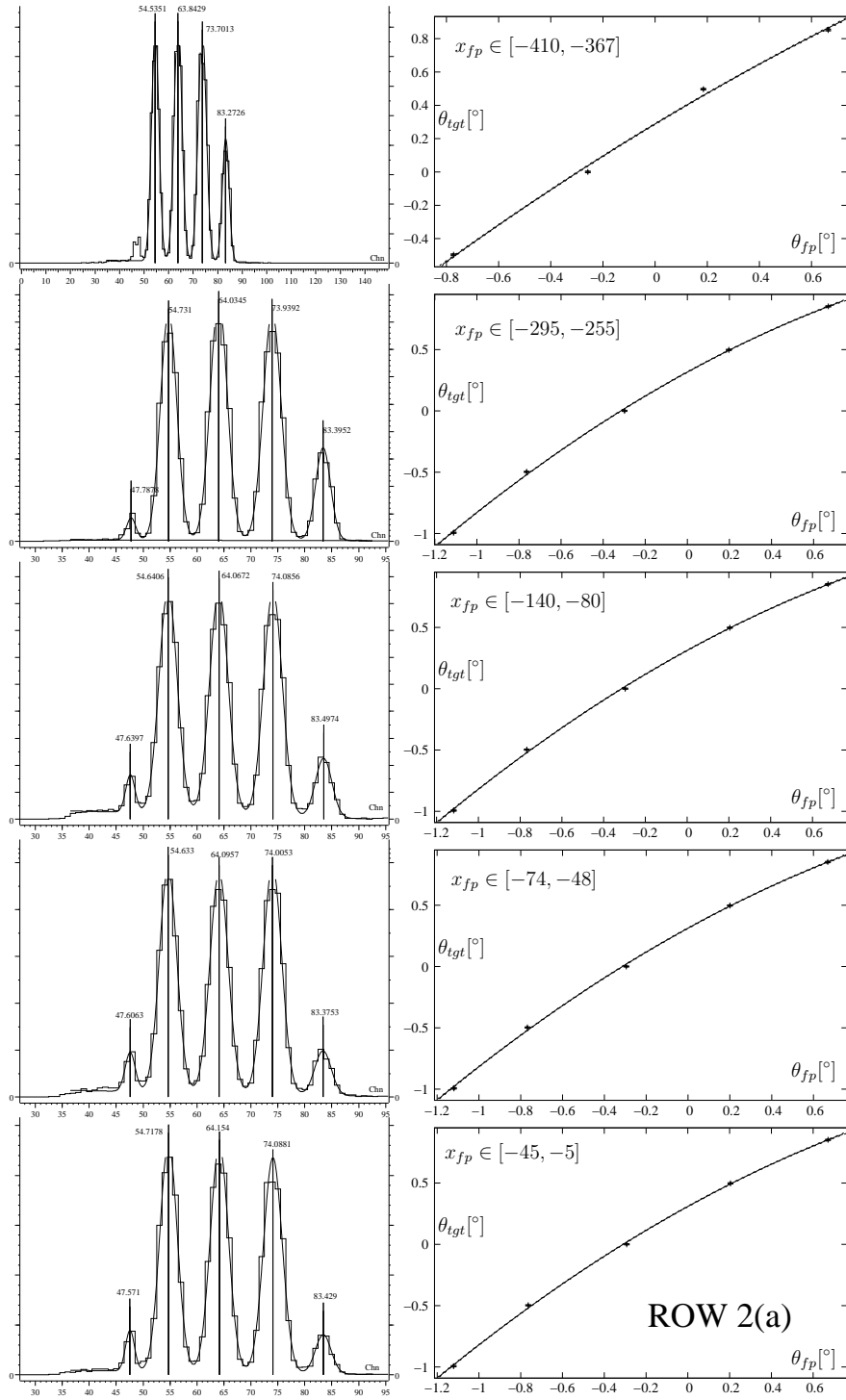


Figure B.24: Projections for the five lowest x-positions of row 2 of the sieve slit image and determination of centroids. The centroids are fitted to their respective original θ_{tgt} position using a second order polynomial function.

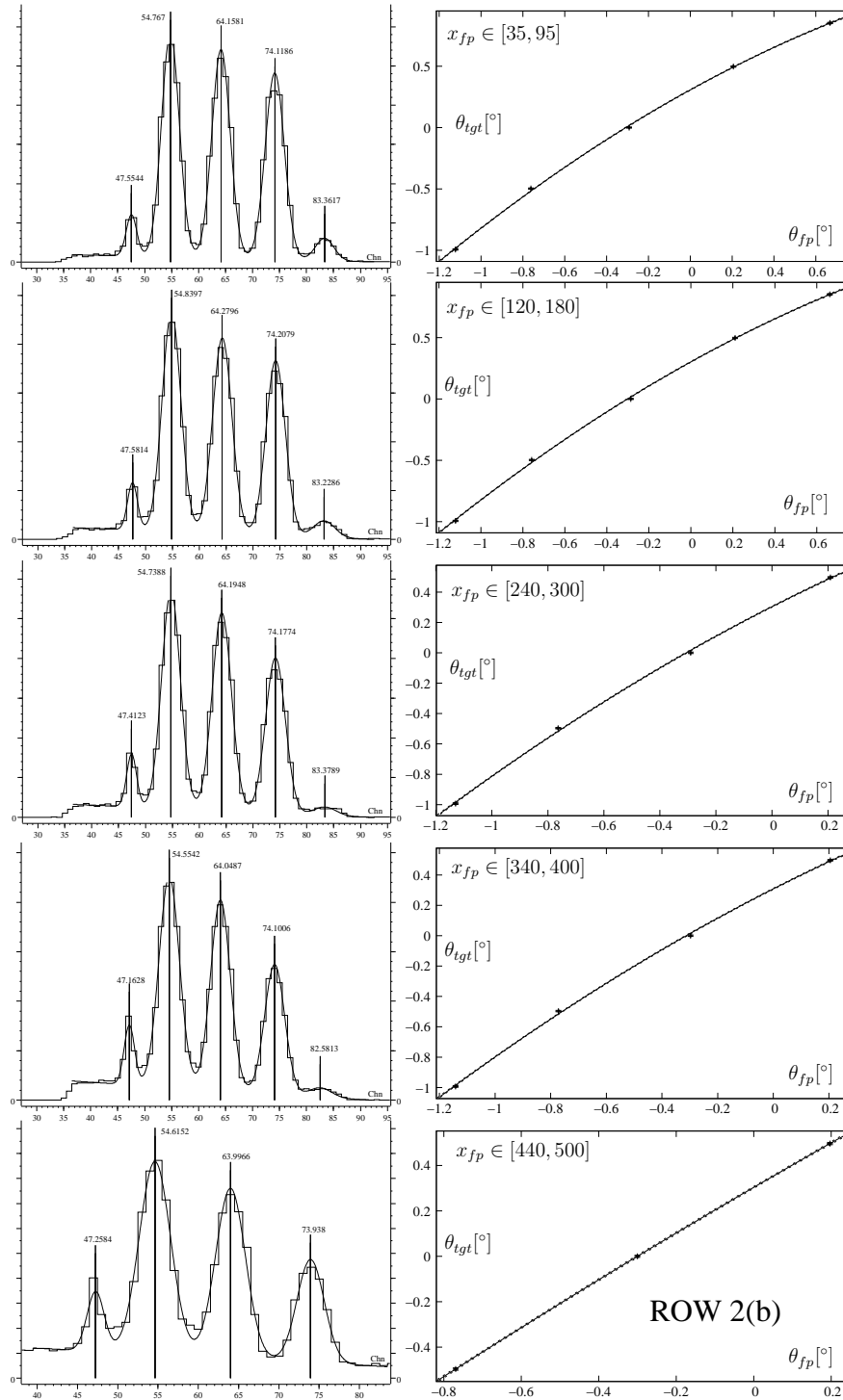


Figure B.25: Projections for the five highest x -positions of row 2 of the sieve slit image and determination of centroids. The centroids are fitted to their respective original θ_{tgt} position using a second order polynomial function.

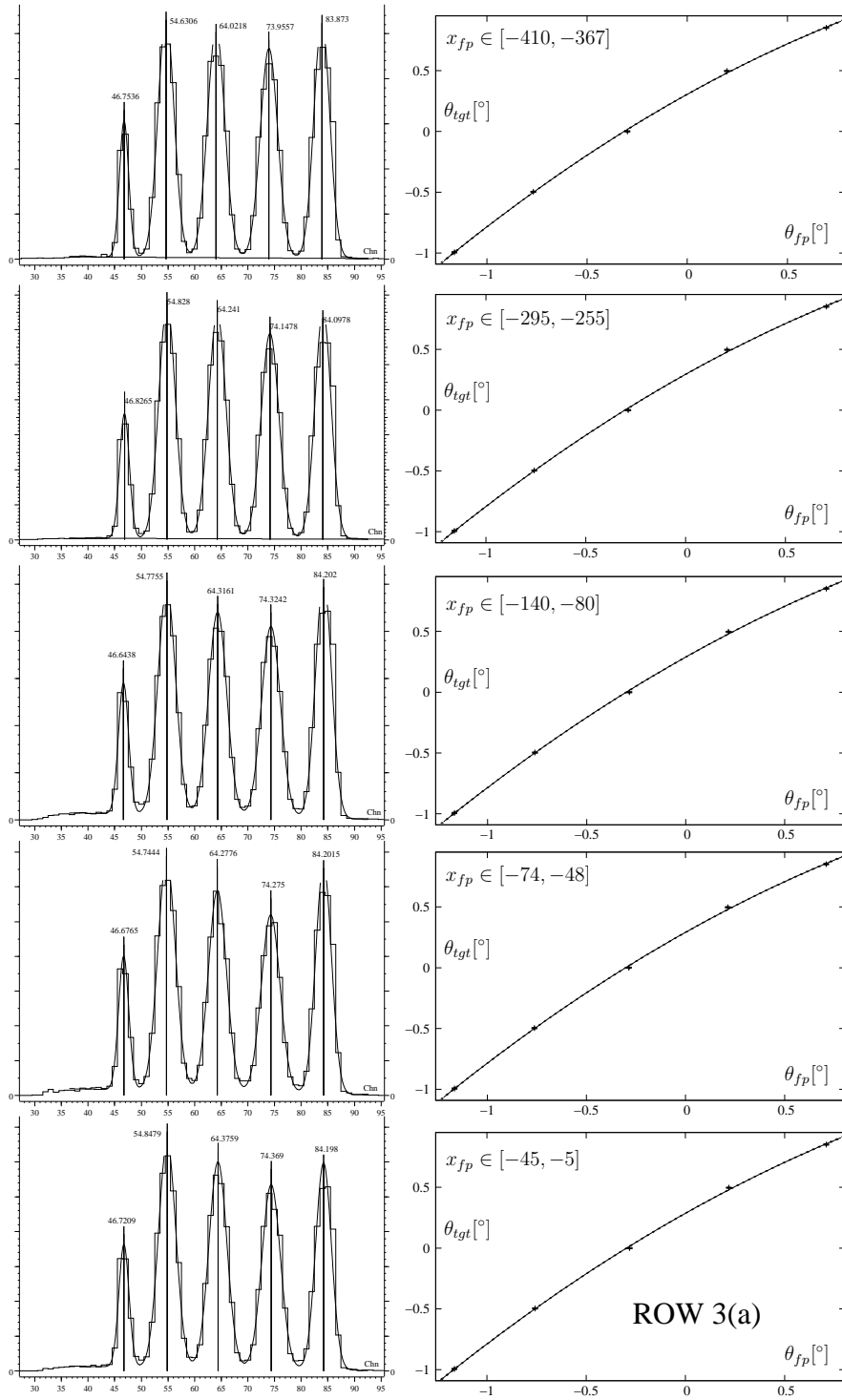


Figure B.26: Projections for the five lowest x -positions of row 3 of the sieve slit image and determination of centroids. The centroids are fitted to their respective original θ_{tgt} position using a second order polynomial function.

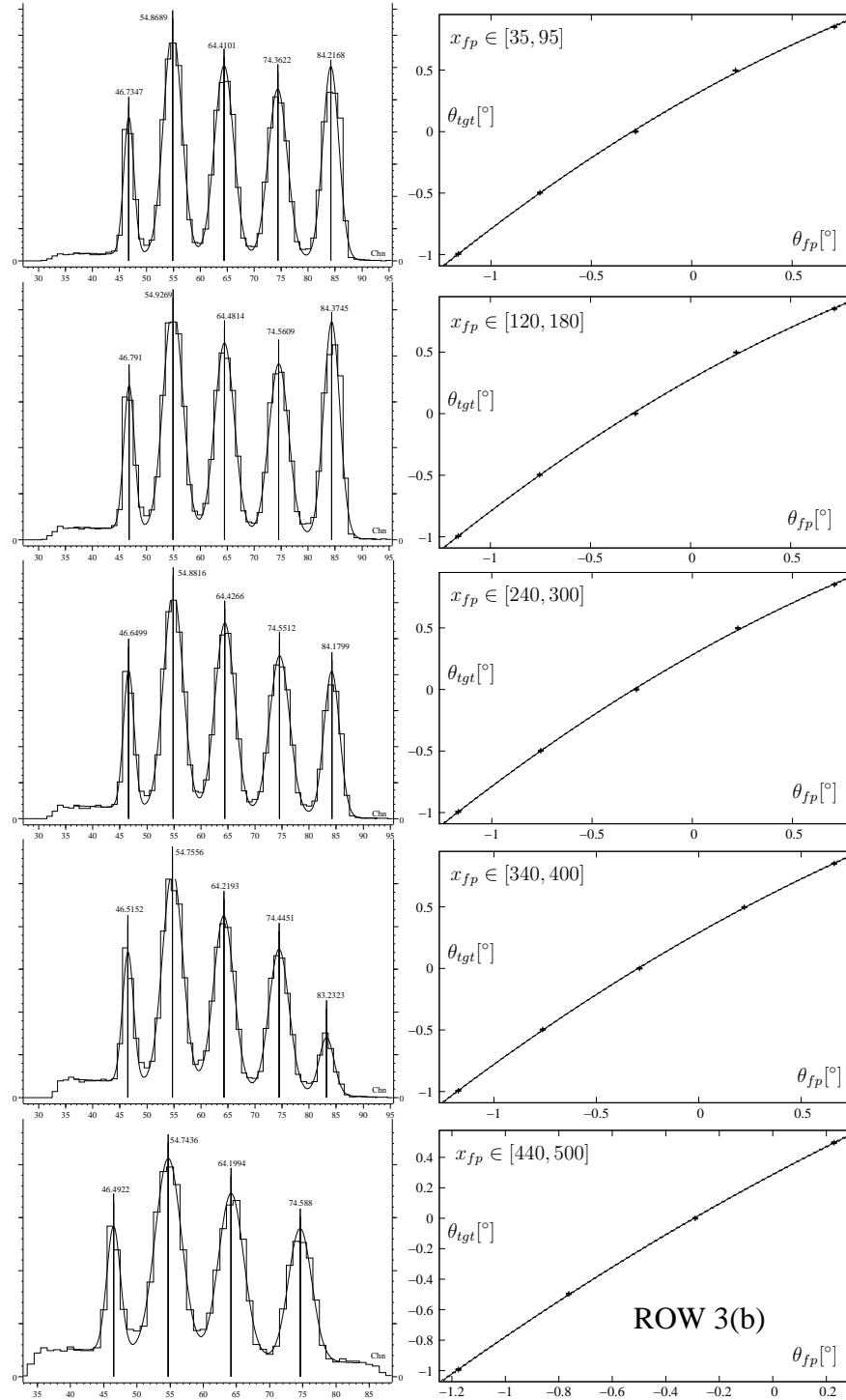


Figure B.27: Projections for the five highest x-positions of row 3 of the sieve slit image and determination of centroids. The centroids are fitted to their respective original θ_{tgt} position using a second order polynomial function.

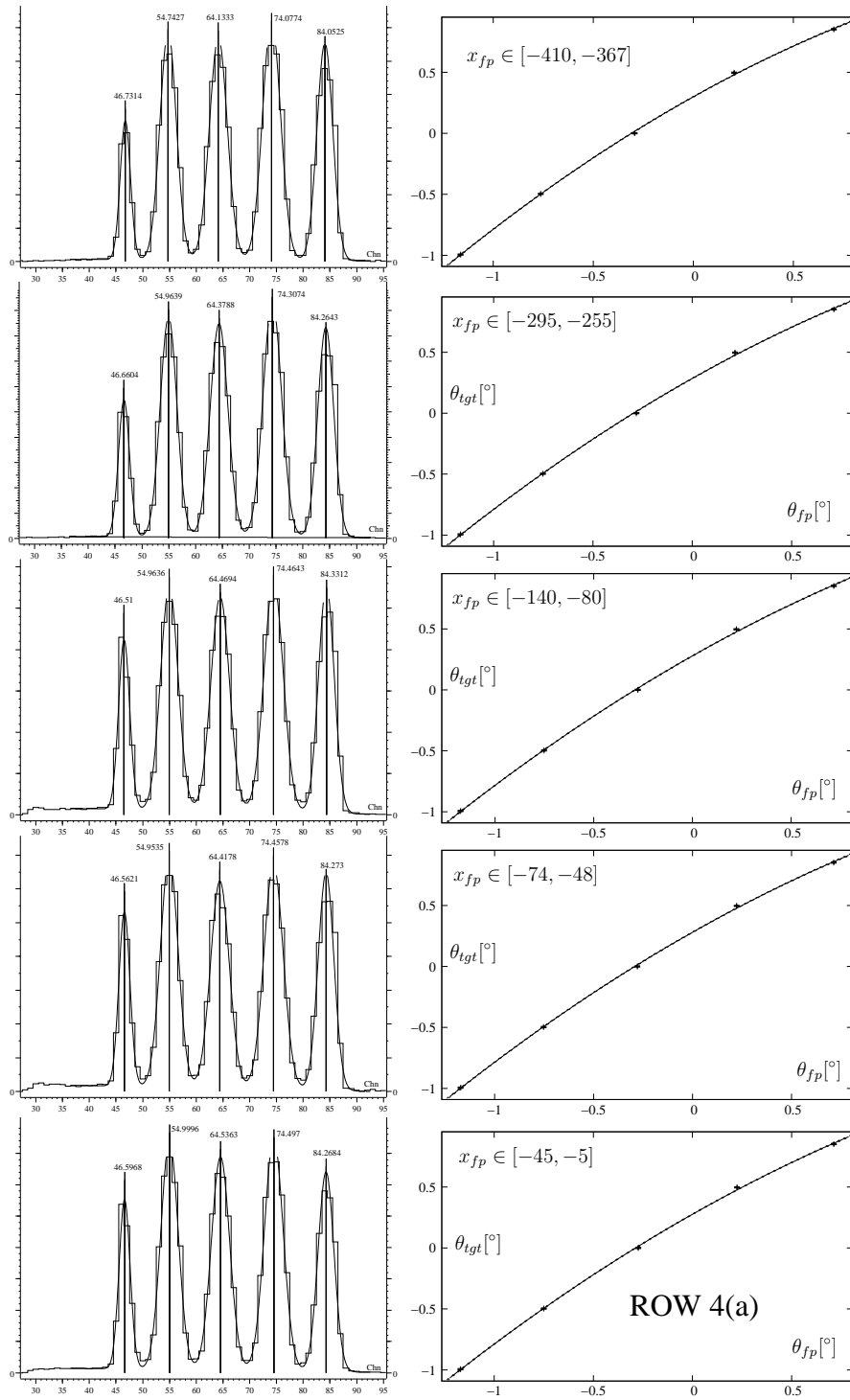


Figure B.28: Projections for the five lowest x -positions of row 4 of the sieve slit image and determination of centroids. The centroids are fitted to their respective original θ_{tgt} position using a second order polynomial function.

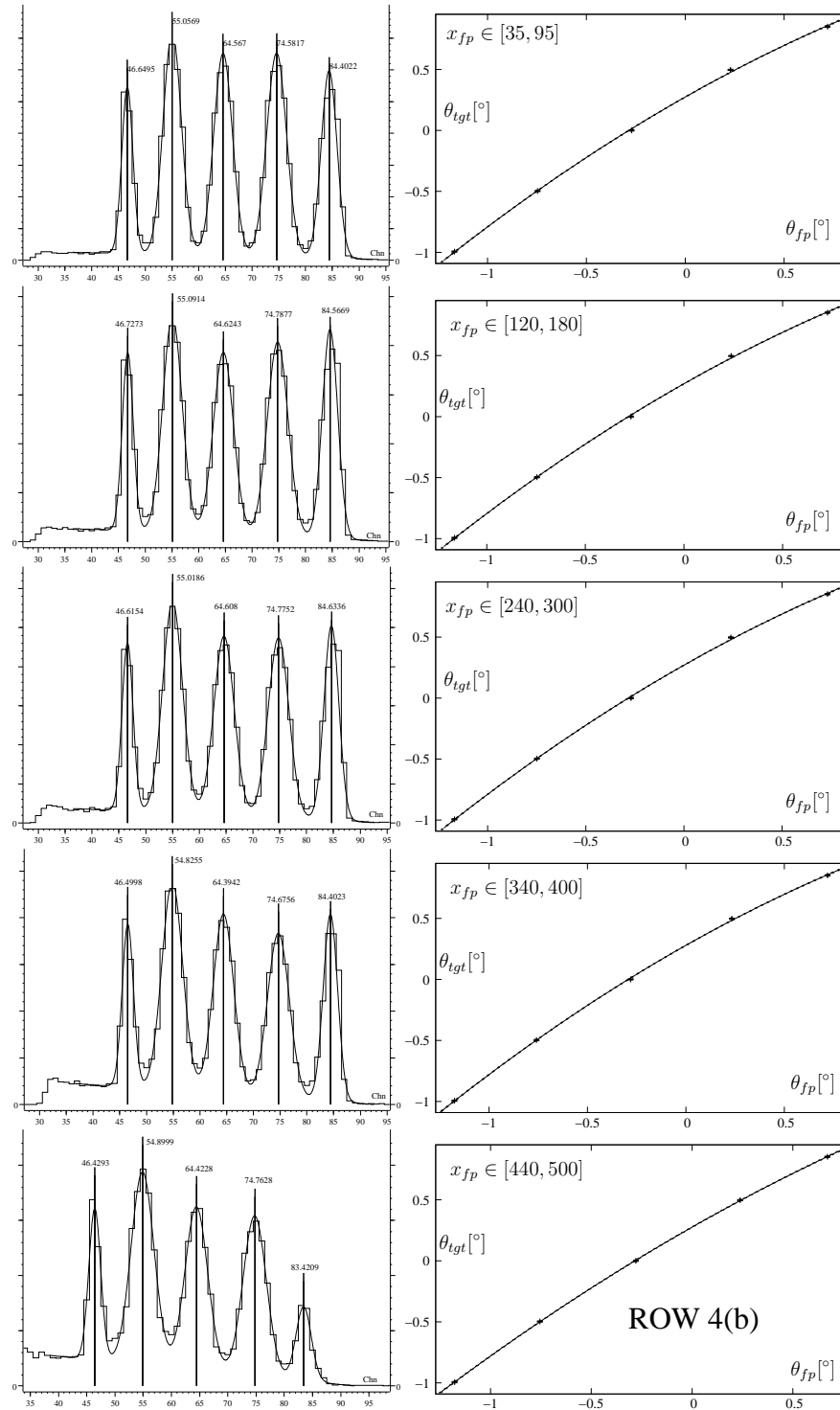


Figure B.29: Projections for the five highest x -positions of row 4 of the sieve slit image and determination of centroids. The centroids are fitted to their respective original θ_{tgt} position using a second order polynomial function.

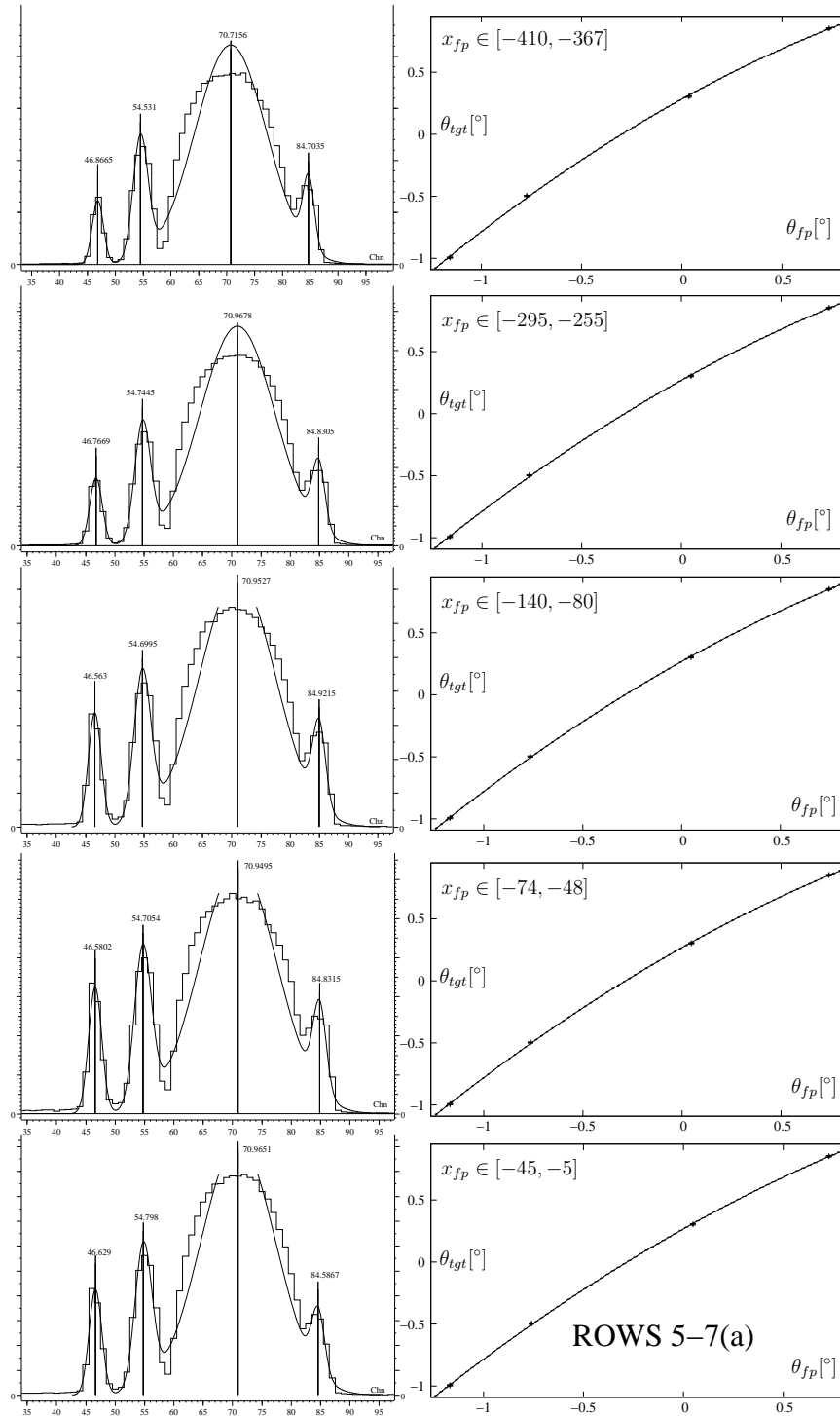


Figure B.30: Projections for the five lowest x -positions of rows 5-7 of the sieve slit image and determination of centroids. The centroids are fitted to their respective original θ_{tgt} position using a second order polynomial function.

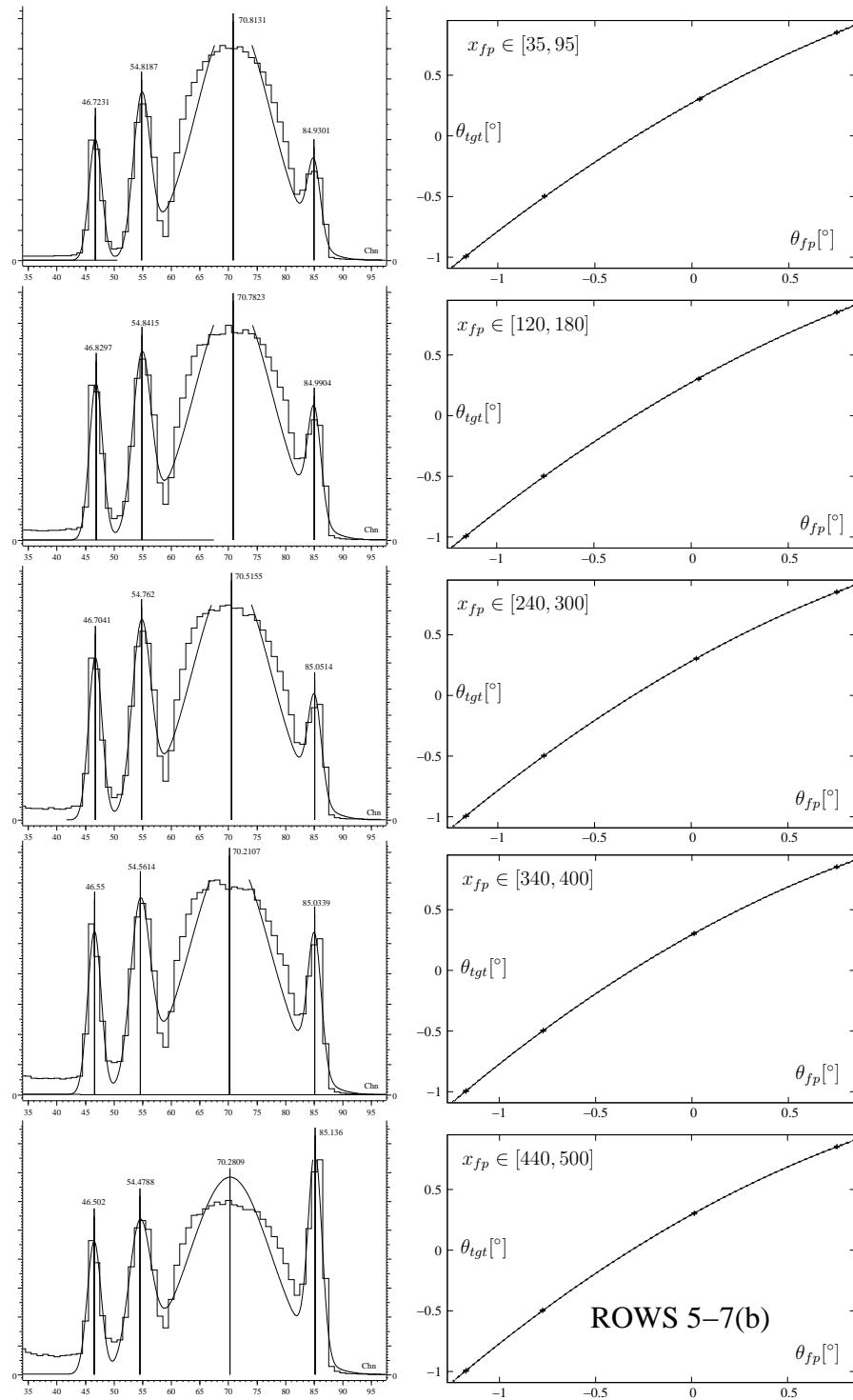


Figure B.31: Projections for the five highest x-positions of rows 5-7 of the sieve slit image and determination of centroids. The centroids are fitted to their respective original θ_{tgt} position using a second order polynomial function.

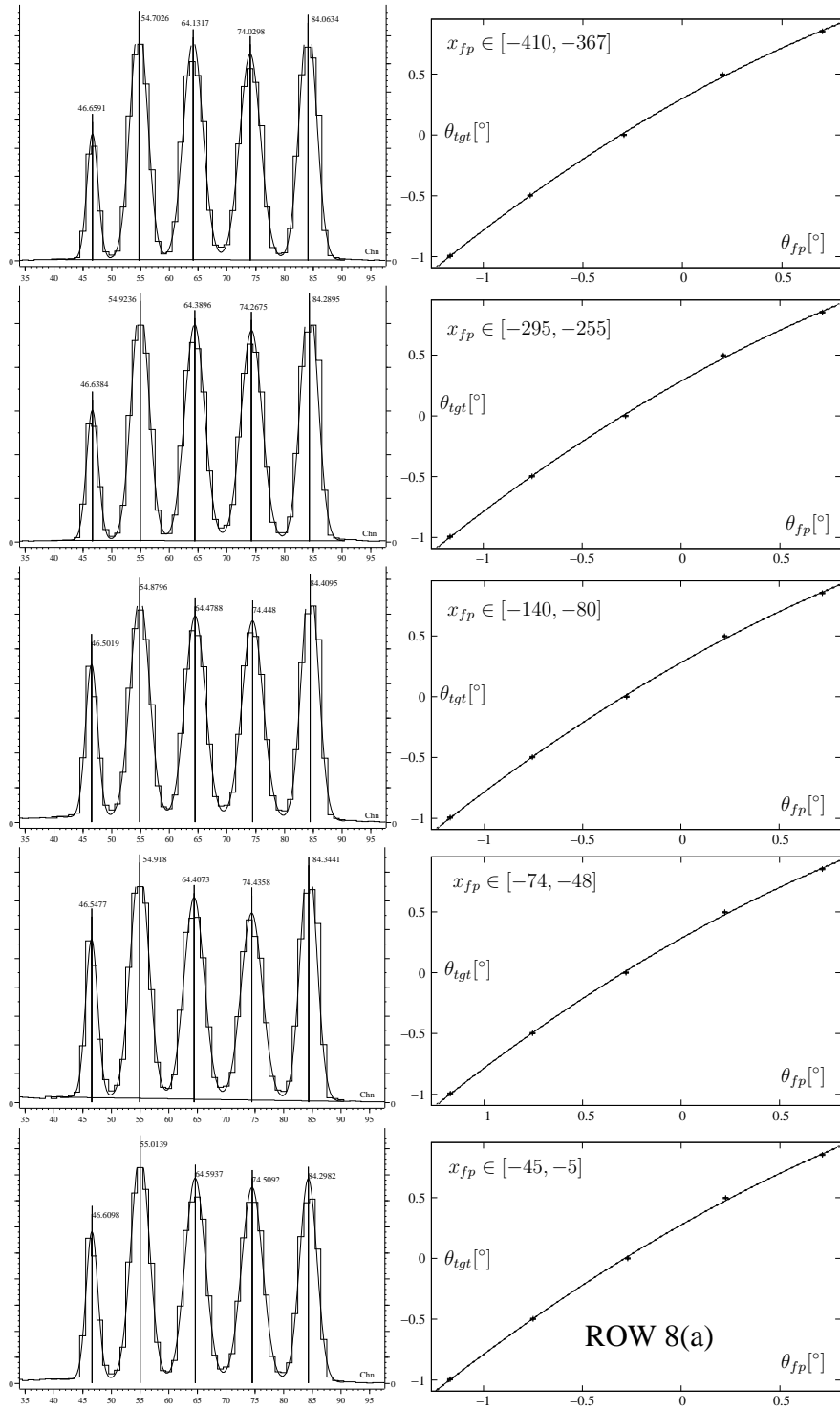


Figure B.32: Projections for the five lowest x-positions of row 8 of the sieve slit image and determination of centroids. The centroids are fitted to their respective original θ_{tgt} position using a second order polynomial function.

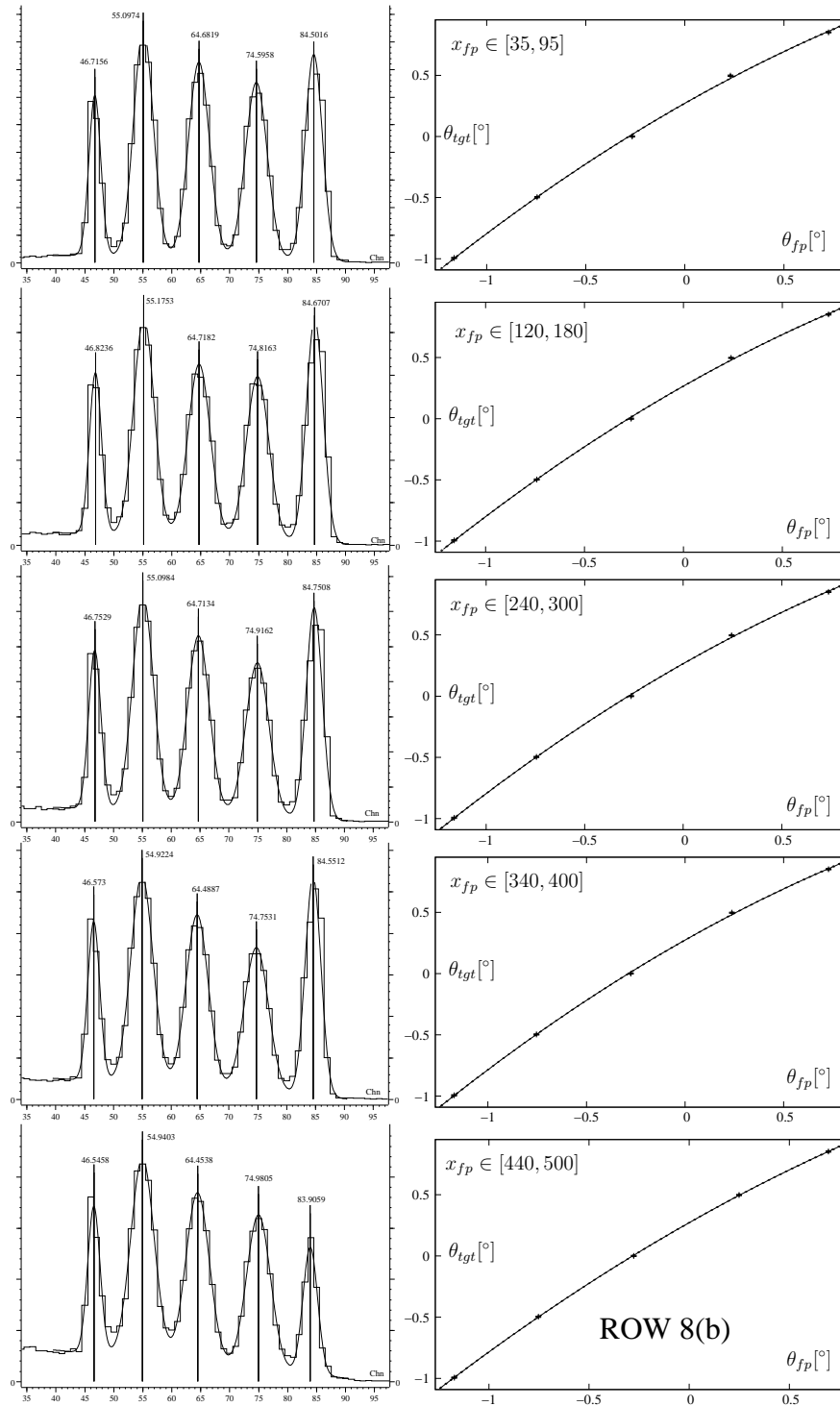


Figure B.33: Projections for the five highest x-positions of row 8 of the sieve slit image and determination of centroids. The centroids are fitted to their respective original θ_{tgt} position using a second order polynomial function.

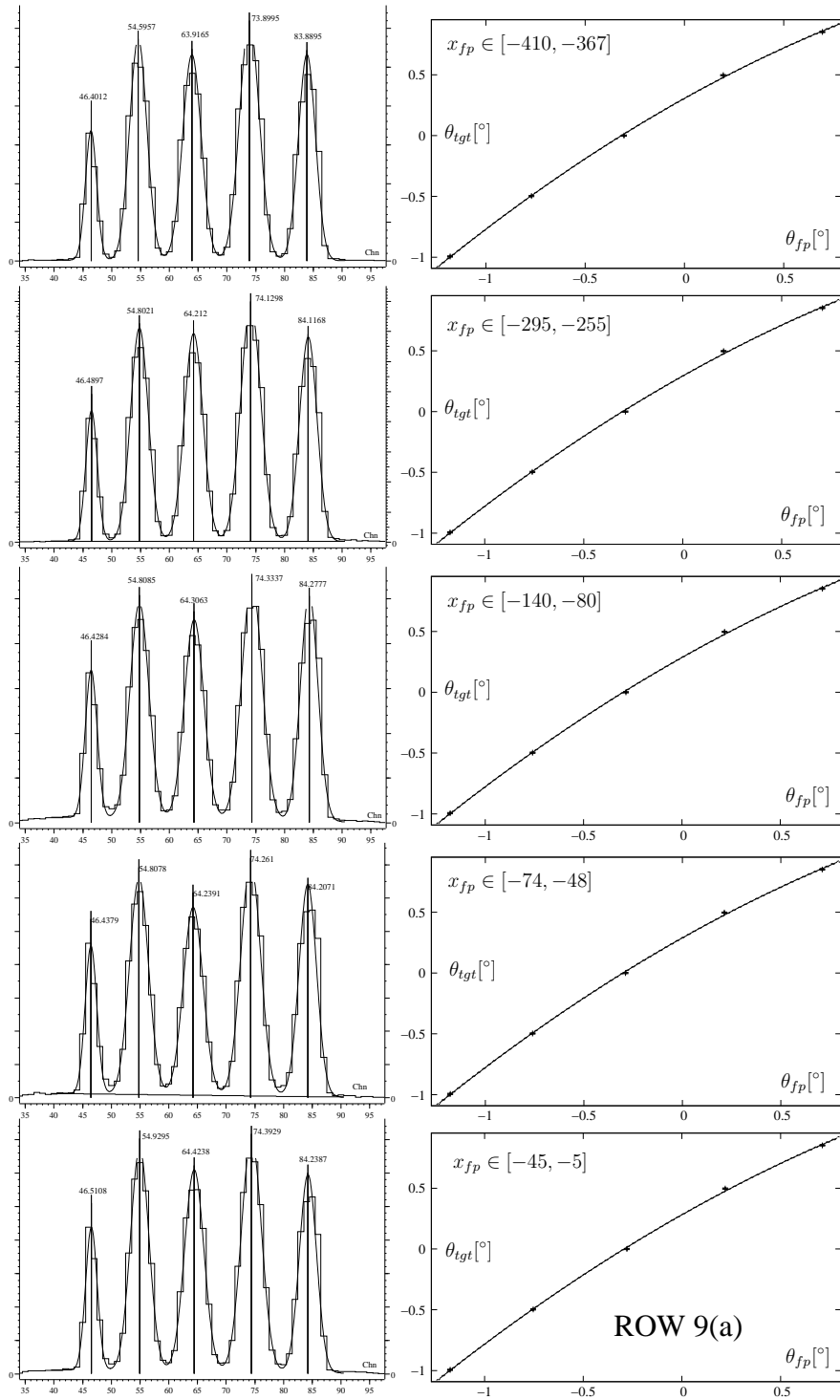


Figure B.34: Projections for the five lowest x -positions of row 9 of the sieve slit image and determination of centroids. The centroids are fitted to their respective original θ_{tgt} position using a second order polynomial function.

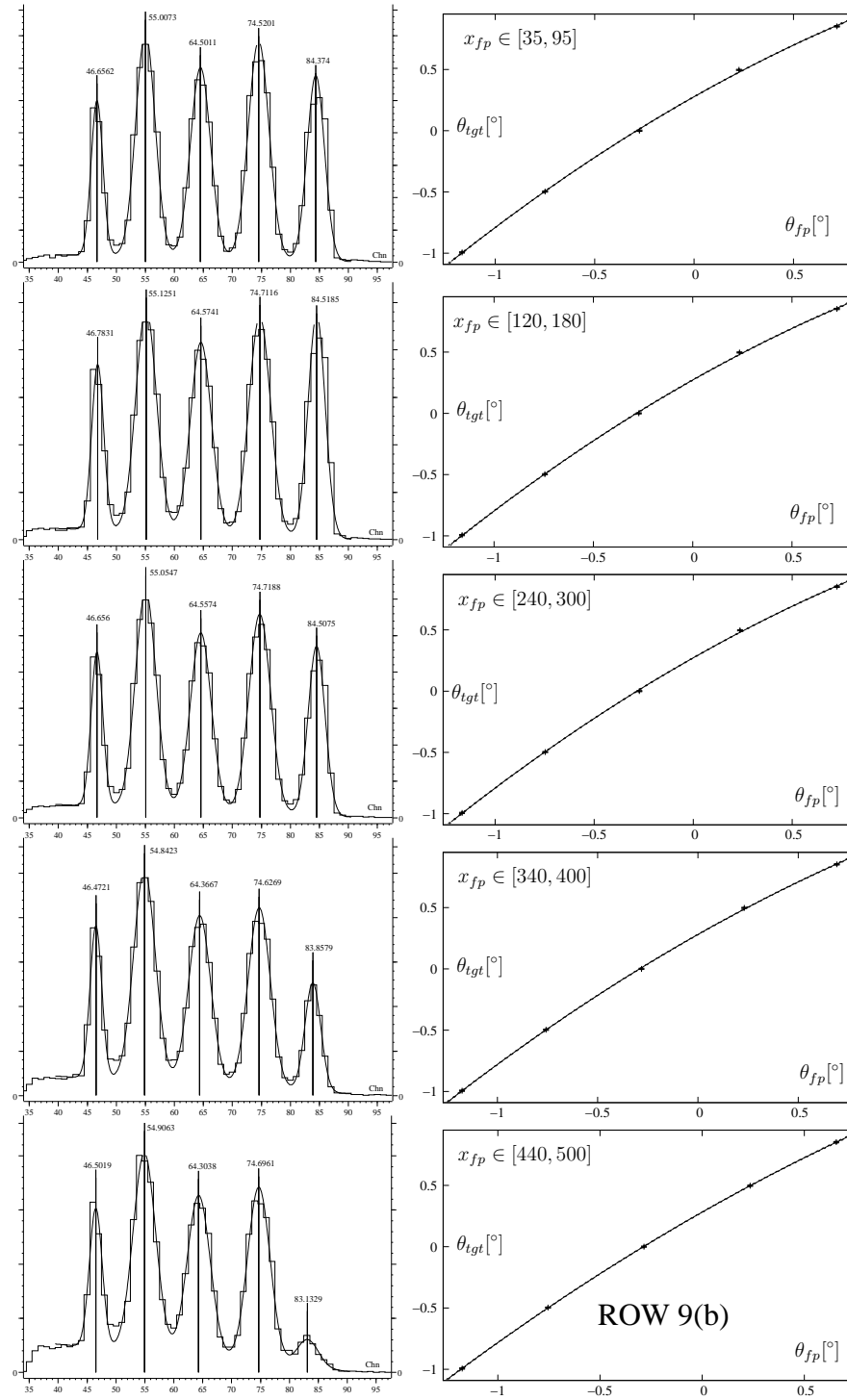


Figure B.35: Projections for the five highest x -positions of row 9 of the sieve slit image and determination of centroids. The centroids are fitted to their respective original θ_{tgt} position using a second order polynomial function.

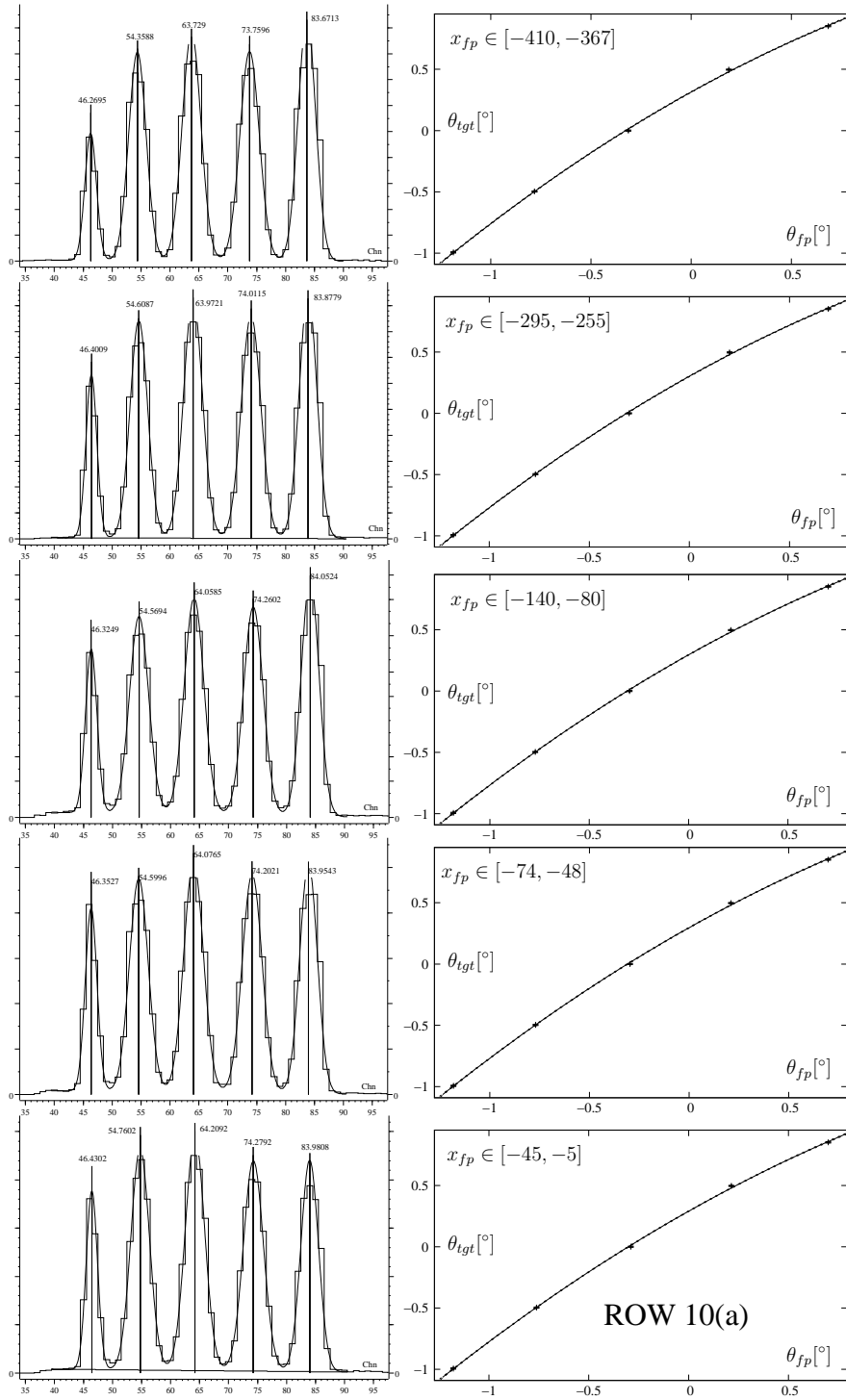


Figure B.36: Projections for the five lowest x -positions of row 10 of the sieve slit image and determination of centroids. The centroids are fitted to their respective original θ_{tgt} position using a second order polynomial function.

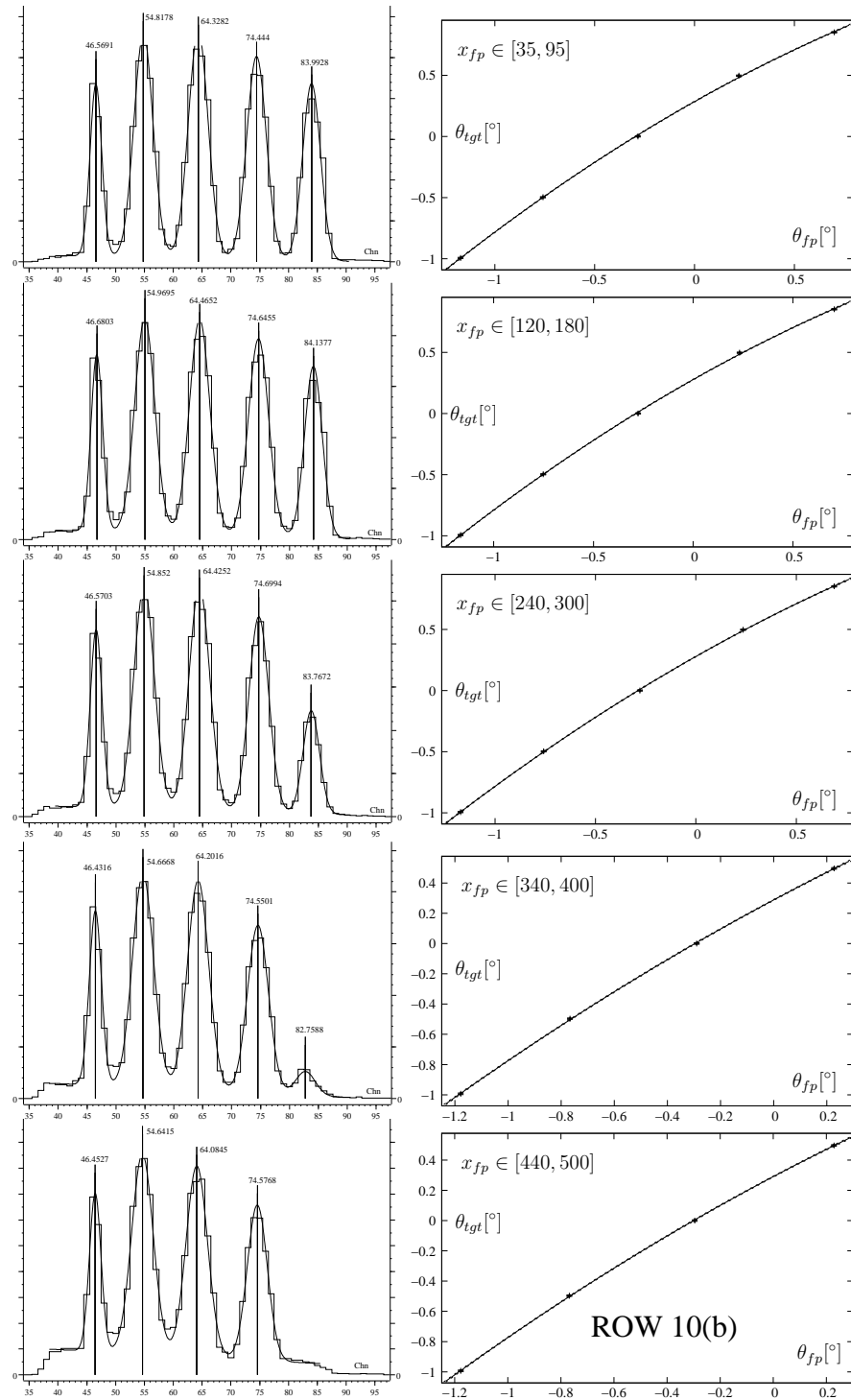


Figure B.37: Projections for the five highest x_p -positions of row 10 of the sieve slit image and determination of centroids. The centroids are fitted to their respective original θ_{tgt} position using a second order polynomial function.

Table B.5: Results of the fit connecting θ_{fp} to the original θ_{tgt} position via $\phi_{tgt} = a + b\theta_{fp} + c\theta_{fp}^2$.

Row		$x \in [-410, -367]$			$x \in [-295, -255]$		
	ϕ_{tgt}	a	b	c	a	b	c
Row 2	-2.270	0.288(4)	0.943(5)	-0.112(11)	0.316(4)	0.937(5)	-0.208(7)
Row 3	-1.703	0.306(3)	0.916(5)	-0.174(6)	0.295(3)	0.918(4)	-0.168(6)
Row 4	-1.135	0.299(3)	0.915(4)	-0.170(6)	0.285(3)	0.918(4)	-0.156(6)
Rows 5-7	0.000	0.283(4)	0.896(4)	-0.173(7)	0.268(4)	0.899(4)	-0.156(7)
Row 8	1.135	0.299(3)	0.914(4)	-0.168(6)	0.285(3)	0.916(4)	-0.156(6)
Row 9	1.703	0.306(3)	0.911(5)	-0.164(6)	0.292(3)	0.915(4)	-0.156(6)
Row 10	2.270	0.315(3)	0.908(5)	-0.166(6)	0.302(3)	0.913(4)	-0.160(6)
Row		$x \in [-140, -80]$			$x \in [-74, -48]$		
	ϕ_{tgt}	a	b	c	a	b	c
Row 2	-2.270	0.312(4)	0.932(5)	-0.199(7)	0.312(4)	0.936(5)	-0.193(8)
Row 3	-1.703	0.288(3)	0.914(4)	-0.158(6)	0.291(4)	0.913(4)	-0.162(6)
Row 4	-1.135	0.278(3)	0.916(4)	-0.146(4)	0.280(4)	0.917(4)	-0.148(6)
Rows 5-7	0.000	0.267(4)	0.894(4)	-0.152(7)	0.267(4)	0.896(5)	-0.151(7)
Row 8	1.135	0.279(3)	0.912(4)	-0.148(6)	0.281(4)	0.914(4)	-0.151(6)
Row 9	1.703	0.286(3)	0.911(4)	-0.151(6)	0.289(4)	0.912(5)	-0.153(8)
Row 10	2.270	0.295(3)	0.908(4)	-0.154(6)	0.296(4)	0.912(5)	-0.153(6)
Row		$x \in [-45, -5]$			$x \in [35, 95]$		
	ϕ_{tgt}	a	b	c	a	b	c
Row 2	-2.270	0.308(4)	0.937(5)	-0.191(7)	0.307(4)	0.940(5)	-0.187(7)
Row 3	-1.703	0.286(3)	0.917(4)	-0.158(6)	0.285(4)	0.918(5)	-0.157(9)
Row 4	-1.135	0.277(3)	0.920(4)	-0.144(6)	0.274(3)	0.918(4)	-0.146(6)
Rows 5-7	0.000	0.266(4)	0.905(5)	-0.144(7)	0.271(4)	0.896(4)	-0.161(7)
Row 8	1.135	0.275(4)	0.920(4)	-0.143(6)	0.271(3)	0.919(4)	-0.147(6)
Row 9	1.703	0.281(3)	0.917(4)	-0.147(6)	0.277(3)	0.917(4)	-0.150(6)
Row 10	2.270	0.290(3)	0.917(4)	-0.149(6)	0.285(4)	0.920(4)	-0.147(5)
Row		$x \in [120, 180]$			$x \in [240, 300]$		
	ϕ_{tgt}	a	b	c	a	b	c
Row 2	-2.270	0.302(4)	0.947(5)	-0.178(8)	0.304(4)	0.938(13)	-0.180(13)
Row 3	-1.703	0.280(4)	0.916(5)	-0.157(6)	0.280(3)	0.919(4)	-0.149(6)
Row 4	-1.135	0.269(4)	0.916(4)	-0.148(6)	0.270(3)	0.912(4)	-0.146(6)
Row 5-7	0.000	0.272(4)	0.896(4)	-0.167(7)	0.281(4)	0.889(4)	-0.175(7)
Row 8	1.135	0.266(4)	0.917(4)	-0.149(6)	0.265(4)	0.913(4)	-0.148(6)
Row 9	1.703	0.272(4)	0.918(5)	-0.151(8)	0.272(3)	0.915(4)	-0.147(6)
Row 10	2.270	0.277(3)	0.922(4)	-0.145(6)	0.278(3)	0.929(5)	-0.133(6)
Row		$x \in [340, 400]$			$x \in [440, 500]$		
	ϕ_{tgt}	a	b	c	a	b	c
Row 2	-2.270	0.308(4)	0.931(13)	0.177(13)	0.304(4)	0.993(18)	-0.062(28)
Row 3	-1.703	0.289(3)	0.938(5)	-0.130(7)	0.287(4)	0.937(12)	-0.129(12)
Row 4	-1.135	0.278(4)	0.910(4)	-0.148(6)	0.276(4)	0.939(5)	-0.117(7)
Rows 5-7	0.000	0.294(4)	0.881(4)	-0.185(7)	0.292(4)	0.877(4)	-0.184(7)
Row 8	1.135	0.274(4)	0.910(4)	-0.148(6)	0.271(4)	0.926(5)	-0.129(6)
Row 9	1.703	0.280(3)	0.924(5)	-0.135(6)	0.281(4)	0.946(5)	-0.118(7)
Row 10	2.270	0.288(4)	0.936(12)	-0.126(12)	0.291(4)	0.926(12)	-0.138(12)

Parameters of the cubic function as a function of ϕ_{tgt}

In the next step, the parameters $a(\phi_{tgt}, x_{fp})$, $b(\phi_{tgt}, x_{fp})$ and $c(\phi_{tgt}, x_{fp})$ derived as in table B.5 were fitted for each x_{fp} region as a function of ϕ_{tgt} . The parameters were fitted as fourth-order polynomial functions of ϕ_{tgt} :

$$a(\phi_{tgt}, x_{fp}) = \alpha_a + \beta_a \phi_{tgt} + \gamma_a \phi_{tgt}^2 + \delta_a \phi_{tgt}^3 + \epsilon_a \phi_{tgt}^4 \quad (\text{B.15})$$

$$b(\phi_{tgt}, x_{fp}) = \alpha_b + \beta_b \phi_{tgt} + \gamma_b \phi_{tgt}^2 + \delta_b \phi_{tgt}^3 + \epsilon_b \phi_{tgt}^4 \quad (\text{B.16})$$

$$c(\phi_{tgt}, x_{fp}) = \alpha_c + \beta_c \phi_{tgt} + \gamma_c \phi_{tgt}^2 + \delta_c \phi_{tgt}^3 + \epsilon_c \phi_{tgt}^4 \quad (\text{B.17})$$

where the fitted parameters $\alpha_{a,b,c}$, $\beta_{a,b,c}$, $\gamma_{a,b,c}$, $\delta_{a,b,c}$ and $\epsilon_{a,b,c}$ still depend on the focal plane position x_{fp} . The results of the fit are summarized in table B.6, and the fits themselves are shown in the figures B.38, B.39 and B.40.

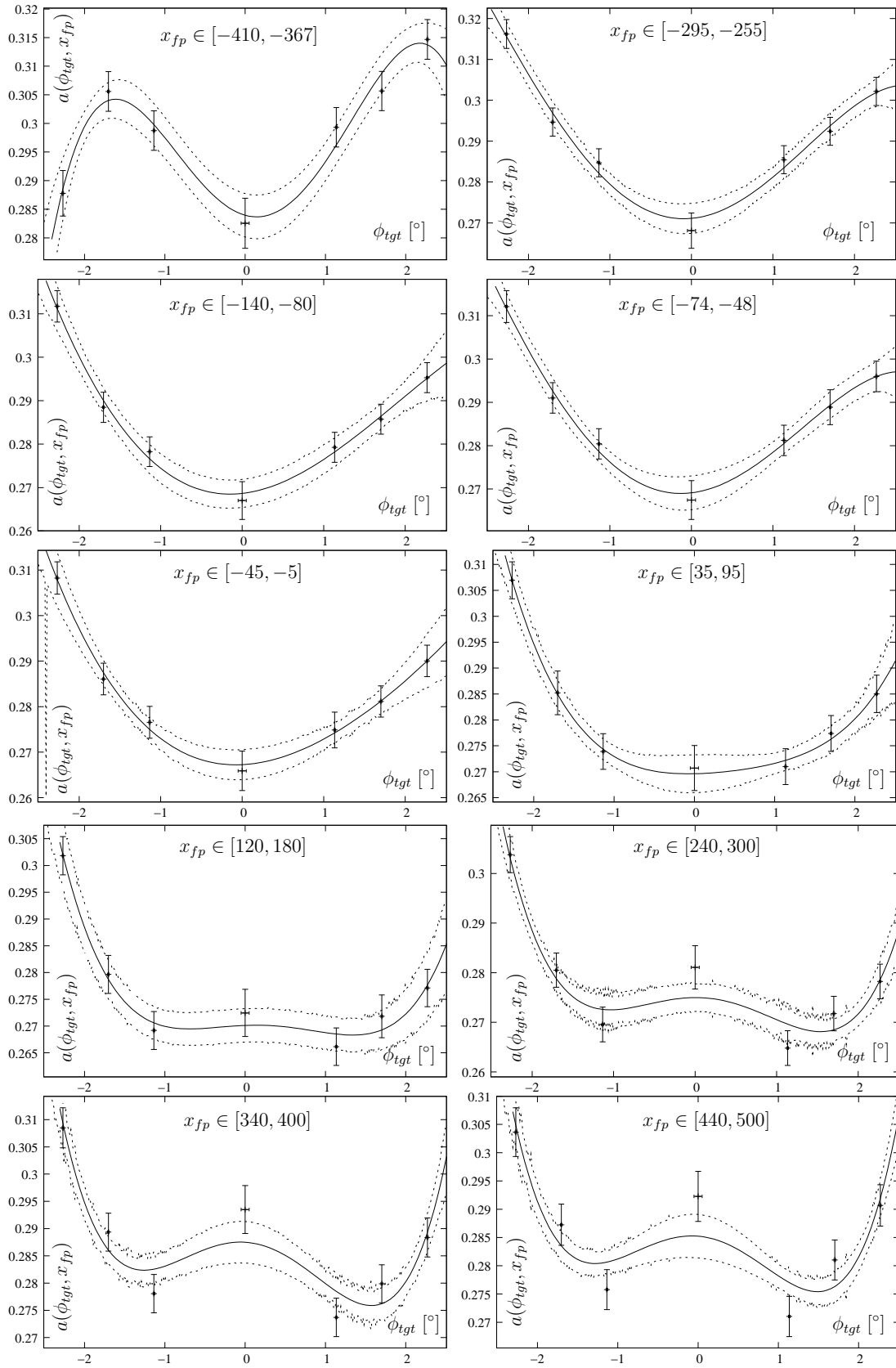
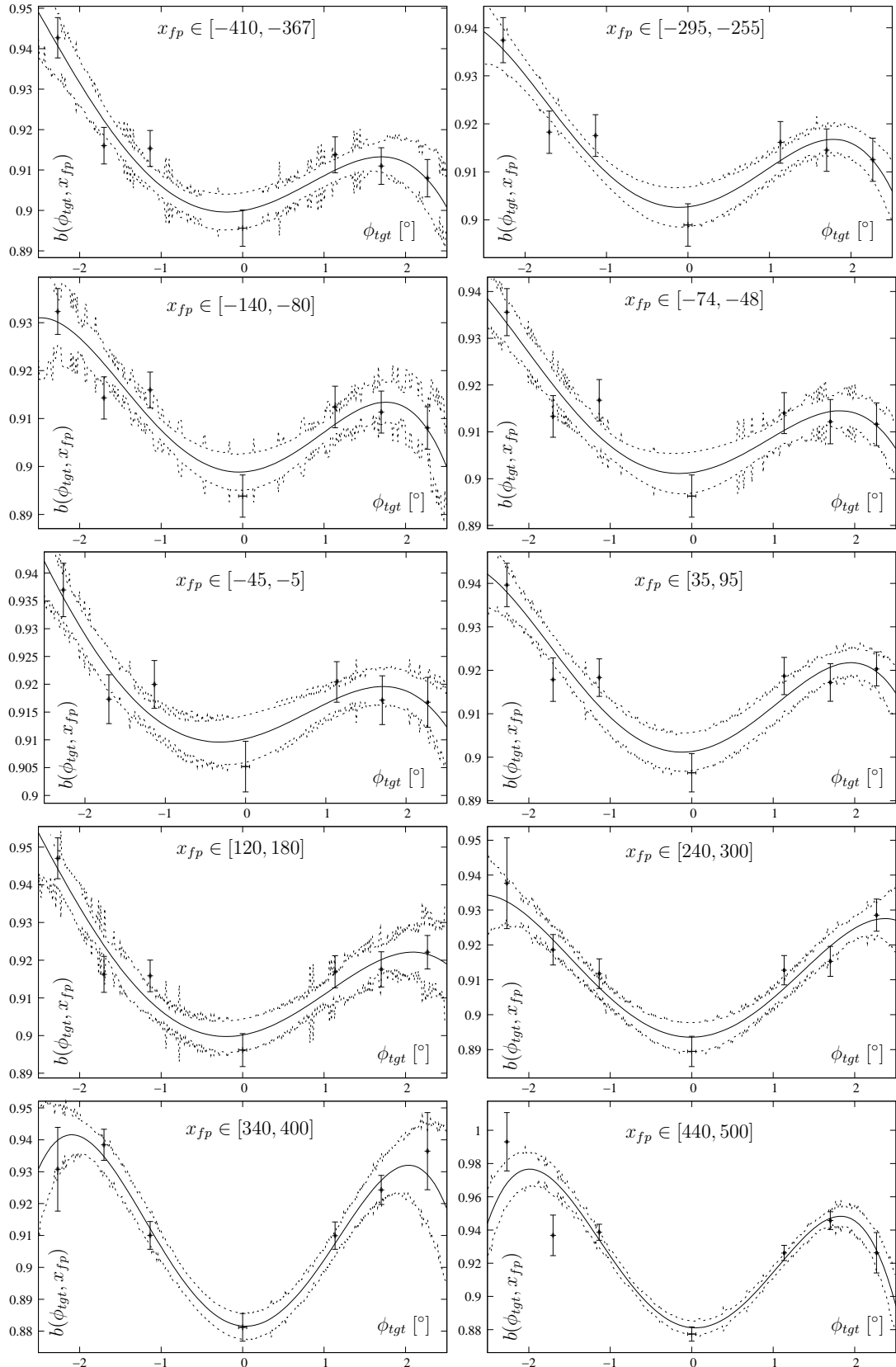


Figure B.38: Fit of the parameter $a(\phi_{tgt}, x_{fp})$ as a function of ϕ_{tgt} for all ten x_{fp} ranges.

Figure B.39: Fit of the parameter $b(\phi_{tgt}, x_{fp})$ as a function of ϕ_{tgt} for all ten x_{fp} ranges.

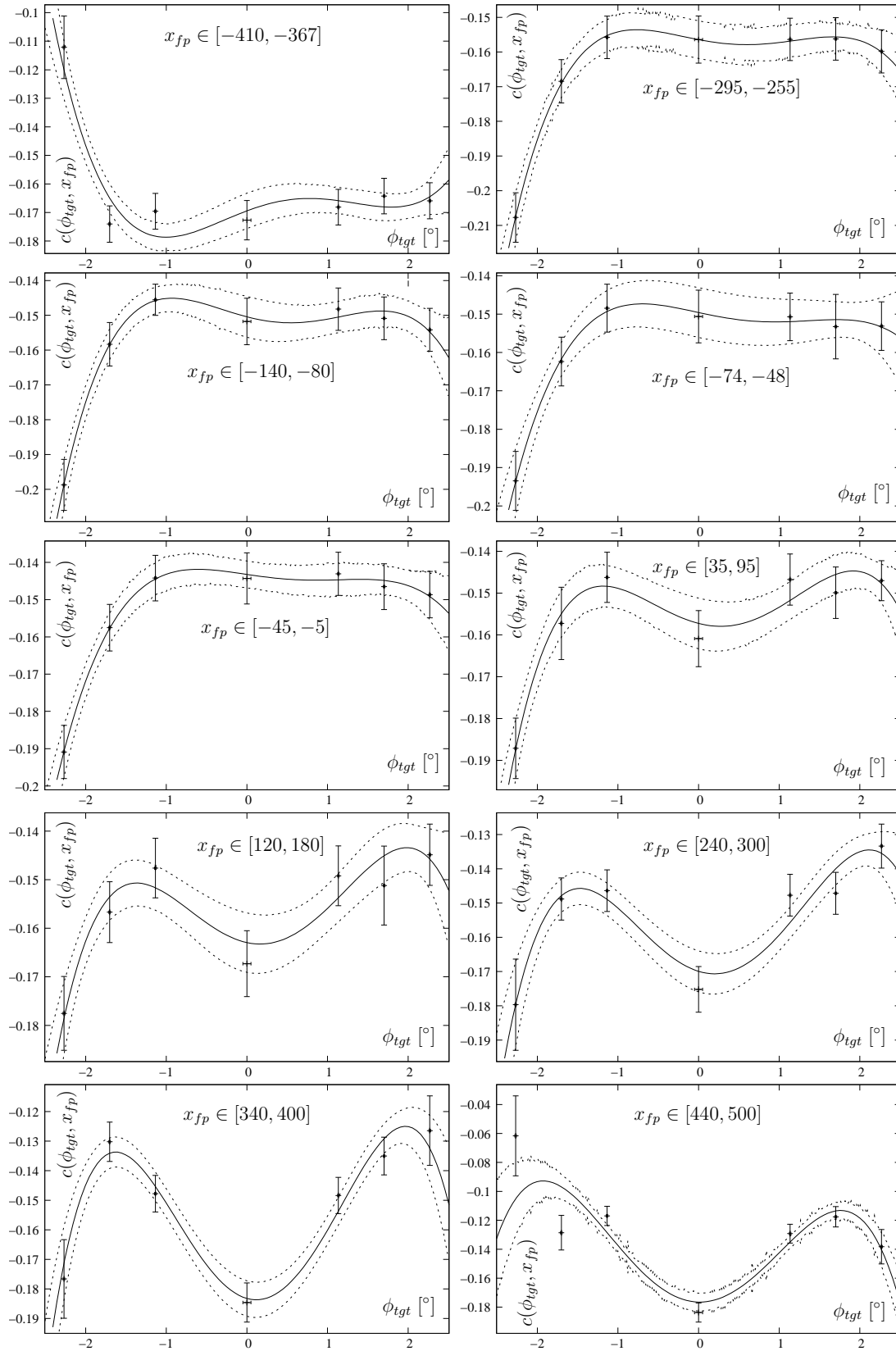


Figure B.40: Fit of the parameter $c(\phi_{tgt}, x_{fp})$ as a function of ϕ_{tgt} for all ten x_{fp} ranges.

Table B.6: Results of the fit of the parameters a, b and c as a function of ϕ_{tgt} .

$a(\phi_{tgt}, x_{fp}) = \alpha_a + \beta_a \phi_{tgt} + \gamma_a \phi_{tgt}^2 + \delta_a \phi_{tgt}^3 + \epsilon_a \phi_{tgt}^4$					
x_{fp}	α_a	β_a	γ_a	δ_a	ϵ_a
-389(5)	0.284(4)	-0.004(4)	0.013(3)	0.0018(8)	-0.0020(6)
-275(5)	0.271(4)	0.002(2)	0.010(3)	-0.0009(3)	-0.0005(5)
-110(5)	0.269(3)	0.002(3)	0.007(2)	-0.0011(8)	-0.00002(5)
-61(5)	0.269(4)	0.002(1)	0.009(3)	-0.0011(1)	-0.0004(5)
-25(5)	0.267(3)	0.001(2)	0.006(2)	-0.0009(4)	0.0001(2)
65(5)	0.270(4)	0.0003(6)	0.002(3)	-0.0010(4)	0.0006(6)
150(5)	0.270(3)	0.001(2)	-0.0019(2)	-0.0012(4)	0.0011(1)
270(5)	0.275(3)	0.0001(28)	-0.005(1)	-0.0011(7)	0.0016(2)
370(5)	0.287(4)	-0.001(2)	-0.008(3)	-0.0007(5)	0.0020(5)
470(5)	0.285(4)	-0.0012(7)	-0.007(3)	-0.0003(2)	0.0019(6)
$b(\phi_{tgt}, x_{fp}) = \alpha_b + \beta_b \phi_{tgt} + \gamma_b \phi_{tgt}^2 + \delta_b \phi_{tgt}^3 + \epsilon_b \phi_{tgt}^4$					
x_{fp}	α_b	β_b	γ_b	δ_b	ϵ_b
-389(5)	0.900(4)	0.0033(5)	0.008(3)	-0.0021(6)	-0.0006(5)
-275(5)	0.903(4)	0.0018(6)	0.008(3)	-0.0013(3)	-0.0008(4)
-110(5)	0.899(4)	0.0009(8)	0.010(3)	-0.0011(7)	-0.0011(4)
-61(5)	0.901(4)	0.002(1)	0.007(4)	-0.00139(9)	-0.0006(5)
-25(5)	0.910(4)	0.003(2)	0.005(3)	-0.00150(9)	-0.0003(5)
65(5)	0.901(4)	0.002(1)	0.010(1)	-0.0013(5)	-0.0009(2)
150(5)	0.900(4)	0.004(2)	0.009(4)	-0.0017(4)	-0.0005(8)
270(5)	0.894(4)	0.0003(12)	0.012(4)	-0.0003(1)	-0.0010(8)
370(5)	0.882(4)	-0.002(3)	0.026(4)	-0.0001(5)	-0.0030(11)
470(5)	0.881(4)	-0.004(2)	0.044(5)	-0.0009(7)	-0.006(1)
$c(\phi_{tgt}, x_{fp}) = \alpha_c + \beta_c \phi_{tgt} + \gamma_c \phi_{tgt}^2 + \delta_c \phi_{tgt}^3 + \epsilon_c \phi_{tgt}^4$					
x_{fp}	α_c	β_c	γ_c	δ_c	ϵ_c
-389(5)	-0.169(6)	0.011(4)	-0.004(5)	-0.004(1)	0.002(1)
-275(5)	-0.156(5)	-0.004(4)	0.002(3)	0.003(1)	-0.001(1)
-110(5)	-0.150(6)	-0.006(4)	0.004(5)	0.003(1)	-0.002(1)
-61(5)	-0.150(6)	-0.005(4)	0.0005(26)	0.003(1)	-0.001(1)
-25(5)	-0.143(4)	-0.003(4)	0.0004(17)	0.002(1)	-0.0011(4)
65(5)	-0.157(6)	-0.005(4)	0.008(5)	0.003(1)	-0.002(1)
150(5)	-0.163(6)	-0.004(4)	0.011(5)	0.002(1)	-0.002(1)
270(5)	-0.170(6)	-0.007(4)	0.017(5)	0.003(1)	-0.003(1)
370(5)	-0.183(6)	-0.008(5)	0.033(5)	0.003(1)	-0.005(1)
470(5)	-0.176(6)	-0.001(4)	0.043(6)	-0.001(2)	-0.006(1)

Determination of b_{ijk} for the reconstruction of θ_{tgt}

Since we chose to calibrate the θ_{tgt} angle after calibrating the ϕ_{tgt} angle (and used this calibration), the description of the parameters of equation (B.2) has to be adapted. The variable y_{fp} is a function of ϕ_{tgt} , therefore a substitution can be done:

$$\begin{aligned}
 \phi_{tgt} &= \phi_{tgt}(y_{fp}, \theta_{fp}, x_{fp}) = \sum_{i=0}^3 \sum_{j=0}^3 \sum_{k=0}^1 a_{ijk} x_{fp}^i \theta_{fp}^j y_{fp}^k \\
 &= \sum_{k=0}^1 a_k y_{fp}^k \\
 \Rightarrow y_{fp} &= y_{fp}(\theta_{fp}, \phi_{tgt}, x_{fp}) = \frac{\phi_{tgt} - a_0(\theta_{tgt}, x_{fp})}{a_1(\theta_{tgt}, x_{fp})} \quad (B.18)
 \end{aligned}$$

The parameters we obtained in the fitting of rows are therefore the parameters \tilde{b}_{ijk} instead of b_{ijk} :

$$\begin{aligned}
 \theta_{tgt} &= \theta_{tgt}(y_{fp}, \theta_{fp}, x_{fp}) = \sum_{i=0}^2 \sum_{j=0}^4 \sum_{k=0}^2 b_{ijk} x_{fp}^i y_{fp}^j \theta_{fp}^k \\
 &= \theta_{tgt}(\phi_{tgt}, \theta_{fp}, x_{fp}) = \sum_{i=0}^2 \sum_{j=0}^4 \sum_{k=0}^2 \tilde{b}_{ijk} x_{fp}^i \phi_{tgt}^j \theta_{fp}^k \quad (B.19)
 \end{aligned}$$

The obtained \tilde{b}_{ijk} are summarized in table B.7, and the details of the fits are shown in the figures B.41, B.42 and B.43.

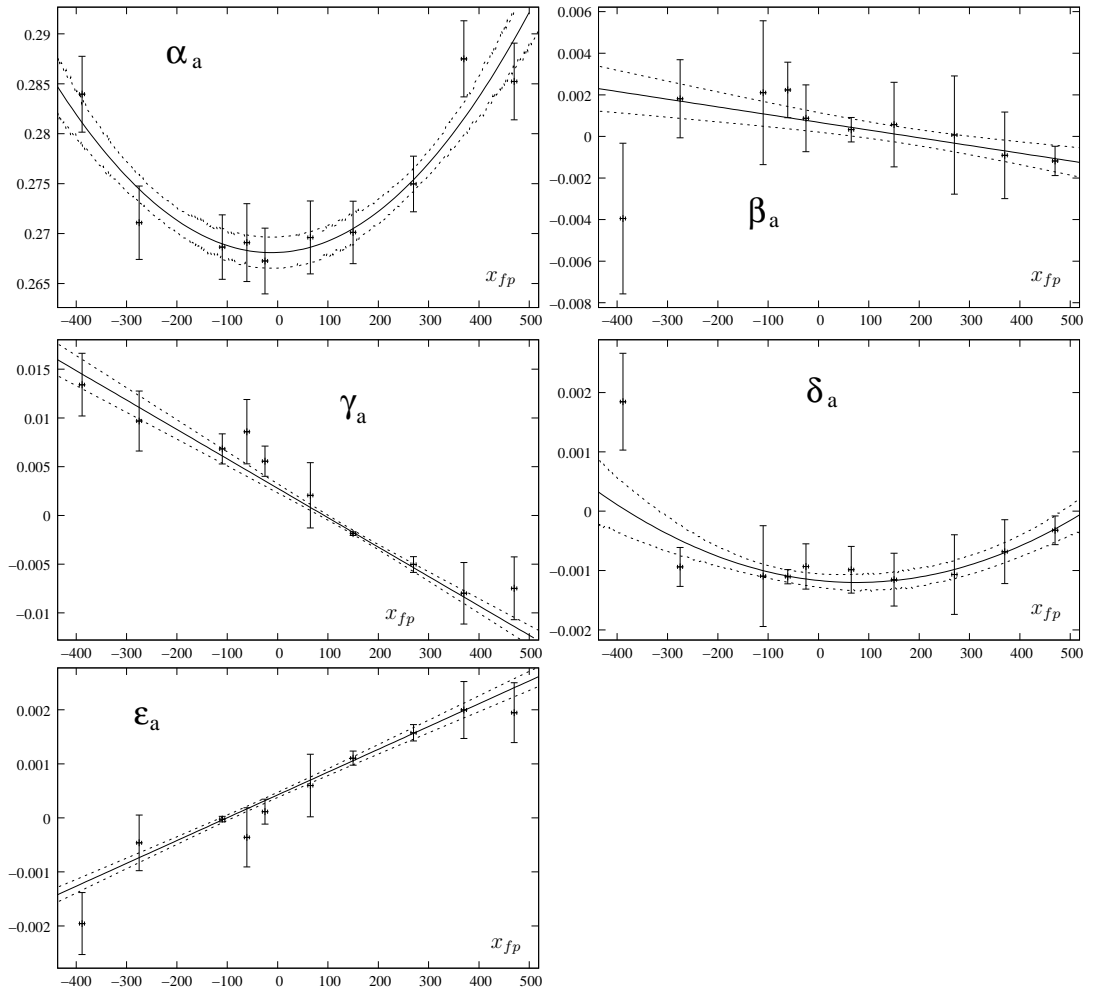


Figure B.41: Fit of the parameters $\alpha_a, \beta_a, \gamma_a, \delta_a$ and ϵ_a as a function of x_{fp} to determine \tilde{b}_{ijk} for $k=0$.

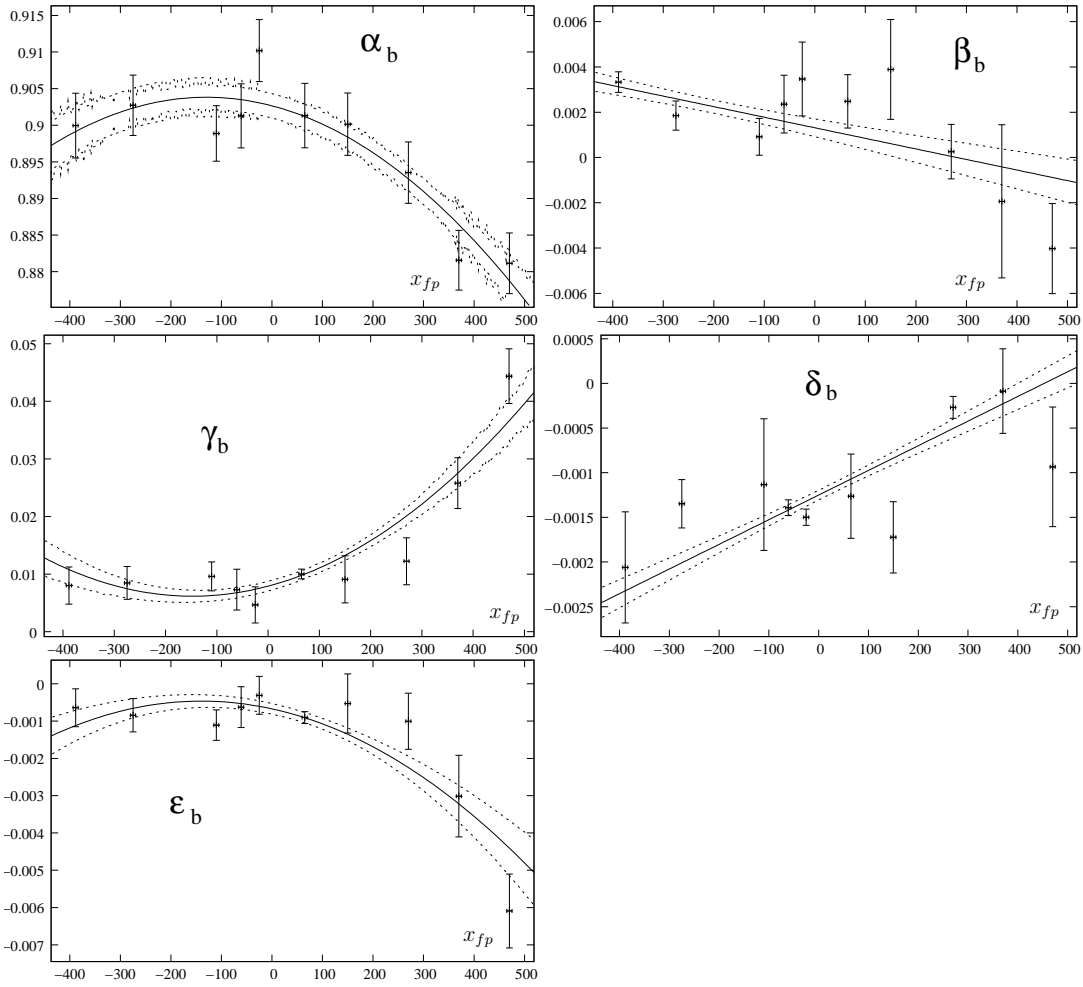


Figure B.42: Fit of the parameters $\alpha_b, \beta_b, \gamma_b, \delta_b$ and ϵ_b as a function of x_{fp} to determine \tilde{b}_{ijk} for $k=1$.

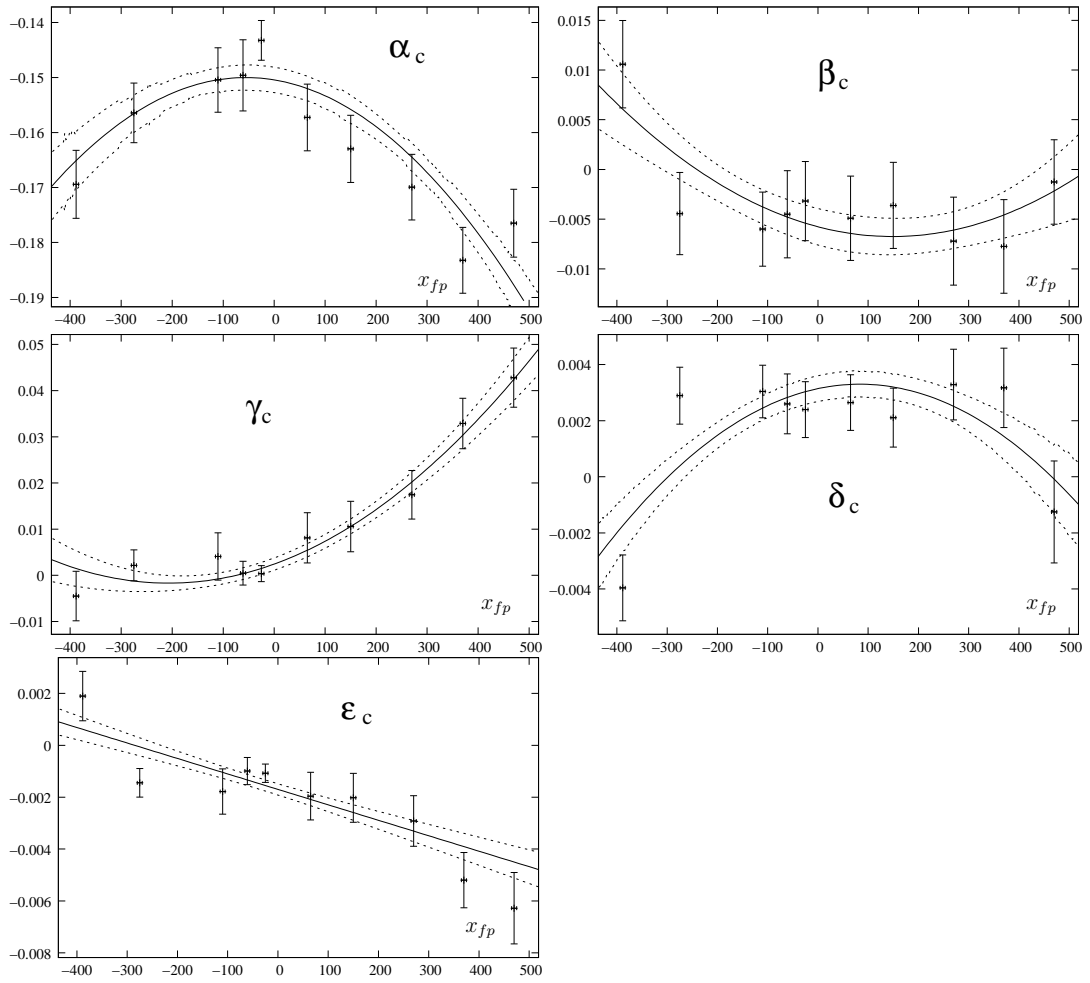


Figure B.43: Fit of the parameters $\alpha_c, \beta_c, \gamma_c, \delta_c$ and ϵ_c as a function of x_{fp} to determine \tilde{b}_{ijk} for $k=2$.

Table B.7: Results of the fit of $\alpha_{a,b,c}$, $\beta_{a,b,c}$, $\gamma_{a,b,c}$, $\delta_{a,b,c}$ and $\epsilon_{a,b,c}$ as a function of focal plane position.

$a(\phi_{tgt}, x_{fp})$ (k=0)	\tilde{b}_{0j0} (i=0)	\tilde{b}_{1j0} (i=1)	\tilde{b}_{2j0} (i=2)
α_a (j=0)	0.2681	2.20E-06	9.19E-08
β_a (j=1)	6.79E-04	-3.71E-06	0.00
γ_a (j=2)	2.79E-03	-3.02E	0.00
δ_a (j=3)	-1.17E-03	-8.76E-07	5.80E-09
ϵ_a (j=4)	4.24E-04	4.22E-06	0.00
$b(\phi_{tgt}, x_{fp})$ (k=1)	\tilde{b}_{0j1} (i=0)	\tilde{b}_{1j1} (i=1)	\tilde{b}_{2j1} (i=2)
α_b (j=0)	0.9026	-1.81E-05	-6.97E-08
β_b (j=1)	1.31E-03	-4.67E-06	0.00
γ_b (j=2)	7.91E-03	2.35E-05	7.97E-08
δ_b (j=3)	-1.25E-03	2.35E-05	7.97E-08
ϵ_b (j=4)	-6.73E-04	-2.96E-06-1.06E-08	
$c(\phi_{tgt}, x_{fp})$ (k=2)	\tilde{b}_{0j1} (i=0)	\tilde{b}_{1j1} (i=1)	\tilde{b}_{2j1} (i=2)
α_c (j=0)	-0.1504	-1.52E-05	-1.36E-07
β_c (j=1)	-5.76E-03	-1.32E-05	4.44E-08
γ_c (j=2)	2.43E-03	3.98E-05	9.62E-08
δ_c (j=3)	3.14E-03	3.79E-06	-2.27E-08
ϵ_c (j=4)	-1.70E-03	-5.96E-06	0.00

B.1.3 Results of the multi-hole slit calibration

The following section summarizes the results of the reconstruction of the horizontal and vertical scattering angles at the target, θ_{tgt} and ϕ_{tgt} . For ten x_{fp} regions, the original multi-hole slit images in θ_{fp} - y_{fp} coordinates (as determined by the raytracing in the MWDCs) are compared to the reconstructed image in θ_{tgt} - ϕ_{tgt} coordinates (reconstructed via the previously determined parameters a_{ijk} and \tilde{b}_{ijk}). In order to be able to judge the quality of the angle reconstruction, the multi-hole slit coordinates are superimposed to the reconstructed images as white lines. The reconstruction is generally very good, except for the $\theta \approx 1^\circ$ range when the focal plane position x_{fp} becomes large (i.e. towards higher excitation energies, see fig. B.48).

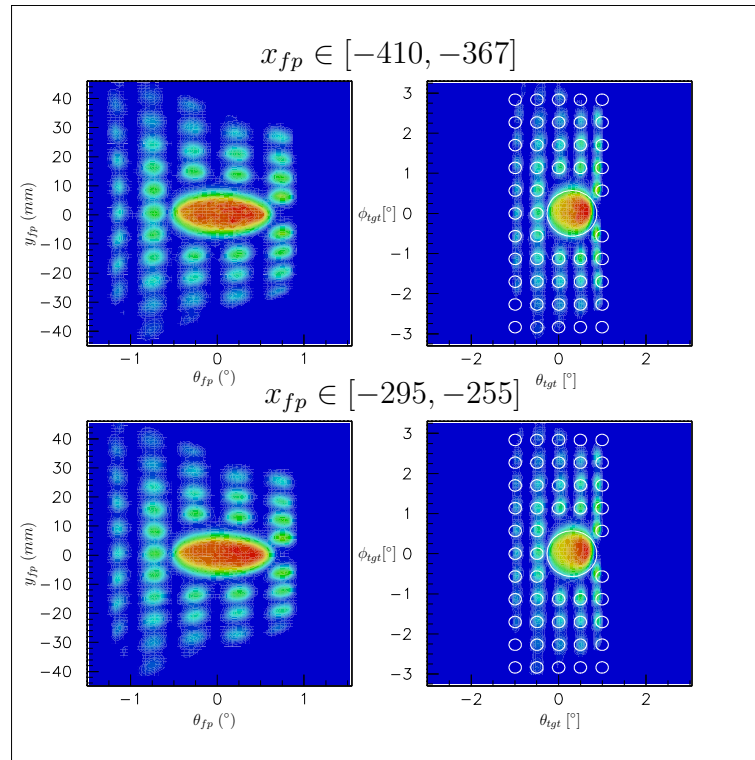


Figure B.44: Results of the sieve slit calibration for $x_{fp} \in [-410, -367]$ and $x_{fp} \in [-295, -255]$.

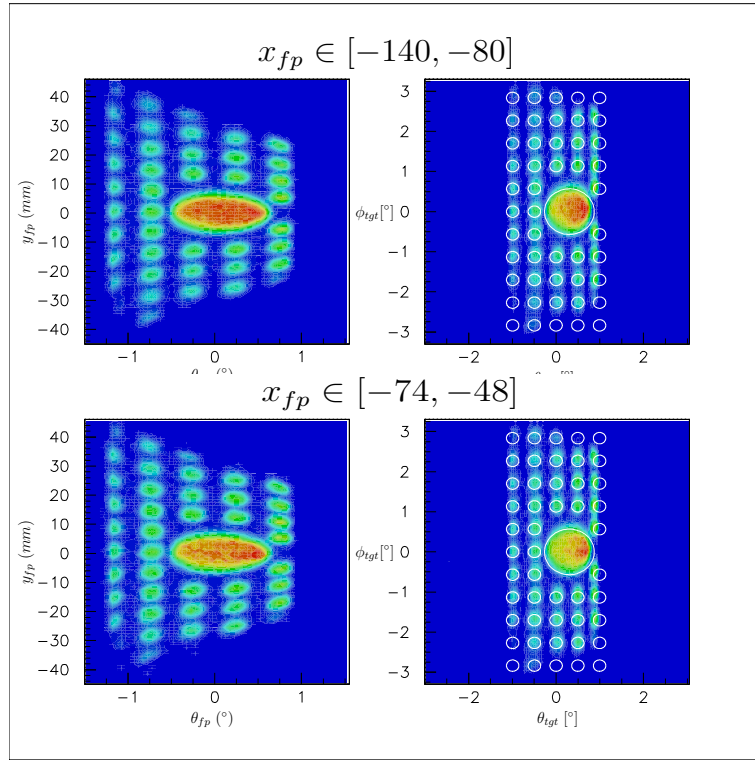


Figure B.45: Results of the sieve slit calibration for $x_{fp} \in [-140, -80]$ and $x_{fp} \in [-74, -48]$.

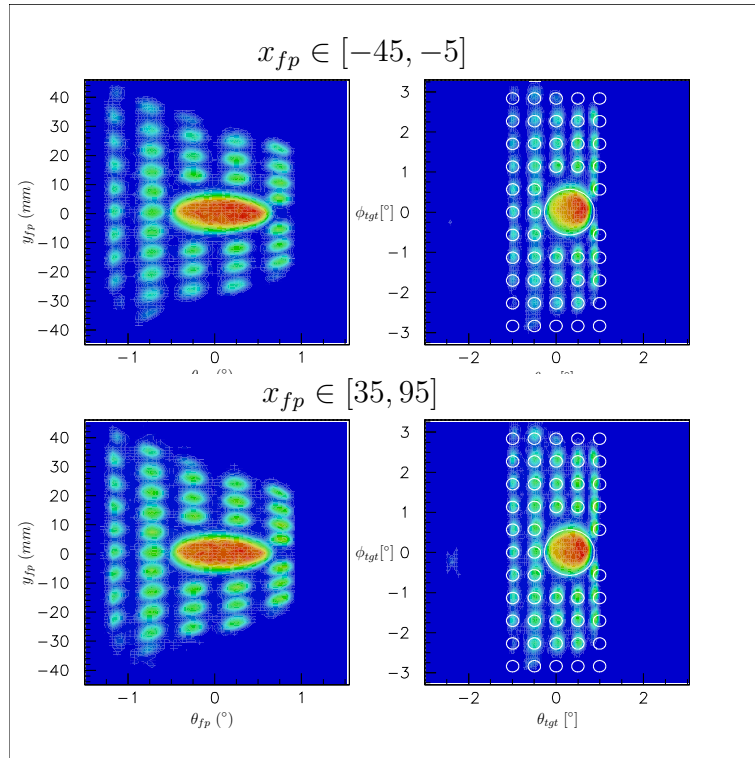


Figure B.46: Results of the sieve slit calibration for $x_{fp} \in [-45, -5]$ and $x_{fp} \in [35, 95]$.

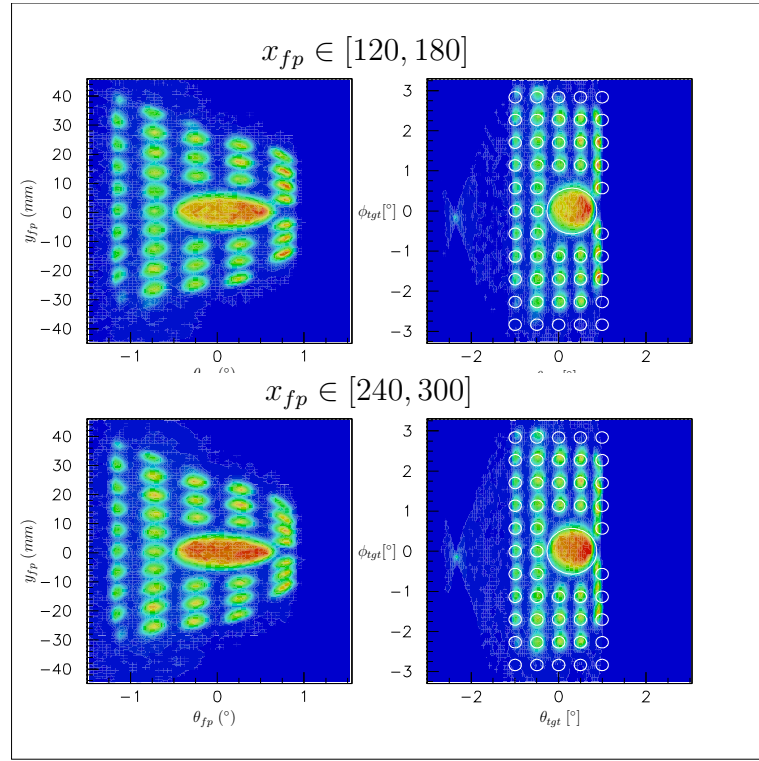


Figure B.47: Results of the sieve slit calibration for $x_{fp} \in [120, 180]$ and $x_{fp} \in [240, 300]$.

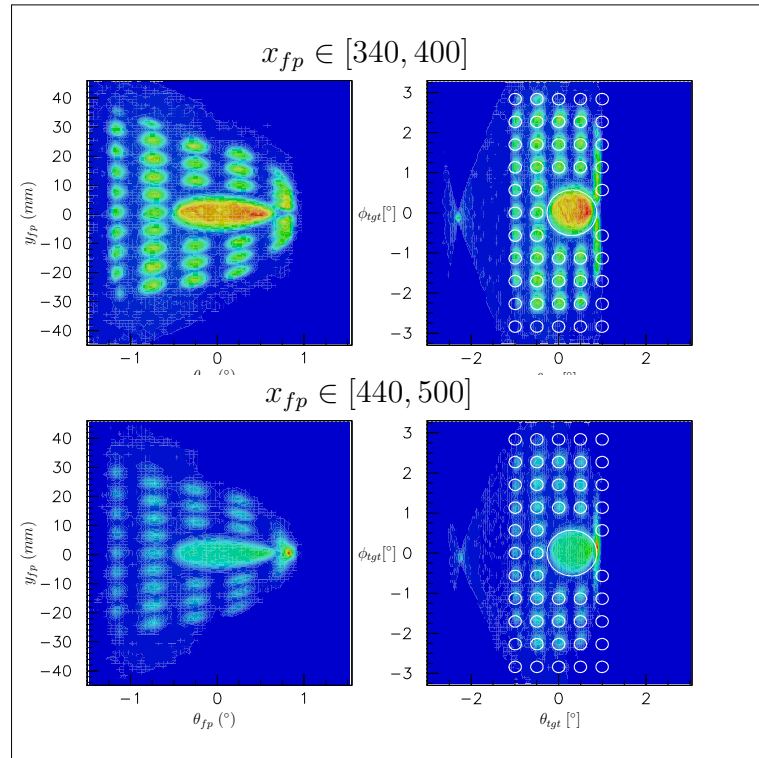


Figure B.48: Results of the sieve slit calibration for $x_{fp} \in [340, 400]$ and $x_{fp} \in [440, 500]$.

B.2 Correction of aberrations

After reconstruction of the horizontal and vertical scattering angles as described in the previous section, higher order ion-optical aberrations are still present in the spectra. They manifest themselves in curved lines (representing the observed peaks) in the x_{fp} vs. θ, ϕ plots (see fig. B.51). In order to correct these aberrations, the inverse transformation to these curved lines has to be applied. This inverse function cannot be given globally, and thus a local inverse mapping has to be found.

One such way is to divide the $x_{fp}-\theta$ and $x_{fp}-\phi$ planes in relatively thin stripes in the angles and reproducing the curved peaks by a cubic spline interpolation, to which the inverse mapping can be deduced. This procedure will be explained in detail in this section. For simplicity, we will only consider the case of θ aberration (the ϕ aberration is treated in exactly the same way).

B.2.1 The aberration as a mapping

We can model the observed aberration as a mapping transforming the rectilinear (desired) coordinates into the curved (observed) ones, as it is shown schematically in fig. B.49. The coordinates (x, θ) are transformed by the mapping T into coordinates (\tilde{x}, θ) (here we assume that the θ coordinate remains fixed in the plane):

$$(\tilde{x}, \theta) = T(x, \theta) \quad (\text{B.20})$$

The whole problem of treating the aberration is thus to find an inverse mapping, T^{-1} , which could transform every observed data point in such a way that the rectilinear spectrum is restored. This is however globally impossible since the mapping is not necessarily injective. We thus have to construct locally an inverse mapping that is rather simple to compute but still very precise in order to conserve the high resolution.

This can be achieved by dividing the $x-\theta$ plane into stripes (thus effectively creating a mesh, together with the $(\tilde{x}, \theta = 0)$ data points) and performing cubic spline interpolations.

B.2.2 Cubic spline interpolation

The method of cubic spline interpolation [Boo78, Sto80] is a well-known procedure to obtain a smooth curve connecting a given set of points. The method constructs a set of $n - 1$ cubic polynomials to n given “control points” and requires only these points as well as a value for the first derivatives at the beginning and the end of the interval where the interpolation takes place. The numerical calculation procedure for this interpolation is well-established and standard codes for various programming languages are available, e.g. [Pre92].

In our specific case, we cut the two-dimensional $x-\theta$ plane in $n - 1$ stripes (n control points) parallel to the x -axis. If we assume that the $\theta = 0$ line is unaffected by the

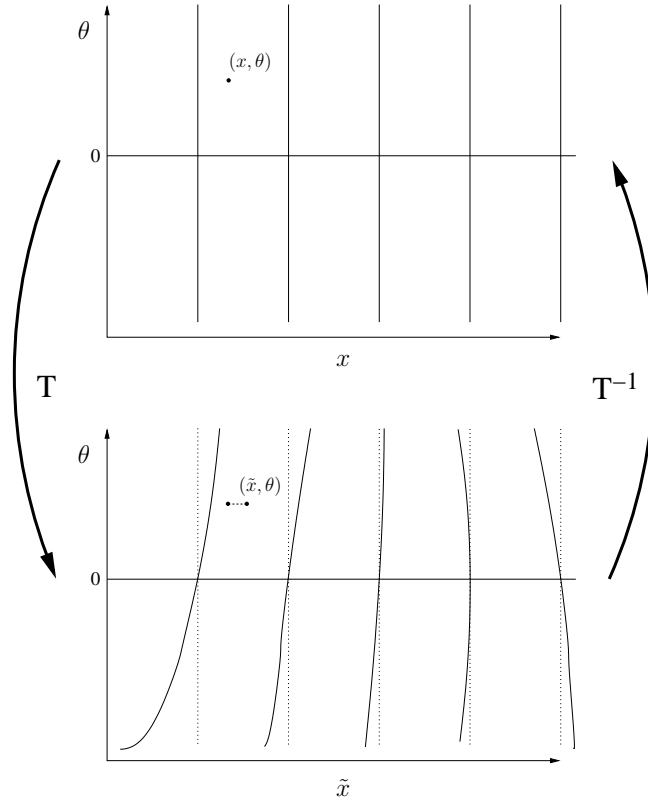


Figure B.49: Model of the observed aberration as a two-dimensional mapping which only changes the x coordinate.

mapping T , we then effectively obtain a mesh for the x - θ plane, defined by the θ -stripes and the $x = x^{(j)}(\theta = 0) = x_0^{(j)}$ values (see fig. B.50). Using the nomenclature defined in fig. B.50, we can calculate a spline function $S_{i,j}(\theta)$ (where i is the index numbering the stripes in θ , $i \in \{1 \dots n-1\}$) for every observed peak j ($j \in \{1, \dots, m\}$) which smoothly interpolates the observed data. An example of one such interpolation is shown in fig. B.51.

Two additional control points, for $i=0$ and $i=n+1$, are required in order to obtain the values of the spline function derivatives $S'_{1,j}(\theta_1)$ and $S'_{n-1,j}(\theta_n)$ at the endpoints of the interval. They are computed simply by taking the difference quotients (here, $x(\theta_i, j)$ denotes the x -coordinate of peak j at the angle θ_i) :

$$S'_{1,j}(\theta_1) = \frac{x(\theta_1, j) - x(\theta_0, j)}{\theta_1 - \theta_0} \quad (\text{B.21})$$

$$S'_{n-1,j}(\theta_n) = \frac{x(\theta_{n+1}, j) - x(\theta_n, j)}{\theta_{n+1} - \theta_n} \quad (\text{B.22})$$

and the spline function can be extended to areas outside of the interval boundaries by using a linear function. Thus the transformed coordinate (\tilde{x}, θ) of a point (x, θ) lying on a peak line can be described as a function of θ as follows (j is the peak index):

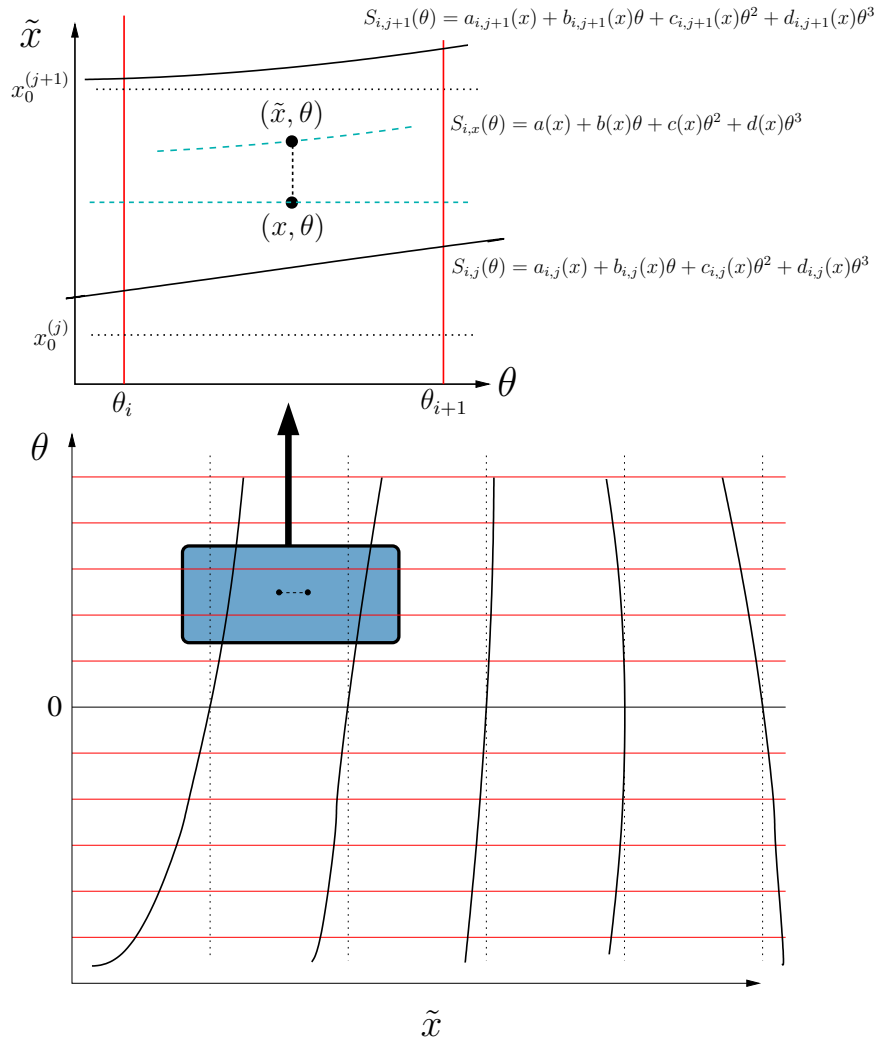


Figure B.50: Schematic drawing of the spline functions as derived from the observed data. The two dimensional spectrum is cut in stripes in θ and control points are marked along the observed “curved” peaks. With these, a smooth cubic spline function can be calculated, and thus an inverse mapping to the aberration can be derived.

$$\tilde{x} = \begin{cases} (x(\theta_1, j) - S'_{1,j}(\theta_1)\theta_1) + S'_{1,j}(\theta_1)\theta & \text{if } \theta < \theta_1 \\ S_{i,j}(\theta) = a_{i,j} + b_{i,j}\theta + c_{i,j}\theta^2 + d_{i,j}\theta^3 & \text{if } \theta_1 \leq \theta \leq \theta_n \\ (x(\theta_n, j) - S'_{n-1,j}(\theta_n)\theta_n) + S'_{n-1,j}(\theta_n)\theta & \text{if } \theta > \theta_n \end{cases} \quad (\text{B.23})$$

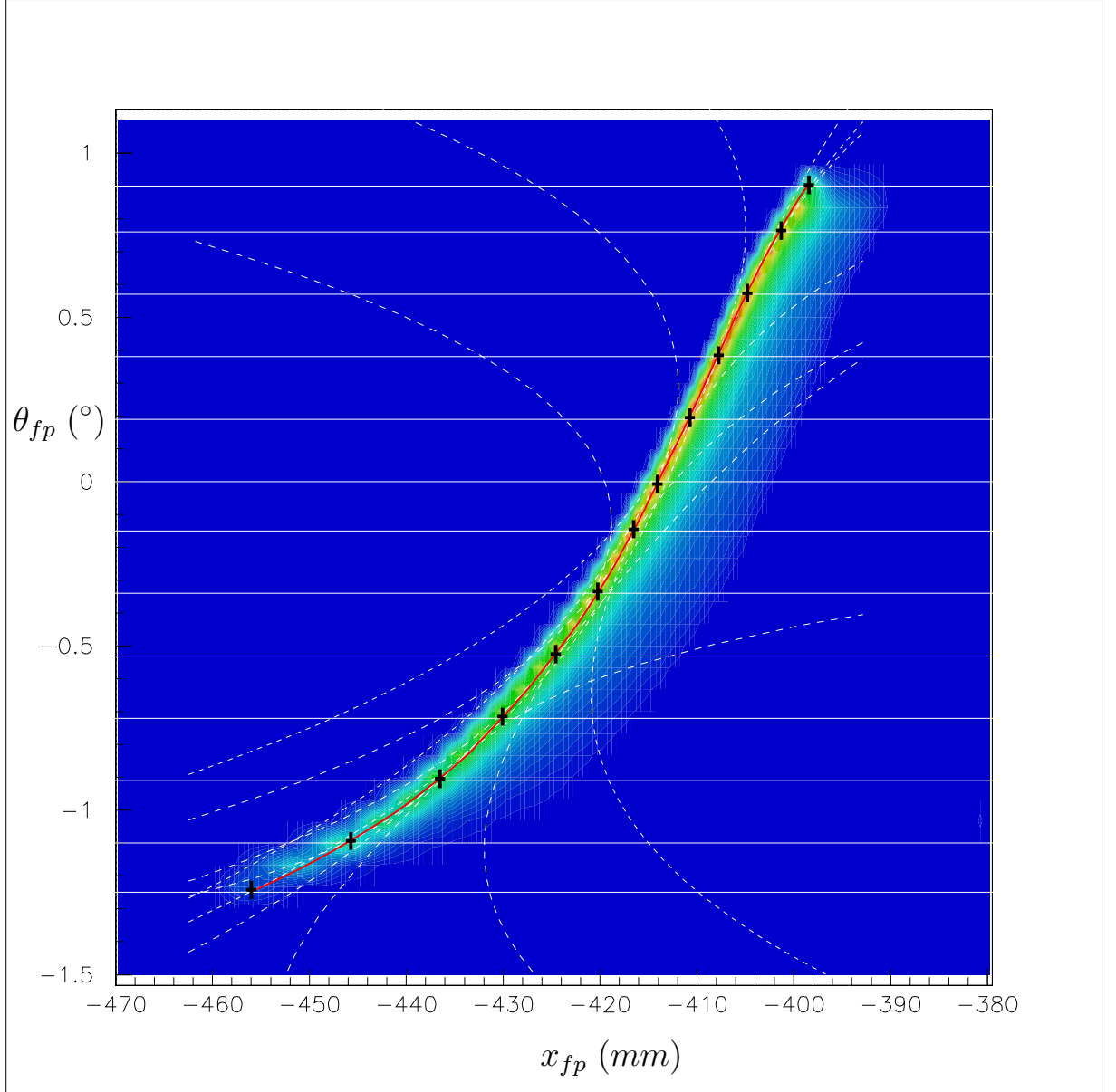


Figure B.51: Example of a cubic spline interpolation of one spectral line in the x_{fp} - θ_{fp} plane. The individual cubic polynomials are shown as white dotted lines, while the resulting overall spline is shown in red. The control points are marked by black crosses.

We know that the original peak line should be a straight line at fixed x-position for all θ values. However, we have to treat all incoming data points, and the overwhelming

majority does not lie exactly on a peak line. If the point (x, θ) in the rectilinear system does not lie on a peak line, we can obtain its transformed coordinate (\tilde{x}, θ) by the following procedure:

1. Choose the right θ -stripe $[\theta_i, \theta_{i+1}]$ (if θ lies outside the interval endpoints, go to point 4)
2. Calculate $S_{i,j}(\theta)$ for all j values (i.e. all peaks), to determine in which x -interval the preimage of \tilde{x} is located. Let us assume it is found that $S_{i,j_p}(\theta) < \tilde{x} < S_{i,j_p+1}(\theta)$, thus $x \in [x_0^{(j_p)}, x_0^{(j_p+1)}]$. If \tilde{x} lies outside of the range where it lies between two peaks, i.e. $j=1$ (below the lowest peak) or $j=m$ (above the highest peak), go to step 5.
3. The two known boundary spline functions $S_{i,j_p}(\theta)$ and $S_{i,j_p+1}(\theta)$ (see fig. B.50) are given by

$$S_{i,j_p}(\theta) = a_{j_p} + b_{j_p}\theta + c_{j_p}\theta^2 + d_{j_p}\theta^3 \quad (\text{B.24})$$

$$S_{i,j_p+1}(\theta) = a_{j_p+1} + b_{j_p+1}\theta + c_{j_p+1}\theta^2 + d_{j_p+1}\theta^3 \quad (\text{B.25})$$

The transformed point (\tilde{x}, θ) should thus be obtained via a cubic polynomial

$$\tilde{x} = S_{i,x}(\theta) = a(x) + b(x)\theta + c(x)\theta^2 + d(x)\theta^3 \quad (\text{B.26})$$

in which the coefficients are still unknown. We can derive these parameters (and by these means, x) if we linearly evolve the coefficients of the boundary spline functions. It can easily be shown that this conserves the smoothness of the obtained “intermediate” spline functions. We would thus get

$$a(x) = a_{j_p} + \frac{x - x_0^{j_p}}{x_0^{j_p+1} - x_0^{j_p}}(a_{j_p+1} - a_{j_p}) \quad (\text{B.27})$$

$$b(x) = b_{j_p} + \frac{x - x_0^{j_p}}{x_0^{j_p+1} - x_0^{j_p}}(b_{j_p+1} - b_{j_p}) \quad (\text{B.28})$$

$$c(x) = c_{j_p} + \frac{x - x_0^{j_p}}{x_0^{j_p+1} - x_0^{j_p}}(c_{j_p+1} - c_{j_p}) \quad (\text{B.29})$$

$$d(x) = d_{j_p} + \frac{x - x_0^{j_p}}{x_0^{j_p+1} - x_0^{j_p}}(d_{j_p+1} - d_{j_p}) \quad (\text{B.30})$$

where x is the unknown original position that we are looking for. By introducing $x_c := \frac{x - x_0^{j_p}}{x_0^{j_p+1} - x_0^{j_p}}$ and inserting the equations for the coefficients into eq. B.26, we get

$$\begin{aligned}\tilde{x} = & a_{j_p} + x_c(a_{j_p+1} - a_{j_p}) + [b_{j_p} + x_c(b_{j_p+1} - b_{j_p})] \theta + \\ & + [c_{j_p} + x_c(c_{j_p+1} - c_{j_p})] \theta^2 + [d_{j_p} + x_c(d_{j_p+1} - d_{j_p})] \theta^3\end{aligned}\quad (\text{B.31})$$

$$= (a_{j_p} + b_{j_p}\theta + c_{j_p}\theta^2 + d_{j_p}\theta^3) + x_c\{(a_{j_p+1} + b_{j_p+1}\theta + c_{j_p+1}\theta^2 + d_{j_p+1}\theta^3) - (a_{j_p} + b_{j_p}\theta + c_{j_p}\theta^2 + d_{j_p}\theta^3)\}\quad (\text{B.32})$$

$$= S_{i,j_p}(\theta) + x_c(S_{i,j_p+1}(\theta) - S_{i,j_p}(\theta))\quad (\text{B.33})$$

where everything is known from the data, except x_c , i.e. x itself, and the original x -position can now be obtained by solving the linear equation:

$$\frac{x - x_0^{j_p}}{x_0^{j_p+1} - x_0^{j_p}} = \frac{\tilde{x} - S_{i,j_p}(\theta)}{S_{i,j_p+1}(\theta) - S_{i,j_p}(\theta)}\quad (\text{B.34})$$

$$\Leftrightarrow x = (x_0^{j_p+1} - x_0^{j_p}) \left(\frac{\tilde{x} - S_{i,j_p}(\theta)}{S_{i,j_p+1}(\theta) - S_{i,j_p}(\theta)} \right) + x_0^{j_p}\quad (\text{B.35})$$

Thus, if θ and \tilde{x} are given, the preimage x can be calculated by finding the correct indices j_p (peak index) and i (stripe index). This procedure will yield the original x -position for all incoming data points that have θ values within the range $[\theta_1, \theta_n]$.

4. if $\theta \notin [\theta_1, \theta_n]$, then calculate \tilde{x} according to eq. B.23 for all j values and obtain the $[x_0^{(j_p)}, x_0^{(j_p+1)}]$ interval in which the preimage x of \tilde{x} is located, as in part 2. From then on, we proceed as in part 3., but this time the boundary functions are not cubic but linear:

$$f_{j_p+1}(\theta) = a_{j_p+1} + b_{j_p+1}\theta\quad (\text{B.36})$$

$$f_{j_p}(\theta) = a_{j_p} + b_{j_p}\theta\quad (\text{B.37})$$

$$\tilde{x} = f_x(\theta) = a(x) + b(x)\theta\quad (\text{B.38})$$

The coefficients are made to evolve linearly within the range $[x_0^{j_p}, x_0^{j_p+1}]$ as well:

$$a(x) = a_{j_p} + \frac{x - x_0^{j_p}}{x_0^{j_p+1} - x_0^{j_p}}(a_{j_p+1} - a_{j_p}) = a_{j_p} + x_c(a_{j_p+1} - a_{j_p})\quad (\text{B.39})$$

$$b(x) = b_{j_p} + \frac{x - x_0^{j_p}}{x_0^{j_p+1} - x_0^{j_p}}(b_{j_p+1} - b_{j_p}) = b_{j_p} + x_c(b_{j_p+1} - b_{j_p}).\quad (\text{B.40})$$

Inserting eqs. B.39 and B.40 into eq. B.38, we obtain

$$\tilde{x} = a_{j_p} + x_c(a_{j_p+1} - a_{j_p}) + (b_{j_p} + x_c(b_{j_p+1} - b_{j_p})) \theta\quad (\text{B.41})$$

$$= a_{j_p} + b_{j_p}\theta + x_c(a_{j_p+1} + b_{j_p+1}\theta - a_{j_p} - b_{j_p}\theta)\quad (\text{B.42})$$

which can be solved to obtain x . Inserting the values from eq. B.23, the solution can be written as

$$x = \begin{cases} (x_0^{j_p+1} - x_0^{j_p}) \left(\frac{\tilde{x} - x(\theta_1, j_p) + S'_{1,j_p}(\theta_1)(\theta_1 - \theta)}{(S'_{1,j_p}(\theta_1) - S'_{1,j_p+1}(\theta_1))(\theta_1 - \theta) + x(\theta_1, j_p+1) - x(\theta_1, j_p)} \right) + x_0^{j_p} \\ \text{(if } \theta < \theta_1) \\ \\ (x_0^{j_p+1} - x_0^{j_p}) \left(\frac{\tilde{x} - x(\theta_n, j_p) + S'_{n-1,j_p}(\theta_n)(\theta_n - \theta)}{(S'_{n-1,j_p}(\theta_n) - S'_{n-1,j_p+1}(\theta_n))(\theta_n - \theta) + x(\theta_n, j_p+1) - x(\theta_n, j_p)} \right) + x_0^{j_p} \\ \text{(if } \theta > \theta_n) \end{cases} \quad (\text{B.43})$$

5. If the x-position of the incoming particle is outside the boundaries defined by the individual splines, i.e. $\tilde{x} < S_{i1}(\theta)$ or $\tilde{x} > S_{im}(\theta)$, it is not possible to linearly evolve the spline coefficients as in step 3. The best way to solve this is by introducing “ghost peaks” with perfectly straight shape (vertical lines) that are located far below the lowest peak and far above the highest peak. This way, the spline coefficients can still evolve naturally and do not change drastically over short ranges in x . If these peaks are introduced, the calculation of the preimage can proceed as in step 3 or 4 (depending on the θ position).

B.2.3 Implementation in computer code

The correction of the aberration was implemented as FORTRAN code in the analyzer code for GRAND RAIDEN written by M. Yosoi [Yos01] to analyze data obtained via the TAMIDAQ acquisition system [Tam97].

The aberration correction was included in the CORRFP1 subroutine, which also includes the sieve slit correction procedure. The CORRFP1 subroutine is contained in the `option_m.f` source code of the Yosoi analyzer. The following sample code is an aberration correction by splines using 7 peaks numbered by $j = 1, \dots, 7$ and 13 θ_{tgt} positions as spline anchor points. These are given as `th(i)`. The x_{fp} positions of the 7 peaks at $\theta_{tgt}=0$ are given by `mid(i)`. The positions $x(\theta_1, j_p)$ and $x(\theta_n, j_p)$ (see previous section) are given by `xta(j)` and `xtb(j)`, respectively.

The coefficients of the various splines are calculated via a separate program, `splicalc`, which uses the spline anchor points determined from the data to compute the spline coefficients (`AG(j,i)`, `BG(j,i)`, `CG(j,i)`, `DG(j,i)`) and the derivatives $S'_{1,j_p}(\theta_1)$ (`slop(j,1)`) and $S'_{n-1,j_p}(\theta_n)$ (`slop(j,2)`). All the values required by the spline correction routine inside the analyzer code are conveniently produced by the `splicalc` program and its output (the numerical value of the variables) has just to be inserted inside the `option_m.f` file at the right place.

Only the code for the correction of θ -aberrations is presented here, the correction of ϕ -aberrations works exactly in the same way. The corrections are carried out subsequently, which means first the correction of θ aberrations needs to be processed by offline analysis, then the output used to determine the required parameters for the ϕ aberration correction.

```

c FIND THE CORRECT STRIPE IN THETA
c (th(i) values compared to AC)
c "i" has to be selected (isel)
c AC=(theta_tgt)
c XC=(x_fp)
c th(i)=(theta_i, spline anchor point)
c xta(j)=(x_fp position at theta_1)
c xtb(j)=(x_fp position at theta_n)

      isel=0
      do 35 i=1,13
        if(AC.gt.th(i)) then
          isel=i-1
        endif
      35   enddo
c      PRINT*, 'selected stripe:', isel

c FIND THE CORRECT PEAK j
c since the stripe has been selected, calculate the
c spline values for all peaks j at "isel" and compare
c with XC to find the correct j.

      if(isel.eq.0)then
c If theta value is below the last spline anchor point,
c use linear continuation
        jsel=0
        do 38 j=1,7
c requires access to x and theta anchor points
c y(i,X)=mid(i) is the x-position
          sjp=(xta(j)-slop(j,1)*th(2))+slop(j,1)*AC
          if(XC.ge.sjp)then
            jsel=j
          endif
        38   enddo

      elseif(isel.ge.1.and.isel.lt.11)then
c Region where regular splines can be used, main part
        jsel=0
        do 36 j=1,7
          sjp=ag(j,isel)+AC*(bg(j,isel)+AC*(cg(j,isel)+
&          AC*dg(j,isel)))
          if(XC.ge.sjp)then
            jsel=j
          endif
        36   enddo

      elseif(isel.ge.11)then
c If theta value is above the last spline anchor point,
c use linear continuation

```

```

        jsel=0
        do 41 j=1,7
c requires access to x and theta anchor points
            sjp=(xtb(j)-slop(j,2)*th(12))+slop(j,2)*AC
            if(XC.ge.sjp)then
                jsel=j
            endif
41        enddo
c
        else PRINT*, '*ERROR* in determination of x-position'
        endif

c then calculate the corrected x-value (preimage, yc)
c Positions outside of spline range have to be considered
c as well (linear interpolation), depends on "isel"
c GHOST PEAKS AT X=-1000 and X=1000 introduced.

c FIRST, POSSIBILITY THAT POINT LIES BELOW THE THETA-SPLINE
c REGION (REGION WHERE LINEAR CONTINUATION IS USED, isel=0)

        if(isel.eq.0)then
            if(jsel.ge.1.and.jsel.lt.7)then
                XC=(mid(jsel+1)-mid(jsel))*(XC-xta(jsel)+slop(jsel,1)*
&          (th(2)-AC))/((slop(jsel,1)-slop(jsel+1,1))*(th(2)-
&          AC)+xta(jsel+1)-xta(jsel))+mid(jsel)

c SLOPE OF GHOST PEAK AT X=-1000. IS ZERO
                elseif(jsel.lt.1)then
                    XC=(mid(jsel+1)+1000.)*(XC+1000.+0.*
&          (th(2)-AC))/((0.-slop(jsel+1,1))*(th(2)-
&          AC)+xta(jsel+1)+1000.)-1000.

c SLOPE OF GHOST PEAK AT X=+1000. IS ZERO
                elseif(jsel.ge.7)then
                    XC=(1000.-mid(jsel))*(XC-xta(jsel)+slop(jsel,1)*(th(2)
&          -AC))/((slop(jsel,1)-0.)*(th(2)-AC)+
&          1000.-xta(jsel))+mid(jsel)
                    endif

c POINT LIES WITHIN THE THETA-SPLINE REGION
c (isel>=1 and =<11)

                elseif(isel.ge.1.and.isel.lt.11)then

                    if(jsel.ge.1.and.jsel.lt.7)then
                        sjp=ag(jsel,isel)+AC*(bg(jsel,isel)+AC*(cg(jsel,isel)
&          +AC*dg(jsel,isel)))

                        sjp1=ag(jsel+1,isel)+AC*(bg(jsel+1,isel)+AC*(cg(jsel+1,
&          isel)+pointx*dg(jsel+1,isel)))

```



```

      dsj=sjp1-sjp

      XC=(mid(jsel+1)-mid(jsel))*((XC-sjp)/dsj)+mid(jsel)

      elseif(jsel.lt.1)then
        sjp=-1000.

        sjp1=ag(jsel+1,isel)+AC*(bg(jsel+1,isel)+AC*(cg(jsel+1,
&         isel)+AC*dg(jsel+1,isel)))

        dsj=sjp1-sjp

        XC=(mid(jsel+1)+1000.)*((XC-sjp)/dsj)-1000

        elseif(jsel.ge.7)then
          sjp=ag(jsel,isel)+AC*(bg(jsel,isel)+AC*(cg(jsel,isel)
&         +AC*dg(jsel,isel)))

          sjp1=1000.
          dsj=sjp1-sjp

          XC=(1000.-mid(jsel))*((XC-sjp)/dsj)+mid(jsel)
          endif

c POINT LIES ABOVE THE THETA-SPLINE REGION
c (WHERE LINEAR CONTINUATION IS USED, isel>=11)

      elseif(isel.ge.11)then
        if(jsel.ge.1.and.jsel.lt.7)then
          XC=(mid(jsel+1)-mid(jsel))*(XC-xtb(jsel)+slop(jsel,2)*
&         (th(12)-AC))/((slop(jsel,2)-slop(jsel+1,2))*(th(12)-
&         AC)+xtb(jsel+1)-xtb(jsel))+mid(jsel)

c SLOPE OF GHOST PEAK AT X=-1000. IS ZERO
          elseif(jsel.lt.1)then
            XC=(mid(jsel+1)+1000.)*(XC+1000.+0.*
&         (th(12)-AC))/((0.-slop(jsel+1,2))*(th(12)-
&         AC)+xtb(jsel+1)+1000.)-1000.

c SLOPE OF GHOST PEAK AT X=+1000. IS ZERO
          elseif(jsel.ge.7)then
            XC=(1000.-mid(jsel))*(XC-xtb(jsel)+slop(jsel,2)*(th(12)
&         -AC))/((slop(jsel,2)-0.)*(th(12)-AC)+
&         1000.-xtb(jsel))+mid(jsel)
            endif

      endif

```

Alternatively, if the aberration is rather symmetrical in the θ or ϕ coordinate, or if states (peak lines) are too close to each other to effectively use the spline interpolation, it is possible to use a polynomial interpolation of the whole peak line (fourth order with no constant term is usually a good choice). Using a fourth order polynomial as the describing function of the aberration for each peak, the coefficients can be evolved linearly as for the spline case. The software above then simplifies since a stripe in θ (or ϕ) no longer needs to be selected or considered in the correction procedure. This can be implemented by using a code such as the following (here, $bg(j)$, $cg(j)$, $dg(j)$, $eg(j)$ represent the linear, quadratic, cubic and quartic coefficients of each fitted peak shape in x - θ space)

```

        if(jsel.ge.1.and.jsel.lt.14)then
          sjp=mid(jsel)+AC*(bg(jsel)+AC*(cg(jsel)+AC*(dg(jsel)
&          +AC*eg(jsel))))
          sjp1=mid(jsel+1)+AC*(bg(jsel+1)+AC*(cg(jsel+1)
&          +AC*(dg(jsel+1)+AC*eg(jsel+1))))

          dsj=sjp1-sjp

          XC=(mid(jsel+1)-mid(jsel))*((XC-sjp)/dsj)+mid(jsel)

          elseif(jsel.lt.1)then
            sjp=-1000.

            sjp1=mid(jsel+1)+AC*(bg(jsel+1)+AC*(cg(jsel+1)
&            +AC*(dg(jsel+1)+AC*eg(jsel+1))))

            dsj=sjp1-sjp

            XC=(mid(jsel+1)+1000.)*((XC-sjp)/dsj)-1000

            elseif(jsel.ge.14)then
              sjp=mid(jsel)+AC*(bg(jsel)+AC*(cg(jsel)+AC*(dg(jsel)
&              +AC*eg(jsel))))

              sjp1=1000.
              dsj=sjp1-sjp

              XC=(1000.-mid(jsel))*((XC-sjp)/dsj)+mid(jsel)
            endif

```

Appendix C

Energy calibration procedure

In order to match the recorded arbitrary channels to the excitation energies present in the spectrum, an energy calibration has to be carried out. To this end, it is necessary to have a reasonable amount of reference peaks with well-known energy over a broad range of excitation energies. During the experiment, spectra of the reactions $^{24,26}\text{Mg}(^3\text{He},\text{t})$ and $\text{PVA}^1(^3\text{He},\text{t})$ were recorded and were analyzed for the energy calibration. Some sharp states in the $^9\text{Be}(^3\text{He},\text{t})^9\text{B}$ spectrum can also be used for the energy calibration.

The excitation energies obtained for different nuclei cannot be immediately compared, as the momentum of the outgoing triton depends on the Q value of the reaction and on the mass of the target nucleus. However, the excitation energies can be compared if we translate them to their magnetic rigidity value², which is equal to the momentum p divided by the charge q_c

$$B r = \frac{p}{q_c} \quad (\text{C.1})$$

where B is the magnetic field of the spectrometer and r is the radius of the mean orbit of the tritons. For the energy calibration, we thus first have to construct a relation between known excitation energies and the recorded channel numbers, and subsequently a relation between energies and magnetic rigidity values. In this way, a channel-energy relation can be derived for arbitrary channels and a given nucleus.

The magnetic rigidity values Br are derived using the relativistic two-body kinematics code `relkin` [Phi67, Poi68, Dav69] with some modifications, including an updated mass excess table [Aud95], a corrected calculation of the reaction threshold and the possibility to calculate values for the zero-degrees scattering angle. The stopping power of chemical elements for charged particles is calculated in a subroutine using the algorithm of Williamson, Boujot, and Picard [Wil66].

To determine the channel positions of known states, raytraced spectra with a scattering angle cut of $0^\circ \leq |\Theta| \leq 0.5^\circ$ were used for the calibration runs. The peak channels

¹Polyvinyl alcohol, $(\text{CH}_2\text{-CH-OH})_n$

²The magnitude of B times the gyroradius of a charged particle equals to its momentum per unit charge, also called *magnetic rigidity* ($B r = \frac{mv_\perp}{|q|}$)

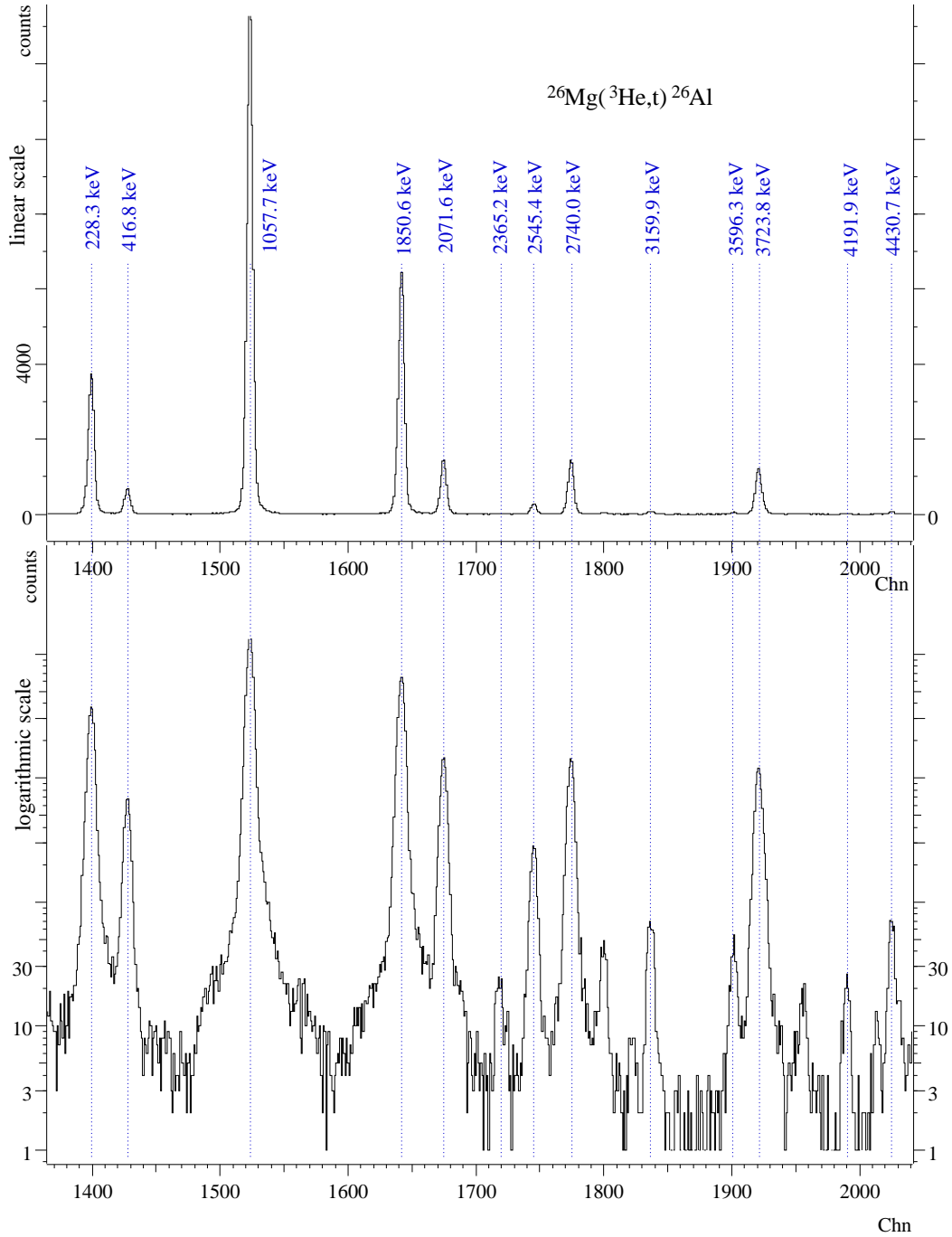


Figure C.1: Lowest part of the recorded spectrum of the $^{26}\text{Mg}(^3\text{He},t)^{26}\text{Al}$ reaction used for the energy calibration. Some peaks are very strong so the spectrum is shown in both linear scale and logarithmic scale.

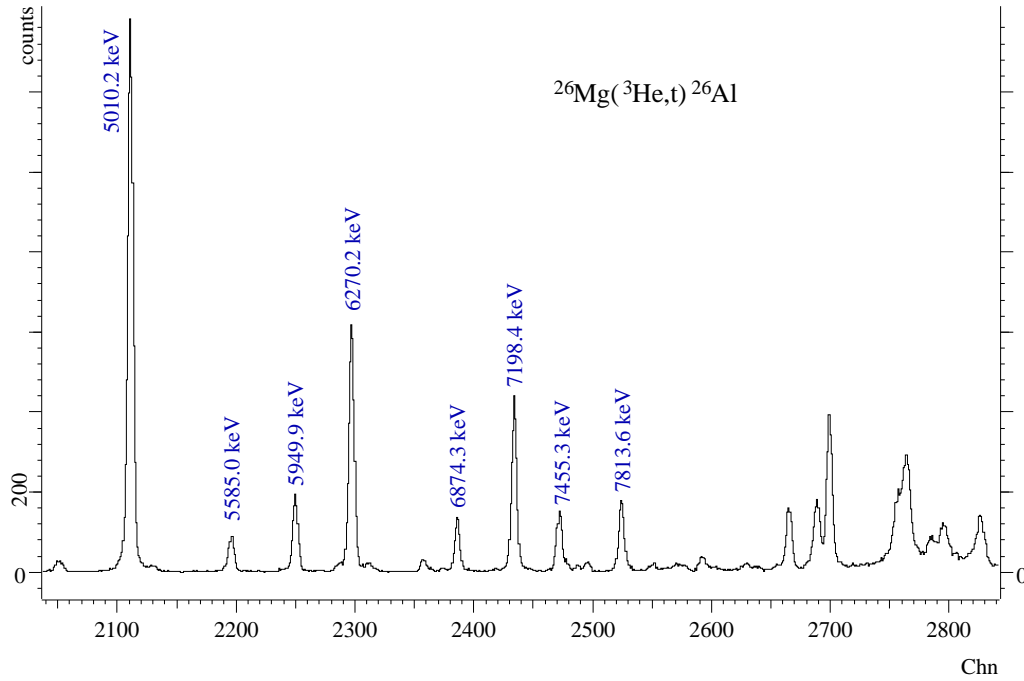


Figure C.2: Higher part of the recorded spectrum of the $^{26}\text{Mg}(^3\text{He},t)^{26}\text{Al}$ reaction used for the energy calibration.

Table C.1: Thickness of targets used in the experiments.

Target	thickness [mg/cm ²]
^9Be	1.73
^{26}Mg	0.872
^{24}Mg	0.815
PVA	1.1

were determined by fitting the spectra and the results are summarized in table C.2, together with the Br values computed with `relkin`. The spectra are shown in figs. C.1, C.2, C.3 and C.4. The calculated Br values are fitted as a second-order polynomial function f of the channel number x . For a better stability of the fit routine, 5000 kG cm is subtracted from the Br value.

$$f(x) = a + bx + cx^2 \quad (\text{C.2})$$

Since the used targets have different thicknesses (see table C.1), the experimental Br values are slightly shifted against the values calculated by `relkin`, which gives a bad fit using the unshifted values (see upper part of figure C.5). Since ^{26}Al has the most data points with high accuracy, all other data points were shifted to match the ^{26}Al Br values as well as possible. A single shift term was used per target nucleus. These terms are given in table C.3. The fact that the constituent nuclei of the PVA target require roughly the same shift term corroborates the assumption that the observed shifts are a

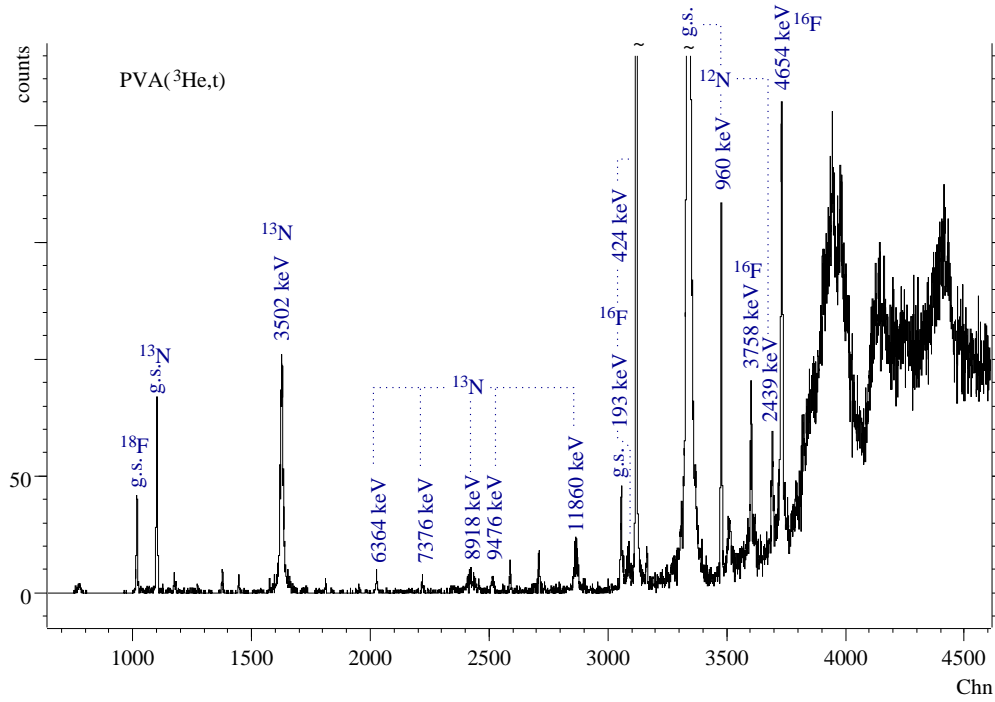


Figure C.3: Recorded spectrum of the $PVA(^3\text{He},t)$ reaction used for the energy calibration. The used peaks belonging to $^{16,18}\text{F}$ and $^{12,13}\text{N}$ are marked.

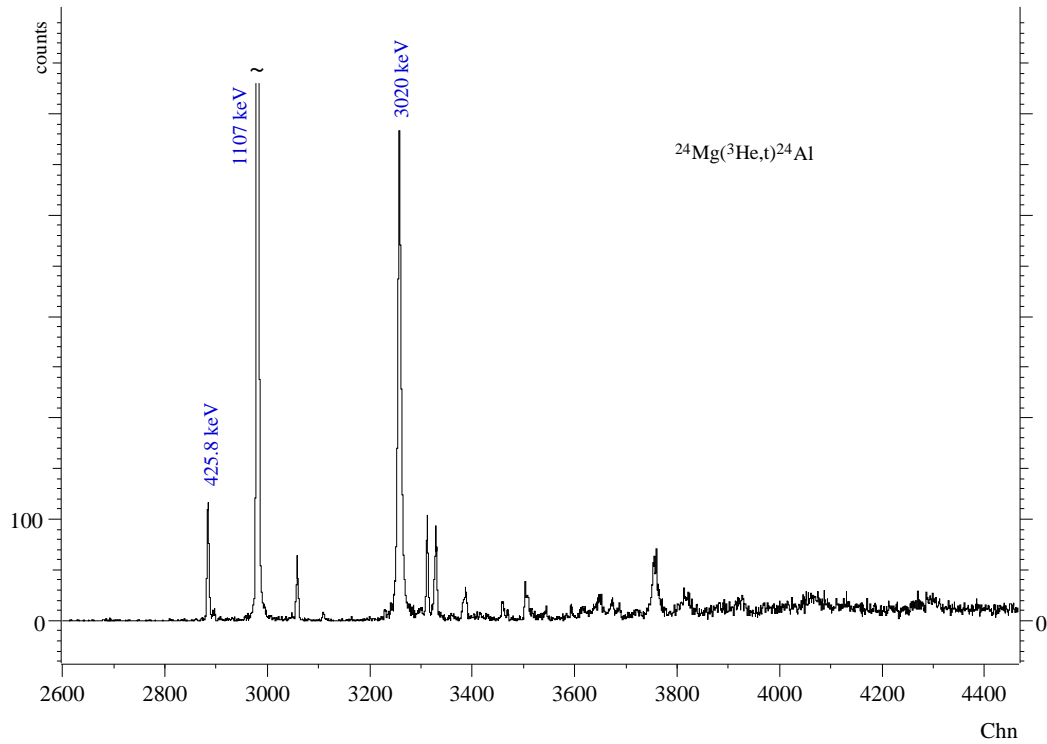


Figure C.4: recorded spectrum of the $^{24}\text{Mg}(^3\text{He},t)^{24}\text{Al}$ reaction used for the energy calibration. Only the energy of the first 1^+ peak (425.8(1) keV) is known with sufficient accuracy to be used in the energy calibration.

Table C.2: Energy levels used for the energy calibration of the spectrum.

Chn [N]	E_x [keV]	Br [kG cm]	Chn [N]	E_x [keV]	Br [kG cm]
²⁶ Al			²⁴ Al		
1399.17(2)	228.305(13)	5283.016(1)	2884.736(86)	425.8(1)	5214.154(1)
1427.517(51)	416.852(3)	5281.734(1)	¹⁸ F		
1523.323(11)	1057.739(12)	5277.375(1)	1017.35(20)	0.0(2)	5300.502(2)
1641.772(15)	1850.62(3)	5271.979(1)	¹³ N		
1674.562(27)	2071.64(4)	5270.47(1)	1101.84(13)	0(1)	5296.671(7)
1718.440(28)	2365.150(18)	5268.475(1)	1626.34(28)	3502(2)	5272.861(14)
1745.136(62)	2545.367(17)	5267.247(1)	¹⁶ F		
1774.082(27)	2740.03(3)	5265.920(1)	3056.2(3)	0(1)	5206.417(7)
1836.67(13)	3159.889(13)	5263.058(1)	3086.00(96)	193(6)	5205.085(41)
1901.70(18)	3596.34(4)	5260.081(1)	3119.109(64)	424(5)	5203.491(34)
1920.975(39)	3723.81(4)	5259.211(1)	3163.44(41)	721(4)	5201.441(28)
1990.03(22)	4191.92(6)	5256.016(1)	3602.62(24)	3758(6)	5180.432(42)
2025.24(13)	4430.72(6)	5254.385(1)	3731.32(14)	4654(6)	5174.218(42)
2111.068(17)	5010.24(7)	5250.426(1)	¹² N		
2196.044(74)	5584.99(6)	5246.497(1)	3338.012(12)	0(2)	5193.054(14)
2249.890(47)	5949.93(8)	5244.001(1)	3477.464(96)	960(12)	5186.401(84)
2297.168(28)	6270.19(11)	5241.809(1)	3691.94(29)	2439(9)	5176.132(63)
2386.173(55)	6874.29(8)	5237.673(1)	⁹ B		
2433.970(31)	7198.44(12)	5235.453(1)	926.86(1)	0(1)	5304.481(7)
2472.091(59)	7455.34(19)	5233.692(2)	1281.599(58)	2345(11)	5288.569(75)
2524.360(51)	7813.63(18)	5231.236(2)	3103.910(72)	14655.0(25)	5204.122(18)
			3456.97(18)	17076(4)	5187.327(28)

target thickness effect. After thus adjusting the Br values, the data was fitted again, this time yielding a reasonable residuum (see bottom part of figure C.5).

In order to get the final energy calibration for a given spectrum, Br values are calculated with `relkin` for various equidistant energies and the relation between Br value y and energy E is again fitted with a second-order polynomial.

$$E(y) = \alpha + \beta y + \gamma y^2 \quad (\text{C.3})$$

Combining the result of this fitting procedure with $f(x)$ derived before, one obtains a direct relationship between channel number x and energy E , which is a polynomial of degree four:

Table C.3: Shift terms of Br against the calculated values for ^{26}Al .

Target nucleus	Shift term [kG cm]
^9Be	0.162
^{26}Mg	0.000
^{24}Mg	-0.177
^{12}C	0.213
^{13}C	0.203
^{16}O	0.236
^{18}O	0.261

$$y = f(x) + 5000 = (a + 5000) + bx + cx^2 \quad (\text{C.4})$$

$$\Rightarrow E(x) = e_1 + e_2x + e_3x^2 + e_4x^3 + e_5x^4 \quad (\text{C.5})$$

where

$$e_1 = \alpha + \beta a - 5000\beta + \gamma a^2 + 5000^2\gamma - 10000a\gamma \quad (\text{C.6})$$

$$e_2 = \beta b + 2\gamma ab - 10000b\gamma \quad (\text{C.7})$$

$$e_3 = \beta c + \gamma b^2 + 2\gamma ac - 10000c\gamma \quad (\text{C.8})$$

$$e_4 = 2\gamma bc \quad (\text{C.9})$$

$$e_5 = \gamma c^2 \quad (\text{C.10})$$

The values obtained from this procedure for the nuclei of interest are summarized in table C.4.

Table C.4: Parameters of the energy calibration function for various nuclei.

Parameter	^9B	^{13}N
e_1	-6075.605	-7231.988
e_2	6.505	6.500
e_3	$5.849 \cdot 10^{-5}$	$6.153 \cdot 10^{-5}$
e_4	$-8.333 \cdot 10^{-10}$	$-7.484 \cdot 10^{-10}$
e_5	$-5.698 \cdot 10^{-15}$	$-5.118 \cdot 10^{-15}$

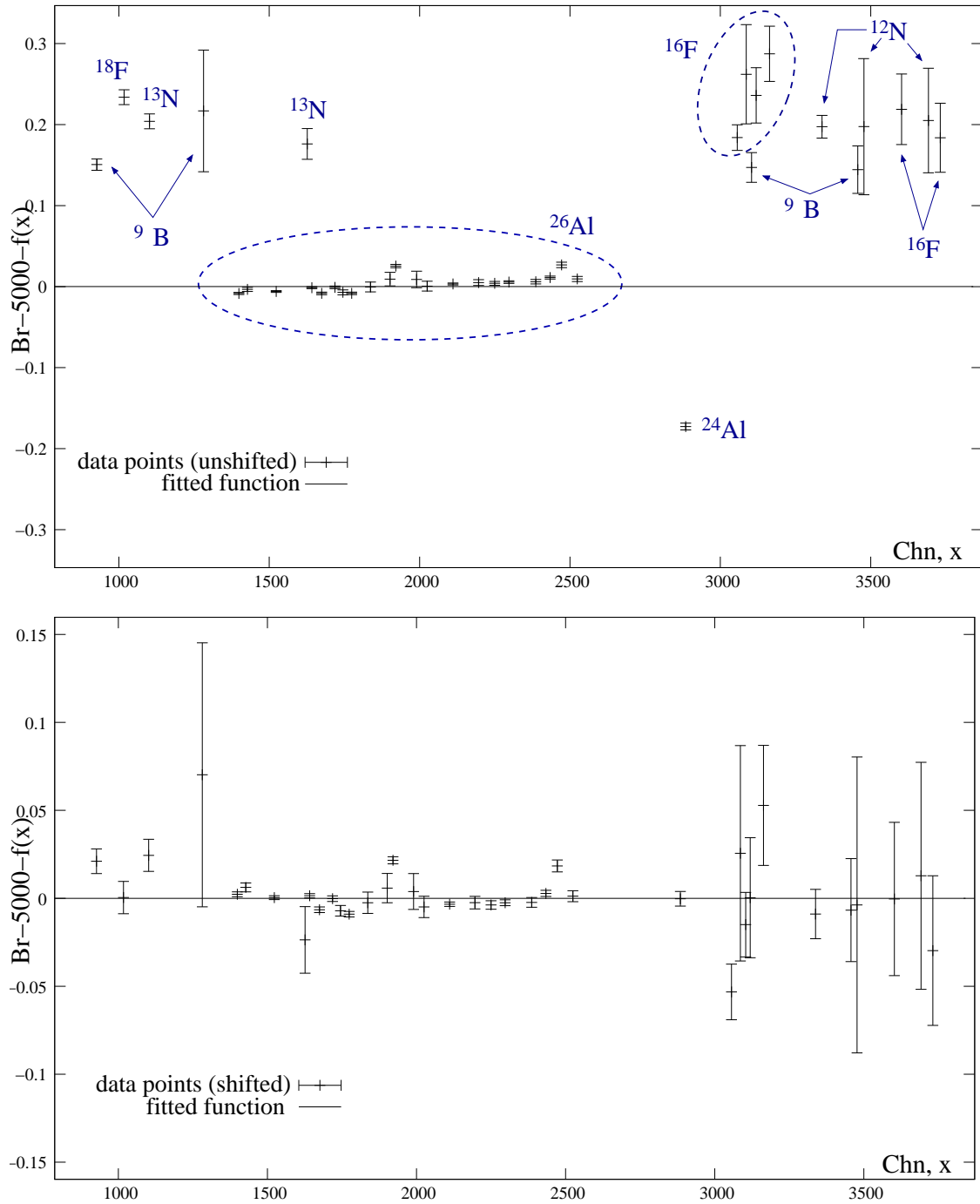


Figure C.5: Residuum of the fit function connecting the channels and the Br values. Due to target thickness effects, the measured Br values differ from the calculated values (using *relkin*) depending on the target, which leads to unconclusive fit results. After a correction for these shifts, an accurate fit function could be derived.

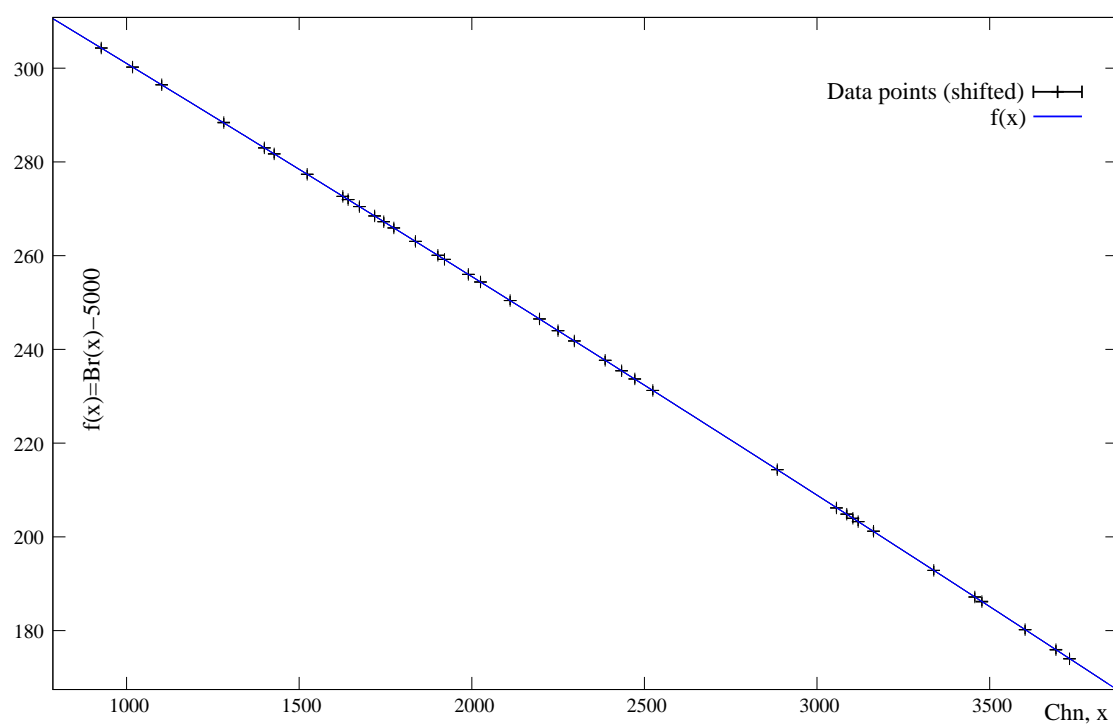


Figure C.6: Graph of the fitted second-order function $f(x)$ establishing the correspondence from channels x to Br values ($Br(x)=f(x)+5000$) for the target nucleus ${}^9\text{Be}$.

Appendix D

RAY-ID data from the MWDCs for both experiments

XXVII APPENDIX D. RAY-ID DATA FROM THE MWDCS FOR BOTH EXPERIMENTS

Table D.1: Raytracing information of the MWDCs for both charge-exchange experiments. The RAY-ID number is the raytracing identification channel of the Yosoi analyzer software. The description of the RAY-ID number is given in the first column. The plane numbers 1,2,4 and 5 correspond to the X- and U-planes of the two MWDCs. Different RAY-ID events are mutually exclusive.

Description	RAY-ID	${}^9\text{Be}({}^3\text{He},t){}^9\text{B}$ experiment
no region ID	-10	624
Bad VDC events	-9	1557711
position ID of all planes unsuccessful	-8	245936
four planes have two good clusters	-7	8594
position ID of only one plane successful (plane 5)	-5	220640
position ID of only one plane successful (plane 4)	-4	75616
position ID of only one plane successful (plane 2)	-2	28006
position ID of only one plane successful (plane 1)	-1	15173
RAY-TRACING SUCCESSFUL	0	30085844
position ID unsuccessful in plane 1	1	59806
position ID unsuccessful in plane 2	2	49791
position ID unsuccessful in plane 4	4	100933
position ID unsuccessful in plane 5	5	54091
position ID unsuccessful in plane 1 AND 2	12	351247
position ID unsuccessful in plane 1 AND 4	14	49965
position ID unsuccessful in plane 1 AND 5	15	9861
position ID unsuccessful in plane 2 AND 4	24	10734
position ID unsuccessful in plane 2 AND 5	25	11508
position ID unsuccessful in plane 4 AND 5	45	202022
Description	RAY-ID	${}^{13}\text{C}({}^3\text{He},t){}^{13}\text{N}$ experiment
no region ID	-10	0
Bad VDC events	-9	996576
position ID of all planes unsuccessful	-8	185007
four planes have two good clusters	-7	370
position ID of only one plane successful (plane 5)	-5	131391
position ID of only one plane successful (plane 4)	-4	49500
position ID of only one plane successful (plane 2)	-2	16768
position ID of only one plane successful (plane 1)	-1	6982
RAY-TRACING SUCCESSFUL	0	4411565
position ID unsuccessful in plane 1	1	21458
position ID unsuccessful in plane 2	2	10875
position ID unsuccessful in plane 4	4	21548
position ID unsuccessful in plane 5	5	11193
position ID unsuccessful in plane 1 AND 2	12	124887
position ID unsuccessful in plane 1 AND 4	14	14736
position ID unsuccessful in plane 1 AND 5	15	4771
position ID unsuccessful in plane 2 AND 4	24	3665
position ID unsuccessful in plane 2 AND 5	25	3047
position ID unsuccessful in plane 4 AND 5	45	34458

Appendix E

Calculation of the factor $F(\omega, 0^\circ)$ using DWBA

Table E.1: Evolution of the relative cross sections for various excitation energies for the ${}^9\text{Be}({}^3\text{He}, t){}^9\text{B}$ reaction.

${}^9\text{Be}({}^3\text{He}, t){}^9\text{B}$ ([Yam95], pure ($p_{3/2}p_{3/2}^{-1}$))				${}^9\text{Be}({}^3\text{He}, t){}^9\text{B}$ ([Yam95], pure ($p_{1/2}p_{3/2}^{-1}$))			
ω [MeV]	$E_x({}^9\text{B})$ [MeV]	$\sigma_{\text{DWBA}}(0^\circ)$ [mb/sr]	$F(0^\circ, \omega)$	ω [MeV]	$E_x({}^9\text{B})$ [MeV]	$\sigma_{\text{DWBA}}(0^\circ)$ [mb/sr]	$F(0^\circ, \omega)$
0	–	54.426	1.0000	0	–	42.640	1.0000
2	0.91	54.045	0.9930	2	0.91	42.339	0.9929
4	2.91	53.423	0.9816	4	2.91	41.839	0.9812
6	4.91	52.566	0.9658	6	4.91	41.147	0.9650
8	6.91	51.487	0.9460	8	6.91	40.272	0.9445
10	8.91	50.197	0.9223	10	8.91	39.227	0.9200
12	10.91	48.716	0.8951	12	10.91	38.026	0.8918
14	12.91	47.062	0.8647	14	12.91	36.688	0.8604
16	14.91	45.259	0.8316	16	14.91	35.232	0.8263
18	16.91	43.330	0.7961	18	16.91	33.679	0.7898

${}^9\text{Be}({}^3\text{He}, t){}^9\text{B}$ ([Kam03], pure ($p_{3/2}p_{3/2}^{-1}$))				${}^9\text{Be}({}^3\text{He}, t){}^9\text{B}$ ([Kam03], pure ($p_{1/2}p_{3/2}^{-1}$))			
ω [MeV]	$E_x({}^9\text{B})$ [MeV]	$\sigma_{\text{DWBA}}(0^\circ)$ [mb/sr]	$F(0^\circ, \omega)$	ω [MeV]	$E_x({}^9\text{B})$ [MeV]	$\sigma_{\text{DWBA}}(0^\circ)$ [mb/sr]	$F(0^\circ, \omega)$
0	-1.09	40.679	1.0000	0	-1.09	31.910	1.0000
2	0.91	40.436	0.9940	2	0.91	31.717	0.9940
4	2.91	40.006	0.9835	4	2.91	31.369	0.9830
6	4.91	39.392	0.9684	6	4.91	30.869	0.9674
8	6.91	38.604	0.9490	8	6.91	30.224	0.9472
10	8.91	37.652	0.9256	10	8.91	29.445	0.9228
12	10.91	36.548	0.8984	12	10.91	28.542	0.8945
14	12.91	35.310	0.8680	14	12.91	27.530	0.8627
16	14.91	33.954	0.8347	16	14.91	26.425	0.8281
18	16.91	32.499	0.7989	18	16.91	25.243	0.7911

Table E.2: Evolution of the relative cross sections for various excitation energies for the $^{13}\text{C}(^3\text{He},\text{t})^{13}\text{N}$ reaction.

$^{13}\text{C}(^3\text{He},\text{t})^{13}\text{N}$ ([Yam95], pure $(p_{1/2}p_{3/2}^{-1})$)				$^{13}\text{C}(^3\text{He},\text{t})^{13}\text{N}$ ([Yam95], pure $(p_{1/2}p_{1/2}^{-1})$)			
ω [MeV]	$E_x(^{13}\text{N})$ [MeV]	$\sigma_{\text{DWBA}}(0^\circ)$ [mb/sr]	$F(0^\circ, \omega)$	ω [MeV]	$E_x(^{13}\text{N})$ [MeV]	$\sigma_{\text{DWBA}}(0^\circ)$ [mb/sr]	$F(0^\circ, \omega)$
0	-2.24	44.559	1.0000	0	-2.24	6.0879	1.0000
2	-0.24	44.291	0.9940	2	-0.24	6.0523	0.9942
4	1.76	43.833	0.9837	4	1.76	5.9916	0.9842
6	3.76	43.187	0.9692	6	3.76	5.9062	0.9702
8	5.76	42.364	0.9507	8	5.76	5.7971	0.9522
10	7.76	41.373	0.9285	10	7.76	5.6655	0.9306
12	9.76	40.228	0.9028	12	9.76	5.5128	0.9055
14	11.76	38.946	0.8740	14	11.76	5.3408	0.8773
16	13.76	37.544	0.8426	16	13.76	5.1514	0.8462
18	15.76	36.042	0.8089	18	15.76	4.9468	0.8126
20	17.76	34.458	0.7733	20	17.76	4.7291	0.7768
22	19.76	32.813	0.7364	22	19.76	4.5008	0.7393

$^{13}\text{C}(^3\text{He},\text{t})^{13}\text{N}$ ([Kam03], pure $(p_{1/2}p_{3/2}^{-1})$)				$^{13}\text{C}(^3\text{He},\text{t})^{13}\text{N}$ ([Kam03], pure $(p_{1/2}p_{1/2}^{-1})$)			
ω [MeV]	$E_x(^{13}\text{N})$ [MeV]	$\sigma_{\text{DWBA}}(0^\circ)$ [mb/sr]	F_{DWBA}	ω [MeV]	$E_x(^{13}\text{N})$ [MeV]	$\sigma_{\text{DWBA}}(0^\circ)$ [mb/sr]	F_{DWBA}
0	-2.24	30.052	1.0000	0	-2.24	4.4686	1.0000
2	-0.24	29.908	0.9952	2	-0.24	4.4482	0.9954
4	1.76	29.625	0.9858	4	1.76	4.4095	0.9868
6	3.76	29.207	0.9719	6	3.76	4.3529	0.9741
8	5.76	28.659	0.9536	8	5.76	4.2789	0.9575
10	7.76	27.990	0.9314	10	7.76	4.1884	0.9373
12	9.76	27.208	0.9054	12	9.76	4.0824	0.9136
14	11.76	26.326	0.8760	14	11.76	3.9620	0.8866
16	13.76	25.357	0.8438	16	13.76	3.8288	0.8568
18	15.76	24.314	0.8091	18	15.76	3.6842	0.8245
20	17.76	23.212	0.7724	20	17.76	3.5298	0.7899
22	19.76	22.066	0.7343	22	19.76	3.3674	0.7536

Appendix F

Publication List

F.1 Journal publications

1. P. von Brentano, V. Werner, R.F. Casten, C. Scholl, E.A. McCutchan, R. Krücken and J. Jolie,
Alternative interpretation of sharply rising $E0$ strenghts in transitional regions,
Phys. Rev. Lett. **93**, 152502 (2004)
2. A. Linnemann, C. Fransen, M. Gorska, J. Jolie, U. Kneissl, P. Knoch, D. Mücher, H.H. Pitz, M. Scheck, C. Scholl and P. von Brentano,
Dipole excitations in ^{96}Ru ,
Phys. Rev. C **72**, 064323 (2005)
3. D.A. Meyer, G.Graw, R. Hertenberger, H.-F. Wirth, R.F. Casten, P. von Brentano, D. Bucurescu, S. Heinze, J.L. Jerke, J.Jolie, R. Krücken, M. Mahgoub, P. Pejovic, O. Möller, D. Mücher, and C. Scholl,
Systematic exploration of 0^+ states in structurally diverse nuclei,
J. Phys. G **31**, S1399 (2005)
4. V. Werner, C. Scholl, and P. von Brentano,
Triaxiality and the determination of the cubic shape parameter K_3 from five observables,
Phys. Rev. C **71**, 054314 (2005)
5. D. Bucurescu, G. Graw, R. Hertenberger, H.-F. Wirth, N. Lo Iudice, A. V. Sushkov, N. Yu. Shirikova, Y. Sun, T. Faestermann, R. Krücken, M. Mahgoub, J. Jolie, P. von Brentano, N. Braun, S. Heinze, O. Möller, D. Mücher, C. Scholl, R. F. Casten, and D. A. Meyer,
High-resolution study of 0^+ and 2^+ excitations in ^{168}Er with the (p,t) reaction,
Phys.Rev. C **73**, 064309 (2006)

6. D.A. Meyer, V. Wood, R.F. Casten, C.R. Fitzpatrick, G. Graw, D. Bucurescu, J. Jolie, P. von Brentano, R. Hertzenberger, H.-F. Wirth, N. Braun, T. Faestermann, S. Heinze, J.L. Jerke, R. Krücken, M. Mahgoub, O. Möller, D. Mücher and C. Scholl,
Enhanced density of low-lying 0^+ states: A corroboration of shape phase transitional behavior,
Phys. Lett. B **638**, 44 (2006)
7. H. von Garrel, P. von Brentano, C. Fransen, G. Friessner, N. Hollmann, J. Jolie, F. Käppeler, L. Käubler, U. Kneissl, C. Kohstall, L. Kostov, A. Linnemann, D. Mücher, N. Pietralla, H. H. Pitz, G. Rusev, M. Scheck, K. D. Schilling, C. Scholl, R. Schwengner, F. Stedile, S. Walter, V. Werner, and K. Wisshak,
Low-lying $E1$, $M1$ and $E2$ strength distributions in $^{124,126,128,129,130,131,132,134,136}\text{Xe}$: Systematic photon scattering experiments in the mass region of a nuclear shape or phase transition,
Phys. Rev. C **73**, 054315 (2006)
8. D.A. Meyer, V. Wood, R.F. Casten, C.R. Fitzpatrick, G. Graw, D. Bucurescu, J. Jolie, P. von Brentano, R. Hertzenberger, H.-F. Wirth, N. Braun, T. Faestermann, S. Heinze, J.L. Jerke, R. Krücken, M. Mahgoub, O. Möller, D. Mücher and C. Scholl,
Extensive investigation of 0^+ states in rare earth region nuclei,
Phys. Rev. C **74**, 044309 (2006)
9. J. N. Orce, C. Fransen, A. Linnemann, C. J. McKay, S. R. Leshner, N. Pietralla, V. Werner, G. Friessner, C. Kohstall, D. Mücher, H. H. Pitz, M. Scheck, C. Scholl, F. Stedile, N. Warr, S. Walter, P. von Brentano, U. Kneissl, M. T. McEllistrem, and S. W. Yates,
Lifetime measurements in ^{93}Nb from photon and inelastic neutron scattering,
Phys. Rev. C **75**, 014303 (2007)
10. A. Linnemann, C. Fransen, J. Jolie, U. Kneissl, P. Knoch, C. Kohstall, D. Mücher, H. H. Pitz, M. Scheck, C. Scholl, F. Stedile, P. von Brentano, N. Warr, and V. Werner,
Low-lying $J=1$ states in ^{106}Cd ,
Phys. Rev. C **75**, 024310 (2007)
11. S. Walter, F. Stedile, J. J. Carroll, C. Fransen, G. Friessner, N. Hollmann, H. von Garrel, J. Jolie, O. Karg, F. Käppeler, U. Kneissl, C. Kohstall, P. von Neumann-Cosel, A. Linnemann, D. Mücher, N. Pietralla, H. H. Pitz, G. Rusev, M. Scheck, C. Scholl, R. Schwengner, V. Werner, and K. Wisshak,
Photon scattering experiments on the quasistable, odd-odd mass nucleus ^{176}Lu ,
Phys. Rev. C **75**, 034301 (2007)

12. M. Scheck, P. von Brentano, C. Fransen, U. Kneissl, C. Kohstall, A. Linnemann, D. Mcher, N. Pietralla, H. H. Pitz, C. Scholl, F. Stedile, S. Walter, V. Werner, and S. W. Yates,
Dipole strength distributions of the stable odd-mass $N=82$ isotones ^{139}La and ^{141}Pr ,
Phys. Rev. C **75**, 044313 (2007)
13. C. Scholl, P. Petkov, V. Werner, A. Linnemann, C. Fransen, T. Adachi, P. von Brentano, A. Dewald, A. Fitzler, Y. Fujita, D. Mcher, J. Jolie, A. Lisetskiy, K. Langanke, G. Martinez-Pinedo, N. Orce, N. Pietralla, N. Warr and K.O. Zell,
New spin assignments in the odd-odd $N=Z$ nucleus ^{42}Sc and the breaking of the ^{40}Ca core,
Phys. Rev. C **75**, 064321 (2007)
14. D. Bucurescu, R.F. Casten, J. Jolie, N. Braun, P. von Brentano, T. Faestermann, S. Heinze, R. Hertenberg, N. Lo Iudice, R. Krcken, M. Mahgoub, D. A. Meyer, O. Mller, D. Mcher, C. Scholl, N. Yu. Shirikova, Y. Sun, A. V. Sushkov and H.-F. Wirth,
High-Resolution Study of 0^+ and 2^+ Excitations in ^{168}Er with the (p,t) Reaction,
Phys. At. Nucl. / Yad. Fiz. **70**(8),1336-1343 (2007)
15. R.G. Zegers, T. Adachi, H. Akimune, S.M. Austin, A.M. van den Berg, B.A. Brown, Y. Fujita, M. Fujiwara, S. Gales, C.J. Guess, M.N. Harakeh, H. Hashimoto, K. Hatanaka, R. Hayami, G.W. Hitt, M.E. Howard, M. Itoh, T. Kawabata, K. Kawase, M. Kinoshita, M. Matsubara, K. Nakanishi, S. Nakayama, S. Okumura, T. Ohta, Y. Sakemi, Y. Shimbara, Y. Shimizu, C.Scholl, C. Simenel, Y. Tameshige, A. Tamii, M. Uchida, T. Yamagata, M. Yosoi,
Extraction of Weak Transition Strengths via the $(^3\text{He},t)$ Reaction at 420 MeV,
Phys.Rev.Lett. **99**, 202501 (2007)
16. R. G. T. Zegers, R. Meharchand, T. Adachi, Sam M. Austin, B. A. Brown, Y. Fujita, M. Fujiwara, C. J. Guess, H. Hashimoto, K. Hatanaka, M. E. Howard, H. Matsubara, K. Nakanishi, T. Ohta, H. Okamura, Y. Sakemi, Y. Shimbara, Y. Shimizu, C. Scholl, A. Signoracci, Y. Tameshige, A. Tamii, and M. Yosoi,
Spectroscopy of ^{24}Al and extraction of Gamow-Teller strengths with the $^{24}\text{Mg}(^3\text{He},t)$ reaction at 420 MeV,
Phys.Rev. C **78**, 014314 (2008)
17. V.Werner, E.Williams, R.J.Casperson, R.F.Casten, C.Scholl, P.von Brentano,
Deformation crossing near the first-order shape-phase transition in $^{152-156}\text{Gd}$,
Phys.Rev. C **78**, 051303 (2008)

18. R.Wadsworth, B.S.Nara Singh, A.N.Steer, D.G.Jenkins, M.A.Bentley, T.Brock, P.Davies, R.Glover, N.S.Pattabiraman, C.Scholey, T.Grahn, P.T.Greenlees, P.Jones, U.Jakobsson, R.Julin, S.Juutinen, S.Ketelhut, M.Leino, M.Nyman, P.Perua, J.Pakarinen, P.Rahkila, P.Ruotsalainen, J.Sorri, J.Uusitalo, C.J.Lister, P.A.Butler, M.Dimmock, D.T.Joss, J.Thomson, S.Rinta-Antila, B.Cederwall, B.Hadinia, M.Sandzelius, A.Atac, L.Betterman, A.Blazhev, N.Braun, F.Finke, K.Geibel, G.Ilie, H.Iwasaki, J.Jolie, P.Reiter, C.Scholl, N.Warr, P.Boutachkov, L.Caceres, C.Domingo, T.Engert, F.Farinon, J.Gerl, N.Goel, M.Gorska, H.Grawe, N.Kurz, I.Kojuharov, S.Pietri, C.Nociforo, A.Prochazka, H.-J.Wollersheim, K.Eppinger, T.Faestermann, C.Hinke, R.Hoischen, R.Kruecken, A.Gottardo, Z.Liu, P.Woods, J.Grebosz, E.Merchant, J.Nyberg, P.-A.Soderstrom, Z.Podolyak, P.Regan, S.Steer, M.Pfutzner, D.Rudolph, *The Northwest Frontier: Spectroscopy of $N \sim Z$ Nuclei Below Mass 100*, Acta Phys.Pol. B **40**, 611 (2009)
19. L. Bettermann, S. Heinze, J. Jolie, D. Mcher, O. Mller, C. Scholl, R. F. Casten, D. Meyer, G. Graw, R. Hertenberger, H. -F. Wirth, and D. Bucurescu, *High-resolution study of 0^+ states in ^{170}Yb* , Phys.Rev. C **80**, 044333 (2009)
20. A. Heusler, G. Graw, Th. Faestermann, R. Hertenberger, R. Krcken, C. Scholl, H. -F. Wirth and P. von Brentano, *Observation of five high-spin members of the $g_{9/2}f_{7/2}$ multiplet in ^{208}Pb* , Eur. Phys. J. A, 1434-6001 (2010)

F.2 Conference proceedings

- V. Werner, C. Scholl, and P. von Brentano, *A measure for triaxiality from K (shape) invariants*, Eur. J. Phys. A **25**, Supp. 1 (2005)
The 4th International Conference on Exotic Nuclei and Atomic Masses,
Pine Mountain, Georgia, USA - September 12-16, 2004
- V. Werner, C. Scholl, P. von Brentano, *Nuclear triaxiality from K (shape) invariants*,
Book of Abstracts, Chalmers University of Technology and Gteborg University
International Nuclear Physics Conference INPC 2004
Gteborg, Sweden - June 27-July 2, 2004
- P. von Brentano, V. Werner, R.F. Casten, C. Scholl, E.A. McCutchan, R. Krcken and J. Jolie *Alternative interpretation of $E0$ strenghts in transitional regions*, Eur. J. Phys. A **25**, Supp. 1 (2005)
The 4th International Conference on Exotic Nuclei and Atomic Masses,
Pine Mountain, Georgia, USA - September 12-16, 2004

- R. F. Casten, P. von Brentano, V. Werner, C. Scholl, E. A. McCutchan, R. Krücken, and J. Jolie
An Alternate Mechanism for $E0$ Transitions in Transitional and Deformed Nuclei,
AIP Conference Proceedings, Volume 726(1), 175-180, ISBN 0-7354-0207-8
Nuclear Physics, Large and Small : International Conference on Microscopic Studies of Collective Phenomena
Morelos, Mexico - April 19-22, 2004
- P. von Brentano, C. Scholl, V. Werner, E. Williams,
Spherical to deformed shape $N=88$ to $N=90$ phase transition from quadrupole invariants q_2 ,
Symmetries and low-energy phase transition in nuclear structure physics
International Workshop, 9-11 October 2005, Camerino, Italy
ed. Giovanni Lo Bianco, p. 33.
- D.A. Meyer, V. Wood, R.F. Casten, C.R. Fitzpatrick, G. Graw, D. Bucurescu, J. Jolie, P. von Brentano, R. Hertenberger, H.-F. Wirth, N. Braun, T. Faestermann, S. Heinze, J.L. Jerke, R. Krücken, M. Mahgoub, O. Möller, D. Mücher and C. Scholl,
Systematic Exploration of 0^+ States in Rare Earth Nuclei,
Fifth Biennial Workshop on Nuclear Structure Physics Near the Coulomb Barrier: Into the 21st Century,
Yale University, New Haven, CT - June 23-25, 2005
- V. Werner, E. Williams, P. von Brentano and C. Scholl,
Structural evolution from shape invariants,
Rev. Mex. Fis. S **52** (4) 103-108 (2006),
XXIX Symposium on Nuclear Physics,
Cocoyoc, Morelos, Mexico - January 3-6, 2006
- D. Bucurescu, R.F. Casten, J. Jolie, N. Braun, P. von Brentano, T. Faestermann, S. Heinze, R. Hertenberger, N. Lo Iudice, R. Krücken, M. Mahgoub, D. A. Meyer, O. Möller, D. Mücher, C. Scholl, N. Yu. Shirikova, Y. Sun, A. V. Sushkov and H.-F. Wirth,
High-Resolution Study of 0^+ and 2^+ Excitations in ^{168}Er with the (p,t) Reaction,
Phys. At. Nucl. / Yad. Fiz. **70**(8),1336-1343 (2007),
International Conference 'Nuclear Structure and Related Topics',
Dubna, Russia - June 12-18, 2006
- C. Scholl, P. Petkov, V. Werner, A. Linnemann, C. Fransen, T. Adachi, P. von Brentano, A. Dewald, A. Fitzler, Y. Fujita, D. Mücher, J. Jolie, A. Lisetskiy, K. Langanke, G. Martinez-Pinedo, N. Orce, N. Pietralla, N. Warr and K.O. Zell,
New spin assignments in the odd-odd $N=Z$ nucleus ^{42}Sc and the breaking of the ^{40}Ca core,
International Nuclear Physics Conference INPC 2007,
Tokyo, Japan - June 3-8, 2007

- C. Scholl, P. Petkov, V. Werner, A. Linnemann, C. Fransen, T. Adachi, P. von Brentano, A. Dewald, A. Fitzler, Y. Fujita, D. MÜcher, J. Jolie, A. Lisetskiy, K. Langanke, G. Martinez-Pinedo, N. Orce, N. Pietralla, N. Warr and K.O. Zell,
New spin assignments in the odd-odd $N=Z$ nucleus ^{42}Sc ,
3rd German-Japanese Workshop on Nuclear Structure and Astrophysics,
だいさんかいにちどくかくこうぞう てんたいかく
第三回 日独 核構造・天体核ワークショップ,
Abtei Frauenwörth, Fraueninsel im Chiemsee, Germany, 29.9-2.10, 2007
- C. Scholl, Y. Fujita, T. Adachi, P. von Brentano, H. Hashimoto, K. Hatanaka, H. Matsubara, K. Nakanishi, Y. Sakemi, Y. Shimbara, Y. Shimizu, Y. Tameshige, A. Tamii, M. Yosoi, and R.G.T. Zegers,
High-resolution $B(GT)$ studies with $(^3\text{He},t)$ reactions,
XIII. International Symposium on Capture Gamma-Ray Spectroscopy and Related Topics
August 25-29, 2008 - Cologne, Germany, Plenary Talk PT-45
published in *AIP Conf. Proc.*, Volume 1090, pp. 544-548

Bibliography

- [Ada07] T. Adachi. High-resolution study of Gamow-Teller transitions in pf-shell nuclei. PhD thesis, Osaka University, 2007.
- [Aki01] H. Akimune, M. Fujimura, M. Fujiwara, K. Hara, T. Ishikawa, T. Kawabata, H. Utsunomiya, T. Yamagata, K. Yamasaki and M. Yosoi. Evidence for a 3.8 MeV state in ^9B . *Phys. Rev. C* **64** (2001) 041305(R).
- [AS91] F. Ajzenberg-Selove. Energy levels of light nuclei $A=13-15$. *Nucl. Phys. A* **523(1)** (1991) 1–196.
- [Aud95] G. Audi and A.H. Wapstra. The 1995 update to the atomic mass evaluation. *Nucl. Phys. A* **595(4)** (1995) 409–480.
- [Aud03] G. Audi, H. Wapstra and C. Thibault. The AME 2003 atomic mass evaluation: (II). Tables, graphs and references. *Nucl. Phys. A* **729** (2003) 337–676.
- [Bac66] D. Bachelier, M. Bernas, I. Brissaud, P. Radvanyi and M. Roy. *Nucl. Phys.* **88** (1966) 307.
- [Bal69] G.C. Ball and J. Cerny. *Phys. Rev.* **177** (1969) 1466.
- [Ber01] U.C. Bergmann, M.J.G. Borge, R. Boutami, L.M. Fraile, H.O.U.Fynbo, P. Hornshøj, B. Jonson, K. Markenroth, I. Martel, I. Mukha, T. Nilsson, G. Nyman, A. Oberstedt, Y. Prezado Alonso, K. Riisager, H. Simon, O. Tengblad, F. Wenander, K. Wilhelmsen Rolander and ISOLDE Collaboration. On the β -decay of ^9C . *Nucl. Phys. A* **692** (2001) 427–450.
- [Bet30] H. Bethe. Zur Theorie des Durchgangs schneller Korpuskularstrahlen durch Materie. *Ann. d. Phys.* **397** (1930) 325–400.
- [Bev69] P.R. Bevington. *Data Reduction and Error Analysis for the Physical Sciences*. McGraw-Hill, New York, 1969.
- [Boh69] A. Bohr and B.R. Mottelson. *Nuclear structure*. W.A. Benjamin, 1969.
- [Boo78] C. De Boor. *A Practical Guide to Splines*. Springer-Verlag, New York, 1978.
- [Buc01] L. Buchmann, E. Gete, J.C. Chow, J.D. King and D.F. Measday. *Phys. Rev. C* **63** (2001) 034303.

- [Car98] D.C. Carey, K.L. Brown and S. Rothacker. Third-Order Transport with MAD input: a computer program for designing charged particle beam transport systems. *SLAC Reports* (<http://www.slac.stanford.edu/pubs/slacreports/>) **530** (1998).
- [Cat04] W. Catford. relativistic kinematics program CATKIN, version 2.02. *unpublished*, <http://personal.ph.surrey.ac.uk/~phs1wc/kinematics/> (2004).
- [Cla90] D.J. Clark and G.J. Wozniak. Fast energy changes with a cyclotron. *Nucl. Instr. and Meth.* **295** (1990) 34–38.
- [Coh59] B.L. Cohen. Resolution of Accelerator Magnetic Analyzing Systems. *Rev. Sci. Instrum.* **30** (6) (1959) 415.
- [Coh65] S. Cohen and D. Kurath. *Nucl. Phys.* **73** (1965) 1.
- [Col06] A.L. Cole, H. Akimune, Sam M. Austin, D. Bazin, A. M. van den Berga, G. P. A. Berg, J. Brown, I. Daito, Y. Fujita, M. Fujiwara, S. Gupta, K. Hara, M.N. Harakeh, J. Jänecke, T. Kawabata, T. Nakamura, D.A. Roberts, B.M. Sherrill, M. Steiner, H. Ueno and R.G.T. Zegers. *Phys. Rev. C* **74** (2006) 034333.
- [Com] J.R. Comfort. Program DW81, extended version of DWBA70 by R. Schaeffer and J. Raynal. *Available online* (<http://unimeg1.la.asu.edu/~comfort/dwba/dwba.html>) **unpublished**.
- [Coo] J. Cook and J.A. Carr. computer program FOLD, Florida State University (unpublished), based on F. Petrovich and D. Stanley, *Nucl. Phys.* A275, 487 (1977), modified as described in J. Cook et al, *Phys. Rev.* C30, 1538 (1984) and R.G.T. Zegers, S. Fracasso and G. Colo (2006). *available online* (<http://www.nsl.msu.edu/~zegers/fold.html>) **unpublished**.
- [Dan00] S. Dangtip, J. Blomgren, N. Olsson, H. Conde, K. Elmgren, J. Rahm, A. Ringbom, G. Tibell, O. Jonsson, L. Nilsson, P.U. Renberg and S.Y. van der Werf. The ${}^9\text{Be}(n,p){}^9\text{Li}$ reaction and the Gamow-Teller unit cross-section. *Nucl. Phys. A* **677** (2000) 3–24.
- [Dav69] J. Davidson, N. Jarmie and A. Niethammer. Relkin: A two-body relativistic kinematics code. *Los Alamos technical reports* **LA-4349** (1969) 8.
- [Dix91] S. Dixit, W. Bertozzi, T.N. Buti, J.M. Finn, F.W. Hersman, C.E. Hyde-Wright, M.V. Hynes, M.A. Kovash, B.E. Norum, J.J. Kelly, A.D. Bacher, G.T. Emery, C.C. Foster, W.P. Jones, D.W. Miller, B. L. Berman and D.J. Millener. Structure of ${}^9\text{Be}$ from proton scattering at 180 MeV. *Phys. Rev. C* **43** (1991) 1758–1776.
- [Faz82] A. Fazely, B. Anderson, A.R. McCarthy, P. Tandy, J. Watson, W. Bertozzi, T.N. Buti, J.M. Finn, J. Kelly, M.A. Kovash, B. Pugh and C.C. Foster. The (p,n) reaction at intermediate energies with ${}^{16,17,18}\text{O}$ and ${}^9\text{Be}$. *IUCF annual reports* (1982) 49.

- [Fle68] D.G. Fleming, J. Cerny, C.C. Maples and N.K. Glendenning. *Phys. Rev.* **166** (1968) 1012.
- [For05] C. Forssen, P. Navratil, W.E. Ormand and E. Caurier. Large basis ab initio shell model investigation of ^9Be and ^{11}Be . *Phys. Rev. C* **71** (2005) 044312.
- [Fra85] M.A. Frangey and W.G. Love. *Phys. Rev. C* **31** (1985).
- [Fuj] H. Fujita. Program S-fit, version 0.5.2. **unpublished**.
- [Fuj97] Y. Fujita, K. Hatanaka, G.P.A. Berg, K. Hosono, N. Matsuoka, S. Morinobo, T. Noro, M. Sato, K. Tamura and H. Ueno. Matching of a beam line and a spectrometer: New beam line project at RCNP. *Nucl. Instr. and Meth. B* **126** (1997) 274.
- [Fuj99a] Y. Fujita, H. Akimune, I. Daito, H. Fujimura, M. Fujiwara, M.N. Harakeh, T. Inomata, J. Jänecke, K. Katori, A. Tamii, M. Tanaka, H. Ueno and M. Yosoi. *Phys. Rev. C* **59** (1999) 90.
- [Fuj99b] M. Fujiwara, H. Akimune, I. Daito, H. Fujimura, Y. Fujita, K. Hatanaka, H. Ikegami, I. Katayama, K. Nagayama, M. Matsuoka, S. Morinobu, T. Noro, M. Yoshimura, H. Sakaguchi, Y. Sakemi, A. Tamii and M. Yosoi. Magnetic spectrometer Grand Raiden. *Nucl. Instr. and Meth. A* **422** (1999) 484–488.
- [Fuj01] H. Fujita, G.P.A. Berg, Y. Fujita, K. Hatanaka, T. Noro, E.J. Stephenson, C.C. Foster, H. Sakaguchi, M. Itoh, T. Taki, K. Tamura and H. Ueno. Better-resolution measurement of vertical scattering angle in a new ion-optical mode of spectrometer "Grand Raiden". *Nucl. Instr. and Meth. A* **469** (2001) 55–62.
- [Fuj02a] H. Fujita, Y. Fujita, G.P.A. Berg, A.D. Bacher, C.C. Forster, K. Hara, K. Hatanaka, T. Kawabata, T. Noro, H. Sakaguchi, Y. Shimbara, T. Shinada, E.J. Stephenson, H. Ueno and M. Yosoi. Realization of matching conditions for high-resolution spectrometers. *Nucl. Instr. and Meth. A* **484** (2002) 17–26.
- [Fuj02b] Y. Fujita, Y. Shimbara, I. Hamamoto, T. Adachi, G.P.A. Berg, H. Fujimura, H. Fujita, J. Görres, K. Hara, K. Hatanaka, J. Kamiya, T. Kawabata, Y. Kitamura, Y. Shimizu, M. Uchida, H.P. Yoshida, M. Yoshifuku and M. Yosoi. *Phys. Rev. C* **66** (2002) 044313.
- [Fuj04a] H. Fujimura, H. Akimune, I. Daito, M. Fujiwara, K. Hara, K.Y. Hara, M.N. Harakeh, F. Ihara, T. Inomata, K. Ishibashi, T. Ishikawa, T. Kawabata, A. Tamii, M. Tanaka, H. Toyokawa, T. Yamanaka and M. Yosoi. Nuclear structure of the spin-isospin excited states in ^{13}N studied via the $(^3\text{He},t)$ and $(^3\text{He},tp)$ reactions at 450 MeV. *Phys. Rev. C* **69** (2004) 064327.
- [Fuj04b] Y. Fujita, P. von Brentano, T. Adachi, G.P.A. Berg, D. De Frenne, K. Fujita, K. Hatanaka, E. Jacobs, K. Nakanishi, A. Negret, L. Popescu, Y. Sakemi, Y. Shimbara, Y. Shimizu, Y. Tameshige, A. Tamii, M. Uchida, M. Yosoi and K.O. Zell. High-resolution study of ^{11}b to ^{11}c Gamow-Teller strengths as a test case of ab initio shell-model calculations. *Phys. Rev. C* **70** (2004) 011306(R).

- [Goo80] C.D. Goodman, C.A. Goulding, M.B. Greenfield, J. Rapaport, D.E. Bainum, C.C. Foster, W.G. Love and F. Petrovich. Gamow-Teller matrix elements from $0^\circ(p,n)$ cross sections. *Phys. Rev. Lett.* **44** (1980) 1755.
- [Gos73] J.D. Goss, A.A. Rollefson, G.L. Marolt and C.P. Browne. *Phys. Rev. C* **7** (1973) 663.
- [Har06] J.C. Hardy and I.S. Towner. Probing the standard model with superallowed nuclear beta decay. *Nucl. Phys. News* **16-4** (2006) 11–17.
- [Har09] J.C. Hardy and I.S. Towner. Superallowed $0^+ \rightarrow 0^+$ nuclear β decays: A new survey with precision tests of the conserved vector current hypothesis and the standard model. *Phys. Rev. C* **79** (2009) 055502.
- [Hin68] F. Hinterberger, G. Mairle, V. Schmidt-Rohr, P. Turek and G.J. Wagner. *Nucl. Phys. A* **106** (1968) 161.
- [Jän93] J. Jänecke, K. Pham, D.A. Roberts, D. Stewart, M.N. Harakeh, G.P.A. Berg, C.C. Foster, J.E. Lisanntti, R. Sawafta, E.J. Stephenson, A.M. van den Berg, S.Y. van der Werf, S.E. Muraviev and M.H. Urin. Fragmentation of Gamow-Teller strength observed in $^{117,120}\text{Sn}(^3\text{He},t)^{117,120}\text{Sb}$ charge-exchange reactions. *Phys. Rev. C* **48** (1993) 2828.
- [Kam03] J. Kamiya, K. Hatanaka, T. Adachi, K. Fujita, K. Hara, T. Kawabata, T. Noro, H. Sakaguchi, N. Sakamoto, Y. Sakemi, Y. Shimbara, Y. Shimizu, S. Terashima, M. Uchida, T. Wakasa, Y. Yasuda, H.P. Yoshida and M. Yosoi. Cross section and induced polarization in ^3He elastic scattering at 443 MeV. *Phys. Rev. C* **67** (2003) 064612.
- [Kat89] I. Katayama. Present and New Cyclotron Facilities and Atomic Physics at RCNP. *Chin. J. Phys.* **27** (1989) 265.
- [Kno82] H.D. Knox and R.O. Lane. Structure of ^{13}C from an R-matrix analysis of $^{12}\text{C} + n$ scattering and reaction cross sections. *Nucl. Phys. A* **3** (1982) 503–524.
- [Koz67] R.L. Kozub, L.A. Kull and E. Kashy. *Nucl. Phys. A* **99** (1967) 540.
- [Kum74] N. Kumar. Effective interaction calculations for nuclei of mass 6 to 9. *Nucl. Phys. A* **225** (1974) 221.
- [Liy99] N. Liyanage, W. Bertozzi, K. Fissum, J. Gao and S. Gilad. Optics Commissioning of the Hall A High Resolution Spectrometers. *Massachusetts Institute of Technology* (<http://www.jlab.org/~fissum/e89003.html>) (1999).
- [Lov81] W.G. Love and M.A. Franey. Effective nucleon-nucleon interaction for scattering at intermediate energies. *Phys. Rev. C* **24** (1981).
- [Mar83] S.A. Martin, A. Hardt, J. Meissburger, G.P.A. Berg, U. Hacker, W. Hürlimann, J.G.M. Römer, T. Sagefka, A. Retz, O.W.B. Schult, K.L. Brown and K. Halbach. The QQDDQ Magnet Spectrometer "Big Karl". *Nucl. Instr. and Meth.* **214** (1983) 281–303.

- [Mea73] D.F. Measday, M. Hasinoff and D.L. Johnson. High-energy levels in ^{13}N . *Can. J. Phys.* **51** (1973) 1227.
- [Mey73] H.O. Meyer and G.R. Plattner. Levels in ^{13}N near $E_x=12$ MeV from $p+^{12}\text{C}$ scattering. *Nucl. Phys. A* **199** (1973) 413–423.
- [Mik88] D. Mikolas, B.A. Brown, W. Benenson, L.H. Harwood, E. Kashy, J.A. Nolen, B. Sherill, J. Stevenson, J.S. Winfield and Z.Q. Xie. branching ratios of ^9C to low lying states in ^9B . *Phys. Rev. C* **37-2** (1988) 766.
- [Nag61] Yukio Nagahara. Elastic and inelastic scattering of protons from carbon nucleus from 6.5 to 16 MeV. *J. Phys. Soc. Jpn.* **16** (1961) 133–147.
- [Nav] P. Navratil. private communication .
- [Nav07] P. Navratil, V.G. Gueorguiev, J.P. Vary, W.E. Ormand and A. Nogga. Structure of $A=10-13$ nuclei with two- plus three-nucleon interactions from chiral effective field theory. *Phys. Rev. Lett.* **99** (2007) 042501.
- [Nor91] T. Noro, M. Fujiwara, O. Kamigaito, S. Hirata, Y. Fujita, A. Yamagoshi, T. Takahashi, H. Akimune, Y. Sakemi, M. Yosoi, H. Sakaguchi and J. Tanaka. Beam test of the focal plane counter system for Grand Raiden. *RCNP Annual report*, (<http://www.rcnp.osaka-u.ac.jp>) (1991) 177–179.
- [Nym90] G. Nyman, R.E. Azuma, P.G. Hansen, B. Jonson, P.O. Larsson, S. Mattsson, A. Richter, K. Riisager, O. Tengblad and K. Wilhelmsen. The beta decay of ^9Li to levels in ^9Be : a new look. *Nucl. Phys. A* **510** (1990) 189–208.
- [Ogi88] K. Ogino, T. Kiyosawa and T. Kiuchi. Stopping powers for MeV tritons in solids. *Nucl. Instr. and Meth. B* **33 (1-4)** (1988) 155.
- [Orm95] W.E. Ormand and B.A. Brown. *Phys. Rev. C* **52** (1995) 2455.
- [Ost92] F. Osterfeld. Nuclear spin and isospin excitations. *Rev. Mod. Phys.* **64** (1992) 491.
- [Phi67] R.E. Phillips and S.T. Thornton. A Fortran program for relativistic kinematic calculations in two-body nuclear reactions. *Oak Ridge National Laboratory Reports ORNL-4179* (1967) 25.
- [Poi68] J. Poirier. Relkin: A relativistic kinematics program. *Fermilab technical memos FERMILAB-TM-0117* (1968) 5.
- [Pre92] W.H. Press, B.P. Flannery, S.A. Teukolsky and W.T. Vetterling. *Numerical Recipes in FORTRAN: The Art of Scientific Computing*. Cambridge University Press, 1986-1992.
- [Pre03] Y. Prezado, U.C. Bergmann, M.J.G. Borge, J. Cederkäll, C.Aa. Diget, L.M. Fraile, H.O.U. Fynbo, H. Jeppesen, B. Jonson, M. Meister, T. Nilsson, G. Nyman, K. Riisager, O. Tengblad, L. Weissmann, K. Kilhelmsen Rolander and ISOLDE Collaboration. Large asymmetry in the strongest β -transition for $a=9$. *Phys. Lett. B* **576** (2003) 55–61.

- [Pug85] B.G. Pugh. The (p,n) reaction on ^9Be and ^{17}O at 135 mev. PhD thesis, Massachusetts Institute of Technology, 1985.
- [Ray67] J. Raynal. *Nucl. Phys.* **97** (1967).
- [Sch08] N. Schwierz, I. Wiedenhöver and A. Volya. Parameterization of the Woods-Saxon potential for shell-model calculations. *arXiv:0709.3525 [nucl-th]*, <http://www.volya.net/ws> (2008).
- [Shi05] Y. Shimbara. High resolution study of Gamow-teller transitions by $^{37}\text{Cl}(^3\text{He},t)^{37}\text{Ar}$ reaction. PhD thesis, Osaka University, 2005.
- [Sto80] J. Stoer and R. Burlisch. *Introduction to Numerical Analysis*. Springer-Verlag, New York, 1980.
- [Tad87] T.N. Taddeucci, C.A. Goulding, T.A. Carey, R.C. Byrd, C.D. Goodman, C. Gaarde, J. Larsen, D. Horen, J. Rapaport and E. Sugarbaker. The (p,n) reaction as a probe of beta decay strength. *Nucl. Phys. A* **469** (1987) 125–172.
- [Tam97] A. Tamii. TAMIDAcquisition users guide. Available online (<http://www.rcnp.osaka-u.ac.jp/Divisions/np1-a/tamidaq/tamidaq.html>) **unpublished** (1997).
- [Til04] D.R. Tilley, J.H. Kelley, J.L. Godwin, D.J. Millener, J.E. Purcell, C.G. Sheu and H.R. Weller. Energy levels of light nuclei $A=8,9,10$. *Nucl. Phys. A* **745** (2004) 155–362.
- [vdW89] S.Y. van der Werf, S. Brandenburg, P. Grasdijk, W.A. Sterrenburg, M.N. Harakeh, M.B. Greenfield, B.A. Brown and M. Fujiwara. The effective ^3He -nucleon force in a microscopic DWBA approach to the $(^3\text{He},t)$ charge-exchange reaction. *Nucl. Phys. A* **496** (1989) 305.
- [Wak02] T. Wakasa, K. Hatanaka, Y. Fujita, G.P.A. Berg, H. Fujimura, H. Fujita, M. Itoh, J. Kamiya, T. Kawabata, K. Nagayama, T. Noro, H. Sakaguchi, Y. Shimbara, H. Takeda, K. Tamura, H. Ueno, M. Uchida, M. Uraki and M. Yosoi. High resolution beam line for the Grand Raiden spectrometer. *Nucl. Instr. and Meth. A* **482** (2002) 79–93.
- [Wan01] X. Wang, J. Rapaport, M. Palarczyk, C. Hautala, X. Yang, D.L. Prout, I. Van Heerden, R. Howes, S. Parks, E. Sugarbaker and B.A. Brown. Zero degree polarization transfer measurements for the $^{13}\text{C}(p,n)^{13}\text{N}$ reaction at 197 mev and empirical Gamow-Teller distribution. *Phys. Rev. C* **63** (2001) 024608.
- [Wat85] J.W. Watson, W. Pairsuwan, B.D. Anderson, A.R. Baldwin, B.S. Flanders, R. Madey, R.J. McCarthy, B.A. Brown, B.H. Wildenthal and C.C. Foster. Relationship between Gamow-Teller transition probabilities and (p,n) cross sections at small momentum transfers. *Phys. Rev. Lett.* **55** (1985) 1369.
- [Wat01] J.W. Watson and Q.Q. Du. On the conversion of charge-exchange cross sections to GT strength: anomalies in odd- A nuclei. *Nucl. Phys. A* **687** (2001) 32c–37c.

- [Wie] I. Wiedenhöver and B. Steckemetz. computer program TOPFIT, Institut für Kernphysik Köln (unpublished). *available online* (<http://www.ikp.uni-koeln.de/src/>) **unpublished**.
- [Wie72] K. Wienhard, G. Clausnitzer and G. Hartmann. Phase Shift Analysis of Elastic Proton Scattering by ^{12}C . *Z. Phys.* **256** (1972) 457.
- [Wil66] C.F. Williamson, J.-P. Boujot and J. Picard. Tables of range and stopping power of chemical elements for charged particles of energy 0.05 to 200 MeV. *CEN Saclay Reports CEA-R 3042* (1966).
- [Yam95] T. Yamagata, H. Utsunomiya, M. Tanaka, S. Nakayama, N. Koori, A. Tamii, Y. Fujita, K. Katorin, M. Inoue, M. Fujiwara and H. Ogata. Elastic scattering of ^3He particles at 450 MeV. *Nucl. Phys. A* **589** (1995) 425–434.
- [Yos96] H.P. Yoshida, T. Baba, T. Noro, M. Kawabata, H. Akimune, H. Sakaguchi, A. Tamii, H. Takeda and T. Kawabata. A new trigger system by using FPGAs. *RCNP Annual report*, (<http://www.rcnp.osaka-u.ac.jp>) (1996) 164.
- [Yos01] M. Yosoi. Analyzer manual for data obtained by TAMIDAQ system. *Available online* (<http://www.rcnp.osaka-u.ac.jp/~yosoi>) **unpublished** (2001).
- [Zeg03] R.G.T. Zegers, H. Abend, H. Akimune, A.M. van den Berg, H. Fujimura, H. Fujita, Y. Fujita, M. Fujiwara, S. Gales, K. Hara, M.N. Harakeh, T. Ishikawa, T. Kawabata, K. Kawase, T. Mibe, K. Nakanishi, S. Nakayama, H. Toyokawa, M. Uchida, T. Yamagata, K. Yamasaki and M. Yosoi. Excitation and Decay of the Isovector Giant Monopole Resonances via the $^{208}\text{Pb}(^3\text{He},\text{tp})$ Reaction at 410 MeV. *Phys. Rev. Lett.* **90** (2003) 202501.
- [Zeg07] R.G.T. Zegers, T. Adachi, H. Akimune, S.M. Austin, A.M. van den Berg, B.A. Brown, Y. Fujita, M. Fujiwara, S. Gales, C.J. Guess, M.N. Harakeh, H. Hashimoto, K. Hatanaka, R. Hayami, G.W. Hitt, M.E. Howard, M. Itoh, T. Kawabata, K. Kawase, M. Kinoshita, M. Matsubara, K. Nakanishi, S. Nakayama, S. Okumura, T. Ohta, Y. Sakemi, Y. Shimbara, Y. Shimizu, C. Scholl, C. Simenel, Y. Tameshige, A. Tamii, M. Uchida, T. Yamagata and M. Yosoi. Extraction of weak transition strengths via the $(^3\text{He}, \text{t})$ reaction at 420 MeV. *Phys. Rev. Lett.* **99** (2007) 202501.
- [Zeg08] R.G.T. Zegers, E.F. Brown, H. Akimune, S.M. Austin, A.M. van den Berg, B.A. Brown, D.A. Chamulak, Y. Fujita, M. Fujiwara, S. Gales, M.N. Harakeh, H. Hashimoto, R. Hayami, G.W. Hitt, M. Itoh, T. Kawabata, K. Kawase, M. Kinoshita, K. Nakanishi, S. Nakayama, S. Okumura, Y. Shimbara, M. Uchida, H. Ueno, T. Yamagata and M. Yosoi. Gamow-Teller strength for the analog transitions to the first $T=1/2, J^\pi=3/2^-$ states in ^{13}C and ^{13}N and the implications for type Ia supernovae. *Phys. Rev. C* **77** (2008) 024307.

List of Figures

1.1	Energy dependence of the central components of the effective interaction	4
1.2	Components of the effective interaction as a function of momentum transfer	5
1.3	$\hat{\sigma}_{F,GT}$ as a function of mass number A for (p,n) reactions at 120 MeV . .	7
1.4	$\hat{\sigma}_{F,GT}$ as a function of mass number A for ($^3\text{He},t$) reactions at 140 MeV/nucleon	8
1.5	Isobar diagram of the A=13 system	9
1.6	Isobar diagram of the A=9 system	10
2.1	The Grand Raiden Spectrometer	13
2.2	Layout of the Grand Raiden Spectrometer	14
2.3	Layout of the focal plane detector system	15
2.4	Schematic illustration of a MWDC	17
2.5	Trigger system circuit diagram	17
2.6	Layout of the WS course beam line setup at the RCNP Ring Cyclotron Facility	19
2.7	Schematic trajectories with different matching conditions	20
2.8	Beam images for different matching conditions	23
2.9	Vertical beam envelope inside the Grand Raiden spectrometer (vertical focus)	24
3.1	Separation of $^3\text{He}^+$ and $^3\text{H}^+$ via the energy loss	29
3.2	Energy loss of $^3\text{He}^+$ and $^3\text{H}^+$ in the scintillators	30
3.3	Position determination in the MWDCs	31
3.4	TDC spectra of the MWDCs for X and U-plane wires	32
3.5	Wire configurations of the X- and U-planes of the MWDCs	33
3.6	Raytracing: x,y and u-position	34

3.7	Raytracing: MWDC coordinates	35
3.8	Metrics of the sieve slit used for angle calibration	36
3.9	Sieve slit images at the focal plane for two different x_{fp} gates	37
3.10	Illustration of the effect of aberration corrections	39
4.1	Peak shape reference for the ${}^9\text{Be}({}^3\text{He},t)$ reaction	42
4.2	Peak shape reference for the ${}^9\text{Be}({}^3\text{He},t)$ reaction	42
4.3	${}^{13}\text{N}$ spectrum for scattering angle $\leq 0.5^\circ$ (full spectrum)	45
4.4	${}^{13}\text{N}$ spectrum for scattering angle $\leq 0.5^\circ$ (0-6.5 MeV excitation energy) .	46
4.5	${}^{13}\text{N}$ spectrum for scattering angle $\leq 0.5^\circ$ (6-16 MeV excitation energy) .	47
4.6	${}^{13}\text{N}$ spectrum for scattering angle $\leq 0.5^\circ$ (6-16 MeV excitation energy) (scaled)	50
4.7	Separation of the ${}^{12}\text{N}$ ground state and the ${}^{13}\text{N}$ $T=3/2$ state at 15.1 MeV	51
4.8	${}^{13}\text{N}$ spectra for different scattering angles (6-19 MeV excitation energy) .	52
4.9	${}^{13}\text{N}$ spectrum for scattering angle $\leq 0.5^\circ$ (17-30 MeV excitation energy) .	53
4.10	${}^9\text{B}$ spectrum for scattering angle $\leq 0.5^\circ$ (full spectrum)	55
4.11	Deconvolution of the lower part of the ${}^9\text{B}$ spectrum for scattering angle $\leq 0.5^\circ$	56
4.12	Broad states making up the lower part of the ${}^9\text{B}$ spectrum for scattering angle $\leq 0.5^\circ$	58
4.13	${}^9\text{B}$ spectrum for scattering angle $\leq 0.5^\circ$ (10-16 MeV excitation energy) .	59
4.14	${}^9\text{B}$ spectrum for scattering angle $\leq 0.5^\circ$ (16-25 MeV excitation energy) .	61
4.15	Angular distributions and ΔL transfer	63
4.16	Identification of $\Delta L=0$ states in ${}^{13}\text{N}$	64
4.17	Identification of $\Delta L=0$ states in ${}^9\text{B}$	65
4.18	Angular aperture and integration surfaces (${}^{13}\text{C}$ target).	68
4.19	Angular aperture and integration surfaces (${}^9\text{Be}$ target).	69
5.1	Single particle energies for light nuclei	77
5.2	Simplified shell model view of possible configurations for β^- -type transi- tions ${}^9\text{Be} \rightarrow {}^9\text{B}$ and ${}^{13}\text{C} \rightarrow {}^{13}\text{N}$	78
5.3	Evolution of the relative cross-section of ${}^9\text{Be}({}^3\text{He},t){}^9\text{B}$ calculated with DWBA	78
5.4	Evolution of the relative cross section of ${}^{13}\text{C}({}^3\text{He},t){}^{13}\text{N}$ calculated with DWBA	79

5.5	Angular distributions of $\Delta L=0$ states in ^{13}N	81
5.6	Angular distribution of the $1/2^-$ ground state of ^{13}N	81
5.7	Angular distribution of the 3.50 MeV, $3/2^-$ state of ^{13}N	82
5.8	Angular distribution of the 8.88 MeV, $1/2^-$ state of ^{13}N	82
5.9	Angular distribution of the 9.48 MeV, $3/2^-$ state of ^{13}N	83
5.10	Angular distribution of the 10.81 MeV, $1/2^-$ state of ^{13}N	83
5.11	Angular distribution of the 11.88 MeV, $(1/2^-, 3/2^-)$ state of ^{13}N	84
5.12	Angular distribution of the 13.47 MeV, $(1/2^-, 3/2^-)$ state of ^{13}N	84
5.13	Angular distribution of the 15.06 MeV, $3/2^-$, $T=3/2$ state of ^{13}N	85
5.14	Angular distribution of the 18.40 MeV, $(1/2^-, 3/2^-)$ state of ^{13}N	85
5.15	Angular distribution of the $3/2^-$ ground state of ^9B	88
5.16	Angular distribution of the 2.36 MeV, $5/2^-$ state of ^9B	88
5.17	Angular distribution of the 2.73 MeV, $1/2^-$ state of ^9B	89
5.18	Angular distribution of the 3.93 MeV, $(\frac{1}{2}^-, \frac{3}{2}^-, \frac{5}{2}^-)$ state of ^9B	89
5.19	Angular distribution of the 12.24 MeV, $5/2^-$ state of ^9B	90
5.20	Angular distribution of the 14.1 MeV, $(\frac{1}{2}^-, \frac{3}{2}^-, \frac{5}{2}^-)$ state of ^9B	90
5.21	Angular distribution of the 14.65 MeV, $3/2^-$ state of ^9B	91
5.22	Angular distribution of the 14.89 MeV, $(\frac{1}{2}^-, \frac{3}{2}^-, \frac{5}{2}^-)$ state(s) of ^9B	91
5.23	Angular distribution of the 16.05 MeV, $(\frac{1}{2}^-, \frac{3}{2}^-, \frac{5}{2}^-)$ state of ^9B	92
5.24	Angular distribution of the 17.1 MeV, $1/2^-$ state of ^9B	92
5.25	β -decays and analog transitions for $A=13$	95
5.26	Distribution of Gamow-Teller strengths to ^{13}N , compared with previous results	98
5.27	β -decays and analog transitions for $A=9$	100
5.28	Distribution of Gamow-Teller strengths to ^9B obtained in the $(^3\text{He}, t)$ experiment	102
6.1	$B(\text{GT})$ ratios in ^{13}N , comparison of $(^3\text{He}, t)$ and (p, n)	104
6.2	$B(\text{GT})$ ratios in ^{13}N , comparison of $(^3\text{He}, t)$ and (p, n)	106
6.3	$B(\text{GT})$ ratios in ^9B , comparison of $(^3\text{He}, t)$ and (p, n)	110
6.4	$B(\text{GT})$ strengths in ^9B and ^9Be , from $(^3\text{He}, t)$ and β -decay	114
6.5	Illustration of the spatial shapes in the $A=9$ system	115

A.1	Geometrical representation of the ray vector components	I
A.2	Coordinate systems for beam optics	III
A.3	Scattering at the target in the horizontal plane	IV
B.1	Sieve-slit images for various x-positions	VIII
B.2	Dimensions of the sieve slit	X
B.3	Sieve slit: projections of columns and fit (1)	XI
B.4	Sieve slit: projections of columns and fit (2)	XII
B.5	Sieve slit: projections of columns and fit (3)	XIII
B.6	Sieve slit: projections of columns and fit (4)	XIV
B.7	Sieve slit: projections of columns and fit (5)	XV
B.8	Sieve slit: projections of columns and fit (6)	XVI
B.9	Sieve slit: projections of columns and fit (7)	XVII
B.10	Sieve slit: projections of columns and fit (8)	XVIII
B.11	Sieve slit: projections of columns and fit (9)	XIX
B.12	Sieve slit: linear parameters as a function of θ_{tgt} (1)	XXII
B.13	Sieve slit: linear parameters as a function of θ_{tgt} (2)	XXII
B.14	Sieve slit: linear parameters as a function of θ_{tgt} (3)	XXIII
B.15	Sieve slit: linear parameters as a function of θ_{tgt} (4)	XXIII
B.16	Sieve slit: linear parameters as a function of θ_{tgt} (5)	XXIV
B.17	Sieve slit: linear parameters as a function of θ_{tgt} (6)	XXIV
B.18	Sieve slit: linear parameters as a function of θ_{tgt} (7)	XXV
B.19	Sieve slit: linear parameters as a function of θ_{tgt} (8)	XXV
B.20	Sieve slit: linear parameters as a function of θ_{tgt} (9)	XXVI
B.21	Sieve slit: determination of coefficients for ϕ_{tgt} calibration (1)	XXVIII
B.22	Sieve slit: determination of coefficients for ϕ_{tgt} calibration (2)	XXVIII
B.23	Sieve slit: Definition of the rows	XXIX
B.24	Sieve slit: projections of row 2 and fit (a)	XXX
B.25	Sieve slit: projections of row 2 and fit (b)	XXXI
B.26	Sieve slit: projections of row 3 and fit (a)	XXXII
B.27	Sieve slit: projections of row 3 and fit (b)	XXXIII
B.28	Sieve slit: projections of row 4 and fit (a)	XXXIV
B.29	Sieve slit: projections of row 4 and fit (b)	XXXV

B.30 Sieve slit: projections of rows 5-7 and fit (a)	XXXVI
B.31 Sieve slit: projections of rows 5-7 and fit (b)	XXXVII
B.32 Sieve slit: projections of row 8 and fit (a)	XXXVIII
B.33 Sieve slit: projections of row 8 and fit (b)	XXXIX
B.34 Sieve slit: projections of row 9 and fit (a)	XL
B.35 Sieve slit: projections of row 9 and fit (b)	XLI
B.36 Sieve slit: projections of row 10 and fit (a)	XLII
B.37 Sieve slit: projections of row 10 and fit (b)	XLIII
B.38 Sieve slit: fit of the $a(\phi_{tgt}, x_{fp})$ as a function of ϕ_{tgt}	XLVI
B.39 Sieve slit: fit of the $b(\phi_{tgt}, x_{fp})$ as a function of ϕ_{tgt}	XLVII
B.40 Sieve slit: fit of the $c(\phi_{tgt}, x_{fp})$ as a function of ϕ_{tgt}	XLVIII
B.41 Sieve slit: determination of \tilde{b}_{ijk} for $k=0$	LI
B.42 Sieve slit: determination of \tilde{b}_{ijk} for $k=1$	LII
B.43 Sieve slit: determination of \tilde{b}_{ijk} for $k=2$	LIII
B.44 Sieve slit: result of the calibration (1)	LV
B.45 Sieve slit: result of the calibration (1)	LVI
B.46 Sieve slit: result of the calibration (1)	LVI
B.47 Sieve slit: result of the calibration (1)	LVII
B.48 Sieve slit: result of the calibration (1)	LVII
B.49 Aberration as two-dimensional mapping	LIX
B.50 Definition of the spline variables	LX
B.51 Example of spline interpolation of one spectral line	LXI
C.1 ^{26}Mg spectrum for the energy calibration (part 1)	LXX
C.2 ^{26}Mg spectrum for the energy calibration (part 2)	LXXI
C.3 PVA spectrum for the energy calibration	LXXII
C.4 ^{24}Mg spectrum for the energy calibration	LXXII
C.5 Residuum of the fit function matching channels and Br values (unshifted and shifted)	LXXV
C.6 Correspondence between Channel number and Br value	LXXVI

List of Tables

1.1	Selection rules for Fermi (F) and Gamow-Teller (GT) transitions. The transitions connect an initial state with angular momentum and parity J_i^π and isospin quantum numbers T_i, T_{zi} to a final state with quantum numbers J_f^π, T_f, T_{zf}	3
2.1	Specifications of the RCNP cyclotrons [Kat89].	12
2.2	Specifications of the Grand Raiden magnetic spectrometer [Kat89, Ada07, Shi05].	13
2.3	Specifications of the MWDCs [Nor91, Ada07, Shi05].	16
2.4	Overview of matching conditions.	21
2.5	Magnet settings of the WS course used for the experiments E237 and E273	22
4.1	Summary of the spectrum deconvolution for excitation energies 0-6.5 MeV.	46
4.2	Summary of the spectrum deconvolution for excitation energies 6.5-16 MeV.	48
4.3	Summary of the spectrum deconvolution for excitation energies 0-10 MeV.	57
4.4	Summary of the spectrum deconvolution for excitation energies 10-16 MeV.	60
4.5	Summary of the spectrum deconvolution for excitation energies 16-25 MeV.	62
4.6	Laboratory scattering angle ranges and corresponding opening angles. . .	67
4.7	Scattering angles in the center of mass and the laboratory frame.	70
4.8	Intensity of the ^3He beam (^9Be target).	71
4.9	Efficiency of the MWDCs (^9Be target).	72
4.10	Efficiency of the MWDCs (^{13}C target).	72
4.11	Intensities of the ^3He beam (^{13}C target).	74
4.12	Total intensity of the ^3He beam on the ^{13}C target	74
5.1	Masses (from [Aud03]) and corresponding reaction Q-values.	76

5.2	Optical potential parameters for ^{12}C from ^3He elastic scattering by <i>Yamagata et al.</i> [Yam95] and <i>Kamiya et al.</i> [Kam03].	76
5.3	0° differential cross-sections for ^{13}N $\Delta L=0$ levels	80
5.4	Absolute differential cross-sections for ^{13}N levels	86
5.5	0° differential cross-sections for ^9B $\Delta L=0$ levels	87
5.6	Absolute differential cross-sections for ^9B levels	93
5.7	B(GT) values obtained for $^{13}\text{C}(\text{g.s.}) \rightarrow ^{13}\text{N}(E_x)$	99
5.8	B(GT) values obtained for $^9\text{Be}(\text{g.s.}) \rightarrow ^9\text{B}(E_x)$	102
6.1	survey of B(GT) values obtained for $^{13}\text{C}(\text{g.s.}) \rightarrow ^{13}\text{N}(E_x)$	107
6.2	B(GT) ratios in ^{13}N	108
6.3	B(GT) values obtained for $^9\text{Be}(\text{g.s.}) \rightarrow ^9\text{B}(E_x)$, derived from (p,n) data by Pugh [Pug85]	109
6.4	B(GT) ratios in ^9B	111
6.5	B(GT) values for the lowest levels in ^9B from shell model	112
B.1	θ_{tgt} positions corresponding to the column numbers.	IX
B.2	Results of the linear fit connecting y_{fp} to original ϕ_{tgt} position via $\phi_{tgt} = ay_{fp} + b$	XX
B.3	Results of the fit of $a(\theta_{tgt}, x_{fp})$ and $b(\theta_{tgt}, x_{fp})$ as a function of θ_{tgt} for different x_{fp} positions.	XXI
B.4	Results of the fit of $\alpha_{a,b}, \beta_{a,b}, \gamma_{a,b}$ and $\delta_{a,b}$ as a function of focal plane position.	XXVII
B.5	Results of the fit connecting θ_{fp} to the original θ_{tgt} position via $\phi_{tgt} = a + b\theta_{fp} + c\theta_{fp}^2$	XLIV
B.6	Results of the fit of the parameters a, b and c as a function of ϕ_{tgt}	XLIX
B.7	Reconstruction of θ_{tgt} : summary of \tilde{b}_{ijk} coefficients	LIV
C.1	Thickness of targets used in the experiments.	LXXI
C.2	Energy levels used for the energy calibration of the spectrum.	LXXIII
C.3	Shift terms of Br against the calculated values for ^{26}Al	LXXIV
C.4	Parameters of the energy calibration function for various nuclei.	LXXIV
D.1	Raytracing information of the MWDCs.	LXXVIII
E.1	Evolution of the relative cross sections for various excitation energies for the $^9\text{Be}(^3\text{He}, t)^9\text{B}$ reaction.	LXXX

E.2	Evolution of the relative cross sections for various excitation energies for the $^{13}\text{C}(^3\text{He},t)^{13}\text{N}$ reaction.	LXXXI
-----	---	-------

Acknowledgements

This work would not have been possible without the help and support of many people, which I sincerely want to thank.

My gratitude goes to Prof. Y. Fujita and Dr. T. Adachi for inviting me to Osaka to perform ($^3\text{He}, t$) experiments at the GRAND RAIDEN spectrometer, supporting my stay in Japan and providing invaluable help with the analysis. I will always remember the time spent in Japan as a very special part of my life.

I also wish to thank all other collaborators in the ($^3\text{He}, t$) experiments for the great effort and teamwork which provided the data basis for this thesis. They are, in alphabetical order: Hisanobu Hashimoto, Prof. Kichiji Hatanaka, Hiroaki Matsubara, Kohsuke Nakanishi, T. Ohta, Yasuhiro Sakemi, Prof. Yoshihiro Shimbara, Yukio Shimizu, Yuji Tameshige, Prof. Atsushi Tamii, Prof. Masaru Yosoi and Prof. Remco Zegers.

I also want to thank Prof. Jolie and all other people in the *Institut für Kernphysik* for excellent working conditions.

I am deeply indebted to Prof. von Brentano for giving me the opportunity to write this work and for supporting me all along the way.

The excellent ^{13}C targets made by Dr. K.O. Zell were invaluable for the experiment.

I also owe a lot to Prof. R. Zegers, Prof. R.V. Jolos, Prof. A. Gelberg and to Dr. G. Martinez-Pinedo for helpful discussions on the analysis.

The financial support of the *Deutsche Forschungsgemeinschaft* (DFG) under contracts Br 799/13-1 and the Ministry of Education Culture, Sports, Science and Technology (MEXT) of Japan under the *21st Century Center of Excellence Program* was much appreciated.

Finally I want to thank my family, my parents and my wife Julia for their love, care and support.

Erklärung

Ich versichere, daß ich die von mir vorgelegte Dissertation selbständig angefertigt, die benutzten Quellen und Hilfsmittel vollständig angegeben und die Stellen der Arbeit – einschließlich Tabellen, Karten und Abbildungen – , die anderen Werken im Wortlaut oder dem Sinn nach entnommen sind, in jedem Einzelfall als Entlehnung kenntlich gemacht habe; daß die Dissertation noch keiner anderen Fakultät oder Universität zur Prüfung vorgelegen hat; daß sie – abgesehen von unten angegebenen Teilpublikationen – noch nicht veröffentlicht worden ist, sowie, daß ich eine solche Veröffentlichung vor dem Abschluß des Promotionsverfahrens nicht vornehmen werde. Die Bestimmungen dieser Promotionsordnung sind mir bekannt. Die von mir vorgelegte Dissertation ist von Professor Dr. P. von Brentano betreut worden.

Ein Teil der Ergebnisse ist in
C. Scholl *et al.*, AIP Conf. Proc., Volume 1090, pp. 544-548
veröffentlicht worden.

Lebenslauf

Name		Clemens Scholl
Anschrift		Maria-Hilfstr. 8, 50677 Köln
Geburtsdatum/-ort		12/1/1981 in Salzburg (Österreich)
Nationalität		deutsch
Eltern		Rudolf Rieser Dr. Bernadette Scholl
Verheiratet mit		Julia Scholl, geb. Gribkova
Schul Ausbildung	1988–1992	Ecole Sainte-Marie, Warnant-Dreye, Belgien (Certificat d'études de base)
	1992–1996	Institut Libre du Condroz, Section Val-Notre-Dame, Antheit, Belgien
	1996–1998	Collège Saint-Benoît de Maredsous, Abtei Maredsous, Belgien (Certificat d'enseignement secondaire supérieur)
Hochschulstudium	09/1998	Immatrikulation an der Universität zu Köln für das Studienfach Physik (Diplom)
	10/2000	Vordiplom in Mathematik
	02/2001	Vordiplom in Physik
	10/2005	Miniforschungspreis 2005
Studienabschluß	07/2006	Diplom im Fach Physik Thema der Arbeit: "Spin and Isospin in the odd-odd N=Z nucleus ^{42}Sc "